Role of membrane tension in the spatial regulation of lysosomal exocytosis

Hugo Lachuer

PSL UNIVERSITÉ PARIS

THÈSE DE DOCTORAT
DE L'UNIVERSITÉ PSL

Préparée à l'Institut Curie

Rôle de la tension de membrane dans la régulation spatiale de l'exocytose lysosomale

Role of membrane tension in the spatial regulation of lysosomal exocytosis

Soutenue par
Hugo Lachuer
Le 05 septembre 2022

Ecole doctorale n° 515
Complexité du vivant

Spécialité
Biologie cellulaire

Composition du jury :

Olivia, DU ROURE Directrice de recherche, ESPCI	*Présidente*
Laura, PICAS Chargée de recherche, Institut de Recherche en Infectiologie de Montpellier	*Rapporteure*
Aurélien, ROUX Professeur des universités, Université de Genève	*Rapporteur*
Thierry, GALLI Directeur de recherche, Institut de Psychiatrie et Neurosciences de Paris	*Examinateur*
Kristine, SCHAUER Directrice de recherche, Institut Gustave Roussy	*Directrice de thèse*
Bruno, GOUD Directeur de recherche, Institut Curie	*Co-directeur de thèse*

institutCurie | PSL

“I have sometimes thought of the phenomenon called 'total reflexion' in optics as a good symbol of the relation between abstract ideas and concrete realities, as pragmatism conceives it. Hold a tumbler of water a little above your eyes and look up through the water at its surface—or better still look similarly through the flat wall of an aquarium. You will then see an extraordinarily brilliant reflected image say of a candle-flame, or any other clear object, situated on the opposite side of the vessel. No candle-ray, under these circumstances gets beyond the water's surface: every ray is totally reflected back into the depths again. Now let the water represent the world of sensible facts, and let the air above it represent the world of abstract ideas. Both worlds are real, of course, and interact; but they interact only at their boundary, and the locus of everything that lives, and happens to us, so far as full experience goes, is the water. We are like fishes swimming in the sea of sense, bounded above by the superior element, but unable to breathe it pure or penetrate it.”

William James, Pragmatism, Lecture IV (1907).

Acknowledgements

Since the beginning of my doctoral thesis, I thought about how to write the acknowledgments. I changed my mind a plethora of times but it remained clear that this section would be long, and it is. When I was an undergraduate student reading experimental cell biology papers, I did not understand why it could take 3 or 4 years to do it. My thesis work made me realize how actual research is far from the naive scientific method sometimes taught: make observation, do a hypothesis and test it. The reality appears to me more chaotic but I believe this tortuous path was necessary to form me as a scientist. My thesis journey also made me realize how much current science is influenced by non-scientific factor: financial, political, sociological, etc. I am constrained to accept Paul Feyerabend's conclusion "Science has ceased to be a philosophical adventure and has become a business" (Against Method, 1975). Scientific institutions are twisted from the exterior by political forces to orient them toward technology, utility and profitability. Despite this pessimistic conclusion, I believe there are still people inside these institutions envisaging science as a will to know. My thesis adventure has been mainly accompanied by colleagues; therefore I wish to dedicate my acknowledgements to them, I hope that my friends and family will not hold that against me.

First of all, I would like to deeply acknowledge my PhD supervisors Kristine Schauer and Bruno Goud. During our first meeting Kristine, you told me that you let your students explore freely the subject. I am grateful for this freedom that allowed me to explore science in my own way, a computational way. I owe you the opportunity to develop an inter-disciplinary culture. We have many disagreements and I guess it is the expected consequence of discussion between two passionate spirits with different backgrounds. It has been a pleasure to work with an open minded and stimulating person: you introduced me to the topic of archaeal eukaryotic origin and found collaborations for innovative approaches such as FLIM. I also acknowledge you for your exigencies with my results teaching me the rigor of the scientific method. I likely inherited from you my interest for the spatial organization of the cell (but not your passion for Myo1C) even if we explore this question in different ways. Congratulations for the set-up of your laboratory and your DR status. I wish to the new Schauer's lab many beautiful scientific discoveries.

Bruno, I always saw you as a person working in the shadows but dedicated to your laboratory. Despite your administrative responsibilities, you managed to keep your lab working with money, papers, collaborations and most importantly scientific quality. I would also keep in my memories the anecdotes that you shared with parsimony, especially your interview with George Emil Palade when you were a young student in the USA (I cannot talk about how you got your driving license here). For the curious minds, Palade asked Bruno to have a look at a Romanian map in his office and to try to detect an anomaly. Bruno was supposed to find that the map reported a bridge on the Danube that had actually never been constructed (tricky interview…). I am also grateful for your support during the publication process but also your help and your efficiency to read and correct my thesis manuscript. I wish you to lessen your administrative charge to focus more on what you appreciate the most during your emeritus.

My thanks then go to me immediate colleagues from the Goud's team. Sabine Bardin, the permanent engineer of the team, you greatly contribute to the experimental quality of the laboratory and the friendly atmosphere. You taught me so many things from the experimental side: from cell culture to western blot. You also gave me basis for molecular biology but I regret not having had the time to

learn more from you. I promise that my cloning skills will progress during my post-doc. For 5 years, I realized how dedicated you are as a lab-manager (UMR-manager?)! You keep the lab well organized, spend so many times placing orders for us, fixing our problems and more recently you handle the shifting process to minimize the impact on our experiments. I know how energy and time consuming your work is: thank you for all you are doing. If I should choose a single French word to characterize your work as engineer and lab manager, I would choose: “carré”! Even if your questions about cell size between conditions during labmeeting is on the verge to become an obsession. Of course, you have also been a precious colleague from the social aspects; we shared many lunches and good moments, but also our daily irritations about some facets of the institute. Finally, I would like to say how easy and pleasant it is to work with a person with your human qualities. I wish to you new emulating projects, in science or in any another field.

I wish to express all my gratitude to my colleagues from the “Schauer sub-team”. Pallavi Mathur, you are definitely my lab-mate and even my doppelganger: we started our PhD together, we experienced many experimental disappointments in parallel, supported each other and spend so many hours in meetings together, and now we are both trying to publish our paper, doing our revision and preparing our PhD defense. I saw you accomplish great cell biology work even if it took my time to correctly understand your entire mTORC1 story (honestly, the redaction of my own manuscript helps me a lot in my understanding of the complicated mTORC1 pathway). I wish you the very best for your post-doc, you already demonstrated how talented you are for cancer and cell signaling problems during your PhD project. There is no doubt: you will rock your post-doc as well! Thank you for your kindness and your supportive behavior during four years. Your help was precious to me, scientifically and emotionally. Anahi Capmany, we did not exchange so much but the very first labmeeting I saw in the team as a master intern was yours. I kept a precise memory of my feelings after your presentation: I am definitely in the good lab to do exciting cell biology projects. I saw you working as hell, dedicated to your work but always friendly and chill. I regret not having had the occasion to spend more time with you but I am sure that you are doing exciting *Chlamydia* projects in Argentina. Katerina –Katka– Jerabkova, you are the second Kristine’s post-doc that I met. Even if your passage in the lab was quick, I really appreciated your presence in the team. As Anahi (but in a different style of course!) you found a nice balance between rigorous and dedicated work, and a friendly and social behavior (Kristine is definitely talented for post-doc recruitment). The first time I saw you, I predicted that I would appreciate you because of your science curiosity and your wonder for biological discoveries (and also because of your lovely geeky t-shirts). I hope you spend nice days in Strasbourg, I saw you already published a nice paper: promising for the future. (I continue to use your western blot buffers, thank you for allowing me to be lazy and never re-do new buffers).

In the sub-team, Kristine always promoted interdisciplinarity, especially with physics. Mathieu Coppey, you are one of the first biophysicist I interacted with. We had many weekly meetings with you and your students. Discussions with you helped me to understand the physical approach of living systems but also (and maybe more importantly) contributed to give me a taste for biophysics. You introduced me to one of your PhD students, co-supervized by Kristine, Kotryna Vaidziulyte. Kotryna, your unwavering good mood is almost suspicious. How do you stay as kind, smiling and peaceful in a thesis even when you face obstacles, from experiments to your defense? Anyway, I can testify how easy and funny it is to discuss with you. Your fancy mind produced at the same time an excellent paper but also created the “cell migration dance” (now well-known by specialists): congratulations. I hope to cross your path again in the future and good luck for your promising post-doc.

Now Kristine has set up her own lab in the Institut Gustave Roussy (congratulation again Kristine). This lab is animated by Alexandre Leuci, Enma Ouni and Julie Patat. Unfortunately, we have had only few meetings together and I regret not to know you better. Alexandre you always have a good joke in mind and I know how precious it is for colleagues to have someone in the lab with such good mood, especially during bad days. Enma, we discussed how we could combine your microscopic acquisitions with my quantitative approaches. Unfortunately, I think we never had the time to push this way but I appreciated to explore these possibilities with you. Science is also made of discussions without tangible impact but it creates stimulations. Julie, you seem to be the new PhD student that takes care of the historical project of the team after Camilla and Pallavi: lysosomes and cancer. Camilla and Pallavi already demonstrated how exciting it is to explore this path but your journey, as their, will be made of many obstacles (and also many joys of course): good luck!

My days in the Schauer subteam are also marked by some great interns that I would like to acknowledge. Anna Yevtushenko, you came from Munich to spend a few months with us. It was really pleasant to work with you. You are an extremely benevolent, curious and friendly person. Despite your efforts I forgot what you taught to me about Cha-cha-cha. I hope that you will enjoy your carrier in pharmacology. I also had the pleasure to supervise two top-notch M2 interns: Pauline Lahure and Anaïs Molineri. You are both two persons easy to work with, you produced great quality work and I learned from our scientific and non-scientific discussions. Pauline, we started your internship with promising results but we have been stopped by the COVID-19 lockdown. We continue to work remotely and our daily exchanges contributed to keep me in a good mood. It is always a pleasure to share a drink with you and chat about politics. You give off a kind of “unconcern stoicism” that is an incredible source of fun and is anxiolytic. I hope that you find your marks as a teacher and that you will thrive in this role. Anaïs, you often challenged me with skeptical questions and your “divergent thinking”. It was extremely rewarding to work with you. I sometimes see our professional paths as mirrored. You started from quantum physics to reach medicine today, and I started medicine to reach biophysics today. We meet each other halfway, at the cell biology corner. Pauline and Anaïs, I hope your internship has been as rewarding for you as your presence has been for me.

The second sub-team in Bruno’s lab is (or was) the Manneville team. Jean-Baptise Manneville you and your team has been an incredible source of stimulation for me, which has been important in my learning of biophysics and quantitative methods. Even if you were not that present in the lab and if we did not discuss that much, I am convinced that you infused an interdisciplinary spirit in the lab to whom I owe a lot. Thank you for that. I wish you all the best with your new team; I will of course follow the rest of your adventure at MSC. Manneville’s subteam welcomed excellent students. First of all, Nathan Lardier (also called Nardier, or even Nardouille). I do not know exactly why but you always evoked me Africa. Your naive mind and your clumsy gesture (making me suspecting that you suffered of a cerebellar ataxia) suggested your second nickname: “girafon” (the French word for baby giraffe). Besides too much time distinguishing riddles, making fun of your unexpected reactions, political debates, I will especially memorize our discussions about my “physics questions”. You spent time to pedagogically answer many of my questions (almost as many as the questions you did not answer). Even if most of your answers sounds like “it is thermodynamics”, you helped me understand important principles of physics: thank you for that. I would like to thank you again for the time you spent checking my lecture notes. I would like to share the memory of a moment that I particularly enjoyed at your side. It was during a late evening at lab, together in front of the whiteboard, thinking together about the “secret Santa perfect loop mathematical problem” instead of working on our PhD

projects. I remember clearly that I told myself that the possibility to explore freely intellectual problems with colleagues only for the pleasure of thought was the privilege of research and it is definitely one of the reason why I would find it very difficult to do any other job. Congratulations for your PhD defense and for your first year of teaching. I know that your students are lucky to have you as a teacher. And now comes the third player of our trio with Nathan and me: David Pereira. I know that you are already upset because I mentioned the "students of the team" and you were a post-doc (and now you are again more upset because you hate appeal to motive, how predictable you are!). It bothers me to admit it, but I owe you one or two things (maybe more but certainly not the difference between plastic and elastic deformation). First, your emblematic "mauvaise foi" taught me how to carry on a conversation in a extremely rigorous and unassailable way. Second, you introduced me to the "sociology of research" when I was still at the beginning of my PhD and it clearly avoided me many mistakes. Finally, our numerous conversations about science and technical details helped me a lot in my ability to run and analyze experiments in a rigorous way. Despite your tendency to repeat the same things over and over again, present trivial principles as extremely advanced and your love for immature games (actually I appreciate this last point, especially our competition to the "round with fingers" game or our lost hours playing GeoGuess), your presence in the lab brought a pleasant atmosphere for all the team. I wish you all the best for your personal and professional life, both look full of nice challenges for you. Now come the moment of the self designated "senior PhD student" but designated by myself as "petit kitten": Yamini Ravichandran. I know that you wish I remembered your general, inspired and "TED-talk"-like advice but I mainly keep in my memories laughter and gossiping moments. Your ice cream breaks and your social behavior bring a lot in our team even if you were present only a few days a week in our lab (but I know that you secretly preferred your Curie team to your Pasteur team). Take care of you and enjoy your post-doc in the Roux lab! Finally, I also appreciated the company of Tanguy Chocat (also designated as "Choca-dance" by David) as a master intern in our lab. The first day I met you, you expressed a (correct) opinion about the inclusion of Nantes in Brittany: I immediately appreciated you. I am impressed about how you stayed perseverant in your research of a PhD, and I sincerely hope that it will be a nice adventure.

I would like to address my sincere acknowledgements to the other members of the Goud team. First of all, Stéphanie Miserey-Lenkei. Thank you for your advice during the labmeetings, your efforts to create social activity in the team and for sharing aliquots from your huge personnal collection of drugs. I regret not having had more time to work with you on the TFM project and its correlation with intracellular events. Good luck to Chandini Bhaskar-Naidu for the new PhD journey that you just started. Your project is scientifically fascinating and I know that with Jean-Baptiste and Stéphanie you are between good hands. Thank you, Pierre Simonin for helping us in the lab as an engineer and good luck for your organoid/mouse project! I would like to address my sincere and deep acknowledgements to Marie-Thérèse –Maïté– Prosperi for your kindness towards me and your interest for biostatistics. I am grateful that you involved me in your project and for trusted me for the quantitative analysis. I hope that you appreciate your last professional adventures in the melanosomes world! Of course my acknowledgements to Maïté are associated to my gratitude toward Evelyne Coudrier. Thank you for putting me in charge of the statistics of your Plekhh1 paper, it has been a precious opportunity. I hope that you enjoy your retirement and that you are taking care of yourself. Evelyne and Maïté, it was a pleasure to hear about your myosin stories for a couple of years. To end with, I would like to pay tribute to the late Michel Bornens. Unfortunately, I only had little contact with Michel but it was sufficient to be inspired by him. I will remember his insatiable curiosity and his effort to stem for cell biology discoveries in the lap of evolution.

My PhD work has required many hours (and even days) of microscopy. It is therefore an obligation to address my acknowledgments to the microscopy team: Vincent Fraisier for fixing all my issues with the TIRF and being enough patient to help me with all my difficulties, Chloé Guedj for your support and for introducing me to FRET microscopy, François Waharte for introducing me to the secrets of the TIRF and Lucie Sengmanivong for handling the TIRF reparation with the Nikon staff. I spent so much time with the TIRF that I should also address my gratitude to this machine. It was a real love story with ups and down: at the beginning I immediately fell in love of your incredible optical capacities, but after some months I discovered all your bugs and problems and thought many time to leave you for a younger system… But after more effort I have learned how to deal with your drawbacks, we spent nights together and I think we produced not that bad images. I acquired and manually detected 175 287 events of exocytosis, representing 6.7 days of acquisition with you. To finish with the microscopic team, I would like to thank Anne-Sophie Macé for our neural network collaboration. Even if it did not give immediate fertile results, it was a stimulating side project and it was a good occasion to learn new deep learning tricks. It was a pleasure to collaborate with you. Congratulation for your CNRS engineer position, you deserve it!

My PhD journey has been accompanied by nice collaborations and I would like to render thanks to the persons involved in these collaborations. Thank you Sandrine Lévêque-Fort for welcoming me at the ISMO and letting me use your TIRF-FLIM, and Laurent Le for the time we spent doing microscopy and discovering together this surprising membrane tension gradient. I particularly appreciated my visits to your lab notably for the friendly and stimulating atmosphere. I learned a lot from our physical discussions. I am honored to have both of you as co-authors on my paper. Actually, I started Flipper-TR measurement before the experiments at ISMO with Marc Tramier and Giulia Bertolin at Rennes. Thank to Giulia and Marc for welcoming me in your lab and letting me try your FAST FLIM system. It was a pleasure to work with such rigorous and supportive persons. Thanks to you, I produced preliminary results that led to the collaboration with Sandrine and Laurent. Talking about Rennes, I also address my gratitude to the members of the SERPICO team, Charles Kevrann and Emmanuel Moebel for helping Anne-Sophie and me with neural network and applying DeepFinder to exocytosis detection. It gives great results and I am sorry to miss the time to push it further. I have also to thank you Alexandre Baffet for trusting me for the biostatistical analysis of one of your paper. Here again, this collaboration helped me a lot as a young scientist considering an academic career. I would like to address my acknowledgments to Véronique Sebille and Yseulys Dubuy for accepting to collaborate on our small side project about biostatistics. I think our project was intellectually challenging and I would have been lost (erring in the Markov world) without your help Yseulys, I hope we will be lucky in the publication process… About biostatistics, I am grateful to Kevin Bleakley for his support for my first publication, to Ute Hahn for taking the time to explain me your work on spatial statistics and to Tarn Duong for your explanation about MISE and checking my code. I also address my acknowledgements to Pierre Sens for our attempts to make a theoretical model of exocytosis spatial organization, to Paolo Pierobon for our (long) talks that were always enriching and encouraging.

The proper functioning of the lab is allowed by plenty of persons in charge of support functions. Thank you Aurélie Lima for the administrative mess that you constantly handle for us. Thank you Charlotte Lozach for managing the administrative tasks in the units (and proposing biscuits and tea (or other drinks…) in your lovely office). Thank you Chedly Chaabani for preparing all our buffers and

media and your constant good mood. Thank you Edwige Delage and Slimane Amin for taking care of the reception of the building.

Fortunately, my PhD journey was not limited to experiments in the lab but I also had the opportunity to do teaching. I agree with Feynman that teaching helps a lot to keep scientific excitement and motivation, as he said “In any thinking process there are moments when everything is going good and you’ve got wonderful ideas. […] And then there are the *longer* periods of time when not much is coming to you. You're not getting any ideas, and if you're doing nothing at all, it drives you nuts! You can't even say "I'm teaching my class.”” (Surely You're Joking, Mr. Feynman!, 1985). First, I am extremely grateful to Chiara Fracassi for allowing me to teach in the CRI AIRE master. Every year, I am waiting my teaching period to share with students my passion and try to find new tricks to blow them with scientific beauty. It also challenges my own understanding of several topics: teach something clearly ask me to push my comprehension at a deeper level in different topics. I would also like to express my deep gratitude for you Thierry Botans. You gave me the opportunity to present scientific stories in front of your class every year even when I was inexperienced. This annual meeting forces me to prepare each year a new presentation on the wonderful stories of evolutionary biology and do a bibliography that I would not do otherwise. Your students are each year extremely curious and enthusiastic, giving me motivation for the full year. I know how lucky they are to have such a dedicated and passionate teacher as you.

I also want to thank members of my thesis committee. Thank you Anna-Maria Lennon-Duménil for your inputs and your support for fundamental science, Gilles Toumaniantz for your encouragements and advice and Sofia Benkhelifa for your involvement.

To finish this already too long section, I would present my acknowledgments to the member of my thesis jury. Thank you Olivia du Roure for your participation, we should meet each other again in the next months for my post-doc. Thank you Thierry Galli for your participation and also your helpful advice about VAMP7 (after all you are the pope of this protein). I started my project with a meeting with you and Kristine and the reading of your publication in iScience and now I will finish it with you in my jury. Thank you Aurélien Roux and Laura Picas for accepting to be referees of this long (sorry for that) PhD manuscript.

I hope that these long acknowledgments illustrate that modern science is a collaborative process and my project has been supported by many persons. Unfortunately, new private management organized competition between scientists altering collaborations and creates toxic environments. Despite this sad reality, I wish to future PhD students to be as lucky as me with the persons they will collaborate with. I address again my sincere acknowledgments to all the persons who contributed to make of my PhD an exciting journey.

Contents

List of acronyms

List of acronyms (and other abbreviations) is divided in 3 sections: common acronyms, protein acronyms and other molecule's acronyms. Each acronym is explained in the text at its first occurrence (and possibly re-explained if needed).

Common acronyms by alphabetical order:

AFM: Atomic Force Microscopy
ALR: Autophagic Lysosome Reformation
CAF: Cancer Associated Fibroblast
CLEAR: Coordinated Lysosomal Expression And Regulation
CLIC: Clathrin-Independent Carrier
CLT: Central Limit Theorem
CMA: Chaperone-Mediated Autophagy
CSR: Complete Spatial Randomness
ECM: ExtraCellular Matrix
EE: Early Endosome
ELR: Endocytic Lysosome Reformation
EM: Electron Microscopy
EMD: Earth Mover's Distance
ER: Endoplasmic Reticulum
ERC: Endocytic Recycling Compartment
ERGIC: Endoplasmic Reticulum Golgi Intermediate Compartment
ESD: Empty Space Distance
FA: Focal Adhesion
FECA: First Eukaryotic Common Ancestor
FLIM: Fluorescence-Lifetime Imaging Microscopy
FRAP: Fluorescence Recovery After Photobleaching
FRET: Förester Resonace Energy Transfer
GEEC: GPI-Enriched Endocytic Compartment
GUV: Giant Unilamellar Vesicle
ILV: IntraLuminal Vesicle
KD: Knock Down
KDE: Kernel Density Estimation
KO: Knock Out
LDCV: Large Dense-Core Vesicle
LDL: Low Density Lipoprotein
LE: Late Endosome
LECA: Last Eukaryotic Common Ancestor
LEL: Late Endosome Lysosome
LRO: Lysosome-Related Organelle
LSD: Lysosomal Storage Disorder
LUV: Large Unilamellar Vesicle
MAD: Maximum Absolute Deviation
MCS: Membrane Contact Site
MLIV: MucoLipidosis type IV
MT: MicroTubule
MVB: MultiVesicular Body
NESS: Non-Equilibrium Steady-State
NND: Nearest Neighbor Distance
NPD: Niemann-Pick Disease
PDAC: Pancreatic Ductal AdenomaCarcinoma
PDE: Partial Differential Equation
PLR: Phagocytic Lysosome Reformation
PM: Plasma Membrane
PMR: Plasma Membrane Repair
PPP: Poisson Point Process
RE: Recycling Endosome
ROS: Reactive Oxygen Species
SMLM: Single Molecule Localization Microscopy
TAM: Tumor Associated Macrophage
TGN: Trans-Golgi Network
TIRFM: Total Internal Reflection Fluorescence Microscopy
ts: thermosensitive
VLD: Vacuole-Like Dilation
VSV: Vesicular Stomatitis Virus
WT: Wild Type

Acronyms of protein names (including protein domain and protein family) by alphabetical order:

AAA-ATPase: ATPases Associated with diverse cellular Activities-ATPase
ALG2: Asparagine-Linked Glycosylation 2 homolog
AMPK: AMP-Dependent-Protein Kinase
Arp1: Actin-related protein 1
ASM: Acid SphingoMyelinase
BK: Big Potassium
BoNT: Botulinium NeuroToxin
BORC: Biogenesis of Lysosome-related Organelle Complex (BLOC)-1-related complex
CaMKKβ: Calcium/CalModulin-dependent protein Kinase kinase β
ASM: Acid SphingoMyelinase
BK: Big Potassium
BORC: Biogenesis of Lysosome-related Organelle Complex (BLOC)-1-related complex
CaMKKβ: Calcium/CalModulin-dependent protein Kinase kinase β
CAPS: Ca2+-dependent Activator Protein for Secretion
CATCHR: Complex Associated with Tethering Containing Helical Rods
CLASP: Cytoplasmic Linker ASsociated Protein
ClC: Chloride Channel
ESCRT: Endosomal Sorting Complex Required for Transport
FLCN: FoLiCuliN
FNIP1/2: FoliculiN-Interacting Protein 1/2
FYCO1: FYVE- and Coiledcoil-domain-containing protein 1
GAP: GTPase-Activating Protein
GDI: Rab GDP Dissociation Inhibitior
GEF: Guanine Exhange Factor
HGSNAT: Heparan-α-GlucoSaminide N-AcetylTransferase
Hsc70: Heat shock cognate 71kDa
JIP4: JNK Interacting Protein 4
K2P: Two-Pore domain K+ channel
LAMP1/2/3: Lysosomal-Associated Membrane Protein 1/2/3
LIMP2: Lysosomal Integral Membrane Protein 2
M6PR: Mannose-6-Phosphate Receptor
MAPK: Mitogen-Activated Protein Kinase
MARKS: Myristoylated Akanine-Rich C Kinase Substrate
MC: Mechanosensitive Channel
MCA: Membrane-to-Cortex Attachement
MCU: Mitochondrial Ca2+ Uniporter
MDR: MultiDrug Resistance
MHC: Major Histocompatibility Complex
MMP: Metalloprotease
MscL: Large-conductance Mechanosensitive channel
MscS: Small-conductance Mechanosensitive channel
MTC: Multisubunit Tethering Complex
mTOR: mechanistic Target Of Rapamycin
Munc: Mammalian uncoordinated
NPC1/2: Niemann-Pick C1/2
NSF: N-ethylmaleimide Sensitive Factor
ORP1L: Oxysterol-binding protein-Related Protein
OSBP: OxySterol-Binding Protein
PIKfyve: PtdIns(3)P 5-kinase FYVE
PIP5K1A: PtdIns(4)P 5-Kinase Type 1 Alpha
PKC: Protein Kinase C
RILP: Rab7-Interacting Lysosomal Protein
RNF26: RiNg Finder 26
SAP: Sphingolipid Activator Protein
SBP: Streptavidin Binding Peptide
SKIP: SifA and Kinesin-Interaction Protein
SLC: SoLute Carrier
SLO: StreptoLysin O
SNAP: Solube N-ethylmaleimide sensitive factor (NSF) Attachment Protein
SNARE: Solube N-ethylmaleimide sensitive factor (NSF) Attachment Protein (SNAP) Receptor
SPPL2a: Signal Peptide Peptidase Like 2a

STARD3: Steroidogenic Acute Regulatory protein (StAR)-Related lipid-Transfer proteins (START) Domain containing 3
TeTx: Tetanus Toxin
TFEB: Transcription Factor EB
TI-VAMP: Tetanus neurotixin Insensitive Vesicle-Associated Membrane Protein
TNFα: Tumor Necrosis Factor α
TRAAK: TWIK-Related Arachidonic acid Activated K+ channel
TREK: TWIK-RElated K+ channel
Trim9: TRIpartite Motif protein 9
TRP: Transient Receptor Potential
TRPML: Transient Receptor Potential cation channel, MucoLipin subfamily
TSC: Tuberous Sclerosis Complex
VAMP: Vesicle-Associated Membrane Protein
VAPA: Vesicle-Associated Membrane-Protein(VAMP) Associated Protein A
V-ATPase: Vacuolar-ATPase
VGCC: Voltage(Gated Ca2+ Channel
VSV-G: Vesicular Stomatitis Virus - glycoprotein G
βGC: β-GlucoCerebrosidase

Other molecule's acronyms:

Acetyl-CoA: Acetyl-Coenzyme A
AMP: Adenosine MonoPhosphate
ATP: Adenosine TriPhosphate
BPM: Bis(Monoacylglycer)Phosphate
EMS: Ethyk MethaneSulfonate
FliptR: Fluorescent LIPid Tension Reporter
GDP: Guanosine DiPhosphate
GlcNAc: N-AcetylGlucosamine
GTP: Guanosine TriPhosphate
M6P: Mannose-6-Phosphate
NEM: N-EthylMaleimide
PtdIns(3)P: PhosphatidylInositol-3-Phosphate
PtdIns(3,5)P2: PhosphatidylInositol-3,5-bisPhosphate
PtdIns(4)P: PhosphatidylInositol-4-Phosphate
PtdIns(4,5)P2: PhosphatidylInositol-4,5-bisPhosphate
UDP: Uridine DiPhosphate

Introduction

Chapter 1

General considerations on the intracellular organization

"Now, after millennia of illusions, doubts, and probing, it turns out that these unique properties [of the living matter] are due to the way in which common chemical elements are put together in time and space"

George Emil Palade, "The Organization Of Living Matter", PNAS, 1964.

Chapter's summary:

One of the striking properties of the eukaryotic cell is the organization of the endomembrane system. Whereas entropic forces tend to dispel organization, each organelle has a specific spatial organization at the whole-cell scale. Based on experimental data, I argue that this organization has three key properties: non-random spatial organization, Non-Equilibrium Steady-State (NESS) and attractivity. Modeling and experimental studies reveal that these properties can be explained by a combination between diffusion and convection. Organelles shuttle between random diffusion in the cytosol and convective motion driven by molecular motors walking on microtubules. The transition from diffusion to convection is described thanks to classical kinetics models. Therefore, the organelle distribution is described thanks to a reaction-diffusion-convection model that can be reduced to a simpler diffusion-convection model thanks to an approximation on the different time scales of these processes. These models fit remarkably well experimental data. However, I explore several limits of these models (well-mixed system approximation, linear kinetics hypothesis and the choice of boundary conditions). Thanks to this biophysical description, I argue that intracellular organization is a self-organized process not relying on specific genes but on physical emerging properties.

1. Intracellular landscape

1.1. The eukaryotic cell

The eukaryotic cell is sometimes wrongly defined phenotypically as the cell with a nucleus, as suggested by the etymology of the term (constructed from the “eu-“ prefix meaning “well” or “true”, and the word “karyon” meaning nucleus). Actually, eukaryotes are defined phylogenetically as a monophyletic group of organisms. Therefore, eukaryotes are the descendents from common ancestors. We classically distinguish two kinds of ancestors, the Last Eukaryotic Common Ancestor (LECA) and the First Eukaryotic Common Ancestor (FECA). Molecular data date the LECA between 1.0-1.6 GA during the proterozoic eon. The oldest accepted eukaryotic fossil is dated back to 1.65 GA (*Valeria lophostriata*, a protist fossil). Evolutionary cell biologists usually agree that FECA appeared after the great oxidation event (2.4 GA) leading to a possible range of 0.75GA (López-García and Moreira, 2020). Recent phylogenetic analysis revel that FECA emerged from an archaeal lineage, the Asgard group. The Asgard group is named after its identification in marine sediments near the Loki’s Castle hydrothermal vents between Greenland and Norway. According to these new data, Asgard archaea is the sister group of eukaryotes (Eme et al., 2017). Because eukaryotes descent from a common ancestor, they share evolutionary novelties so-called synapomorphies. The most striking feature of the eukaryotic cell is the presence of a nucleus and compartments limited by a lipid membrane and called organelles (**Figure 1**). The process of eukaryogenesis is still poorly understood and controversial. It is still debated if the nucleus appeared before or after organelles, and when mitochondria arrived in the eukaryotic cell (López-García and Moreira, 2020). Eukaryotic cell organization varies between the different lineage and even inside a single multi-cellular organism; its organization depends on the cell type. However, we can provide a minimal description of the organelles present in the eukaryotic cell. The most large and abundant organelle is the Endoplasmic Reticulum (ER), a structure made of sheets and tubules sprawling in the whole cytosol. Beside its functions in lipid metabolism, its main role is to be an important site of protein synthesis. Connected to the ER, the Golgi apparatus is made out of a stack of membrane disks. The Golgi apparatus is the site of post-translational modifications of neo-synthesized proteins. ER and Golgi apparatus form the so-called anterograde secretory pathway, responsible for the secretion of proteins. Secreted proteins can be captured by other cells through the endosomal system, a set of small organelles involved in the capture of extra-cellular molecules. The endosomal system contains lysosomes that are small acidic organelles full of digestive enzymes. Lysosomes digest macromolecules and release the resulting building blocks into the cytosol. This endosomal system is detailed in chapter 2. Another organelle, sometimes unfairly underlooked, is the peroxisome. Peroxisomes are small round organelles often characterized by the presence of a crystalloid core. They work as a detoxification center, doing hydrogen peroxide chemistry. It has many additional functions such as β-oxidation, the fatty acids catabolic pathway. However in mammalian cells the β-oxidation takes also place in another organelle: the mitochondrion. This organelle made of a double membrane, crista structures and its own genetic material has a particular evolutionary origin. Mitochondria are ancient α-proteobacteria. It has been proposed since 60 years that these bacteria have been phagocyted into a bigger cell, a model called endosymbiosis theory. This view has been challenged recently by the hydrogen hypothesis. In this latter model, a methanogenic archaea is symbiotically associated to α-proteobacteria producing H_2 and CO_2 as a waste of its anaerobic metabolism. These waste products

are used as fuel for the energetic metabolism of the methanogenic archaea which produce methane (CH_4) as a waste (Martin et al., 2017). Although this evolutionary origin remains uncertain, it is clear that current mitochondria are the power house of the cell, producing energy, under the form of ATP though an oxidative metabolism consuming metabolites such as fatty acids and pyruvate. These different organelles (ER, Golgi apparatus, endosomes, mitochondria, peroxisomes; etc.), making the uniqueness of eukaryotes, are dispersed in the cytosol. However, contrarily to common textbook views, they are not static structures randomly distributed in the cytosol. Contrary, cells maintain a specific intracellular organization with outstanding properties (**Figure 1**).

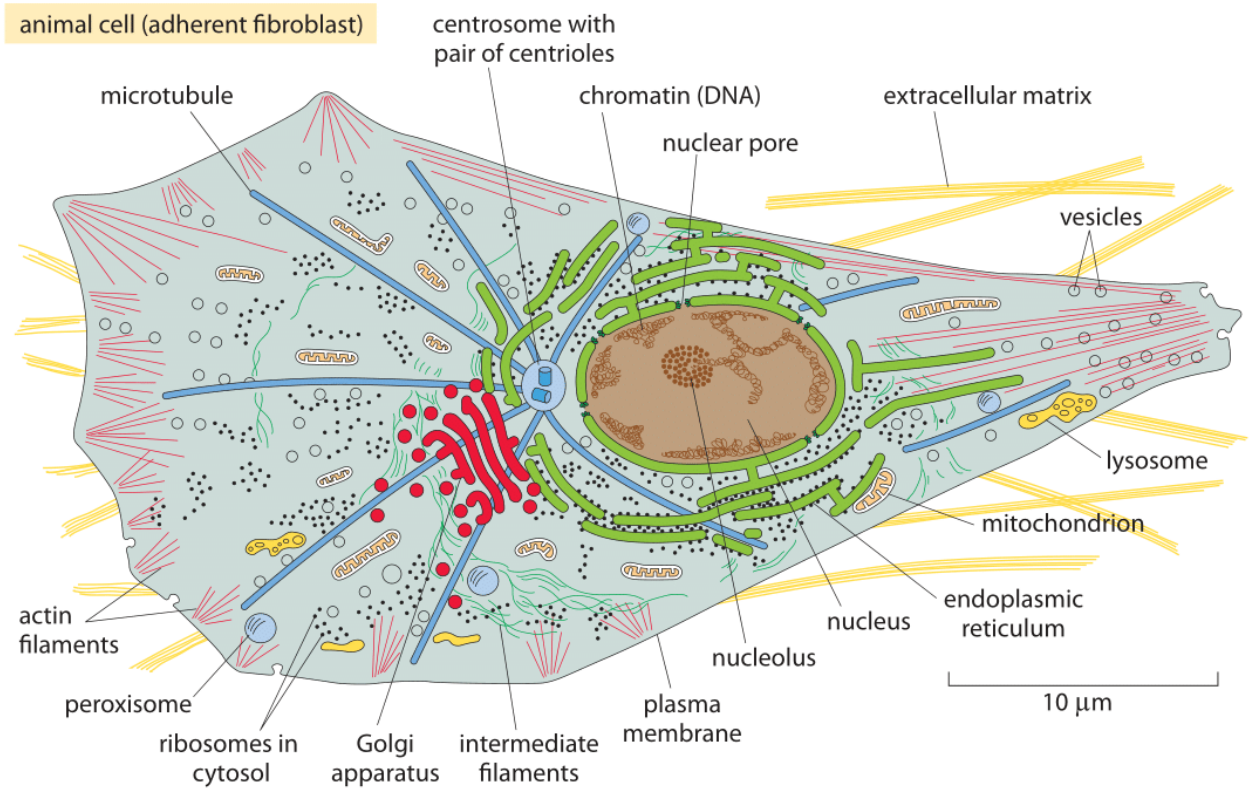

Figure 1. Eukaryotic cell, from Physical Biology of the Cell.

1.2. Intracellular organization

One outstanding conserved feature of life is its ability to spontaneously create patterns. It is such a striking feature that Jacques Monod included this criterion in his life definition under the name of autonomous morphogenesis (Monod, 1970). Patterning in living matter appears at many scales, from the spatial distribution of termite mounds over thousands of kilometers, to the hexagonal organization of an epithelium at the micrometer scale (Tarnita, 2018). My PhD work focuses on the spatial organization of lysosomal exocytosis. I would like to introduce the subject within the more general problem of cellular spatial organization, especially organization of organelles.

The eukaryotic cell is made of different organelles forming the so-called endomembrane system. This compartmentalization allows the existence of high local concentrations and the possibility to

segregate biochemical reactions that are incompatible. However, this compartmentalization requires interplay between organelles, especially by membrane exchange - known as intracellular trafficking - and a precise intracellular organization. I have identified 3 key features characterizing organelle organization: i) Organelle organization is a Non-Equilibrium Steady-State, ii) Organelle organization is not random and iii) Organelle organization has an attractive state. These features could be seen as a physical translation of the biological concept of homeostasis that is vague when applied to the endomembrane organization.

1.3. Non-Equilibrium Steady-State

The organelle landscape is often described as a steady-state, meaning that it remains fairly constant over time (Pelham, 1996). However, this steady-state statement is limited because i) the cell organization is not constant along the cell cycle (Carlton et al., 2020) and ii) the cell is a stochastic universe with small random fluctuations around a steady-state. Therefore, the steady-state statement can be seen as a good approximation at time scales shorter than the cell cycle. For example, it has been demonstrated that lysosomal organization is at steady-state during a time window of several minutes to hours (Pelham, 1996; Ba et al., 2018; Guardia et al., 2019) (**Figure 2**).

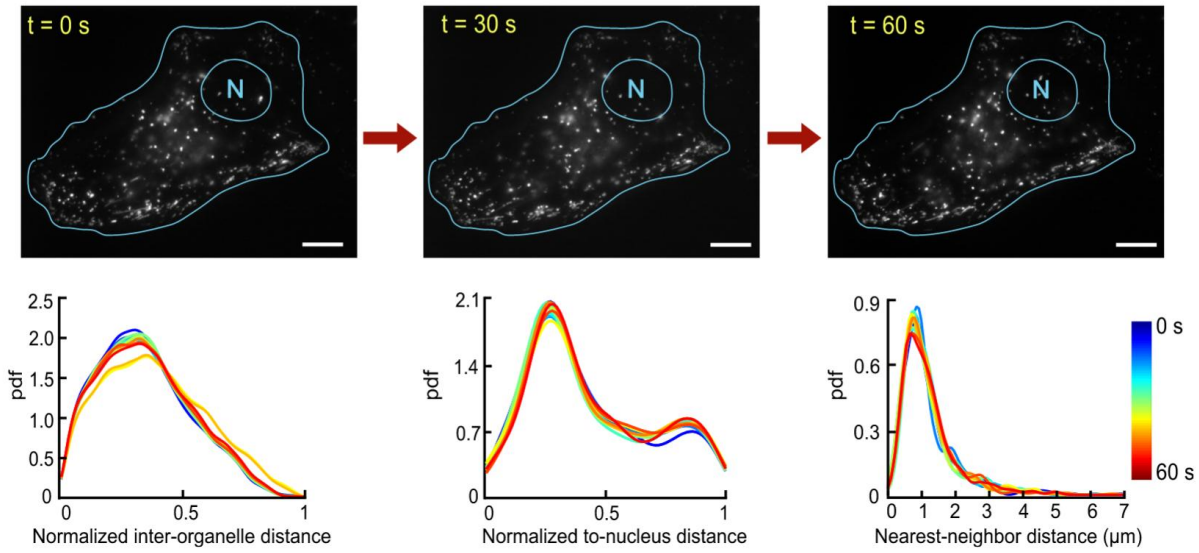

Figure 2. Lysosomal organization is a NESS, from Ba et al. (2018). Top row: Lysosomal staining for 3 time points showing that individual lysosomes move *i.e.* consume energy for active motion. Bottom row: distribution of distances (inter-organelle distance, organelle-to-nucleus distance and nearest-neighbor distance) at different time points. The distributions are stable over 1 min revealing a steady-state.

At steady-state, spatial parameters such as distance to the nucleus, inter-organelle distance and nearest-neighbor distance are constant in average. Additionally, the organelle connections (especially Membrane Contact Site (MCS)) defining the organelle network have been found to be stable during at least several minutes (Valm et al., 2017). Steady-state should not be understood as the immobility of individual organelles but the conservation of global organization despite individual movement. Due to these individual movements based on molecular-motors, the system is out of

equilibrium: it consumes energy. Such a system is called a Non-Equilibrium Steady-State (NESS) that is typical for biological samples including cells.

1.4. Non-random distribution

A basic question when organelles are observed in cells is to know if their positioning is random or not. A distribution of organelles can be simplified as a point pattern if the typical size of the object is small compared to the distances between objects. In statistics, a "uniformly random" distribution of points is described as a Complete Spatial Randomness (CSR). Formally, a CSR is defined by the fact that i) each point location is independent from the other points; and ii) the probability to find a point in a sub-region only depends on the ratio between this sub-region's volume (or area in 2D) and the total volume (or area). Diggle defined two main deviations from this CSR pattern (Diggle, 2003): i) clustering (i.e. aggregation) and ii) dispersion (i.e. points repel each other mutually forming a regular grid) (**see chapter 4 for more details**).

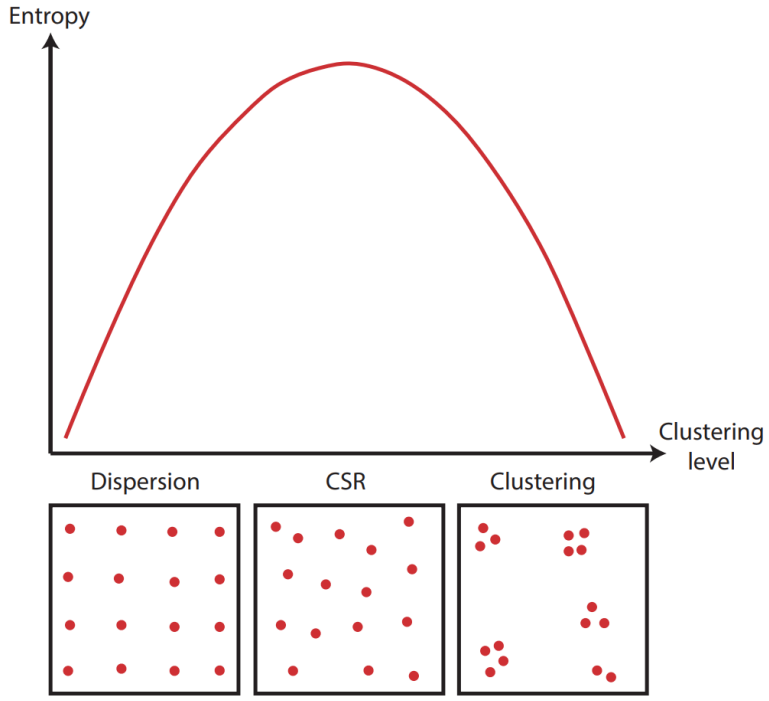

Figure 3. Entropy as a function of the clustering level of the spatial point pattern.

From the physicist's point of view, the randomness of organelle distribution could be expected, because organelles are subjected to diffusion. In a 37°C liquid, diffusion is a strong factor for small organelles. The strength of the diffusion is inversely proportional to the size of the object. For example, the diffusion coefficient of the nucleus would be ~1000 times lower than the one of a small synaptic vesicle. It is known that several organelles, for instance lysosomes, can move a few microns in a few seconds by diffusion. Taking a diffusion coefficient of $D = 0.07 \mu m^2.s^{-1}$, a lysosome moves $\Delta x = 4\mu m$ in $\tau = 60s$ and in 2D ($\Delta x = \sqrt{4D\tau}$) (Bandyopadhyay et al., 2014). When measured, organelle random motion sometimes exceeds the theoretical magnitude of a pure thermal diffusion. It has been proposed that a non-thermal "active" diffusion also occurs in the cell additionally to the

classical thermal diffusion. This active diffusion is due to cytoplasm being stirring by cytoskeleton and motors, and it could speed up the homogenization of organelle distribution (Brangwynne et al., 2009). Note that the thermal diffusion is a consequence of the second law of thermodynamics: the entropy of an isolated system can only increase. The entropy quantifies how many microstates (point patterns in our case) correspond to one macrostate (global statistical properties of a point pattern). Intuitively, there are multiple ways to make a CSR pattern, whereas a dispersed or clustered pattern corresponds to a restricted number of point patterns. Thereby, the maximum entropy of a point pattern is reached for a CSR pattern and decreases with clustering and dispersion (**Figure 3**).

However, the cell is not a thermodynamic isolated system and CSR could be avoided by energy consumption, such as active transport along the cytoskeleton by molecular motors. The non-random organization of cellular structures could be understood as an adaptation to support a function: a spatial-organization function relationship (van Bergeijk et al., 2016; Vaidžiulytė et al., 2019). Many examples can be found for non-random organization: for instance, organelles such as lysosomes and mitochondria often accumulate perinuclearly (Collins et al., 2002; Jongsma et al., 2016). A more quantitative systematic analysis reveals that diverse organelles (early endosomes, lysosomes, multi-vesicular bodies, etc.) have an unique and well-defined distribution (Schauer et al., 2010a; Duong et al., 2012). More recently and using spatial statistics, it has been demonstrated that lysosomes are not randomly distributed at the whole cell scale (**Figure 4**) (Ba et al., 2018).

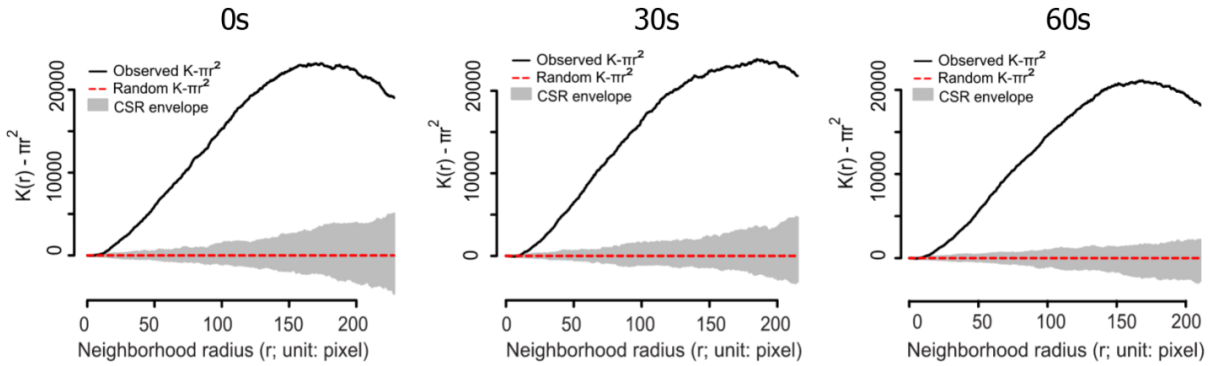

Figure 4. Lysosomal organization is clustered, from Ba et al. (2018). Lysosomal organization measured by the Ripley's K function for the same cell at 3 time points. The red-dashed line represents theoretical expectation in case of CSR, gray shades is a CSR simulation envelope representing random fluctuations. The black line is the experimental curve. Experimental curve higher than CSR expectation indicates that the spatial organization of lysosomes is clustered.

Intriguingly, the non-random positioning of organelles could stem from the non-independent nature of organelles that need connectivity. It has emerged during the last years that the organelle landscape is defined by systematic organelle MCS. This leads us to think of organelles as a network that constantly communicates, exchanges material and changes topology. Indeed, it has been demonstrated that this organelle network is not randomly established (Valm et al., 2017), confirming a non-random spatial organization of each organelle. For example, it has been reported that mitochondria and ER structures are close to secretory sites, probably because they play a role in the regulation of exocytosis by Ca^{2+} signaling (Villanueva et al., 2014). Interestingly, a feedback regulation between MCS and cellular organization seems to exist. For example, the spatial organization of lysosomes determines its MCSs with ER (Ba et al., 2018), and in return, MCSs are able to control the positioning of lysosomes (Pu et al., 2016; Jongsma et al., 2016; Bonifacino and Neefjes, 2017; Neefjes et al., 2017; Cabukusta and Neefjes, 2018).

However, entropy maximization of the whole system does not always lead to CSR. Indeed, the entropy of the point pattern could be in conflict with entropy of a sub-part of the system. For example, membrane proteins that affect membrane fluctuations could be clustered because it maximizes the entropy of membrane fluctuations while decreasing entropy due to the distribution of proteins (Johannes et al., 2018). Some cellular constituents seem to follow a CSR distribution. For example, the distribution of cargos along the flagellum of the *Trypanosoma brucei*, a protist parasite, has been described as a CSR (Yunta et al., 2014). Moreover, it has been proposed that dendritic spines positioning is following a CSR (Jammalamadaka et al., 2013; Morales et al., 2014), although others have obtained contradictory observations (Yadav et al., 2012).

1.5. Attractivity

Interestingly, after a reversible perturbation of the endomembrane organization, cell spontaneously converges to its physiological steady-state organization. For example, after a reversible coupling of lysosomes to anterograde or retrograde kinesin motors forcing a peripheral or central clustering, lysosomes are able to spontaneously re-find their original steady-state organization in a dozen of minutes (**Figure 5**) (Guardia et al., 2019). In the words of dynamical system theory, this reference state is called an "attractor". When a system has an attractor, despite a large range of perturbations, the system converges toward the reference state. This provides robustness to the system. Although the attractor is a steady-state, it can be plastic and depend on the environmental cues. For example, the spatial organization of lysosomes is influenced by different factors such as cholesterol concentration (Rocha et al., 2009), intracellular pH (Walton et al., 2018) or extracellular matrix elasticity (Wang et al., 2018b). Moreover, some cellular deregulations can lead to pathological steady-states: for example, cells from Huntington's patients present a pathological accumulation of perinuclear lysosomes (Erie et al., 2015). Changing parameters of the system (external cues or genotype), the attractor can change. But once the attractor is determined, the system spontaneously converges to its attractor despite punctual perturbations.

One major question is how the cell ensures a steady-state attractor. Indeed, an attractor is not necessarily a steady-state and can be oscillatory or even chaotic. Oscillatory behavior is common in biochemical pathways such as the famous yeast glycolysis oscillations (Selkov, 1968, 1996). Chaotic behavior is also predicted to occur in physiological conditions (Aon et al., 2011), and it has been observed in one ecological system (Benincà et al., 2015) and diverse biochemical systems (Olsen and Degn, 1977; Decroly and Goldbeter, 1982; Olsen and Degn, 1985; Baier and Sahle, 1998). However, these biochemical observations are mainly made *in vitro* (Aon et al., 2011) and the chaotic behavior is suggested by theoretical models and not directly by empirical observations. Yet, the conditions for the existence of an oscillatory or chaotic regime seem to be easily met in biological systems. For example, oscillations and chaos can emerge in non-linear system with time-delay (Mackey and Glass, 1977). It has been observed in minimal models and under particular conditions that feedback loops can indeed create instability in the system (Baier and Sahle, 1998; Hancock et al., 2017). Despite these theoretical expectations, observations of organelle organization support the steady-state hypothesis (Schauer et al., 2010a; Duong et al., 2012, 2012; Ba et al., 2018; Guardia et al., 2019) and computational models of organelle organization often converges to a steady-state (Dinh et al., 2006; Birbaumer and Schweitzer, 2011; Gou et al., 2014). Unfortunately, these studies did not report a

rigorous stability analysis. In other models, the steady-state is expected and used as an hypothesis that greatly facilitates the resolution of differential equations (Higuchi et al., 2014; Lin et al., 2016).

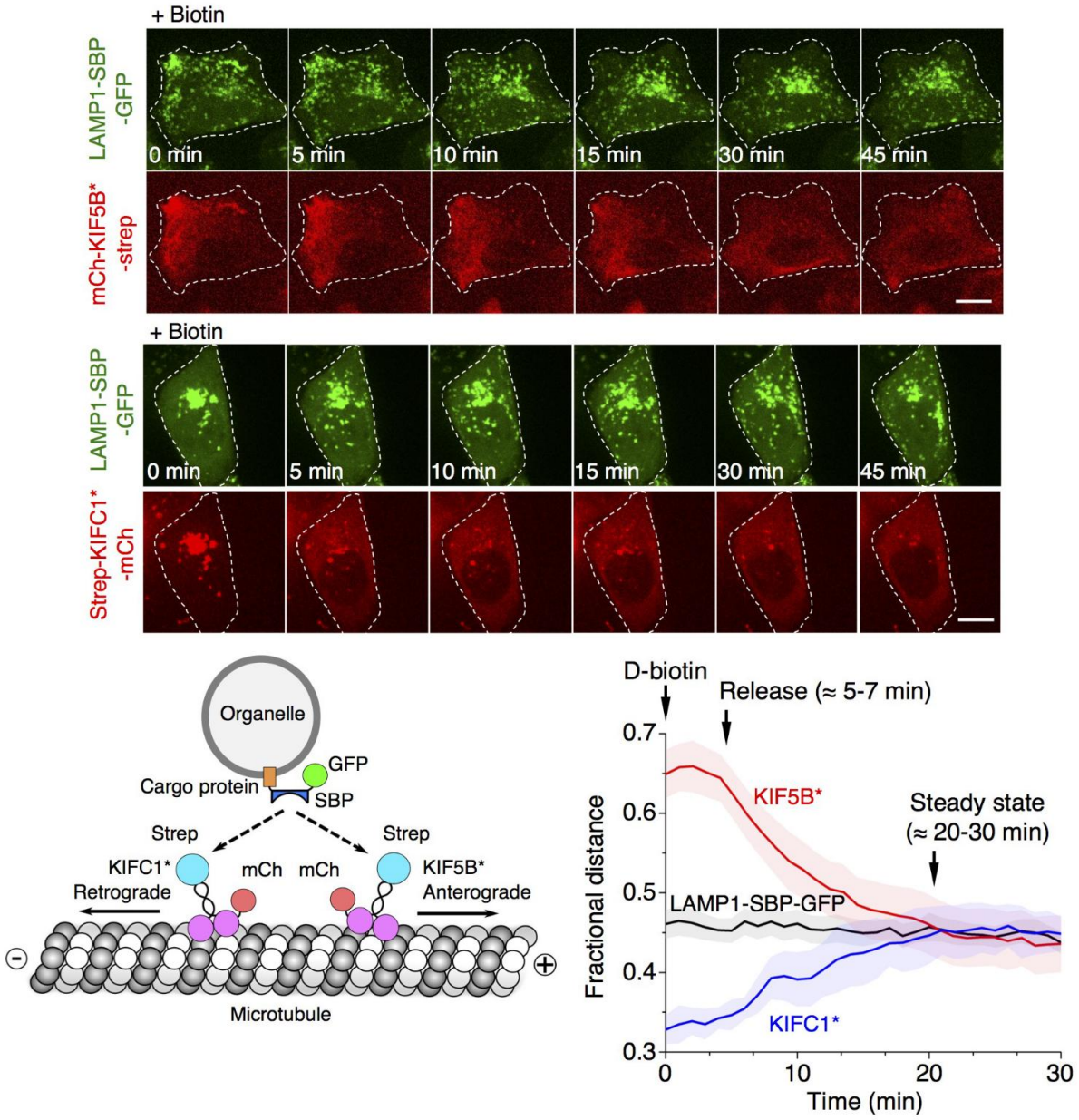

Figure 5. Attractivity of the steady-state spatial organization of lysosomes, from Guardia et al. (2019). The experiment works with a modified cargo protein that has a SBP (Streptavidin Binding Peptide) domain that spontaneously binds modified motor proteins expressing a streptavidin domain. Upon biotin addition, the coupling is lost, because the association constant between SBP and biotin is much higher than the one between SBP and streptavidin. Coupling to KIF5B clusters lysosomes peripherally whereas coupling with KIF1C clusters lysosomes at the cell center. After biotin addition, lysosomes quickly re-organized in a steady-state identical to control conditions.

2. How is a non-random steady-state organization within cells achieved and maintained?

2.1. General mechanisms

One main challenge in biology is to understand how the non-random steady-state distribution of cell compartments is achieved and maintained. Because cells are self-organized, the challenge is to understand how the cell organelle landscape emerges from the complex interaction of the cell elementary parts. In this respect, there is not a single gene, or not even one gene regulatory network that organizes the cell as highlighted by Franklin Harold in his brilliant review (Harold, 2005). Rather, organelle organization emerges from many genes, in the Harold's words "Cell architecture, for the most part, arises *epigenetically*, from the interactions of many (if not all) gene products". The word "epigenetically" should be understood in its original sense proposed by Waddington: "causal interactions between genes and their products which bring the phenotype into being." (Waddington, 1968). Thus, a comprehensive understanding of intracellular organization requires the investigation of the interactions between genes and the resulting emerging laws. I highlight below recent experimental and theoretical approaches.

2.2. Convection-diffusion model

The first models of organelle transport were based on "internal state" differential equations (Blum and Reed, 1988; Smith and Simmons, 2001; Maly, 2002a). The idea is that the organelle can switch from one state to another. Most of the models take in consideration the following states: i) free diffusion in cytosol, ii) anterograde directed motion, iii) retrograde directed motion. Some early models in neurons did not take in consideration diffusion (Blum and Reed, 1988, 1989), or bidirectional transport (Rubinow and Blum, 1980; Blum and Reed, 1988, 1989; Friedman and Craciun, 2005). Of course, these models can include others states, such as immobilization or diffusion in the actin network. These models include coupling between different states leading to the addition of reaction terms. Therefore, these seminal models are reaction-diffusion-convection models. For example, an organelle distribution model with 3 states: i) diffusion ii) microtubule (+) transport and iii) microtubule (-) transport is modeled by this set of Partial Differential Equations (PDEs):

$$\begin{cases} \dfrac{\partial c_{cyt}}{\partial t} = d\vec{\nabla}^2 c_{cyt} - c_{cyt}(k_{on}^{+} + k_{on}^{-}) + c_{+}k_{off}^{+} + c_{-}k_{off}^{-} \\ \dfrac{\partial c_{+}}{\partial t} = -\vec{v}.\vec{\nabla}c_{+} + c_{cyt}k_{on}^{+} - c_{+}k_{off}^{+} \\ \dfrac{\partial c_{-}}{\partial t} = \vec{v}.\vec{\nabla}c_{-} + c_{cyt}k_{on}^{-} - c_{-}k_{off}^{-} \end{cases}$$

(**Figure 6**), with d the diffusion coefficient, $\|\vec{v}\|$ the velocity of molecular motors transport on microtubules (MTs) and k_{on}^{+}, k_{off}^{+}, k_{on}^{-}, k_{off}^{-} the binding/unbinding rates. However, it has been shown that these reaction-diffusion-convection models can be approximated by simpler diffusion-

convection models (Grünbaum, 2000; Maly, 2002a, 2002b; Dinh et al., 2006) formalized in the Fokker-Planck equation:

$$\frac{\partial C}{\partial t} \approx D\vec{\nabla}^2 C - \vec{V}.\vec{\nabla}C \qquad with \quad C = c_{cyt} + c_+ + c_-$$

with D and $\vec{V}$ new velocity and diffusion coefficient (**see box 1**). This approximation has been widely used (Maly, 2002a, 2002b; Dinh et al., 2006). It relies on the hypothesis that the reaction timescales are small compared to convection/diffusion timescales (**see box 1**). Moreover, this approximation is valid only after a delay τ inversely proportional to binding/unbinding rates, to reach a quasi-equilibrium state. First, I will review papers that accept this approximation and use diffusion-convection models, and second, I will examine this approximation.

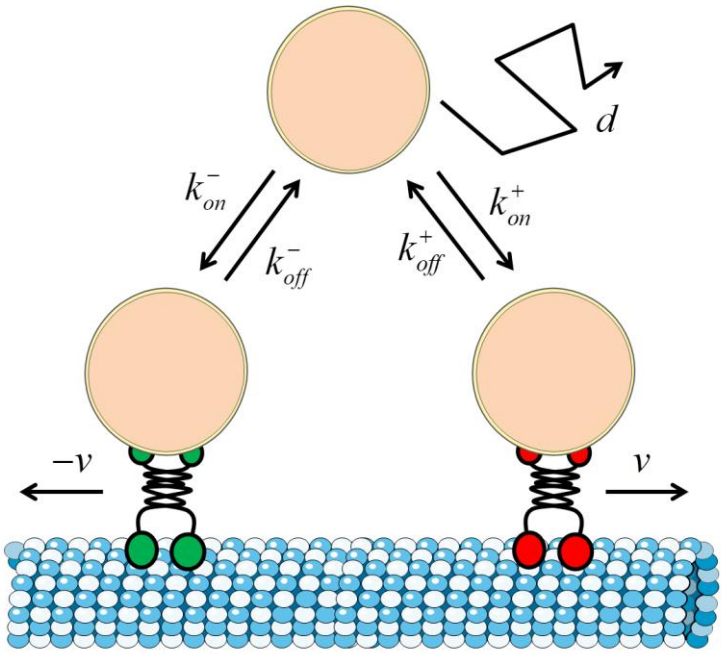

Figure 6. 3 states model. The organelle diffuses with a diffusion coefficient d when free in the cytosol. The organelle can bind/unbind molecular motors moving with a velocity v (anterograde) and –v (retrograde).

The purpose of a diffusion-convection equation is to focus on the balance between different types of motion: a random passive diffusion and an active convective flow. The first one is driven by thermal fluctuations and characterized by its diffusion coefficient D whereas the second is mainly achieved by energy consuming processes relying on molecular motors that create an emerging convective flow characterized by a velocity $\vec{v}$. The relative importance of convection flow on the diffusion is quantified by the Péclet number Pe ($Pe = \|\vec{v}\|L/D$ where L is a characteristic length). Whereas diffusion leads to a CSR distribution, convective flow can create non-random cellular patterns. Thereby, a low Péclet number corresponds to a cell with a low rate of energy consuming motility leading to a spatial distribution close to CSR. Contrarily, a high Péclet number corresponds to the opposite situation leading to non-random organization. As an illustration, I have simulated organelle distributions using a convection-diffusion equation in spherical 2D cells for different Péclet Numbers (**Figure 7**). The analysis of these distributions by Ripley's K function (a measure of point pattern organization, see chapter 4 for details) reveals that the clustering increases with Péclet number. Thus, a convective flow based on energy consumption is the main way for the cell to achieve a non CSR distribution.

Box 1 : Quasi-equilibrium approximation

We will assume a rapid and uniform equilibrium between the three states. To have the proportion of the three states, we need to find the steady-state for the following system:

$$\begin{cases} \dfrac{dc_{cyt}}{dt} = c_{cyt}(k_{on}^{+} + k_{on}^{-}) + c_{+}k_{off}^{+} + c_{-}k_{off}^{-} \\ \dfrac{dc_{+}}{dt} = c_{cyt}k_{on}^{+} - c_{+}k_{off}^{+} \\ \dfrac{dc_{-}}{dt} = c_{cyt}k_{on}^{-} - c_{-}k_{off}^{-} \end{cases}$$

The steady-states:

$$\begin{cases} \dfrac{dc_{+}}{dt} = 0 \quad \Rightarrow \quad c_{+} = c_{cyt}\dfrac{k_{on}^{+}}{k_{off}^{+}} \\ \dfrac{dc_{-}}{dt} = 0 \quad \Rightarrow \quad c_{-} = c_{cyt}\dfrac{k_{on}^{-}}{k_{off}^{-}} \end{cases}$$

Using the relationship between the total concentration and the concentrations for the different states:

$$C = c_{cyt} + c_{+} + c_{-} \quad \Rightarrow \quad c_{cyt} = \frac{C}{1 + \dfrac{k_{on}^{+}}{k_{off}^{+}} + \dfrac{k_{on}^{-}}{k_{off}^{-}}}$$

$$\Rightarrow \quad c_{+} = \frac{\dfrac{k_{on}^{+}}{k_{off}^{+}}C}{1 + \dfrac{k_{on}^{+}}{k_{off}^{+}} + \dfrac{k_{on}^{-}}{k_{off}^{-}}} \quad \text{and} \quad c_{-} = \frac{\dfrac{k_{on}^{-}}{k_{off}^{-}}C}{1 + \dfrac{k_{on}^{+}}{k_{off}^{+}} + \dfrac{k_{on}^{-}}{k_{off}^{-}}}$$

Now, summing the three coupled PDEs, we obtain:

$$\frac{\partial C}{\partial t} = d\vec{\nabla}^2 c_{cyt} - \vec{v}.\vec{\nabla}(c_{+} - c_{-})$$

Using our kinetic equilibrium approximation, we obtain:

$$\frac{\partial C}{\partial t} = D\vec{\nabla}^2 C - \vec{V}.\vec{\nabla}C$$

With:

$$D = \frac{d}{1 + \dfrac{k_{on}^{+}}{k_{off}^{+}} + \dfrac{k_{on}^{-}}{k_{off}^{-}}} \quad and \quad \vec{V} = \frac{\dfrac{k_{on}^{+}}{k_{off}^{+}} - \dfrac{k_{on}^{-}}{k_{off}^{-}}}{1 + \dfrac{k_{on}^{+}}{k_{off}^{+}} + \dfrac{k_{on}^{-}}{k_{off}^{-}}}\vec{v}$$

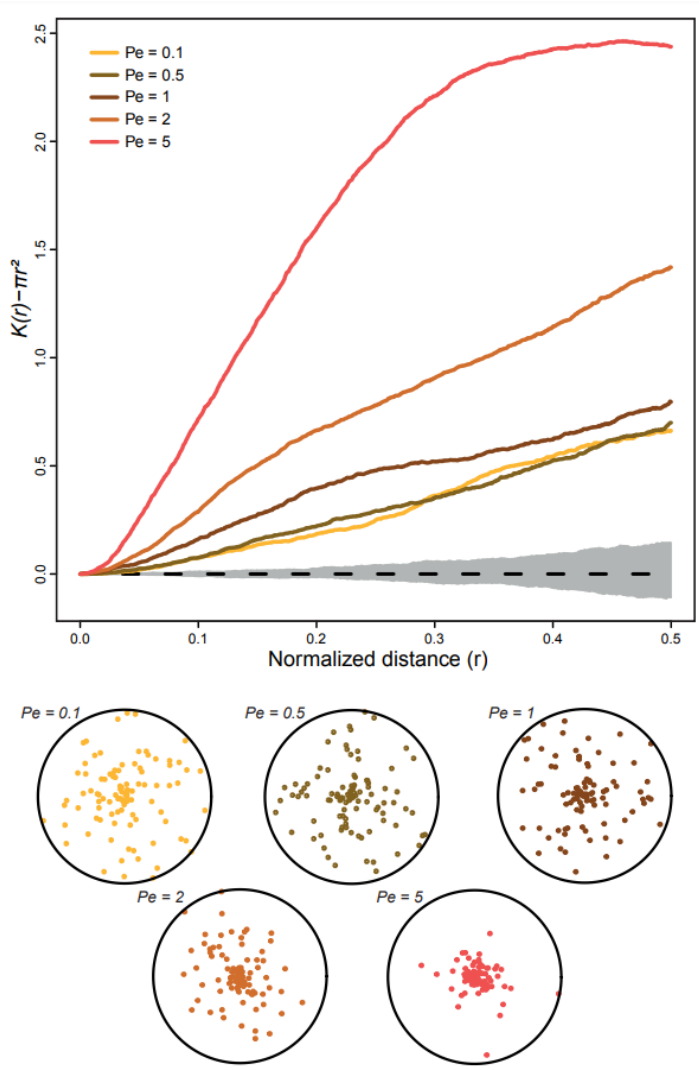

Figure 7. Simulated steady-state distributions of a 2D circular system for different Péclet numbers. The simulated drift is a centripetal flow with a velocity v. The dashed line indicates the expected value for a CSR distribution of particles with an error envelope in gray. The observed Ripley's K functions curves are superior to the expected one, indicating clustering. Moreover the clustering level correlates with Péclet number.

A lot of experimental and theoretical work using convection-diffusion models has been performed in hyphae of filamentous fungi (especially *Ustilago maydis*) (Lin and Steinberg, 2017). For example, Gou et al. modeled the early endosomes (EEs) distribution in the hyphae. They considered a hierarchical model made of three layers: MTs grid, motor activity and EE movement (Gou et al., 2014). This model does not include any feedback or local regulation. The model fits well the experimental data and predicts a uniform distribution of the EEs except at the hyphal tips where enrichment is expected. Lin et al. modeled peroxisomes distribution in *U. maydis* hyphae directly using Fokker-Planck equation (Lin et al., 2016). The peroxisome distribution is uniform along the hypha, but a MT depolymerization causes an accumulation at the growing tips. Microscopy reveals a myosin V-dependent flux toward the tips. The active movements of peroxisome on MTs, by hitchhiking of EEs, avoid an accumulation due to the polar myosin V flux. A model based on Fokker-Planck equation was also able to fit these experimental observations. A similar regulation of peroxisome distribution has been found in mammal cells, opening the door to a general model. The efficiency of modeling in hyphae is probably due to the simplicity of the hyphae structure: isotropic cylindrical geometry that can be modeled as a 1D filament with a clear polarization. Numerous older studies have analyzed axons, probably for the same reason (Reed and Blum, 1986; Blum and Reed, 1988, 1989; Friedman and Craciun, 2005).

Some modeling has also been performed on animal cells. For example, the distribution of endosomes (Pangarkar et al., 2005) and lipid droplets in embryonic *Drosophila* cells (Maly, 2002a), as well as endocytosed virus (Lagache and Holcman, 2008; Lagache et al., 2009) was efficiently modeled by the Fokker-Plack equation. Some general 1D models have been proposed (Smith and Simmons, 2001). Additionally, diffusion-convection models were applied to membrane-less organelle patterning. Membrane-less organelles are large structures without membranes, such as ribosomes or RNA granules (stress granules, P-bodies, etc.), assembled through the condensation of diverse proteins and RNA. Higuchi et al. have characterized the ribosome distribution in *U. maydis* hyphae and found a uniform distribution except at the tips where ribosome concentration is low (Higuchi et al., 2014). By experimental work, they showed that this distribution is due to polysome hitchhiking on EEs. A simple model based on the Fokker-Planck equation, considering the nucleus as a source of ribosome sub-units, was able to perfectly fit the observed ribosomal distribution, as well as several mutant phenotypes. However, the distribution of RNA granules has not been quantified yet but bulk RNA is known to be non-randomly distributed (Buxbaum et al., 2015), which has been recently quantified (Samacoits et al., 2018). The explanation of the spatial patterning of membrane-less organelles is challenging, because active transport seems marginal for these organelles, even though ribosomes hitchhike on EEs in fungi (Higuchi et al., 2014) and RNA granules hitchhike on lysosomes in mammalian cells (Liao et al., 2019). Moreover, some of these granules can undergo fusion and fission (Kedersha et al., 2005; Decker and Parker, 2012; Lee et al., 2020). This fusion/fission dynamics combined with diffusion could create a branching Brownian motion that could be enough to create spatial clustering (Houchmandzadeh et al., 2015). Yet, this analysis has not been applied to study organelle distribution. This approach could also be promising for mitochondria that undergo fusion and fission. The relevance of such models should be evaluated considering the time scale of the fusion/fission events in comparison to the diffusion timescale.

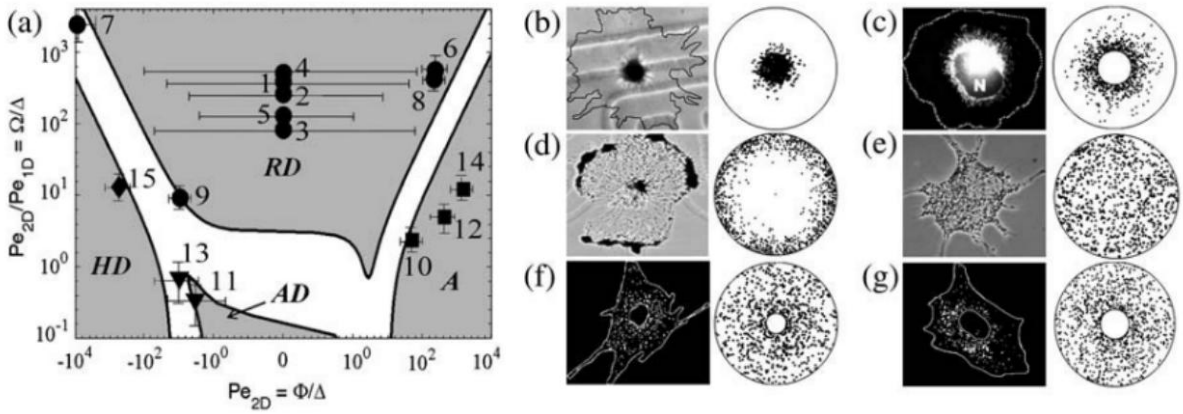

Figure 8. Spatial organization by a convection-diffusion model, from Dinh et al. (2006). The model is described with two Péclet numbers and defines 4 different regions. A: Aggregation (aggregation near the cell center), RD: Radial Dispersion (concentration proportional to 1/r), AD: Areal Dispersion (uniform concentration) and HD: Hyper Dispersion (aggregation near the cell periphery). White area indicates transition patterns and numbers represent experimental data points. On the right part some qualitative comparisons between predicted patterns and experimentally observed organelle distributions. b) Melanosomes in fish melanophores stimulated with melatonin, c) Mitochondria in tau-transfected CHO cells, d) melanosomes in fish melanophores treated with an actin disrupting drug, e) melanosomes in *Xenopus* melanophores stimulated with a drug, f) endosomes in human fibroblasts, and g) peroxisomes in *Drosophila* S2 cells.

Thus, convection-diffusion models are able to reproduce the spatial organization of organelles in a large diversity of situations and a general model of organelle distribution has been proposed (Dinh et al., 2006). This model postulates that organelles can be in 4 states: diffusion, anterograde trafficking on MTs, retrograde trafficking on MTs, or linked to actin (**Figure 8**). These considerations are included into a general diffusion-convection model with the quasi-equilibrium approximation. The model is controlled by two parameters (Péclet numbers). According to the chosen parameters, this model generates different kind of organizations. Surprisingly, this simple model is able to produce patterns similar to a good range of experimental data. This results illustrates that cell organization could potentially be understood with general physical principles.

2.3. Convection-diffusion-reaction and stability

The quasi-equilibrium approximation mentioned earlier can be questioned. For example, for some simulations, Dinh et al. used small kinetics rates (leading to time scale as large as $\sim 10^3$s $\sim$ 15min) (Dinh et al., 2006). This does not bias steady-state numerical solutions but could affect simulations before reaching this point. A full reaction-diffusion-convection model could be more appropriate for non-steady analysis with slow kinetics. Reaction-diffusion models are already well known since the seminal Turing paper of 1952 (Turing, 1952). The Turing model is able to reproduce complex self-organized morphogenesis patterns (Kondo and Miura, 2010) in a broad variety of situations (Kondo and Asai, 1995; Jacobo and Hudspeth, 2014; Blagodatski et al., 2015; Sekimura et al., 2015; Fofonjka and Milinkovitch, 2021). It has been recently proposed that the Turing model is a general principle of cellular self-organization at molecular scale (Halatek et al., 2018) neglecting convective flow. Moreover, Turing model has a robustness problem. Diverse variations (in parameters, initial conditions, presence of noise or delay) can vanish the pattern (Bard and Lauder, 1974; Murray, 1982; Maini et al., 2012). This fragility has called into question its biological plausibility for some morphogenetic processes such as digit formation (Bard and Lauder, 1974). However, the addition of convection could stabilize the model. Indeed the quasi-equilibrium approximation can be used to demonstrate the stability under certain conditions, because it transforms a potentially unstable reaction-diffusion-convection model into a stable convection-diffusion model. Some papers use the full reaction-diffusion-convection model (Smith and Simmons, 2001; Dinh et al., 2005). For example, 4-states models using reaction-diffusion-convection proposes that melanosome distribution is controlled mainly by MT binding rate (Slepchenko et al., 2007). Another paper proposes that endosome clustering is controlled by a Péclet number and an organelle interaction coefficient (Pangarkar et al., 2012). The common point to these models is that they do not generate instability or oscillations confirming the stabilization effect of convection.

2.4. Limits of the convection-diffusion model

The models previously described rely on different hypothesis/simplifications that can be interrogated skeptically: i) well-mixed system, ii) linear kinetics and iii) boundary conditions.

i) Well-mixed system: The well-mixed system hypothesis states that cytosol is homogeneous and that concentrations are constant. It is perfectly clear that it is a crude hypothesis for some constituents. For example, due to its astral organization, it has been suggested that the MT effective binding rate is space-dependent (Slepchenko et al., 2007). Moreover it has been demonstrated theoretically and *in vitro* (Nédélec et al., 2001), as well as *in cellulo* (Lin et al., 1996) that the molecular motor associated to MTs are also not homogenously distributed. Moreover, recent evidences clearly confirmed that the cell cytoplasm is not a well-mixed system (Baum et al., 2014; McLaughlin et al., 2020; Xiang et al., 2020). For example, the measured diffusion coefficients in *Schizosaccharomyces pombe* vary over 100-fold within single cells. These variations are likely due to intracellular spatial heterogeneity of cytoplasm viscosity, demonstrating that it is not a well-mixed system (Garner et al., 2022). Therefore, it would be interesting to extend the use of inhomogeneous models i.e. models where diffusion coefficient, velocity and effective binding rates depend on the localization in the cell.

ii) Linear kinetics: It is often hypothesized that binding/unbinding processes can be modeled by first order reactions. This relies on the hypothesis that molecular motors are in excess and thus pseudo-first order approximations ($k[free\ motor][free\ organelle] = k'[free\ organelle]$ because $[free\ motor]$ is roughly constant) can be used. This approximation seems justified by the fact that the number of molecular motors is indeed much higher than the number of organelles. Schwanhausser et al. reported ~360 000 copies of the dynein heavy chain DYNC1H1 (Schwanhäusser et al., 2011) per cell whereas the order of magnitude of organelle number is likely around 1 000. Even if the motor proteins are in excess, the linear kinetics is still a strong hypothesis. The binding of several motor for a single organelle could create complex cooperative non-linear kinetics. Electron Microscopy (EM) studies show that the distribution of organelle-motor cross-bridges is centered around 2, ranging from one to five (Gross et al., 2007). Some early theoretical studies in neurons take in consideration the binding of several motors per vesicles (Blum and Reed, 1988) with kinetics close to Hill's model (Hill, 1910). More recent experimental studies highlight the possibility of a cooperative behavior of dynein motors (Torisawa et al., 2014; Tan et al., 2018) which seems weaker, if not absent, for kinesins (Jamison et al., 2010).

iii) Boundary conditions: Boundaries of a system can have an important influence on the system. For example, it has been recently reported that smooth muscle cell shape regulates the distribution of some organelles (Calizo et al., 2020). The authors also demonstrated numerically that the cell shape influences reaction-diffusion patterns, which was confirmed in a second theoretical study (Eroumé et al., 2021). Experimentally, the fractal borders of the cell, often under-estimated, could have an impact on the accumulation of organelles on varicosities (Slepchenko et al., 2002). From the theoretical part, boundary conditions can also have an impact on the stability of the system. For example, it has been reported that Dirichlet boundary condition (i.e. fixed concentrations at boundaries) enhances stability of the Turing model (Dillon et al., 1994). However, in cell biology, the relevant boundary condition is often a no-flux condition (Robin boundary condition).

2.5. Agent-based models and stochastic modeling

In addition, some authors proposed an agent-based approach to model organelle dynamics (Mayorga et al., 2018). In agent-based modeling, the system is modeled by a set of discrete entities called agents. Each agent behaves according to a set of predefined rules. Emerging effects can appear from individual behavior of agents. These models are more susceptible to describe local regulations (Dalmasso et al., 2017; Dinh et al., 2007) or feedbacks (Mayorga et al., 2017). Unfortunately, these models have not been used extensively to investigate the spatial distribution of organelles. Conversely to models based on PDEs, these models are stochastic. Given the possible low number of organelles, the stochastic fluctuations could be important and accurately modeled by this approach. Future work should show if they are consistent with models based on PDEs and how they compare to these.

2.6. Self-organization of the organelle landscape

Self-organization is the emergence of a spatio-temporal organization resulting only from the interactions of the individual components. Contrarily to self-assembly, self-organization involves energy consumption (Misteli, 2001; Karsenti, 2008; Wedlich-Söldner and Betz, 2018). The importance of self-organization has been already discussed in the context of cellular architecture (Misteli, 2001; Wedlich-Söldner and Betz, 2018) and has been already directly observed, for example in the case of MT network organization (Malikov et al., 2005). More recently, some authors argued that the formation of distinct organelles could be self-organized (Binder et al., 2009; Vagne et al., 2020). Reaction, diffusion and convection seem to be sufficient conditions for the intracellular organelle self-organization.

My PhD work focuses on the spatial organization of exocytosis sites. I will demonstrate that it shares common properties with the organization of the organelle landscape. First of all, exocytosis is clearly not randomly distributed (**see chapter 2 and results**) moreover biophysical models based on PDEs are probably a good strategy to help us understand its properties (**see discussion**). Of course, a biological view on exocytosis is complementary to the physical approach. Therefore the next chapter will present molecular regulations and physiological contexts of exocytosis.

Chapter 2

Lysosomal exocytosis

"Within every cell, there are exquisitely evolved molecular machines, nucleic acids, enzymes, the cell architecture. Every cell is a triumph of natural selection, and we're made of trillions of cells. Within us, is a little universe."

Carl Sagan, 1980, "Cosmos: A Personal Voyage" TV series.

Chapter's summary:

The lysosome is a small acidic organelle discovered in 1955 by Christian de Duve's team. Lysosomes are responsible for the digestion of macromolecules in building blocks reusable by the cell. Lysosomes receive their digestive contents by three pathways: phagocytosis, endocytosis and autophagy. From the molecular point of view, lysosomes are characterized by a specific ionic, lipidic and carbohydrate signature. The lysosomal membrane contains many channels, transporters and pumps such as V-ATPase, and the lysosomal lumen contains about 60 types of hydrolases. Many cytosolic proteins are associated to lysosomal membrane to regulate their trafficking, tubulation, fission processes and metabolism. Long time seen only as digesting bags, lysosomes are involved in numerous cellular functions: autophagy, adhesion, cell migration, metabolism, transcriptional regulation, plasma membrane repair and secretion. Secretory functions are presented in details and compared with conventional exocytosis of Golgi-derived vesicles. Lysosomal and Golgi-derived vesicles rely on the SNARE machinery discovered between 1980s and 2000s. To catalyze exocytosis, the SNARE machinery forms a complex made of 3 proteins interacting via a coiled-coil domain formed with 4 α-helices. Today, 38 SNAREs are known among mammals, forming different sub-families according to a conserved sequence called the SNARE motif: R, Qa, Qb and Qc. Exocytosis is regulated by additional mechanisms: Ca^{2+}, cortical actin, lipids and various additional proteins. Lysosomal exocytosis relies on the v-SNARE VAMP7 and the t-SNAREs syntaxin 3 (or 4) and SNAP25 (or SNAP23). Similarly to conventional Golgi-derived vesicle exocytosis, lysosomal exocytosis is regulated by Ca^{2+} and the cytoskeleton. Lysosomal exocytosis fills plethora of physiological roles (e.g. secretion of digestive enzymes, plasma membrane repair, secretion of exosomes, etc.) but has also implication in pathological contexts (cancer invasion, intracellular infection, LSDs, etc.). While it is clear that Golgi-derived vesicles exocytosis sites are not randomly distributed, the spatio-temporal regulation of lysosomal exocytosis is largely unknown.

1. The lysosome

1.1 History

In 1882, Ilya Ilitch Metchnikov set up his private laboratory in Messina (Sicily) to work on marine zoology. He observed migratory cells in starfish larvae around wound. He hypothesized that these cells are involved in the defense of the organism against foreign bodies by engulfing them: “One day when the whole family had gone to a circus to see some extraordinary performing apes, I remained alone with my microscope, observing the life in the mobile cells of a transparent starfish larva, when a new thought suddenly flashed across my brain. It struck me that similar cells might serve in the defence of the organism against intruders. […] There was a small garden to our dwelling, in which we had a few days previously organised a “Christmas tree” for the children on a little tangerine tree; I fetched from it a few rose thorns and introduced them at once under the skin of some beautiful star-fish larvae as transparent as water. I was too excited to sleep that night in the expectation of the result of my experiment, and very early the next morning I ascertained that it had fully succeeded” (Hirsch, 1959). He observed mobile cells around the thorn confirming his hypothesis (**Figure 9**). He named these cells “phagocytes” (meaning “eating cells”). He considered the possibility that phagocytosis was an evolutionary conserved mechanism from unicellular eukaryotes to mammal leukocytes. Using pH sensitive colorants, he observed a modification of the color after internalization of the dye by phagocytes (Metchnikov, 1893). From these observations, he understood that an acidic vacuole containing digestive products should exist. It was the first prediction of the existence of an intracellular lysis compartment.

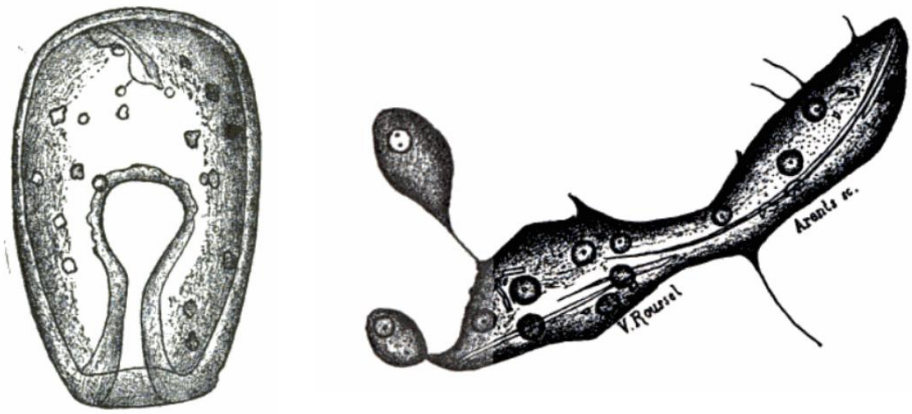

Figure 9. Illustrations from Metchnikov lectures at Pasteur Institute in 1891. Left: starfish (*Astropecten* sp.) larvae under gastrulation. The larva is injured with a sharp body surrounded by mobile cells. Right: zoom on the sharp body. Migratory cells surround the foreign body and fuse around it to form a “plasmodia”.

In 1948, Christian de Duve established a new research team at the Louvain University. He worked on carbohydrate metabolism, especially the biochemical mechanisms that underlie the glucose release by the liver induced by insulin. He identified the hepatic glucose-6-phophatase as a key enzyme of the glycogenolysis. De Duve and his students (Jacque Berther and Lucie Dupret) endeavored to

identify the intracellular localization of this enzyme. Using differential centrifugation, recently introduced by Albert Claude, that preserves the integrity of intracellular structures, they found the enzyme in the microsomial fraction of rat liver samples. As a control, they followed the distribution and the activity of acid phosphatase in the different fractions. Surprisingly, the total acid phosphatase activity after centrifugation was only 10% of the activities reported in previous studies. De Duve related that "…we could have rested satisfied with this result, dismissing the first series of assays as being due to one of those troublesome gremlins that so often infest laboratories, especially late at night. This would have been a pity, since chance had just contrived our first meeting with the lysosome." (Bainton, 1981). The curiosity of the team pushed them to store the samples at 4°C and to re-analyze them 5 days later. During this second measurement, the enzyme activity of acid phosphatase drastically increased. The latency of phosphatase enzyme activity was attributed to a physical barrier, an organelle membrane (Bainton, 1981; Sabatini and Adesnik, 2013). Previous sample preparations destroyed this membranous barrier explaining the differences in the measured activities due to the slow degradation of the membrane (**Figure 2**).

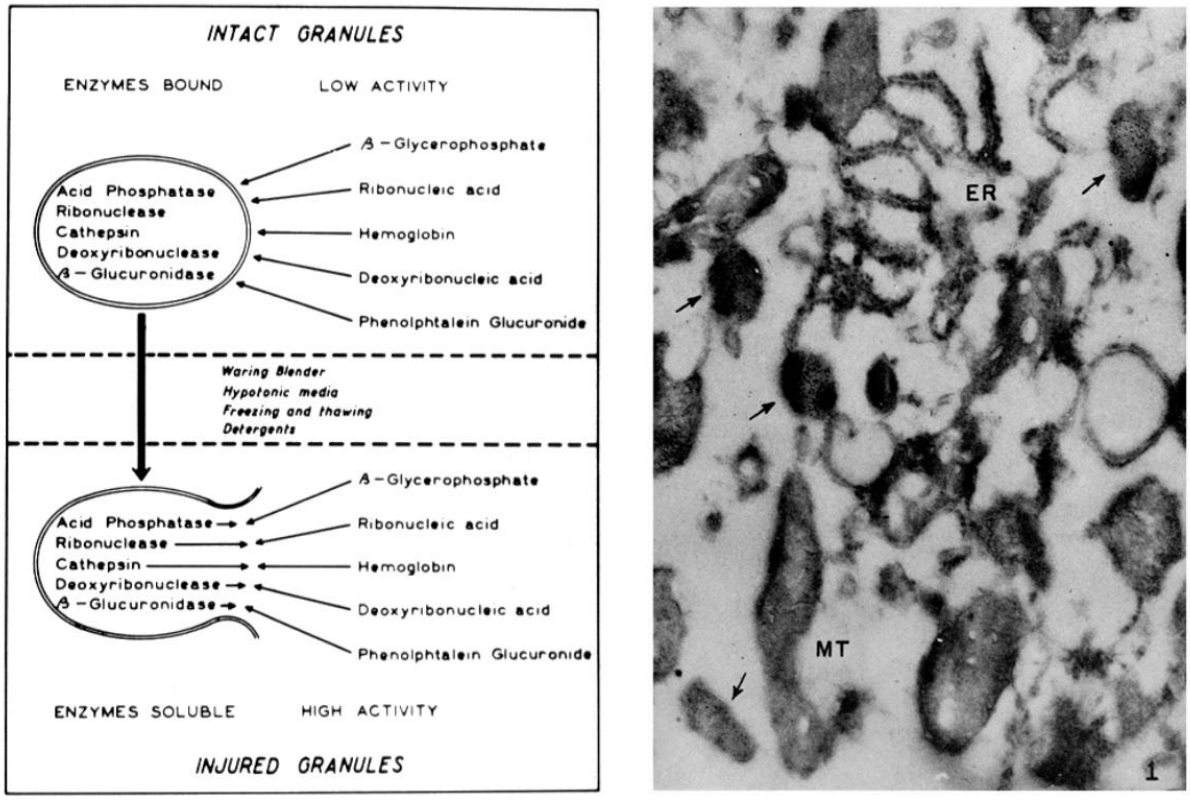

Figure 10. Left: de Duve biochemical model for enzyme latencies (reproduced by Bainton). In samples with intact lysosomes, substrates are not accessible to the enzymes resulting in low enzymatic activity. After membrane rupture, the measured enzymatic activity increases. Right: Lysosomal fraction after differential centrifugation from rat liver, observed by EM. ER indicates endoplasmic reticulum, MT mitochondria, and arrows show lysosomes. Historical observations by Novikoff et al.

Initially, it was thought that the compartments retaining the enzymes were mitochondria. Françoise Appelmans studied acid phosphatase in the mitochondrial fraction. She split the mitochondrial fraction in two sub-fractions: a heavy one containing the cytochrome oxydase (a mitochondrial

marker) and a light one containing the acidic phosphatase. In 1955, de Duve identified 4 other enzymes (β-glucuronidase, cathepsin D, ribonuclease and desoxyribonuclease) in this light fraction. All these enzymes are hydrolases and additionally they share the property of having an optimal acidic pH. De Duve concluded that this fraction is composed of organelles retaining acidic hydrolases and occupying a digestive function. In his seminal paper, he named this new organelle, discovered by serendipity, “lysosomes” (meaning lytic bodies) (De Duve et al., 1955). Remarkably, de Duve discovered lysosomes without any direct observation, only by masterfully exploiting differential centrifugation. In the same year, Alex Novikoff obtained the first electron micrographs of partially purified lysosomes, published in 1956 (**Figure 10**) (Novikoff et al., 1956). These electron micrographs revealed characteristic bodies than had been already observed in hepatocytes by Rouiller in 1954, named “Pericanalicular Dense Bodies”.

De Duve also noticed that urate oxydase had the same distribution than acid phosphatase by centrifugation. Latter work, partially done by de Duve team, split the light fraction in two sub-fractions: one containing lysosomes and the other containing a new mysterious organelle. In 1965, de Duve named this new organelle “peroxysomes” (meaning body with a large amount of oxygen) (De Duve, 1965). Here again, EM observations revealed that these organelles had been already observed in 1954 by Rhodin and named “microbodies”, and confirmed in 1956 by Rouiller (Rouiller and Bernhard, 1956; Bainton, 1981).

Despite these observations, the function of lysosomes remained unclear. In the ‘50s, Werner Strauss tried to understand how extracellular molecules were internalized by endocytosis. During the course of his research, he observed that radiolabeled proteins, internalized by the cell, localized in granules (now identified as lysosomes) but under a cleaved form (Strauss, 1954). Zanvil Cohn fed macrophages with radiolabeled bacteria. He also observed the accumulation of radioactive fragments inside the lysosomes. Cohn concluded that lysosomes behave as a “cell stomach” digesting foreign bodies engulfed by the cell (Cohn, 1963).

Today, lysosomes are recognized as essential organelles of the eukaryotic cell and their dysfunction can lead to severe diseases such as Lysosomal Storage Disorders (LSDs). Christian de Duve received the Nobel Prize in Physiology or Medicine with Albert Claude and George Emil Palade in 1974 for “their discoveries concerning the structural and functional organization of the cell” founding modern cell biology.

1.2. The modern concept of lysosome

Lysosomes are small (diameter ~0.2-0.5µm), acidic (pH ~4.5-5) and catabolic organelles characterized by ~60 luminal hydrolases. They are involved in the degradation and the turn-over of macromolecules and are therefore naively seen as a “waste bag” or a “recycling bin”. A typical mammalian cell contains hundreds of lysosomes with heterogeneity in their morphologies, sizes and numbers (Xu and Ren, 2015). These different subpopulations are believed to have different functions (Johnson et al., 2016; Zhu et al., 2021). Lysosomes are not randomly distributed in the cell (Ba et al., 2018). Microscopic observations distinguish several lysosomal subpopulations at the cell scale. The majority of lysosomes are part of a non mobile juxtanuclear population called perinuclear cloud, whereas the other peripheral lysosomes are more dynamic (Cabukusta and Neefjes, 2018).

The importance of the lysosome for cell physiology is illustrated by its implication in a number of pathological contexts, such as LSD, where the primary cause is a dysfunction of lysosomal hydrolases (or more rarely other lysosomal proteins). Additionally to these "purely" lysosomal diseases, lysosomes are involved in many neurodegenerative diseases (Alzheimer's disease, Parkinson's disease, Huntington's disease, etc.), which are characterized by accumulations of abnormal proteins indicating a defect in the clearance pathway (Zhang et al., 2009). In cancer, lysosomes also play a central role. During oncogenic transformation, lysosome number, size, morphology, pH and the expression of hydrolases change (Nishimura et al., 2003; Mathur et al., 2022). Additionally, the lysosomal secretion of metalloproteases (MMPs) can facilitate cancer invasion through the digestion of the Extra-Cellular Matrix (ECM) (Hoshino et al., 2013; Machado et al., 2015).

1.3. Lysosome-related organelles and the vacuole

Lysosome-Related Organelles (LROs) are cell type-specific organelles that share in common some lysosomal proteins (e.g. CD63) and derive (at least partially) from the endosomal system. Cells can exhibit classical lysosomes in addition to these LROs. LROs usually include melanosomes in melanocytes, Weibel-Palade bodies in endothelial cells, cytotoxic granules in lymphocytes, dense granules in platelets, lamellar bodies in type II pneumocytes, acrosomes in sperms, etc. Similarly to lysosomes, LRO biogenesis can process through endosomal maturation as well documented for melanosomes (Delevoye et al., 2019). However, some LROs originate from the *Trans*-Golgi Network (TGN) such as Weibel-Palade bodies (Delevoye et al., 2019). The heterogeneity of LROs in morphology, function, origin and molecular compositions challenges the pertinence to regroup them under a common name.

Rather than being classified as LRO, the vacuole in plants or fungi is considered as an analogue of animal lysosomes despite many differences. Whereas lysosomes are small and numerous, fungi have larger (5µm) but less numerous vacuoles (1 to 5) occupying 20% of the cell volume; and plants have even larger vacuoles filling 30% to 90% of the cell volume. It is clear that vacuoles have a lytic activity and are the final compartment of the endocytic route however vacuoles have a less acidic intraluminal pH (5.5–6.2 for yeast and plant) (de Marcos Lousa and Denecke, 2016). Interestingly, tonoplast (vacuole membrane) is aquaporin rich, whereas lysosomal membranes do not contain aquaporin (Maurel et al., 2015). Moreover, the pathways to target proteins to lysosomal/vacuolar compartments are very different. Enzymes are targeted to lysosomes thanks to a post-translational modification in mammalian cells, whereas vacuolar proteins targeting is based on a sequence motif, such as the N-terminal QRPL motif in S*accharomyces cerevisiae* (de Marcos Lousa and Denecke, 2016). Lastly, vacuoles differ from lysosomes by their functions. Plants maintain a constant turgor pressure despite modifications in the environment tonicity by regulating the osmolarity in the vacuole (Marty, 1999). In addition, the so called "protein storage vacuoles" accumulate proteins in the seed that will be degraded during germination, playing a role of an energy storage center. Although historical studies distinguish protein storage vacuoles and lytic vacuoles, recent studies tend to abolish this distinction, because lytic and storage activities can coexist in the same vacuole (Jiang et al., 2001).

The diversity of lytic compartments, from lysosomes to vacuoles and including LROs illustrates that these organelles represent a spectrum of characteristics and functions with blurry borders. This is reminiscent of the essential problem of evolutionists to define species as stable boxes (Vasilyeva and Stephenson, 2013).

1.4. Endosomal maturation and lysosomal biogenesis

Lysosomes are the degradative compartment and the terminal stage of the endosomal maturation. Endocytosed material traffick through Early Endosomes (EE, also called sorting endosomes) and Late Endosome (LE) before reaching the lysosomes (**Figure 11**).

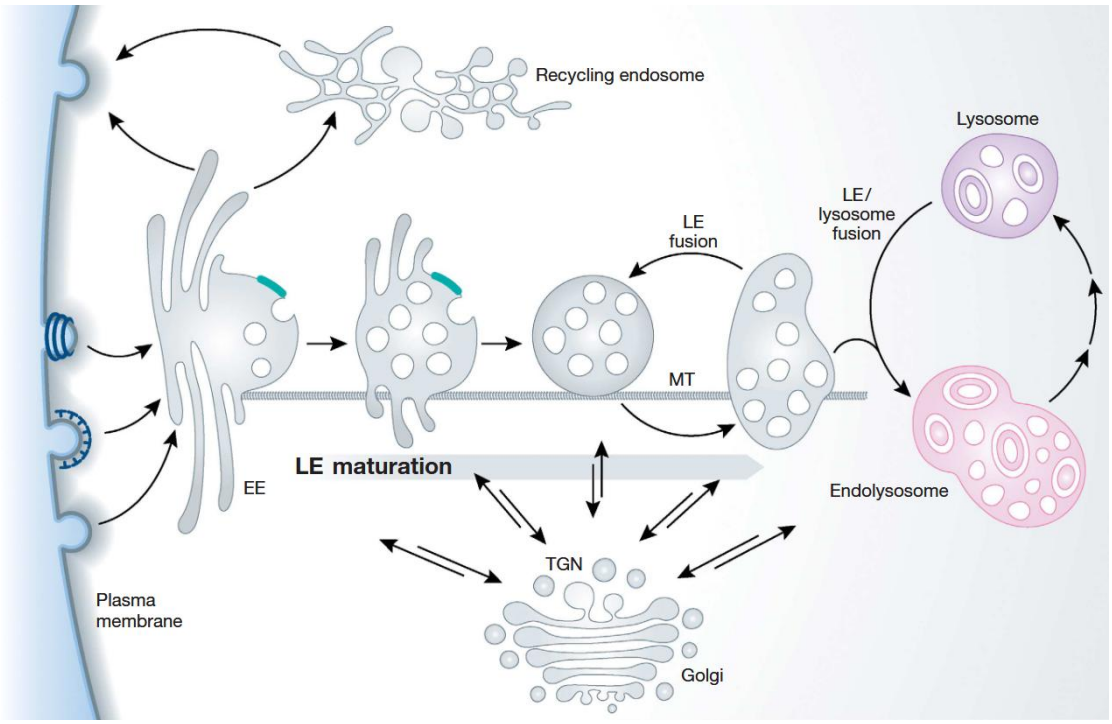

Figure 11. Endosomal maturation from Huotari and Helenius (2011). Endocytosed vesicles fuse with EE. Endocytosed material can be recycled towards the PM either directly (fast recycling) or through the recycling endosome compartment (ERC) (slow recycling), or recycled towards the TGN. EEs maturate to LEs through the progressive accumulation of hydrolases coming from the TGN and acidification by the V-ATPase. LEs maturate into bona fide lysosomes or fuse with pre-existing lysosomes to form endolysosomes.

First, endocytic vesicles fuse with EEs. EEs are small, heterogeneous and slightly acidic (pH ~ 6.5) organelles patrolling in the cytosol (Mindell, 2012; Huotari and Helenius, 2011). EEs are characterized by a vacuolar body (100-500nm in diameter) elongated in several tubular domains (20-50nm in diameter) (**Figure 12A-B**). EEs also contain a small quantity of IntraLuminal Vesicles (ILVs, 40-60nm in diameter) formed by the inward budding of the EE membrane. EE membrane is characterized by "plaques" (sometimes referred as flat bristle-like plaques, bilayered-clathrin coat or flat-clathrin coat) visible in EM. These plaques are composed of clathrin and components of the Endosomal Sorting Complex Required for Transport (ESCRT) complex. This machinery sorts ubiquitylated cargos towards ILV budding sites and initiates the inward budding (Huotari and Helenius, 2011; Cullen and Steinberg, 2018). Most of endocytosed proteins are recycled to the Plasma Membrane (PM) and a minority is targeted to lysosomes. To achieve this sorting, EEs have membrane domains enriched in certain proteins (Rab4, Rab5, Rab11, Arf1/COPI and retromer). These domains organize the budding of vesicles containing specific cargos from the tubular domains (Huotari and Helenius, 2011; Cullen and Steinberg, 2018). These vesicles recycle cargos either by targeting the PM directly, a pathway called "fast recycling", or going through Recycling Endosomes (RE, also called Endocytic Recycling Compartment ERC) before reaching the PM, a pathway called "slow recycling". Why different kinetic pathways exist is poorly understood but they could regulate the cytosolic resident time of

internalized receptors and ensure robustness of the recycling pathway (Cullen and Steinberg, 2018). Lastly, EEs can also recycle cargo toward the TGN thanks to the retromer machinery (Bonifacino and Rojas, 2006).

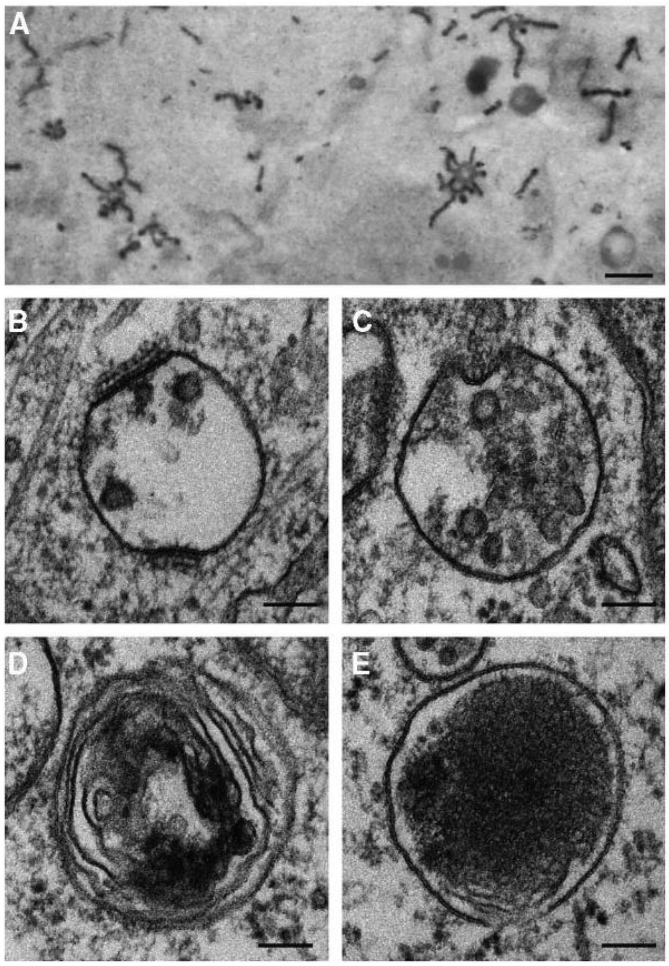

Figure 12. EM of the endosomal compartments from Huotari and Helenius (2011). A: EEs with their central vacuolar domain extended by tubular domains. B: EE with few ILVs and characteristic bilayered-clathrin coat. C: LE characterized by the high number of ILVs. D: Endolysosome partially electron dense. E. Lysosome with an electron dense lumen. Scale bars: 500nm in A, 100 nm in B-E.

LEs are usually circular organelles (250-1000nm in diameter) that have accumulated numerous ILVs (typically $\geqslant$30) and with a more acidic lumen (pH~6) (**Figure 12C**) (Huotari and Helenius, 2011; Mindell, 2012). LEs express some lysosomal markers such as LAMP1. LEs can be experimentaly difficult to distinguish from lysosomes (**Figure 12D-E**). Especially the distinction with a subpopulation of endosomes called MultiVesicular Bodies (MVBs) is particularly subtle. MVBs are an endocytic compartment discovered in 1959 by Keith Porter by EM (Sotelo and Porter, 1959). Similarly to endosomes, MVBs are characterized by ILVs and bilayered-clathrin coats (Hanson and Cashikar, 2012). MVBs are often physically associated to ER (Eden et al., 2012). Due to the practical difficulty to distinguish these organelles, and differences between classifications according to the authors, they are commonly mentioned as LE/Lysosome (LEL) pool.

Lysosomal biogenesis has been controversial with two concurrent models: maturation and vesicular transport models (**Figure 13**). The vesicular transport model states that EEs, LEs and lysosomes are stable compartments exchanging material through vesicular trafficking. In this model, lysosomal biogenesis is achieved through the homotypic fusion of vesicles coming from LE. In contrast, the maturation model states that EE undergo a maturation to become a LE and ultimately a lysosome

(Storrie and Desjardins, 1996; Mullins, 2010). Despite the likely existence of vesicular trafficking between endosomal compartments, the maturation model is today recognized as the main mechanism of lysosomal biogenesis. EEs and LEs maturation is supported by the fusion with vesicles containing hydrolases coming from the TGN (**Figure 11**). Moreover the V-ATPase, a proton pump, progressively acidifies endosomes during their maturation. The progressive accumulation of enzymes and acification turn EEs to LEs and LEs to lysosomes (Xu and Ren, 2015).

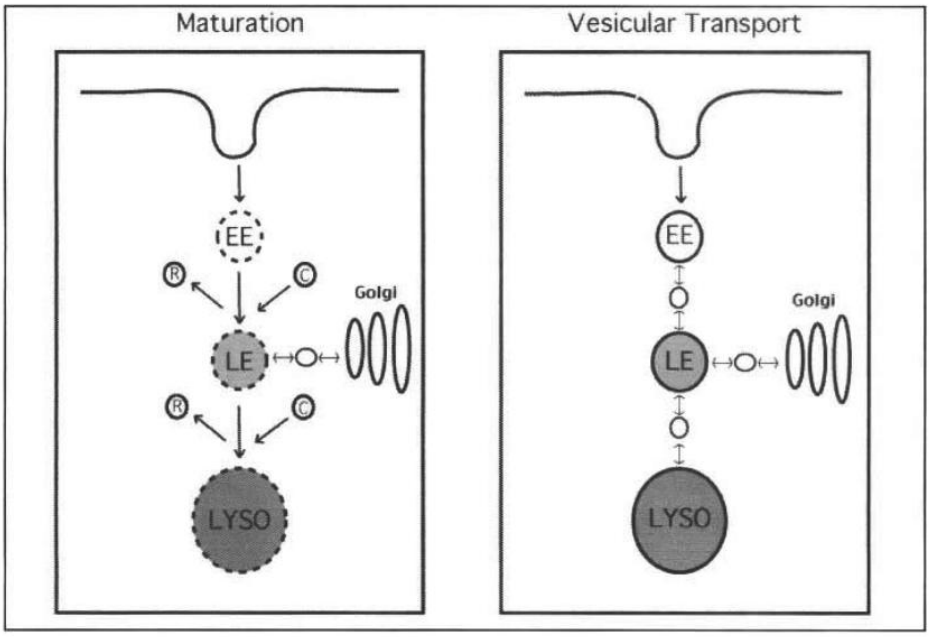

Figure 13. Models of lysosomal biogenesis from Mullins. In the maturation model, EE turns in LE and LE turns in lysosome thanks to the gain (C) and the loss (R) of certain molecules. In the vesicular transport model, EEs, LEs and lysosomes are stable different organelles exchanging material through vesicular trafficking.

Endosomal maturation is molecularly supported by Rab cascades (**Figure 14**). Rab proteins are small GTPases from the Ras superfamily. The members of the Rab family are key regulators of trafficking. They associate with specific organelles and define their identity. In their GDP-bound form, Rabs are cytosolic and in complex with GDI (Rab GDP Dissociation Inhibitor). Following GDP-GTP exchange catalyzed by Guanine Exchange Factors (GEFs), Rabs are inserted into target membranes thanks to geranylgeranylation of one or two C-terminal cysteines, and recruit a wide variety of effectors. GTP hydrolysis is then activated by GTPase-activating proteins (GAPs), and Rabs can be extracted from membranes by GDI and start a new cycle of activity (Stenmark, 2009; Hutagalung and Novick, 2011). As mentioned above, the successive recruitment of different Rabs, the so-called Rab cascade underlies endosomal maturation. Before their internalization, some membrane proteins can be ubiquitinated. Rab5 is specifically recruited on EE by its GEF (Rabex5) that is bound to these ubiquitinated cargos. Rab5 is EE specific and recruits diverse effectors defining the organelle function/identity. Among recruited effectors is the GEF of Rab7 (Mon1-Ccz1). Once activated, Rab7 recruits its own effectors, which leads to a change in organelle identity. Additionaly, Rab5 GAP (possibly TBC1D18) is recruited, depleting active Rab5. This molecular transition from Rab5 to Rab7 orchestrates the transition from EE to LE (Rink et al., 2005; Langemeyer et al., 2018; Hiragi et al., 2021). After endosome-lysosome fusion, Rab7 is also inactivated thanks to its GAP (such as TBC1D5 or TBC1D15), dissociates from membranes and can be re-used for a new Rab cascade (Langemeyer et al., 2018).

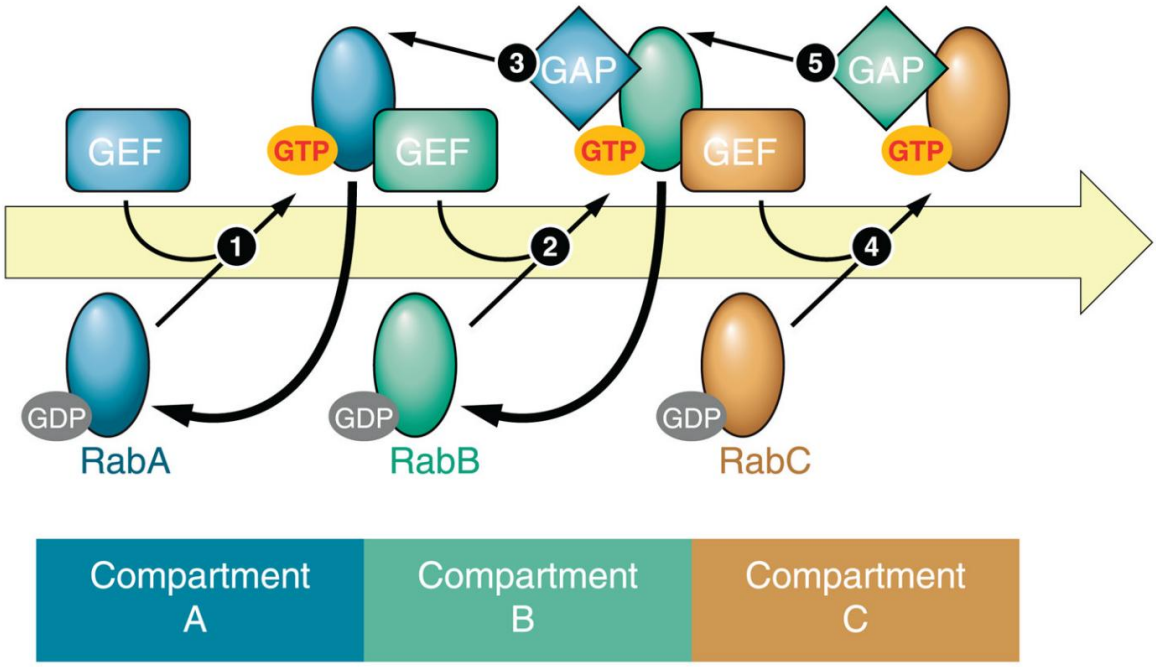

Figure 14. Principle of the Rab cascade, from Hutagalung and Novick (2011). The GTP-bound RabA associated to the compartment A recruits its effectors. Among RabA effectors, there is the GEF of RabB. The recruitment of GTP-bound RabB and downstream recruitment of RabB effectors change the compartment identity. Moreover, among RabB effectors, there is the GAP of RabA. Therefore the initial recruitment of RabA is self-inhibitory through the recruitment of RabB, transforming the compartment identity. Additional Rab (RabC in this example) can prolong the cascade.

1.5. Lysosomal degradation pathways

Lysosomes are loaded with their digestive contents through 3 different pathways: phagocytosis, endocytosis and the autophagy pathway (**Figure 15**). I already mentioned endocytosis in the section dedicated to endosomal maturation. Phagocytosis is a special type of endocytosis involved in the engulfment of large particles, typically bacteria, in immune cells. The capture of such large particles leads to the formation of a phagosome without lytic activity. To catalyze the degradation of the foreign particle, the phagosome fuses with a lysosome forming a phagolysosome. Similarly, a LE can fuse with a lysosome to form an endolysosome to fully digest its content. Noteworthy, endosome/lysosome fusion is not necessarily total and can be limited to a “kiss-and-run” process in which a transient fusion between the organelles allows a partial shuffling of their contents before scission. Autophagy will be described in details in the next sections. Briefly, macroautophagy consists in the engulfment of an intracellular organelle leading to the formation of an autophagosome. Similarly to the two other pathways, the autophagosome fuses with a lysosome to form an autophagolysosome to digest its content. After digestion, the reformation of the lysosomal pool is achieved through the tubulation of phagolysosome/endolysosome/autophagolysosome forming a protolysosome. Tubulation is achieved by the scission of the protolysosome regenerating the lysosomal pool (Yang and Wang, 2021). Indeed, these tubules mature into lysosomes to be ready for a new round of fusion with endosome/phagosome/autophagosome. These mature lysosomes are less acidic and less active than endolysosomes (Bright et al., 2016). This indicates that the reception of contents to be digested triggers lysosomal activity. An old nomenclature underlies this point by

distinguishing lysosomes before fusion, called primary lysosomes, and lysosomes with a content to digest (i.e. endolysosome/phagolysosome/autophagolysosome), called secondary lysosomes (Desnick and Schuchman, 2002).

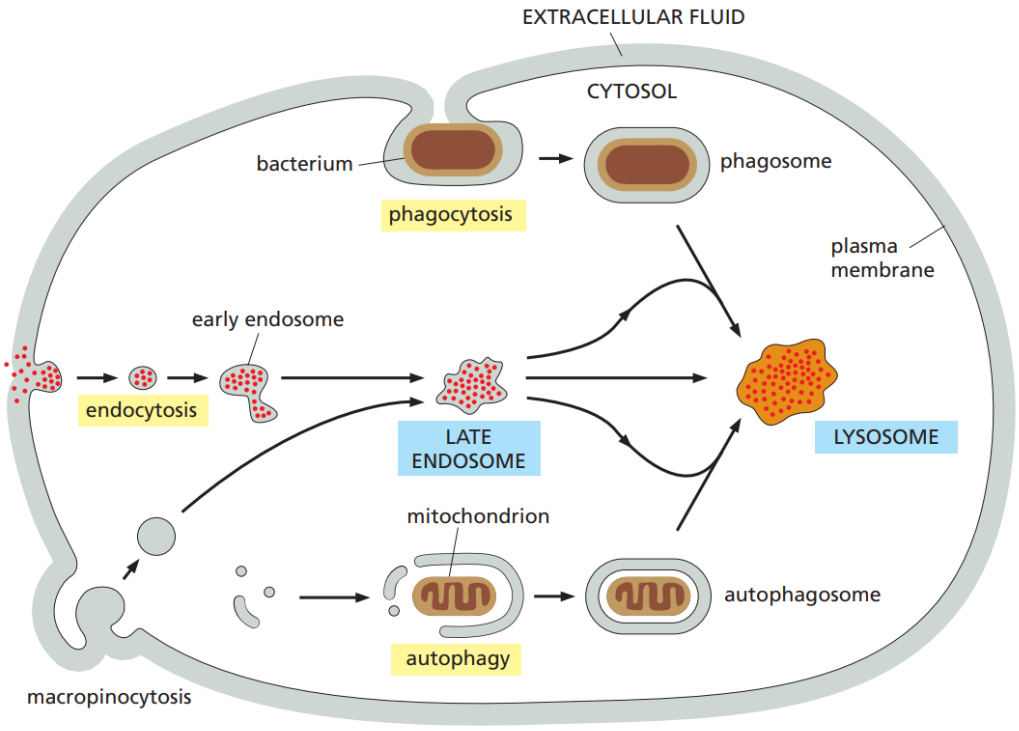

Figure 15. Lysosomal degradation pathways, from Molecular Biology of the Cell (6th edition). Lysosomes obtain their digestive content through 3 different pathways: phagocytosis, endocytosis (including macropinocytosis) and autophagy.

1.6. Non-protein molecular features and ionic concentrations of lysosomes

The proteome is a key element in the molecular description of lysosomes. However, lysosomes are also characterized by a non-protein special molecular composition. First, lysosomal membrane lipids are rich in sphingomyelin and the non-common bis(monoacylglycero)phosphate (BMP). Moreover during endosomal maturation, PtdIns(3)P, characteristics of endosomes, is replaced by PtdIns(3,5)P_2. Lysosomal membranes are also characterized by glycoproteins which are highly N-glycosylated, giving rise to a special carbohydrate signature (Rudnik and Damme, 2021).The lysosomal membrane separates the lysosomal lumen from the cytosol. This allows to separate different ionic concentrations in lysosomes and the cytosol that are regulated by different channels and transporters (**Figure 16**). Of course, due to its acidic pH, lysosomes contain a high concentration of H^+. But the concentrations of Na^+ and K^+ ions are also different compared to their cytosolic concentrations. Indeed, lysosomal concentrations are closer to the extracellular ones indicating their endocytic origin. Lysosomes are also characterized by a high concentration of Ca^{2+}, and they are sometimes viewed as a calcium storage compartment (Li et al., 2019). The higher concentrations of H^+, Na^+ and Ca^{2+} in the lysosomal lumen leads to a negative membrane potential $\Delta\psi = \psi_{cytosol} -$

ψ_{lumen} ranging between -20 to -40mV (Xu and Ren, 2015). However, a positive $\Delta\psi$ close to 20mV has been reported in enlarged *ex-situ* lysosomes (Wang et al., 2017; Li et al., 2019). These conflicting results could be explained either by lysosomal heterogeneity and/or measurements in non-physiological conditions. The lysosomal enlargement by the drug vacuolin-1 is necessary for patch-clamping. Vacuolin-1 leads to rapid homotypic endosomal/lysosomal fusion. Fusion will preserve electrophysiological properties of lysosomes if fused compartments are similar and their functions are not impaired. The knowledge of the exact value of $\Delta\psi$ (probably between -40 and 20mV) is not critical since the equilibrium potentials of ions (except Cl^-) are out of this range. Therefore, the prediction of ionic flux is still robust. Finally, the ionic composition of lysosomes is also characterized by the presence of metals such as Fe^{2+} and Zn^{2+} (Li et al., 2019).

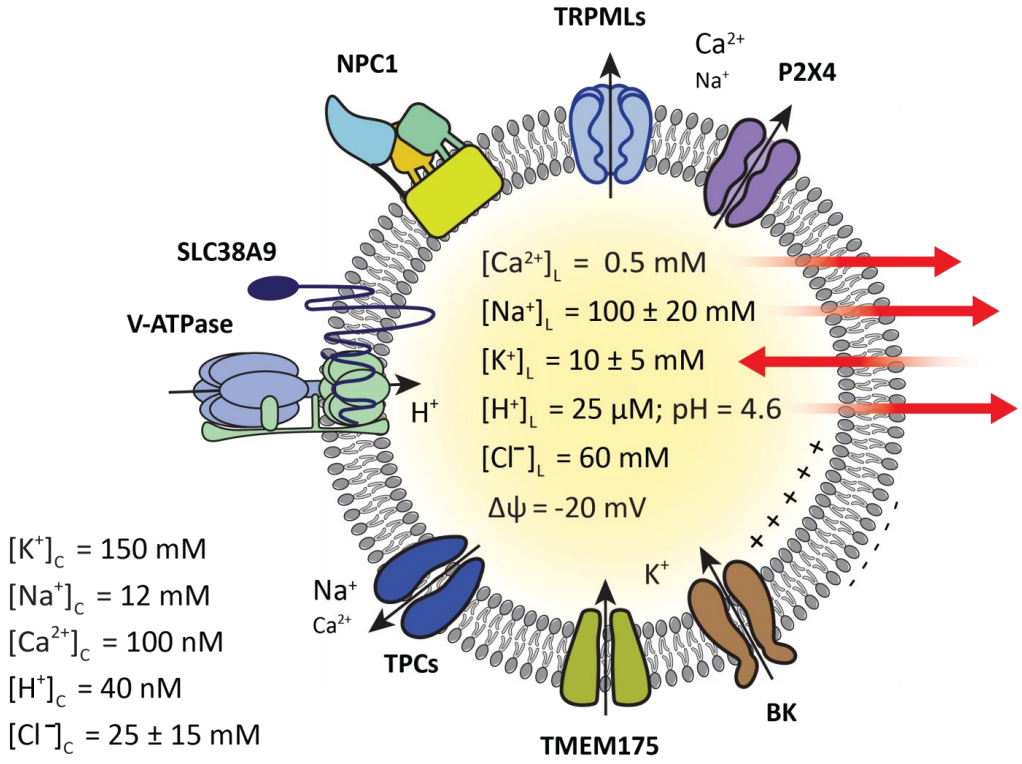

Figure 16. Ionic concentrations, channels and pumps of lysosomes, modified from Li et al. (2019). The arrows indicate the spontaneous flux of the different ions with the given concentrations and a $\Delta\psi$ of -20mV. Cl^- is close to its equilibrium potential (around -23mV for these concentrations).

1.7. Lysosomal hydrolases and Mannose-6-Phosphate pathway

Lysosomal proteome is still uncertain and the number of detected proteins varies between several hundreds to two thousands (Schröder et al., 2010). Nevertheless, differences between cell lines have been reported, highlighting the lysosomal heterogeneity (Akter et al., 2020). The lysosomal proteome can be divided into 3 parts: luminal, transmembrane and cytosolic proteins associated to lysosomal membranes. To begin with, I will briefly review luminal proteins and the cellular mechanisms of targeting of these proteins to lysosomes.

Lysosomal luminal proteins (also called matrix proteins) are mainly acidic hydrolases i.e. enzymes that use water to break covalent bonds and optimized for acidic pH. They degrade macromolecules into their building blocks, ensuring recycling and turn-over of molecules. Lysosomes contain ~60 different acidic hydrolases. This diversity of hydrolases fits the diversity of substrates; among hydrolases we can cite: nucleases (DNase, RNase), proteases (such as cathepsins or MMPs), glycosidases, lipases, phosphatases, sulfatases, phospholipases, etc. The targeting of hydrolases to lysosomes involves the well characterized mannose-6-phosphate (M6P) pathway (**Figure 17**).

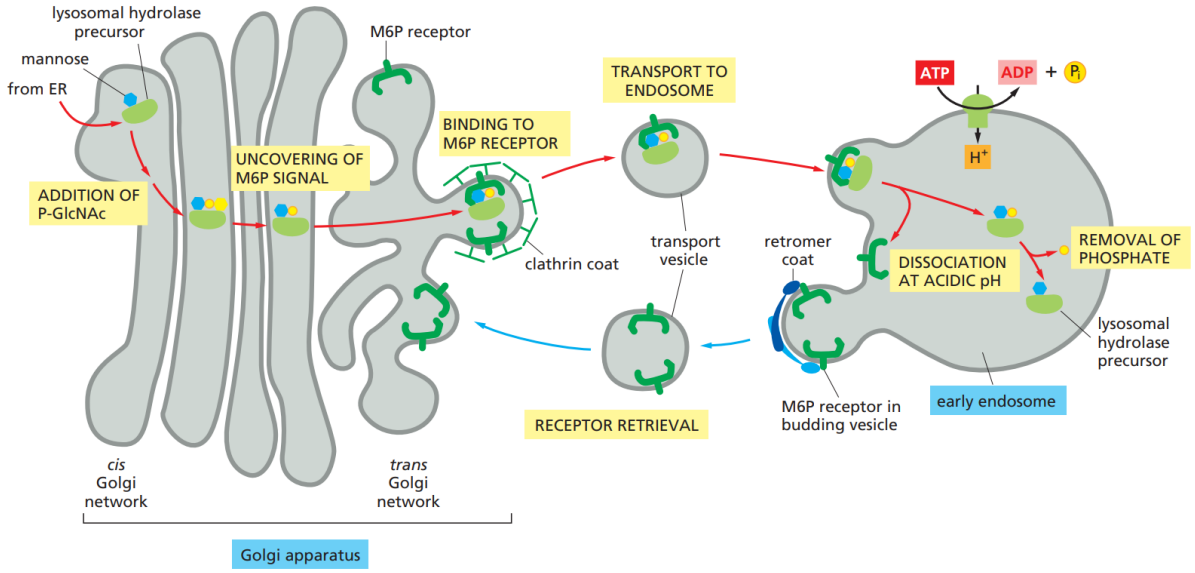

Figure 17. M6P pathway, from Molecular Biology of the Cell (6th edition). A M6P tag is added to luminal hydrolases in the *cis*-Golgi by the GlcNAc phosphotransferase. The M6P tag is recognized in the TGN by M6PR and triggers the recruitment of a clathrin coat. Clathrin coat allows the budding of a vesicle. The vesicle fuses with endosome. Due to the acidic endosomal pH, the hydrolase unbinds M6PR and the phosphate is cleaved, avoiding re-binding to M6PR. The M6PR is recycled to TGN thanks to the retromer machinery.

Neo-synthetized hydrolases receive a M6P tag in the *cis*-Golgi. The N-acetylglucosamine-1-phosphate transferase (GlcNAc phosphotransferase) recognizes lysosomal hydrolases through a signal patch (i.e. a group of residues not contiguous in the sequence but spatially close in the folded protein). It transfers a N-acetylglucosamine-phosphate motif from an UDP-N-acetylglucosamine molecule to the carbone 6 of a terminal mannose of a N-linked oligosaccharide of a lysosomal hydrolase. The N-acetylglucosamine part is further released, creating the M6P tag. M6P is recognized by M6P Receptor (M6PR) in the TGN. M6PR recruits a clathrin coat triggering vesicle budding. After budding, the vesicle containing hydrolases fuses with an endosome to support their maturation into a lysosome. Once fused with the endosome, due to a lower pH, hydrolases unbind M6PR. M6PR can be recycled to TGN thanks to the retromer machinery. Noteworthy, the phosphate of the M6P tag is removed in the endosome to avoid the possibility to recycle M6PR with the bound hydrolase.

Some studies report the presence of M6PR at the PM. It is believed that some soluble lysosomal proteins follow the constitutive secretory pathway. PM M6PR are able to bind these proteins and re-target them to lysosomes through an endocytic pathway (**Figure 18**). This pathway is qualified as indirect in contrast to the direct transport from TGN to endosomes (Braulke and Bonifacino, 2009). Alternative lysosomal targeting mechanisms independent of M6P also exist. For example, the Sortilin receptor binds Acid SphingoMyelinase (ASM) and Sphingolipid Activator Protein (SAP) to transport them from Golgi apparatus to lysosomes. β-GlucoCerebrosidase (βGC) is also a striking example of

luminal lysosomal protein transported in a M6PR-independent manner. βGC binds the Lysosomal Integral Membrane Protein 2 (LIMP2) in the ER. LIMP2 targets βGC to lysosomes (Saftig and Klumperman, 2009). These targeting mechanisms are essential for lysosomal physiology. As an example, a mutation in the GlcNac phosphotransferase can impair M6P tagging. If so, lysosomal enzymes are not recognized by M6PR and follow the classical secretory pathway and are released extracellularly. This situation is known as mucolipidosis type II (anciently I-cell disease). I-cell is a reference to the large vacuolar inclusions observed in patients. In addition to classical LSD symptoms (hepatosplenomegaly, neuromotor retard), patients have a high concentration of lysosomal enzymes in blood. This disease is the most often fatal in childhood (Khan and Tomatsu, 2020).

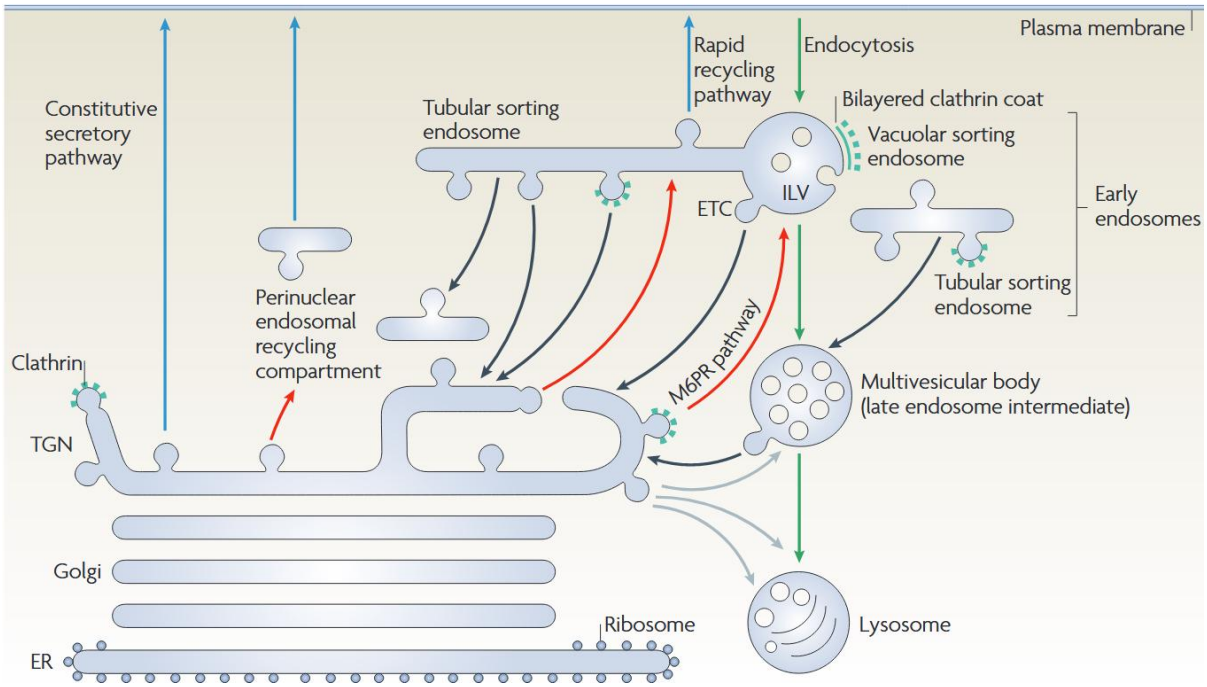

Figure 18. Interactions between the endomembrane pathway and the constitutive secretory pathway, from Saftig and Klumperman (2009). Blue arrows illustrate the constitutive anterograde pathway from ER, to Golgi apparatus and finally to the PM. Red arrows illustrate how neo-synthesized lysosomal proteins can escape the constitutive secretory pathway through the M6P pathway (direct transport). However, some soluble lysosomal proteins and M6PR can follow the constitutive secretory pathway. These proteins can be re-targeted to lysosomes through the endocytic pathway represented by green arrows (indirect transport). Gray arrows illustrate the possibility of direct transport from TGN to lysosomes in a M6P-independent manner.

1.8. Transmembrane lysosomal proteins

The functions supported by transmembrane lysosomal proteins are more diverse than those supported by luminal ones. Transmembrane proteins are involved in i) transport across the lysosomal membrane, ii) trafficking, iii) enzymatic reactions and iv) structural functions.

i) Transport across the lysosomal membrane: There is a high diversity of proteins in this class as already illustrated (**Figure 16**). The main proteins are listed at the end of this section (**Table 1**). The best known lysosomal protein involved in transport across the membrane is the Vacuolar-ATPase (V-ATPase). It pumps H^+ from the cytosol to the lysosomal lumen. The V-ATPase is similar to the ATP synthase (F-ATPase) but works in reverse: it hydrolyses ATP in ADP to transport H^+ against the electrochemical gradient. V-ATPase is a multisubunit complex made of a V_1 sub-complex in the cytosolic side responsible for ATP hydrolysis and a V_0 sub-complex embedded in the lysosomal membrane responsible for H^+ translocation. The dynamic assembly/disassembly balance of V_0 and V_1 regulates the activity of the pump (Mindell, 2012; Collins and Forgac, 2018). Once assembled, the V-ATPase undergoes a rotational motion to pump H^+. The V-ATPase is responsible for the lysosomal acidification during endosomal maturation from EE (pH=6.5), to LE (pH=6) and finally lysosome (pH=4.5-5) (Mindell, 2012). Terminal lysosomes display heterogeneity in their pH even at the cell scale: peripheral lysosomes are less acidic than juxta-nuclear ones. This effect is due to a lower V-ATPase activity and a passive H^+ leak (Johnson et al., 2016). The H^+ leaking is likely due to an unidentified channel called LysoH (Li et al., 2019).

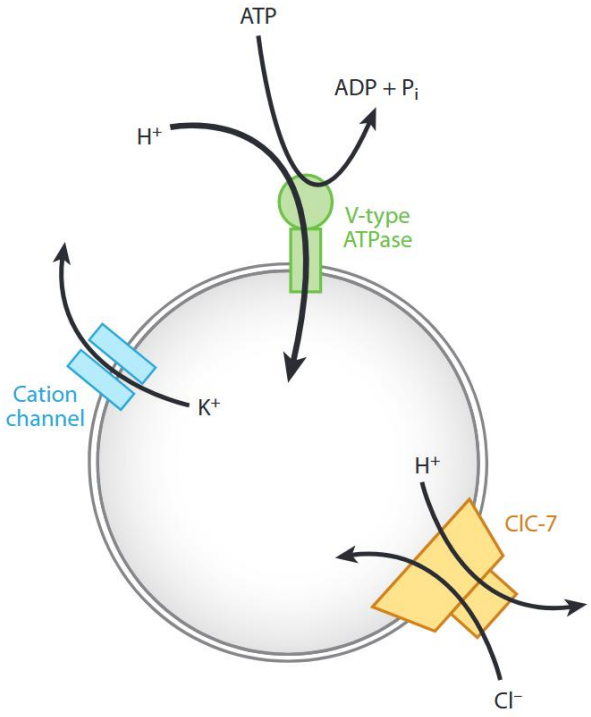

Figure 19. Mechanism of lysosomal acidification, from Mindell (2012). The V-ATPase pumps H^+ thanks to ATP hydrolysis. The electrogenic effect is compensated by the efflux of K^+ and the influx of Cl^-. The influx of Cl^- is mainly achieved by the antiporter ClC-7 which exchanges one Cl^- against the efflux of one H^+. The efflux of H^+ could appear as paradoxical. However, ClC-7 displaces 2 net charges allowing the importation of 2 H^+ by the V-ATPase. In conclusion, the common work of V-ATPase and ClC-7 results in the net importation of 1 H^+, keeping the lysosomal potential constant.

V-ATPase function is critical to assure acidic pH necessary for hydrolase activity. Assuming a luminal pH of 4.5 and a cytosolic pH of 7.2, the luminal H^+ concentration is about 500 fold higher than the cytosolic one ($\frac{[H^+]_{lumen}}{[H^+]_{cytosol}} = 10^{7.2-4.5}$). In addition to this strong chemical gradient, the V-ATPase has an electrogenic effect: H^+ pumping increases the electrical gradient (by decreasing $\Delta\psi$). A counter ion flux is needed to compensate for this electrogenic effect. Indeed, a too high electrochemical gradient would exceed the energy supplied by ATP hydrolysis. Even if the counter ion flux is not fully elucidated (Ishida et al., 2013), it relies mainly on the influx of Cl^- by the Chloride Channel 7 (ClC-7) and the efflux of K^+ through cation channels and transporters (**Figure 19**) (Mindell, 2012). Other members of the chloride channel ClC family could be involved such as ClC-3 and ClC-6. Despite their names, ClC-3/6/7 do not behave as channels but as Cl^-/H^+ antiporters. By importing one Cl^- and

exporting one H^+, ClC-7 creates a -2 net charge displacement in the lumen allowing the importation of 2 H^+ by the V-ATPase. This cycle enriches the lysosome in one H^+ without affecting the lysosomal potential.

Proteins from the SoLute Carrier (SLC) family transport small solutes resulting from the degradation of macromolecules, from the lysosomal lumen to the cytosol. SLCs can either act as uniporters (e.g. SLC2A8, a GLUT transporter involved in glucose/fructose/galactose efflux from lysosome), symporters (e.g. SLC15A3 efflux H^+ to efflux di- and tripeptides) (Smith et al., 2013) or potentially as antiporters. SLC38A9 received special attention because in addition to its role as an arginine transporter, its N-terminus tail can activate metabolism (details in next sections). Because of its additional receptor function, SLC38A9 fulfills the definition of a transceptor (Rebsamen et al., 2015).

Niemann-Pick C1 (NPC1) is an important lysosomal cholesterol transporter. Low Density Lipoproteins (LDLs) are lipidic structures containing cholesterol esters and circulating in the blood. Endocytosed LDLs are digested by lysosomal lipases, releasing free cholesterol. The luminal protein Niemann-Pick C2 (NPC2) binds cholesterol and brings it to the luminal pocket of NPC1. By a non-elucidated mechanism, NPC1 can translocate cholesterol from the lysosomal lumen to either the lysosomal membrane or the cytosol (Pfeffer, 2019). Interestingly, NPC1 is necessary for the creation of MCSs with peroxisomes and ER to transfer cholesterol (Chu et al., 2015; Höglinger et al., 2019). Interestingly, lysosomes are able to transfer cholesterol to mitochondria but through a NPC1-independent mechanism based on Steroidogenic Acute Regulatory protein (StAR)-Related lipid-Transfer proteins (START) Domain containing 3 (STARD3) (Meng et al., 2020). Nevertheless, alternative mechanisms of lysosome-ER cholesterol transfer based on LIMP-2 (Heybrock et al., 2019) and OxySterol-Binding Proteins (OSPB) (especially OSBP-related protein 1L (ORP1L)) exist (Meng et al., 2020). Among these cholesterol transporters, the NPC1/2 system plays a central role illustrated by its pathological implications. Niemann-Pick Disease (NDP) is a recessive genetic disease classified in 4 subtypes: A, B, C and E. NPD type C is characterized by a mutation in NPC1 (95% of the patients) or in NPC2 (5%). NPD type D is an historical subtype including all the patients descending from an unique Acadian (today Nova Scotia) couple who married in the 1700s (Winsor and Welch, 1978). Later work demonstrates that NPD type D is characterized by the mutation G3097T in NPC1 (Greer et al., 1998). Therefore, NPD type D is currently included in NPD type C. NPD type C causes accumulation of cholesterol esters and glycosphingolipids in lysosomes, and cholesterol depletion in the other membranes. The accumulation of undigested material in lysosomes classifies NPD as a LSD. NPD first impairs organs where cholesterol and sphingolipids biochemistry is important. It is clinically characterized by hepatosplenomegaly and progressive neuronal dysfunction such as ataxia. Clinical outputs range from neonatal death to adult neurodegenerative disease (Pacheco and Lieberman, 2008).

Mucolipin subfamily (TRPML) contains TRPML1 (MCOLN1), TRPML2 (MCOLN2) and TRPML3 (MCOLN3). Mucolipins are members of the Transient Receptor Potential (TRP) channel family localized on lysosomes. Among them, TRPML2 and 3 are poorly understood whereas TRPML1 has been well investigated. TRPML1 is a non-selective cation channel permeable to Ca^{2+}, Na^+, K^+ but also Fe^{2+} and Zn^{2+} metals. However TRMPL1 is impermeable to H^+. The localization of TRPML1 on lysosomes is challenging for electrophysiological approaches. Only recently, the enlarged lysosomes by vacuolin-1 allowed the patch-clamp analysis of TRPML1. TRPML1 is potentially regulated by luminal pH and lysosomal electrical potential $\Delta\psi$, but the most accepted mechanism of regulation is by the presence of PtdIns(3,5)P_2 (Wang et al., 2014). TRPML1 can be also activated by artificial compounds such as ML-SA1. Despite its speculative roles in metal homeostasis, TRPML1 is known to be the major lysosomal Ca^{2+} channel. Interestingly, TRPML1 interacts with Big Potassium (BK) channels, a family of voltage-gated K^+ channel. Ca^{2+} efflux through TRPML1 activates BK. The K^+ influx

could act as a counter-ion to avoid severe modification of the membrane potential $\Delta\psi$ and facilitate Ca^{2+} efflux (Cao et al., 2015).

Lysosomal Ca^{2+} concentration is about 0.5mM, 5000 fold higher than in the cytosol (about 100nM). Therefore, lysosomes can be seen as a calcium storage compartment. However, once diluted in the much larger cytosolic volume, the increase of Ca^{2+} could be minor. Assuming 100 lysosomes with a radius 0.250µm in a cell with a radius of 10µm releasing their full Ca^{2+} content: the Ca^{2+} concentration only increases by 0.8µM ($[Ca^{2+}]_{lyso} \times 100 \times \left(\frac{r_{lyso}}{r_{cell}}\right)^3$). As a comparison, the Ca^{2+} sensor synaptotagmin has a Ca^{2+} affinity in the 10µM range (Fernandez et al., 2001). Although some experimental evidences seem to indicate that lysosomes could substantially increase the Ca^{2+} concentration under special conditions (Shang et al., 2016), simulation studies reveal that modifications of Ca^{2+} concentration caused by a single channel could be high but local (submicrometric scale) (Shuai and Parker, 2005). Although the number of TRPML1 copies per lysosome is not known, the small surface of lysosomes probably limits the efficiency of Ca^{2+} efflux. To play its role, lysosomal Ca^{2+} release probably requires a correct lysosomal positioning. For example, through MCS, TRPML1 is able to transfer Ca^{2+} to the mitochondrial matrix (Yang et al., 2020). It has been also demonstrated that lysosomal Ca^{2+}, once released, can bind calcineurin, mediating the dephosphorylation of the transcription factor EB (TFEB) (Medina et al., 2015). Dephosphorylated TFEB is translocated into the nucleus, activating the genetic program for lysosomal biogenesis and autophagy (Yang et al., 2020). Additionally, TRPML1 can directly activate autophagy through the activation of the Calcium/CalModulin-dependent protein Kinase kinase β (CaMKKβ) (Scotto Rosato et al., 2019). Furthermore, Ca^{2+} released by TRPML1 can activate the Asparagine-Linked Glycosylation 2 homolog (ALG2), recruiting dynein and leading to retrograde trafficking (Li et al., 2016). Finally, it has been postulated that lysosomes, thanks to TRPML1, could self-provide the Ca^{2+} necessary for their exocytosis (Di Paola et al., 2018).

Interestingly, mutations in TRPML1 cause Mucolipidosis Type IV (MLIV) clinically characterized by psychomotor retardation and corneal opacities. This disease is rare in the whole population (prevalence of 1:40.000), however 70% of patients are Ashkenazi Jewish descendants with two main mutations (one mutation at the spliceosome acceptor site for intron 3 and a 6434bp genomic deletion). The MLIV prevalence in jewish population is as high as 1:100. At the cellular scale, MLIV is characterized by an accumulation of gangliosides, phospholipids and mucopolysaccharides in lysosomes (Di Paola et al., 2018). Contrary to other LSDs, MLIV is not characterized by an enzymatic defect. However, TRPML1 mutations impair lysosomal exocytosis (LaPlante et al., 2006).

Other members of the TRP family, such as TRPM1/2 and TRPA1, are also involved in the lysosomal Ca^{2+} regulation. Ca^{2+} channels that are not members of TRP family also exist, such as P2X4, a cation channel extremely permeable to Ca^{2+} and regulated by the luminal pH and ATP concentration. These channels could be involved in similar functions than TRPML1 such as regulating exocytosis. Additionaly these channels seem to be also expressed in some LROs. For example, P2X4 is involved in the pore expansion during lamellar body exocytosis in type II pneumocytes (Murrell-Lagnado and Frick, 2019). To ensure its role as a calcium storage compartment, lysosomes need to import Ca^{2+}. CAX is a Ca^{2+}/H^+ antiporter that consume the H^+ gradient to import Ca^{2+} (Melchionda et al., 2016).

V-ATPase	Pump	Lysosomal acidification by H^+ pumping
SLC (SLC2A8, SLC11A1, SLC11A2, SLC15A3, SLC17A5, SLC29A3, SLC30A2, SLC36A1, SLC66A4, etc.)	Transporter	Transport of ions and small solutes (sialic acid, glucuronic acid, histidine, glucose, nucleosides, neutral amino acids, metal ions, etc.)
ClC-3, ClC-6, ClC-7	Chloride-Proton antiporter	Influx of 1 Cl^- and efflux of $1H^+$
CAX	Ca2+/H+ antiporter	Efflux of 1 H^+ and influx of 1 Ca^{2+}
TRPML1	Cation channel	Efflux of Ca^{2+} (K^+, Na^+, Fe^{2+}, Zn^{2+})
TRPML2/3	Non selective cations channels	Similar to TRPML1 (?)
TRPM1/2	Ligand-gated non specific cation channel	Efflux of Ca^{2+}
TRPA1	Ligand-gated non specific cation channel	Efflux of Ca^{2+}
P2X4	Cation channel	Efflux of Ca^{2+}
VGCC	Voltage-gated calcium channel	Efflux of Ca^{2+}
BK	Voltage-gated K+ channel	Influx of K^+
TMEM175	K+ channel	Influx of K^+
TPC1/2	Voltage-gated and ligand gated Na+ channel	Efflux of Na^+
NPC1	Translocation protein	Efflux of cholesterol toward ER and peroxysome
STARD3	Translocation protein	Efflux of cholesterol toward mitochondria
OSBP/ORP (ORP1L)	Translocation protein	Efflux of cholesterol toward ER
LIMP2	Translocation protein	Efflux of cholesterol toward ER

Table 1. Main proteins involved in transport across the lysosomal membrane.

ii) Fusion machinery: Some lysosomal membrane proteins are involved in the membrane fusion machinery and can drive exocytosis and fusion with endosome/phagosome/autophagosome. This will be reviewed in the section dedicated to the SNARE machinery.

iii) Enzymatic functions: Some transmembrane proteins support enzymatic functions. For example, Signal Peptide Peptidase Like 2a (SPPL2a) is a lysosomal protease (Schröder et al., 2010) that cleaves the intraluminal domain of the Tumor Necrosis Factor α (TNFα) (Spitz et al., 2020). A second interesting example is Heparan-α-GlucoSaminide N-AcetylTransferase (HGSNAT). HGSNAT is the only documented lysosomal enzyme that is not a hydrolase. It transfers cytosolic acetyl-CoA to heparin in the lysosomal lumen (Bame and Rome, 1985; Durand et al., 2010). This reaction is necessary for heparan degradation and mutation in HGNSAT results in Mucopolysaccharidosis type IIIC (also called Sanfilippo syndrome type C).

iv) Structural functions: The most emblematic lysosomal protein is maybe Lysosomal-Associated Membrane Protein 1 (LAMP1 also called CD107a). LAMP2 is the paralog of LAMP1 sharing 37% of homology. LAMP1 and LAMP2 together contribute to about 50% of all lysosomal transmembrane

proteins and are widely used as lysosomal markers. Both proteins have the same structure: a large luminal domain, a single transmembrane domain and a small 11 residues long cytosolic C-terminus tail. Their luminal domains are highly glycosylated, tripling their mass from ~40kDa to ~120kDa (Eskelinen, 2006). With other proteins, the glycosylation of LAMP1 and LAMP2 creates a dense luminal coat of 5 to 12nm thickness visible in EM: the lysosomal glycocalyx (Neiss, 1984, 1986). Glycocalyx is thought to be a protective layer limiting the access of hydrolases to transmembrane proteins and membrane lipids. LAMP1 KO mice are viable and fertile with only a weak phenotype of astrogliosis and immunoreactivity. LAMP1 KO seems to be compensated by LAMP2 upregulation. However, LAMP2 KO mice die at the age of 20-40 days for 50% of them. At cellular scale, LAMP2 KO mice are characterized by an accumulation of autophagic vacuoles. Moreover, LAMP2 KO mice have a larger but weaker heart. This is consistent with Danon disease, a genetic disease caused by LAMP2 mutation and characterized by a hypertrophic cardiomyopathy. Therefore, LAMP2 seems to partially encompass LAMP1 functions and compensates for its KO but the inverse is not true. LAMP1/2 double KO is lethal between embryonic days 14.5 and 16.5 (Eskelinen, 2006). Despite these observations highlighting the crucial roles of LAMP1/2, their functions remain poorly understood. Cells deficient for LAMPs have a phenotype with excessive cholesterol storage. LAMPs can bind cholesterol through their luminal tails, acting either as a reservoir for cholesterol transporters or directly promote cholesterol free diffusion in the lysosomal membrane (Meng et al., 2020). Noteworthy, a third paralog so-called LAMP3 exists but is limited to lysosomes of dendritic cells.

CD63 is also an interesting lysosomal glycoprotein. CD63 is a member of the tetraspanin family characterized by 4 transmembrane domains, a small and a large extracellular loop. The transmembrane helices enclose a cholesterol molecule (Lang and Hochheimer, 2020). CD63 is a marker of MVBs, present on ILVs membranes but also on MVB external membranes. As for LAMP1 and LAMP2, CD63 function is not understood but it is an highly glycosylated protein participating to the glycocalyx (Pols and Klumperman, 2009).

1.9 Cytosolic proteins associated with lysosomes

Cytosolic proteins associated with lysosomal membranes are diverse. I will review three well known types of lysosomal associated proteins of the first importance: proteins involved in i) lysosomal positioning, ii) lysosomal tubulation/fission and iii) the regulation of mTORC1.

i) Proteins involved in lysosomal positioning: These proteins recruit adaptors for molecular motor proteins. Three kinds of molecular motors are involved in lysosome positioning: kinesins driving the anterograde transport (+ tips directed MT transport), dynein driving the retrograde transport (- tips directed MT transport) and myosins with a more complex role.

Kinesin-1 is a heterotetramer composed of two heavy chains (KIF5A, KIF5B or KIF5C) and two light chains (KLC1, KLC2, KLC3 or KLC4). Kinesin-1 is the major molecular motor responsible for the anterograde displacement of lysosomes. The octameric BLOC-1-related complex (BORC) is associated with the cytosolic lysosomal membrane leaflet through the myristoylation of the N-terminus of one of its sub-unit, the myrlysin protein (BORCS5). BORC recruits the Arf-like small GTPase Arl8 from the cytosol. Arl8 recruits two of its effectors, SifA and kinesin-interaction protein (SKIP), a kinesin adaptor (Pu et al., 2016). When SKIP is free in the cytosol, it is under an auto-inhibitory state. When Arl8 recruits SKIP, it turns off this autoinhibition and SKIP is able to connect lysosomes to kinesin-1 (**Figure 20.D**) (Keren-Kaplan and Bonifacino, 2021). The association of BORC and Arl8 is also able to recruit

kinesin-3 (KIF1A and KIF1Bβ for lysosomal transport) in a SKIP-independent manner. Interestingly, KIF5B preferentially transports lysosomes on perinuclear MTs enriched in acetylated α-tubulin, whereas KIF1Bβ and KIF1A drive lysosomes on peripheral MTs enriched in tyrosinated α-tubulin (Guardia et al., 2016).

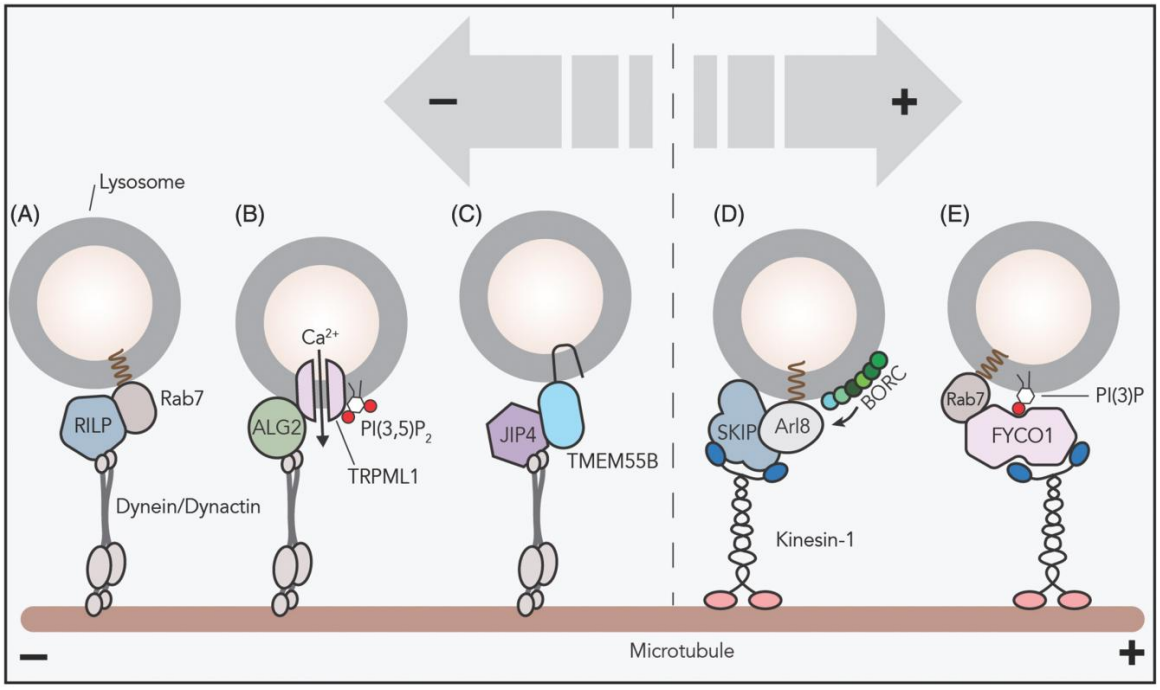

Figure 20. The different mechanisms of molecular motor recruitment, from Cabukusta and Neefjes (2018). A) Dynein/dynactin recruitment through the Rab7 effector RILP. B) Dynein/dynactin recruitment through the activation of TRPML1 by PtdIns(3,5)P2. Ca^{2+} release activates ALG2 recruiting dynein/dynactin. C) Dynein/dynactin recruitment through the JIP4/TMEM55B complex. D) Kinesin-1 recruitment through BORC. BORC recruits Arl8. Arf8 recruits its effector, the kinesin adaptor SKIP. E) Kinesin-1 recruitment through Rab7 bound to FYCO1.

An alternative mechanism can load kinesin-1 on lysosomes through Rab7 (**Figure 2E**). GTP-bound Rab7 is associated to lysosomal membranes. The ER-anchored protein protrudin can bind simultaneously Rab7-GTP and lysosomal PtdIns(3)P thanks to its FYVE domain. This interaction creates a MCS between lysosome and the ER. Independently, non protrudin-bound Rab7 recruits its effector FYVE- and COiledcoil-domain-containing protein 1 (FYCO1). Protrudin is able to bind kinesin-1 and to transfer it to the adaptator protein FYCO1 (**Figure 21**) (Raiborg et al., 2015; Pu et al., 2016).

Retrograde trafficking is mediated by dynein accompanied by its activator dynactin. The recruitment of dynein-dynactin complex is also regulated by Rab7. Rab7-GTP recruits its effectors Rab7-Interacting Lysosomal Protein (RILP) and ORP1L. RIPL plays the role of a linker between Rab7 and the dynactin subunit $p150^{Glued}$. The Rab7-RILP-ORP1L complex also promotes the interaction between lysosomal membrane bound βIII-spectrin and the dynactin subunit actin-related protein 1 (Arp1). Interactions of ORP1L with its partners activate dynein (**Figure 20A**) (Pu et al., 2016). Noteworthy, these interactions depend on the lysosomal cholesterol level. Under low cholesterol condition, ORP1L binds the ER protein Vesicle-Associated membrane-protein associated Protein A (VAPA) and the formation of lysosome-ER MCSs allowing lipid exchange. Indeed, ORP1L transports cholesterol and PtdIns(4)P between ER and lysosomal membranes (Wijdeven et al., 2016). ORP1L-VAPA interaction results in the dissociation of dynein (**Figure 21**). Under high cholesterol conditions, such as NPD type C, lysosomes are clustered in the juxta-nuclear region (Rocha et al., 2009; Pu et al.,

2016). Thus, the cholesterol level could be an important parameter to control the output of Rab7, which has the potentiality to initiate anterograde and retrograde movements.

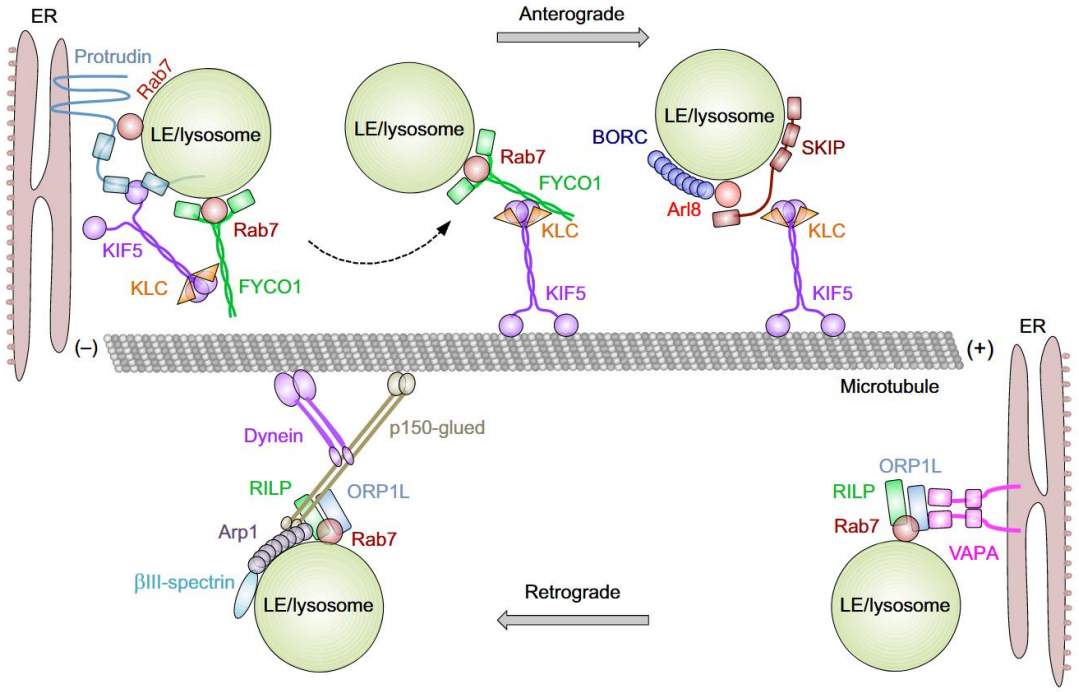

Figure 21. MCSs with ER regulate lysosomal positioning, Pu et al. (2016). Top: Protrudin binds Rab7 and PtdIns(3)P creating a MCS. Protrudin binds kinesin-1 and can transfer it to FYCO1 (itelf bound to another lysosomal copy of Rab7). The translocation of the kinesin-1 on FYCO1 detaches lysosome from ER and initiates an anterograde movement. Bot: The complex Rab7-RILP-Arp1-βIII-spectrin binds dynein/dynactin complex for retrograde motion. However, it is a cholesterol dependent process. Under low cholesterol concentration, the cholesterol sensor ORP1L binds VAPA, creating a MCS with ER.

As for retrograde trafficking, different mechanisms for the recruitment of dynein exist. As previously explained, Ca^{2+} release by TRPML1 activates ALG2 that recruits dynein and leads to retrograde trafficking (**Figure 20B**) (Li et al., 2016). The transmembrane protein TMEM55B is also able to recruit dynein through the dynein adaptor JNK Interacting Protein 4 (JIP4) (**Figure 20C**). The TMEM55B protein level is controlled by nutrient status. Upon starvation, TMEM55B is transcriptionaly upregulated, leading to a perinuclear clustering (Willett et al., 2017). To date, it is unclear if ALG2- and TMEM55B-dependent retrograde trafficking are independent of the Rab7-RILP-ORP1L complex.

The actin cytoskeleton has additionally a clear role in lysosomal trafficking, since actin depolymerization by latrunculin A treatment increases lysosomal mobility and decreases their directionality. This interaction seems to be mediated by myosin IB (Cordonnier et al., 2001). The unconventional myosin VIIa is also associated with lysosomes (Soni et al., 2005). In melanocytes, Rab27A is able to recruit myosin Va and myosin VIIa through its effector Stomatin-like protein 2 (Slp2). Myosin recruitment accumulates melanosomes at the cell periphery. It seems that the same mechanism is involved in the docking of cytotoxic T cells granules at the PM (Cabukusta and Neefjes, 2018).

Lysosomal trafficking is characterized by an alternance of progressive displacements with periods of pause, a movement coined as “stop-and-go”. Stop periods have been proposed to rely on the establishment of MCS with ER thanks to VAPA and protrudin, as explained earlier (Pu et al., 2016). These stops could also be due to MCS establishment mediated by the protein RiNg Finger 26

(RNF26), an ER resident E3 ligase. RNF26 binds and ubiquitinates sequestosome 1 (SQSTM1 also known as p62). SQSTM1 is an ubiquitin scaffold protein interacting with lysosomal ubiquitin adaptors TOLLIP, EPS15 and TAX1BP1. These interactions capture lysosomes, especially in the perinuclear regions. This lysosomal capture is reversible thanks to the deubiquitinating enzyme USP15 (Jongsma et al., 2016).

ii) Lysosomal tubulation/fission machinery: This machinery is essential for the reformation of the lysosomal pool after the endolysosome/phagolysosome/autophagolysosome formation. However, this machinery is still poorly known. The tubulation and fission of membranes from endolysosomes (known as Endocytic Lysosome Reformation or ELR) seems to require PtdIns(3)P 5-kinase FYVE (PIKfyve). Through its FYVE domain, it binds PtdIns(3)P phospholipids that are characteristic of endosomal membranes. Once bound, PIKfyve has a 5'kinase activity that phosphorylates PtdIns(3)P, producing PtdIns(3,5)P_2 characteristic of lysosomal membranes. PtdIns(3,5)P_2 activates the TRPML1 channel. These factors seem required for the regeneration of lysosomes from endolysosomes (Yang and Wang, 2021). The reformation of lysosomes from phagolysosomes (known as Phagocytic Lysosome Reformation, or PLR) is similar, it involves PIKfyve and TRPML1. However the reformation of lysosomes from autophagolysosomes (known as Autophagic Lysosome Reformation, or ALR) is different. The formation of PtdIns(4,5)P_2 on autophagolysosome membranes recruits clathrin through the adaptin AP-2. This mechanism forms microdomains able to recruit KIF5B by direct interaction with PtdIns(4,5)P_2. Probably resulting from the pulling force of KIF5B, a tubule is initiated, forming a so-called proto-lysosome (Cabukusta and Neefjes, 2018; Yang and Wang, 2021). The kinase PIP5K1A (PtdIns(4)P 5-Kinase Type 1 Alpha) is recruited on the protolysosomal tubule, generating new PtdIns(4,5)P_2, recruiting new clathrin. This new round of clathrin recruitment leads to the protolysosomal scission by dynamin-2 (Yang and Wang, 2021).

iii) Proteins involved in the regulation of mTORC1: The mechanistic (originally "mammalian") Target Of Rapamycin (mTOR) is a serine/threonine kinase. In mammalian cells, mTOR forms two complexes: mTORC1 and mTORC2. mTORC1 is formed by RAPTOR, PRAS40, FKBP12-rapamycin, mLST8, DEPTOR and mTOR (Liu and Sabatini, 2020). mTORC1 has various functions but it is recognized as a master regulator of protein synthesis and cell growth. This role is achieved by its interaction with lysosomes and by the regulation of lysosomal pathways (**Figure 22**) (Liu and Sabatini, 2020).

Cytosolic mTORC1 is inactive but under certain conditions, mTORC1 is recruited and activated on lysosomes. The lysosomal Ragulator complex recruits two heterodimers, RagA/B and RagC/D. Rags are small GTPase. Under RagA/B-GTP RagC/D-GDP state, mTORC1 is recruited. Once associated to the lysosomal membrane, mTORC1 interacts with the small GTPase Rheb anchored to lysosomal membrane. Rheb GTP-bound triggers a conformational change in mTORC1 that makes its kinase site competent. In summary, activation of mTORC1 is a two-steps process: recruitment by Rags and activation by Rheb. mTORC1 activity is regulated by nutrient availability. Under low nutrient conditions, the GAP GATOR1 hydrolyses GTP of RagA/B whereas under nutrient rich conditions, the protein GATOR2 inhibits GATOR1. In parallel, a complex composed of Foliculin (FLCN) and FLCN-Interacting Protein (FNIP) 1 or 2 promotes GTP hydrolysis of RagC/D. The GAP activity of FLCN/FNIP complex seems regulated by the nucleotide state of RagA/B. Alternatively; Rheb is controlled by the GAP Tuberous Sclerosis Complex (TSC). Growth factor pathways are able to inhibit TSC. TSC is activated by the AMP-Dependent-Protein Kinase (AMPK) (Corradetti et al., 2004). AMPK is an energy sensor activated by high ADP/ATP and AMP/ATP ratios (Shin and Zoncu, 2020).

mTORC1 promotes protein synthesis through the phosphorylation of S6K1 and 4E-BP1 and inhibits lysosomal pathways through phosphorylation of ULK1/2. ULK1/2 is a key regulator of autophagy and is inhibited by phosphorylation (Shin and Zoncu, 2020). Moreover, mTORC1 phosphorylates TFEB, a

transcription factor of the MiT/TFE family characterized by a basic helix-loop-helix leucine zipper structure. When phosphorylated, TFEB is retained in the cytosol, whereas when unphosphorylated, TFEB translocates into the nucleus and activates the Coordinated Lysosomal Expression And Regulation (CLEAR) network. The CLEAR network is an ensemble of lysosomal genes co-regulated with a palindromic 10-base motif (called an E-box) in their promoters (Settembre and Medina, 2015). Therefore, through the transcriptional activation of the CLEAR network, TFEB promotes lysosomal biogenesis and autophagy.

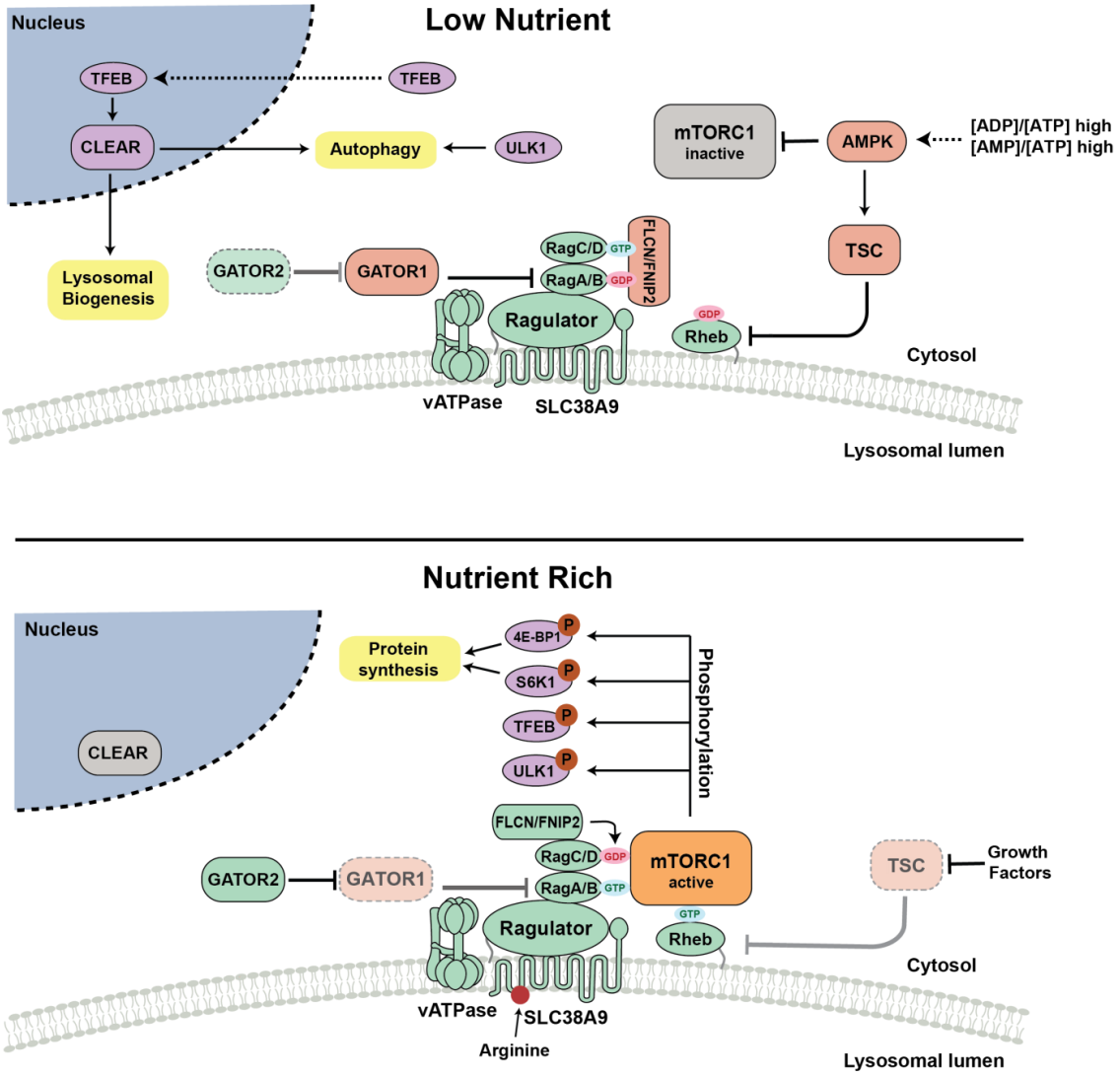

Figure 22. mTORC1 regulation and cellular outputs, modified from Shin and Zoncu (2020). Top: Under low nutrient conditions, RagA/B GDP-bound and RagC/D GTP-bound cannot recruit mTORC1. GATOR1 hydrolyzes GTP of RagA/B, and the GATOR1 inhibitor is inactive. Rheb GDP-bound is controlled by the GAP TSC. TSC is regulated by AMPK, itself controlled by ratios of [ADP]/[ATP] and [AMP]/[ATP]. Additionally, AMPK directly inhibits mTORC1. Under these conditions, ULK1 is free to promote autophagy and TFEB to translocate into the nucleus to promote the transcription of the CLEAR network. CLEAR network upregulation enhances autophagy and lysosomal biogenesis. Bottom: Under nutrient rich condition, RagA/B GTP-bound and RagC/D GDP-bound recruits mTORC1. This nucleotide configuration is achieved through the activation of the inhibitor of GATOR1, GATOR2, and the activation of the FLCN/FNIP2 complex, which hydrolyze GTP of RagC/D in GDP. Moreover, growth factors inhibit TSC and under its GTP form, Rheb activates mTORC1. Activated mTORC1 phosphorylates ULK1 inactivating it, leading to an inhibition of autophagy. mTORC1 also phosphorylates TFEB, retaining it in the cytosol and leading to a downregulation of the CLEAR network. Lastly, mTORC1 phosphorylates 4E-BP1 and S6K1 promoting protein synthesis. Green color indicates positive regulators of mTORC1, red negative regulators, violet molecular outputs and yellow general cellular outputs.

To summarize, under low nutrient conditions, RagA/B is GDP-bound, RagC/D GTP-bound and Rheb GDP-bound. Therefore, the recruitment and the activation of mTORC1 is not possible and ULK1/2 directly activates autophagy whereas TFEB translocates into the nucleus to transcriptionaly promotes lysosomal biogenesis and autophagy. In contrast, under nutrient rich conditions, RagA/B GTP-bound, RagC/D GDP-bound and Rheb GTP-bound forms recruit and activate mTORC1. By its kinase activity, mTORC1 inhibits autophagy and lysosomal biogenesis but promotes anabolic activities. Other factors participate in the regulation of mTORC1 activity. For example, the lysosomal transporter SLC38A9 has been proposed to detect luminal amino acid abundance and interact with Ragulator (Rebsamen et al., 2015; Wang et al., 2015).

1.10. Physiological functions

The lysosome has been naively seen as the cellular degradation and recycling bin. However, its function is not restricted to degradation, it is involved in many cellular processes: i) autophagy, ii) cell death, iii) secretion, iv) adhesion and cell migration, v) metabolic/transcriptional regulation and vi) plasma membrane repair. I will briefly review these diverse functions:

i) Autophagy: As explained earlier, the fusion of a lysosome with an endosome/phagosome/autophagosome allows the digestion of their content. Macromolecules are degraded in building blocks and translocated in the cytosol thanks to lysosomal transporters and channels to be reused. However, the recycling role of lysosomes in autophagy is not restricted to the formation of an autophagolysosome. 3 types of autophagy are usually distinguished: macroautophagy, microautophagy and Chaperone-Mediated Autophagy (CMA) (**Figure 23**) (Boya et al., 2013). Macroautophagy, sometimes named only autophagy for simplicity, is the pathway consisting of the formation of a membrane (called phagophore) enclosing cellular content (organelles and cytosolic solutes). It forms a double membrane structure called autophagosome. This pathway is under the control of the ULK1/2 complex and indeed depends on the fusion with lysosomes (Yang and Klionsky, 2010). However microautphagy and CMA do not require fusion with lysosomes.

Microautophagy involves the invagination or the protrusion of endosomal/lysosomal membranes engulfing material that is afterward degraded. The importance of this pathway is still debated for mammalian cells (Mijaljica et al., 2011). This pathway can capture bulk cytosol or target some cargos. The chaperone Heat Shock Cognate 71kDa protein (Hsc70) is believed to mediate the interaction between specific proteins and the endosomal/lysosomal membrane in microautophagy (Kaushik and Cuervo, 2018). In mammals, evidence supports that micro-autophagy does not occur in lysosomes but in endosomes, a process so-called endosomal microautophagy. Endosomal microautophagy is similar to the formation of ILVs in MVBs. Contrarly to ILVs that are released as exosomes, the endosomal microautophagy forms vesicles that are degraded in the endosome or upon fusion with a lysosome (Tekirdag and Cuervo, 2018). In yeast, microautophagy is better understood and has different molecular machineries to target various organelles: mitochondria, peroxisomes, ER, etc. A striking example of the fabulous capacity of yeast microautophagy is the so-called piecemeal microautophagy of the nucleus. After the formation of a nucleus-vacuole junction through the interaction of the vacuolar membrane protein Vac8p and the outer-nuclear envelope protein Nvj1p, and under starvation, the vacuole is able to pinch-off and engulf non essential parts of the nucleus (Kvam and Goldfarb, 2007).

The CMA is always selective contrary to macro- and microautophagy. Proteins degraded by this pathway are recognized through a specific KFERQ sequence. This sequence is detected by the chaperone Hsc70. Hsc70 delivers the target protein to the lysosomal membrane. Hsc70 interacts with the cytosolic tail of LAMP2A (one of the three splice variants of LAMP2: LAMP2A, LAMP2B and LAMP2C). The target protein is then unfolded by Hsc70 and trimerization of LAMP2A creates a translocon complex. This complex is able to transport the target protein from the cytosol to the lysosomal lumen (Kaushik and Cuervo, 2018).

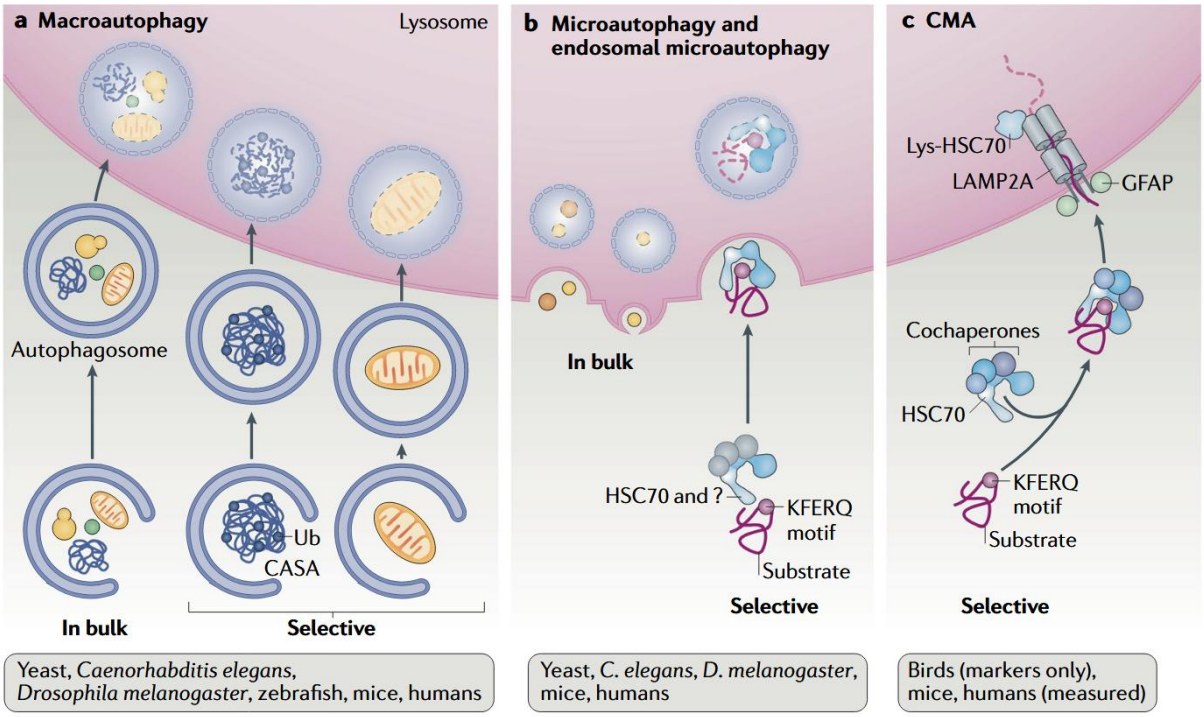

Figure 23. The different types of autophagy, from Kaushik and Cuervo (2018). Macroautophagy is the capture (selectively or not) of organelles and/or solutes by a phagophore forming an autophagosome. The autophagosome fuses with lysosome to degrade its content. Microautophagy is the lysosomal capture of material through the invagination or the protrusion of its membrane. Selectivity of cargo is possible, likely mediated by Hsc70. CMA is a selective autophagic process where a target is recognized by HSC70 through a KFERQ motif. The recognized protein is translocated in the lysosomal lumen by a LAMP2A trimer.

ii) Cell death: Originally, Christian de Duve described lysosomes as a "suicide bag" (de Duve, 1983). Later, De Duve became skeptical about this hypothesis but more recent work seems to validate his view. Indeed, different stimuli (fungal/bacterial toxins, viral proteins, Reactive Oxygen Species (ROS), hydrolases, etc.) induce a lysosomal permeabilization. A massive permeabilization releases H^+ ions and hydrolases leading to necrosis, while a mild permeabilization activates the intrinsic apoptosis pathways. The liberation of lysosomal cathepsins cleaves the pro-apoptotic protein BID and the anti-apoptotic protein BCL2 (Aits and Jaattela, 2013). Actually, the exact output of lysosomal permeabilization is influenced by several factors. For example, if lysosomes are rich in iron and ROS, they trigger ferroptosis instead of classical apoptosis (Wang et al., 2018a).

iii) Secretion: Lysosomes can contributre to exocytosis. This secretory pathway supports different functions. These functions will be reviewed in the next sections.

iv) Adhesion and cell migration: Lysosomes are involved in migration and cell adhesion. For example, it has been reported that activated integrins α5β1 are not degraded in lysosomes after

internalization but targeted to the PM for recycling (Dozynkiewicz et al., 2012). Moreover, a subpopulation of lysosomes positive for the Mitogen-Activated Protein Kinase (MAPK) scaffold complex p14-MP1, targets specifically Focal Adhesions (FAs). The KO of p14 elongates FAs and impairs migration. It is believed that this targeting is necessary for FAs remodeling and cell migration (Schiefermeier et al., 2014). Interestingly, FAs are able to exercise a feedback on lysosomal associated proteins. Indeed, it has been demonstrated that a physical association of lysosomes with FAs activates mTORC1 (Rabanal-Ruiz et al., 2021). Moreover, it has been proposed that lysosomes could provide an autocrine matrix (i.e. ECM components provided by the cell for itself), because endocytosed fibronectin is not digested in lysosomes but secreted (Sung et al., 2011).

In dendritic cells, a stimulation by lipopolysaccharides activates the lysosomal Ca^{2+} channel TRPML1. The released Ca^{2+} is able to activate myosin II at the cell rear promoting fast and directional migration (Bretou et al., 2017). The activation of myosin II at the cell rear is achieved by a physical coupling between the actomyosin and lysosomes through Rab7 (Vestre et al., 2021). The implication of lysosomal Ca^{2+} in migration has been confirmed in other studies. For example CAX (Ca^{2+}/H^{+} antiporter) is required for neural crest cell migration *in vivo* (Melchionda et al., 2016).

v) Metabolic/transcriptional regulation: The role of lysosomes in metabolic/transcriptional regulation relies on mTORC1. As already explained earlier, under nutrient-rich conditions, mTORC1 is associated with lysosomes promoting anabolism and inhibiting catabolism (autophagy and lysosomal biogenesis). It also plays a transcriptional role by phosphorylating TFEB, retaining it in the cytosol and blocking the transcriptional activation of the CLEAR network. In contrast, upon starvation, mTORC1 is cytosolic and inactive, promoting autophagy and CLEAR network transcription.

vi) Plasma Membrane Repair (PMR): It has been experimentally observed that after PM damage, a massive lysosomal exocytosis takes place. Holes in PM dramatically increase intracellular Ca^{2+} concentration. Original explanations of PMR postulate that Ca^{2+} increase triggers homotypic fusion of lysosomes, forming a large compartment, a “patch”. This patch would physically clog the hole by fusing with PM (**Figure 16A**). The so-called “patch hypothesis” has been rejected in favor of a model based on a massive lysosomal exocytosis triggered by Ca^{2+}. This bring of membranes would reduce membrane tension, facilitating the physical rapprochement and the fusion of the edges of the PM hole (**Figure 16B**). This mechanism could be supported by a contractile actomyosin cytoskeleton (McNeil, 2002; Andrews et al., 2014; Andrews and Corrotte, 2018).

PM damage induced by bacterial pores such as StreptoLysin O (SLO) cannot be repaired by these mechanisms. It has been proposed that these pores could be excluded from PM through the budding of an extracellular vesicle induced by the ESCRT machinery (**Figure 24D**). However this model is poorly supported by observation. Here again, experimental observations show that the insertion of SLO is followed by a massive lysosomal exocytosis in 30s. After 30 min, SLO is observed in lysosomal compartments. The exocytosis/endocytosis model proposes that after massive exocytosis, SLO is endocytosed and degraded (**Figure 24C**) (McNeil, 2002; Andrews et al., 2014; Andrews and Corrotte, 2018). The prior massive exocytosis could have different functions. First, the quick liberation of hydrolases and acidification could be an evolutionary strategy to kill a putative bacterial aggressor (Andrews and Corrotte, 2018). Second, it could reduce membrane tension, facilitating endocytosis. Third, it has been demonstrated that lysosomal exocytosis releases ASM. Exocytosed ASM locally transforms PM sphingomyelins in ceramides, tuning PM mechanical properties to facilitate endocytosis (Tam et al., 2010).

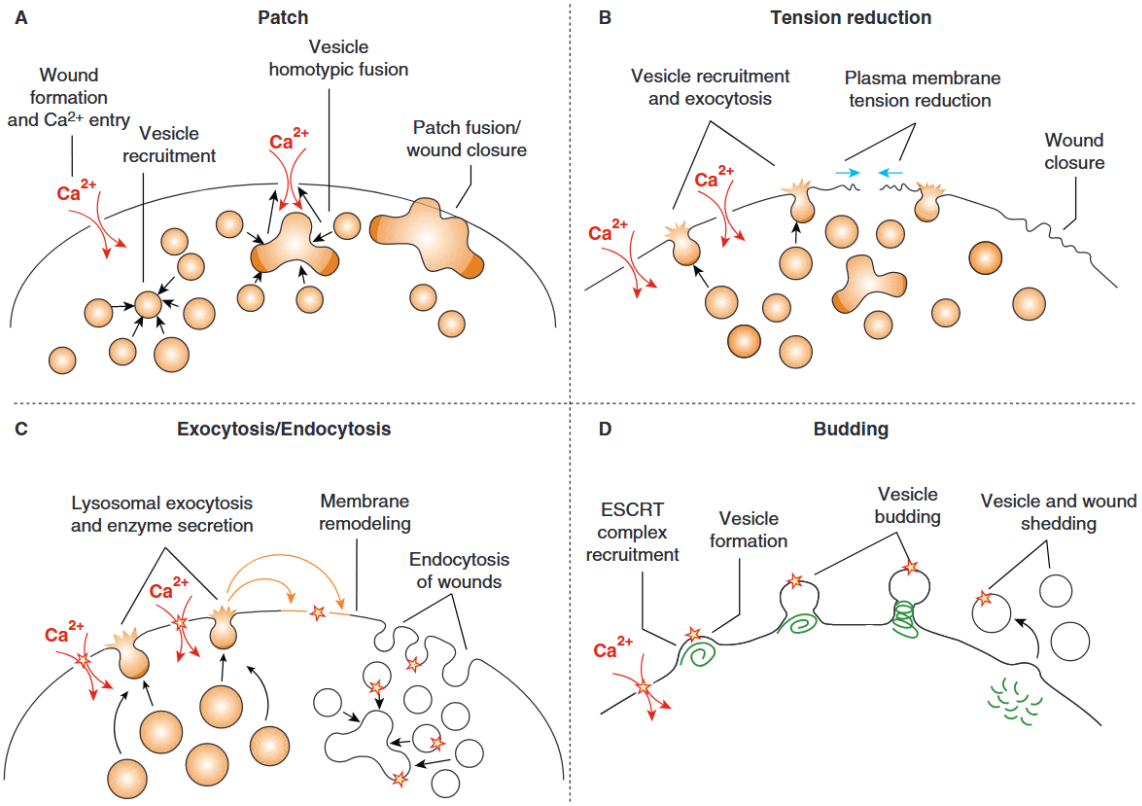

Figure 24. Different models of PMR, from Andrews and Corrotte (2018). A: Patch model. Ca^{2+} entry triggers homotypic fusion of lysosomes, creating a patch. The patch fuses with PM to close the wound. B: Tension reduction model. Ca^{2+} entry triggers massive exocytosis, reducing membrane tension. The reduced membrane tension allows the wound closure, either spontaneously or underlied by an actomyosin contraction. C: Exocytosis/Endocytosis model. The insertion of bacterial pores in PM creates a Ca^{2+} flux. Ca^{2+} entry triggers massive exocytosis followed by massive endocytosis. Bacterial pores are removed from PM by endocytosis and then degraded. D: Budding model. Bacterial pores are removed from PM by the budding of an extracellular vesicle supported by the ESCRT complex.

2. Exocytosis

2.1. History

The discovery of the secretory property of cells is difficult to date but probably occurred early in the history of biology. However, the cellular and molecular descriptions of this process have been achieved only recently. In the ‘60s, Palade and Jamieson described the secretory pathway in acinar pancreatic cells. Cells were incubated with radioactive amino acids in famous pulse-chase experiments. Combining ultra-centrifugation and radioautography, they demonstrated that acinar enzymes journey from the ER to the Golgi apparatus, and from the Golgi apparatus to zymogene granules. These granules are exocytosed at the apical side of the cell, into the gland lumen (Jamieson and Palade, 1967; Palade, 1975). Christian de Duve coined the term « exocytosis » during a

conference in 1963, as an antonym of « endocytosis », a term also invented by him. However, the molecular machinery required for the secretion pathway, including exocytosis, was lacking.

In 1979 at Berkeley, Peter Novick and Randy Schekman endeavored to identify genes involved in secretion in the model yeast *Saccharomyces cerevisiae* using forward genetics. They induced mutations in yeast with Ethyl MethaneSulfonate (EMS) and selected for thermosensitive (ts) secretory mutants (*sec*). At the non-permissive temperature of 37°C, *sec* mutants would have a defect in their secretory process. Selection was based on treatment with toxic chromate imported intracellularly by the sulfate permease protein. Only *sec* mutants would survive because a defect in the trafficking of this protein to the PM would not allow these mutants to uptake chromate. The mutants *sec 1-1* and *2-1* have been identified thanks to this strategy. At 37°C, the *sec 1-1* mutant is characterized by an accumulation of intracellular vesicles and a blocked growth, rescued at the permissive temperature of 24°C (**Figure 25**) (Novick and Schekman, 1979). They hypothesized that ts secretory-defective mutants should not be rare and tried to identify new mutants. Because secretory-defective mutants are denser than WT cells due to the accumulation of non-secreted material, the Schekman's team isolated *sec* mutants by density gradient. A total of 188 mutant clones have been isolated, classified in 23 complementation groups (i.e. 23 putative genes). EM revealed that 10 groups are associated to an accumulation of secretory vesicles, 9 with an accumulation and distortion of the ER, and 2 with a toroid-shaped organelle called "Berkeley body" (the 2 other groups have no EM phenotype or a more complex phenotype) (**Figure 26**) (Novick et al., 1980). The functions of the *sec* genes have been inferred from these phenotypes (Novick et al., 1981).

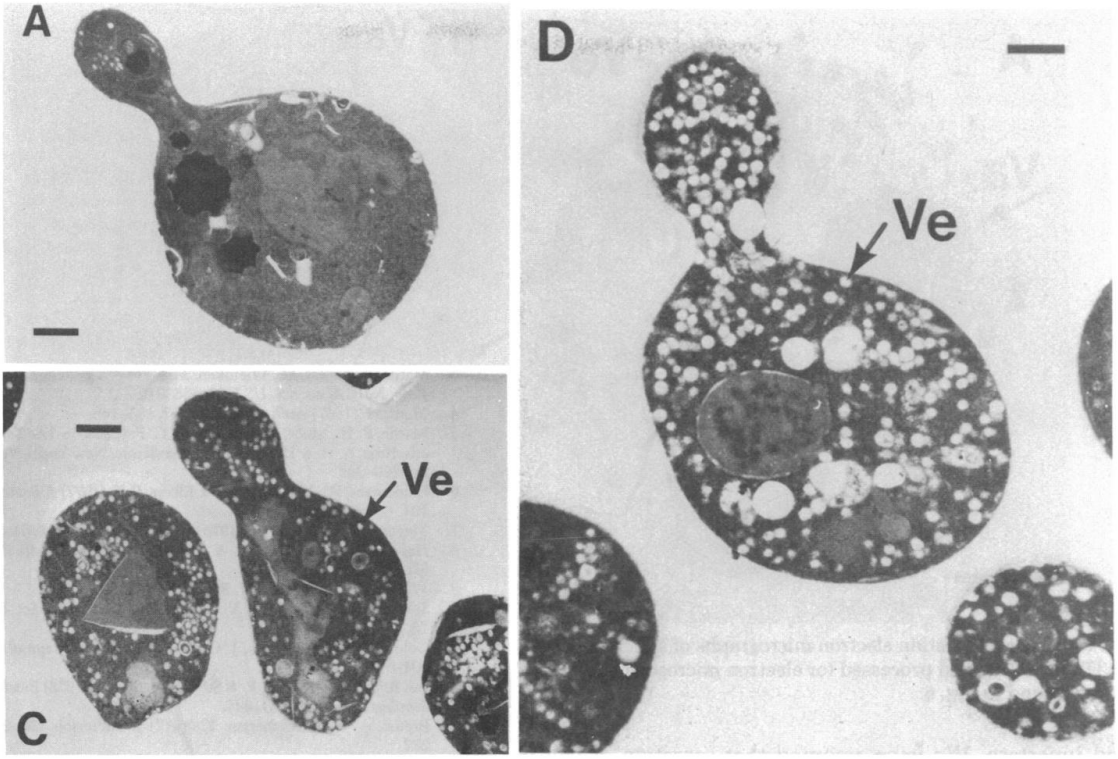

Figure 25. EM micrographs of the *Sec1-1* mutant from Novick and Schekman (1979). A: WT cell at 37°C. C: *Sec 1-1* mutant grown at the non-permissive temperature of 37°C for 1h. D: *Sec 1-1* mutant grown at 37°C for 3h. Ve indicates a vesicle and the scale bar is 0.5µm.

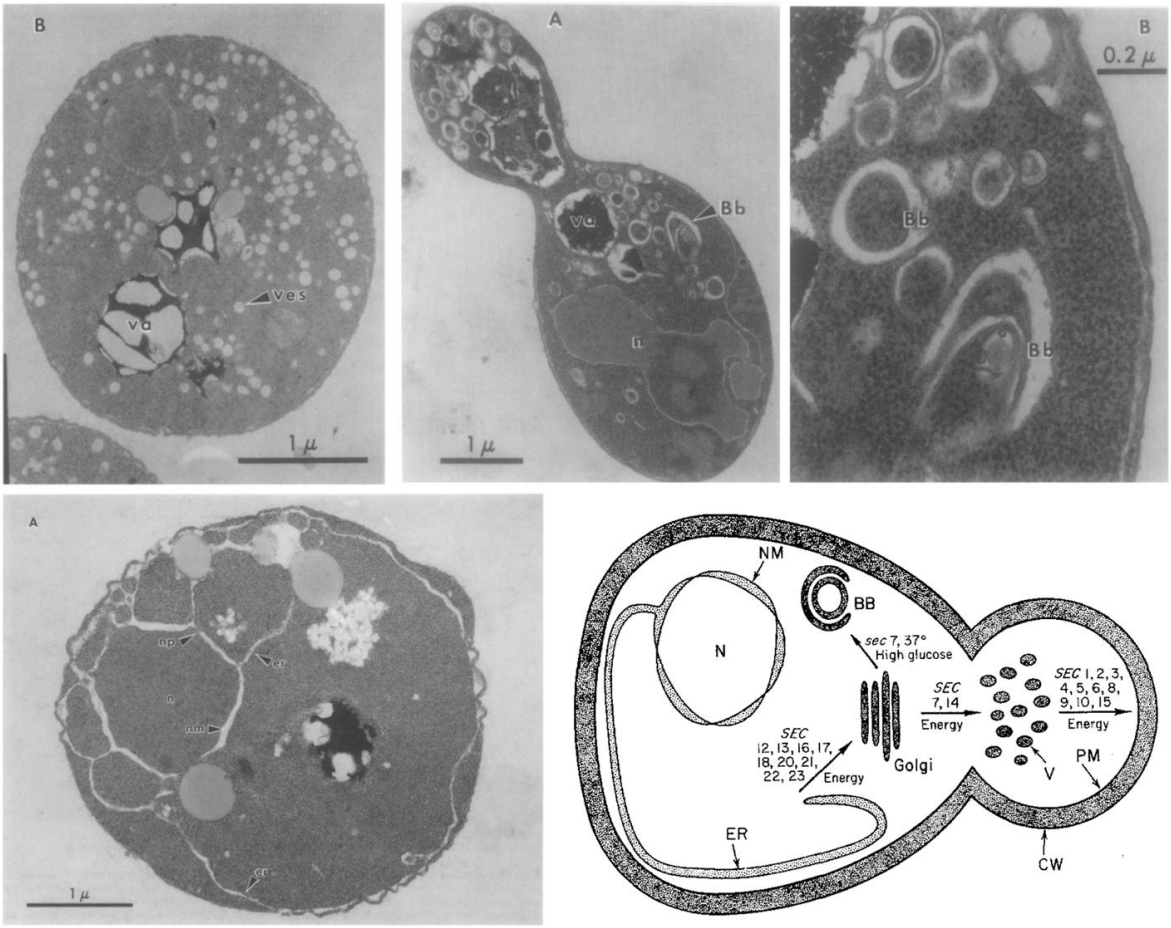

Figure 26. *Sec* mutants and functions, from Novick et al. 1980, 1981. In the read direction: *Sec4-2* mutant incubated at 37°C for 2h presenting an accumulation of vesicles; *Sec7-1* mutant incubated at 37°C for 2h presenting a strange toroid organelle named Berkeley body; Higher magnification of the previous cell; *Sec 16-2* mutant incubated at 37°C for 2h presenting ER enlargement; schematic of the inferred *sec* genes functions in 1981. Va: vacuole, Ves: vesicles, N: nucleus, Bb: Berkeley body, ER: endoplasmic reticulum, NP: nuclear pore, NM: nuclear membrane.

In parallel, in the '80s, the Rothman's team at Stanford tried to dissect the secretory pathway in mammalian cells, focusing on Golgi apparatus trafficking. They used the clone 15B of CHO cells that display an impaired activity of the Golgi resident enzyme, GlcNAc transferase 1. They infected these cells with Vesicular Stomatitis Virus (VSV), inducing the expression of the glycoprotein G (VSV-G). This protein is glycosylated with a GlcNAc moiety in the medial cisternae of the Golgi apparatus in WT cells but not in clone 15B. Rothman's team isolated the Golgi apparatus of these cells and mixed them with the Golgi apparatus purified from WT CHO cells. This remarkable *in vitro* system allows the reconstruction of the Golgi trafficking using radiolabeled GlcNAc glycosylation of VSV-G as readout of correct trafficking. In the case where some factors necessary for Golgi trafficking are not present, the unglycosylated VSV-G is stuck in the *cis*-Golgi from clone 15B cells and does not reach the medial cisternae from WT cells. The factors necessary for Golgi trafficking are mainly ATP and cytosol (Balch et al., 1984). Replacing CHO cytosol by yeast cytosol did not impair Golgi trafficking, revealing an unexpected evolutionary conservation of the mecanisms of secretion (Dunphy et al., 1986). The identification of the molecular factors regulating trafficking was still lacking. N-EthylMaleimide (NEM) was then identified as a drug blocking trafficking. The treatment of both Golgi fractions (the WT and the 15B) with NEM totally inhibited VSV-G transport in the cell-free *in vitro* system. However, the

treatment of only one fraction did not alter transport. Rothman's team concluded on the existence of a NEM-Sensitive Factor (NSF) provided either by one or the other fraction, and on the requirement of NSF for correct Golgi trafficking (Glick and Rothman, 1987). The inhibition of NSF by NEM is characterized by an accumulation of uncoated vesicles (Malhotra et al., 1988). NSF has been purified the same year and identified as a tetramer with ~76kDa monomers (later recognized as a hexamer with a monomeric weight of ~82kDa) (Block et al., 1988). The NSF sequence has been identified as homologous to the *Sec18* gene from yeast, confirming the evolutionary conservation of the molecular mechanisms of the secretory pathway (Wilson et al., 1989).

These discoveries have been completed by studies on synapses. The Richard Schellers' team isolated synaptic vesicles from the electric ray *Torpedo californica*. They constructed a cDNA library from mRNA expressed in the nervous system. This library has been screened for synaptic genes using polyclonal antiserum raised against purified synaptic vesicles. From this screen, they identified the Vesicle-Associated Membrane Protein 1 (VAMP-1), a new synaptic transmembrane protein with a predicted anchor domain (Trimble et al., 1988). The screening of a cDNA library from whole rat brain using *T. californica* VAMP-1 cDNA allowed the identification of rat VAMP-1 (84% homology) and VAMP-2 (75-77% homology) (Elferink et al., 1989). Another team identified synaptobrevin in rat brain using electrophoresis of purified synaptic vesicles and subsequent separation of integral membrane proteins (Baumert et al., 1989). Thomas Südhof et al. cloned the gene coding for mammalian synaptobrevin and revealed that it was the homolog of *T. californica* VAMP-1 gene. In addition, antibodies against rat VAMP-1 revealed that this protein also exists in *Drosophila melanogaster* (Südhof et al., 1989). Electrophysiological measurements in *Aplysia californica* demonstrated that tetanus (TeTx) and botulinum (BoNT) toxins block neuronal transmission. These toxins are known to be proteases. Electrophoresis of synaptic vesicles treated with toxins showed an alteration of a band. This band was shown to correspond to the recently identified synaptobrevin (Schiavo et al., 1992).

Matthews et al. identified two monoclonal antibodies obtained from hybridomas that specifically stained rat synapses. These antibodies recognized a protein of 65kDa (named p65, today known as synaptotagmin) at the surface of synaptic vesicles. The same antibodies were able to detect synaptotagmin in shark, amphibian, birds and mammals, highlighting again the evolutionary conservation of the secretory machinery (Matthew et al., 1981). The Südhof's team reported a homology between synaptotagmin and the C_2-domain of Protein Kinase C (PKC), proposing that p65 could bind either Ca^{2+} or phospholipids. SDS-PAGE elecrophoresis of p65 incubated with radiolabeled phosphatidylserine confirmed that p65 bind phospholipids (Perin et al., 1990). By equilibrium dialysis, the Südhof's team demonstrated that phospholipid binding is Ca^{2+}-dependent (Brose et al., 1992). It was already known that neuronal exocytosis was Ca^{2+}-dependent but the identification of the molecular sensor was lacking until this publication. Latter work of the team using a mutant with a lower Ca^{2+} affinity, confirmed the function of synaptotagmin. This mutation reduces neurotransmitter release in cultivated hippocampal neurons with autapses isolated from mice (Fernández-Chacón et al., 2001).

In parallel, the Rothman's team demonstrated that the binding of NSF to Golgi membranes requires cytosol. They treated isolated Golgi membranes with NEM to block endogenous NSF activity and added purified NSF in presence or absence of cytosol. NSF activity was measured with the *in vitro* Golgi transport assay. They hypothesized that NSF function requires a cytosolic factor, Soluble NSF Attachment Protein (SNAP) and an integral membrane receptor (Weidman et al., 1989). They purified 3 cytosolic proteins required for Golgi trafficking (Clary and Rothman, 1990) and identified them *a*

posteriori as SNAP proteins (Clary et al., 1990). The addition of purified SNAP in yeast cytosol of the *sec17* mutant rescued the deficient transport phenotype. Still taking advantage of the *in vitro* system, the Rothman's team determined that SNAP is required for the fusion step in the Golgi cisternal transport. At this point, the association of NSF-SNAP and an integral membrane protein forming a "fusion machine" was thought to be required for membrane fusion (Clary et al., 1990). This integral membrane receptor, named SNAP Receptor (SNARE), has been identified using beads coated with antibodies recognizing NSF. Using a mixture of membranes with their integral membrane proteins, SNAP and NSF, the beads allowed the isolation of the "fusion machine" and then the elution of SNAREs. The isolated SNAREs were syntaxin, SNAP-25 and Synaptobrevin-2. It was already known that syntaxin was associated with PM and Synaptobrevin-2 (VAMP2) with synaptic vesicles, suggesting that these proteins could interact at the PM during docking of the vesicles and exocytosis. James Rothman called the SNARE associated to the vesicle "vesicle-SNARE" (v-SNARE), and the one associated to the target membrane (PM or Golgi membranes) target-SNARE (t-SNARE) (**Figure 27**) (Söllner et al., 1993). Since then, more SNAREs have been identified and classified (Fasshauer et al., 1998). From the 23 genes initially characterized by Schekman and Novick, *Sec9* and *Sec22* are SNAREs, and many other genes encode proteins interacting with SNAREs (Schekman and Novick, 2004).

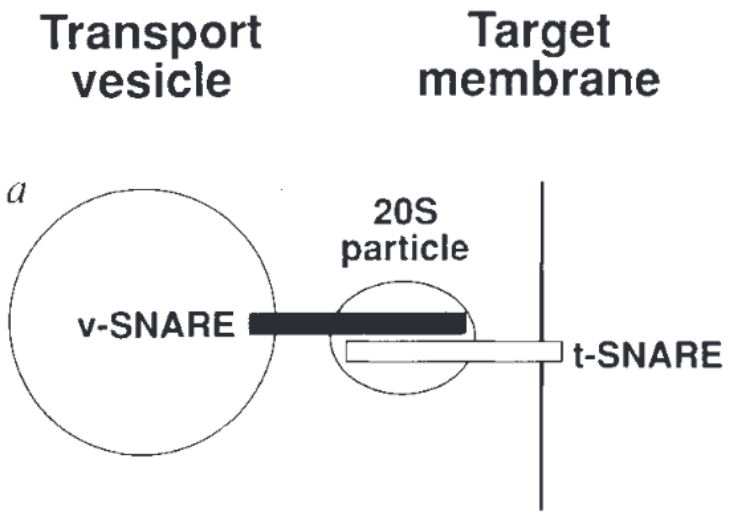

Figure 27. SNARE fusion machinery model proposed by James Rothman, from Söllner et al, 1993. The vesicle interacts with a target membrane through the interaction of a v-SNARE and a t-SNARE. In 1993, it was believed that this interaction involved the 20S particle containing NSF and SNAPs.

A few years later, the crystal structure of the SNARE complex has been obtained, showing that α-helices of SNAP-25, synaptobrevin and syntaxin are organized in a coiled-coil domain in the SNARE complex (**Figure 28**) (Sutton et al., 1998). Randy Schekman, James Rothman and Thomas Südhof received the Nobel Prize in Physiology or Medecine in 2013 for "their discoveries of machinery regulating vesicle traffic, a major transport system in our cells".

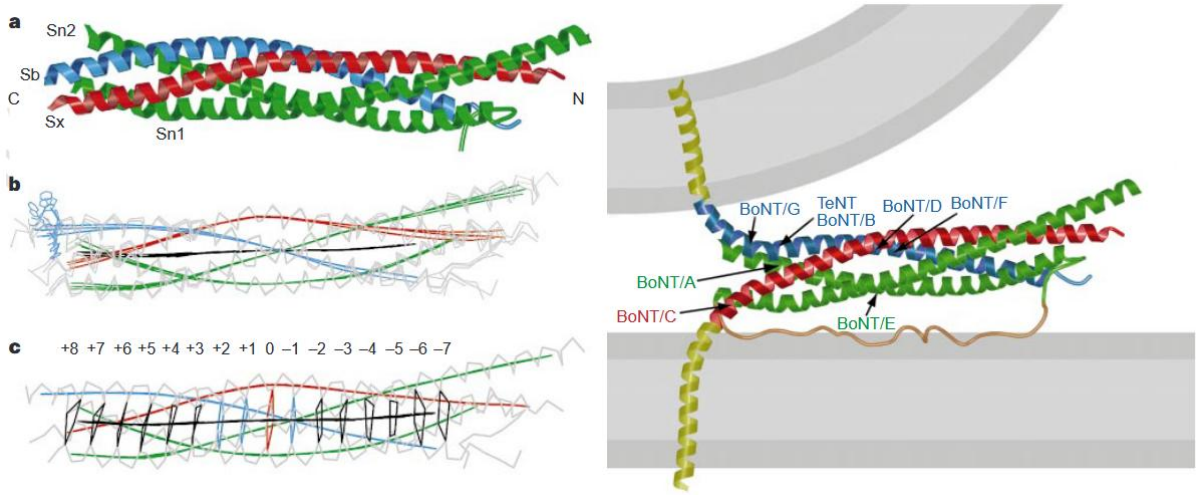

Figure 28. Crystal structure of the SNARE synaptic fusion complex from Sutton et al. (1998). A: Structure of the SNARE complex with synaptobrevin 2 (blue), syntaxin-1A (red) and SNAP-25B (green). B: Conformational variability. C: SNAREs interactions through 16 layers. Right: Model of the synaptic SNARE complex with the membranes.

2.2. Molecular machinery

Exocytosis, and more generally membrane fusion, relies on the SNARE machinery. SNAREs are evolutionary-conserved molecules sharing a SNARE domain (also called SNARE motif) of about 60 residues constituting an α-helix (Weimbs et al., 1997). SNAREs are shared among all eukaryotes, indicating that exocytosis is a new shared evolutionary novelty (a synapomorphy) (Kloepper et al., 2007). Surprisingly, SNARE-like proteins have been identified in the genomes of archaea, in the *Heimdallarchaeota* clade (Neveu et al., 2020). This is a clade from the Asgard group named after the realm of the deities in Norse mythology, which was used for the archaea originally identified in marine sediments near the Loki's Caslte hydrothermal vents between Greenland and Norway (Loki referring to the God of malice, discord and illusions in the Norse mythology). Asgard archeae is the sister group of eukaryotes according to the established theory on archaeal eukaryotic origin (Eme et al., 2017). Archaeal SNARE-like proteins are able to bind eukaryotic SNAREs. A horizontal gene transfer is unlikely, suggesting a common ancestor between Asgard and eukaryotes with a prototypic SNARE machinery (Neveu et al., 2020). The function of archaeal SNAREs is unknown as archaea do not contain endomembranes, and it is therefore unlikely that exocytosis exist in archaea according to our current knowledge. However some authors do not exclude the possible existence of an endomembrane system in archaea, despite the absence of direct observations until now (Imachi et al., 2020; Avcı et al., 2022).

Among the ~38 known mammalian SNAREs (**Table 2**), 34 contain one SNARE motif in their C-terminus whereas 4 SNAREs (SNAP-23, SNAP-25, SNAP-29 and SNAP-47) have two tandem SNARE motifs separated by a linker region (Hong, 2005; Holt et al., 2006; Wang et al., 2006). Among the SNAREs with tandem SNARE motifs, the N-terminal SNARE motif is more conserved across SNARE proteins than with the C-terminal SNARE motif inside the same protein. As Rothman originally

proposed, SNAREs are functionally classified as t-SNAREs localized on the target membrane and v-SNAREs localized on the vesicle (Söllner et al., 1993). Latter phylogenetic analyses distinguished two clusters: R-SNAREs and Q-SNAREs (Fasshauer et al., 1998). Q and R refer to glutamine and arginine residues at specific positions. More advanced phylogenetic analyses on the SNARE motif split Q-SNARE motifs in three clusters: the Qa subfamily (also known as Syn), Qb subfamily (also known as S25N, based on the homology with the N-terminal SNARE motif of SNAP25), Qc (also known as S25C, based on the homology with the C-terminal SNARE motif of SNAP25) (**Figure 29**) (Bock et al., 2001; Hong, 2005). Therefore, SNAREs with tandem SNARE motifs are classified as QbQc SNAREs since the N-terminal motif is a Qb and the C-terminal one is Qc. Two of the Sec22 isoforms (Sec22a and Sec22c) and Sec20 are ambiguously classified in phylogenies and sometimes not considered as SNAREs in mammals (Hong, 2005; Sun et al., 2020). The R-subfamilly is also known as VAMP (**Figure 29**) (Bock et al., 2001; Hong, 2005).

Name	Location	AA	SNARE motif	TM domain	Synonyms	Type
Syntaxin1	PM	288	202-254	266-288	HPC-1	Qa
Syntaxin2	PM	288	201-253	265-286	Epimorphin	Qa
Syntaxin3	PM	289	201-253	264-288		Qa
Syntaxin4	PM	297	210-262	274-296		Qa
Syntaxin5	Golgi	301	219-271	208-301		Qa
Syntaxin6	TGN and endosomes	255	173-225	235-255		Qa
Syntaxin7	EE and LE	261	175-227	238-259		Qa
Syntaxin8	EE and LE	236	155-207	216-233		Qa
Syntaxin9	Endosome	294	218-271	Palmitoylation	Syntaxin19	Qa
Syntaxin10	TGN	249	167-219	229-249		Qa
Syntaxin11	TGN and LE	287	214-266	Palmitoylation		Qa
Syntaxin13	EE	276	188-240	251-273	Syntaxin12	Qa
Syntaxin16	TGN	325	240-292	302-322		Qa
Syntaxin17	ER	302	172-224	230-250		Qa
Syntaxin18	ER	335	253-305	314-33		Qa
SNAP-23	PM	211	24-76 and 156-208	Palmitoylation	Syndet	Qbc
SNAP-25	PM	206	29-81 and 150-202	Palmitoylation		Qbc
SNAP-29	Golgi and endosomes	258	60-112 and 206-258	no	GS32	Qbc

SNAP-47	Synaptic vesicle, TGN (?)	413 (mouse)	119-171 and 353-403 (mouse)	no		Qbc
VAMP1	Synaptic vesicle	118	34-86	97-117	Synaptobrevin1	R
VAMP2	Synaptic vesicle	116	32-84	95-114	Synaptobrevin2	R
VAMP3	EE and RE	100	15-67	78-98	Cellubrevin	R
VAMP4	TGN and EE	141	53-105	119-137		R
VAMP5	PM	116	6-58	73-93		R
VAMP7	Golgi, LE, Lysosome	220	126-178	189-214	TI-VAMP	R
VAMP8	EE and LE	100	13-65	76-99	Endobrevin	R
Ykt6	Golgi	198	139-191	Palmitoylation + Farnesylation		R
Sec22a	ER and ERGIC	282	135-187	190-208		?
Sec22b	ERGIC and cis-Golgi	215	135-187	196-215	ERS-24	R
Sec22c	ER and ERGIC	250	135-185	186-204		?
Bet1	ERGIC and cis-Golgi	118	36-88	96-115		Qc
GS15	Golgi	111	25-77	87-106		Qc
GS27	ERGIC and Golgi	212	130-182	192-212	Membrin, Gos-27	Qb
GS28	Golgi	250	170-222	231-250	Gos-28	Qb
Vti1a	trans-Golgi	217	132-184	193-214	Vtil-rp2	Qb
Vti1b	EE and LE	232	146-198	207-229	Vtil-rp1	Qb
Slt1	ER	259	173-225	232-252	Usul, p31	Qc
Sec20	ER	228	132-184	203-220	Bnip1	?

Table 2. Mammalian SNAREs and their properties, updated from Hong (2005). Information given is for human SNAREs excepted for SNAP-47 (mouse).

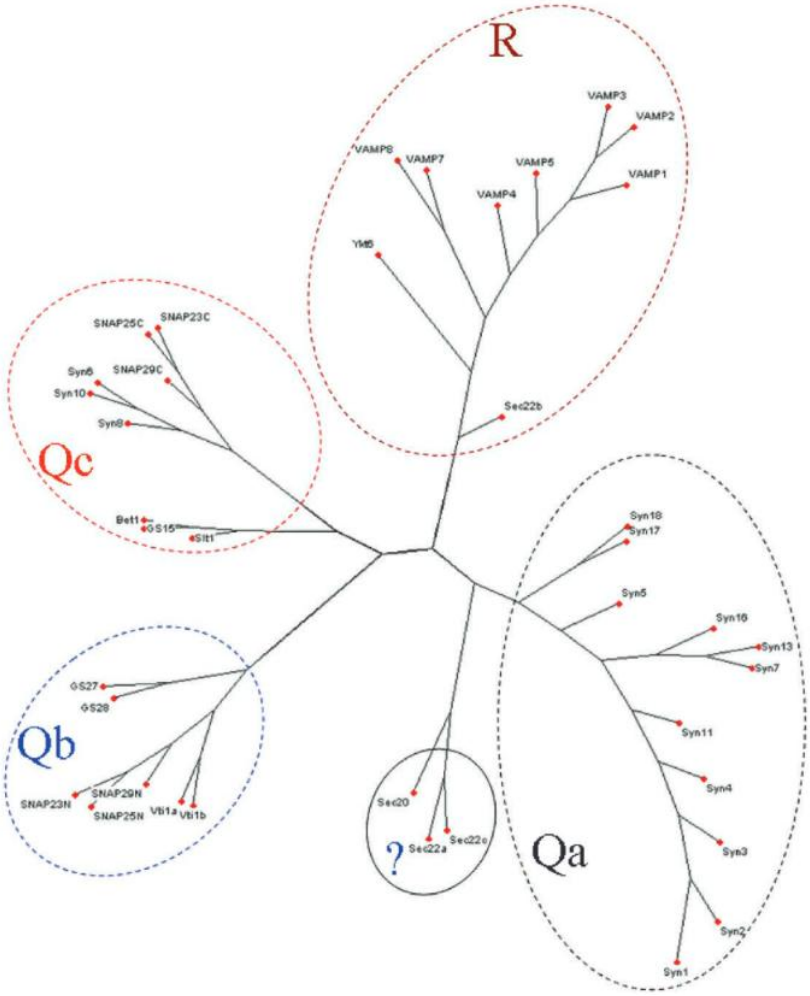

Figure 29. Phylogeny of human SNARE motifs from Hong (2005). SNAREs are clustered in four groups: R, Qa, Qb and Qc. The phylogenetic tree is based only on the SNARE motif.

Among the ~38 mammalian SNAREs, 32 contain a single C-terminal hydrophobic transmembrane region to anchor the SNARE in membranes (**Figure 30**). 6 SNAREs lack the transmembrane domain and are associated to membranes via farnesylation (Ykt6) and/or palmitoylation of cysteine residues (SNAP-23, SNAP-25, Ykt6, STX11 and STX9/19). Some SNAREs are associated with membranes by electrostatic interactions with other SNAREs (SNAP-29, SNAP-47) (Vogel and Roche, 1999; Hong, 2005; Holt et al., 2006; Wang et al., 2006; Ampah et al., 2018; Mastrodonato et al., 2018). Most of the SNAREs are characterized by a long N-terminal domain with 3 different motifs: i) 3 helices α (named Ha, Hb and Hc) organized in a coiled-coil structure (e.g. syntaxins), ii) a longin domain i.e. a profilin-like structure composed of a β-sheet sandwiched between one and two α-helices (e.g. VAMP7) and iii) a targeting motif for the Golgi apparatus (e.g. VAMP4) (Hong, 2005).

The formation of a SNARE complex is required to trigger membrane fusion. Usually, the v-SNARE is composed of one R-SNARE and the t-SNAREs is actually a dimer made of an heavy chain (from Qa family) and a light chain (from QbQc family) (Hong, 2005). In yeast, t-SNAREs can be trimeric with the participation of Qa, Qb and Qc SNARE (Fukuda et al., 2000; Baker et al., 2015; Grissom et al., 2020). Whatever the composition, the SNARE complex requires the interaction of 4 SNARE motifs in a parallel four-helical bundle structure called trans-SNARE complex or SNAREpin. In the bundle, each

helix is connected to the others through 16 residues defining 16 layers. At the middle of the layer, three glutamines (from the Q-SNAREs) and one arginine (from the R-SNARE) are interacting in the so-called “zero ionic-layer”. These residues are the most conserved in the SNARE motif (Hong, 2005; Kloepper et al., 2007). For the canonical synaptic SNARE complex, arginine is provided by VAMP2, one glutamine comes from syntaxine-1 and two glutamines come from SNAP-25. Layers are counted from -7 (in the N-terminus) to 8 (in the C-terminus). While the interactions in the other layers are hydrophobic (mainly formed of valine, leucine and isoleucine residues forming a leucine zipper), the zero ionic layer exhibits dipole-dipole interactions. The hydrophobic layers act as a water-tight seal to shield the dipole interactions of the zero ionic layer (Urbina and Gupton, 2020). Surprisingly, the hypothesized “3Q:1R rule” is not correct since a mutation from arginine to glutamine in the R-SNAREs do not impair SNARE complex functionality in yeast (Katz and Brennwald, 2000). However, the interaction of QabcR SNARE complex is likely more stable than other combinations.

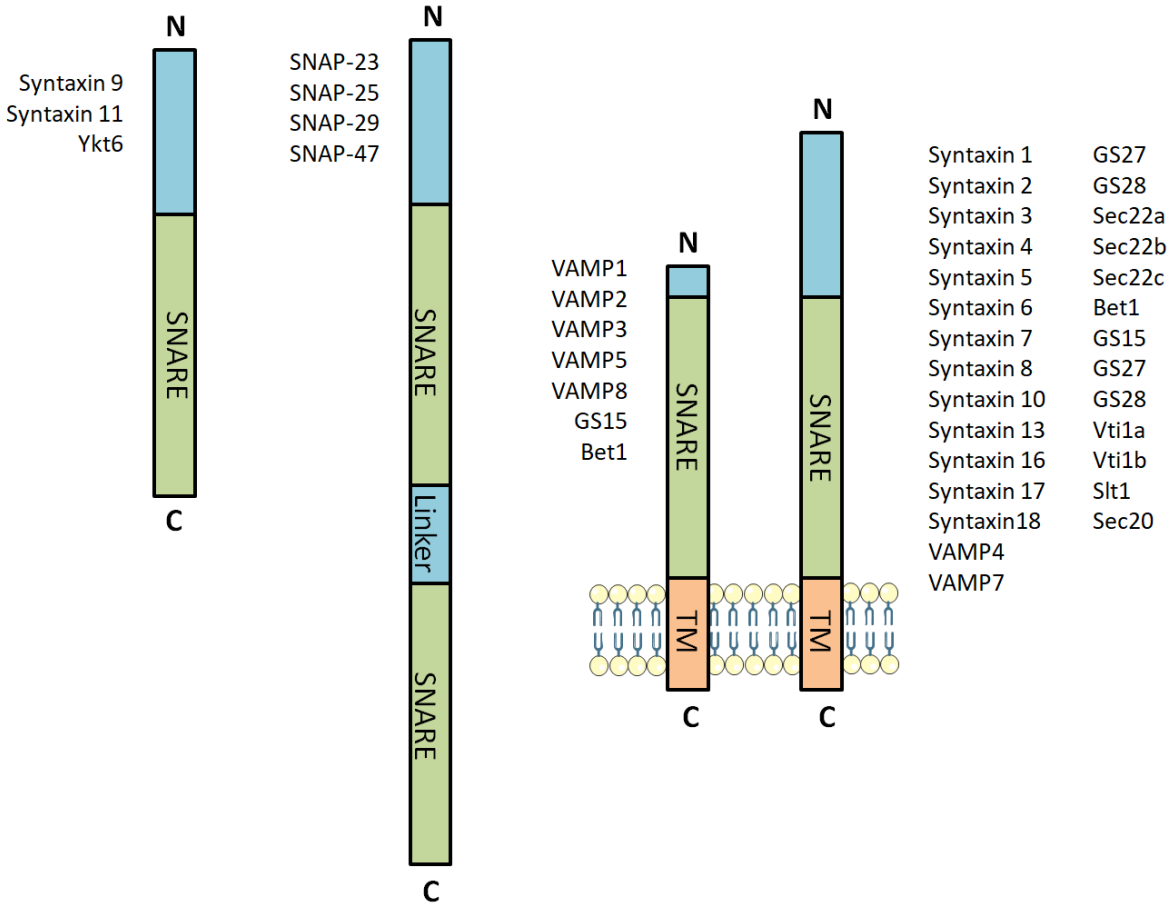

Figure 30. SNARE structures, redrawn and updated from Hong (2005).

Exocytosis without SNAREs is likely an exergonic process, but at a rate too low to be compatible with life (**Box 2**). Thus, the SNARE complex plays the role of a catalyst that decreases the energy barrier. The zipping of the *trans*-SNARE complex creates an inward force bringing a vesicle in close contact with the target membrane (**Figure 31**). The membranes meet, go transiently into an hemi-fusion state, in which the cytosolic leaflets fuse, before the fusion pore opens, allowing the release of the

vesicle content (Südhof and Rothman, 2009). After fusion, when totally zipped, the SNARE complex is called *cis*-SNARE. The SNARE zipping is an exergonic process releasing ~35k_BT (Li et al., 2007). The energy barrier for spontaneous fusion of the vesicle with the membrane is ~40-120 k_BT (Südhof and Rothman, 2009; Kasai et al., 2012). Therefore, 2 to 3 SNAREs are sufficient to drastically reduce the energy barrier. Of course, exocytosis is still limited by the (much lower) energy barrier of SNARE zippering. In living cells, two SNARE complexes are required for the exocytosis of one synaptic vesicle and 3 to 5 for the larger vesicles of chromaffin cells (Kasai et al., 2012).

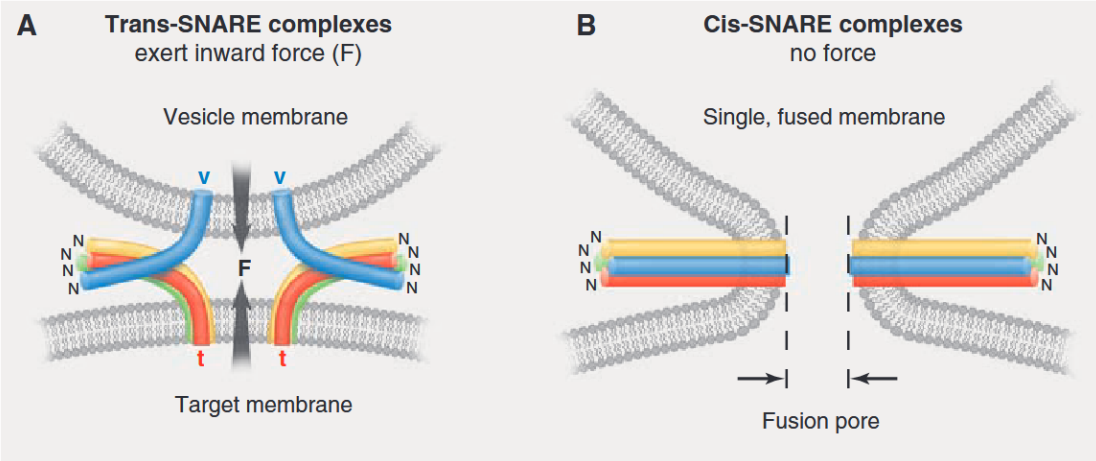

Figure 31. The SNARE complexes catalyze exocytosis, from Südhof and Rothman (2009). The zippering of the *trans*-SNARE complexes generates a force forcing the contact between the vesicle and the target membrane. The full zippering, forming the so-called *cis*-SNARE complex, opens the fusion pore

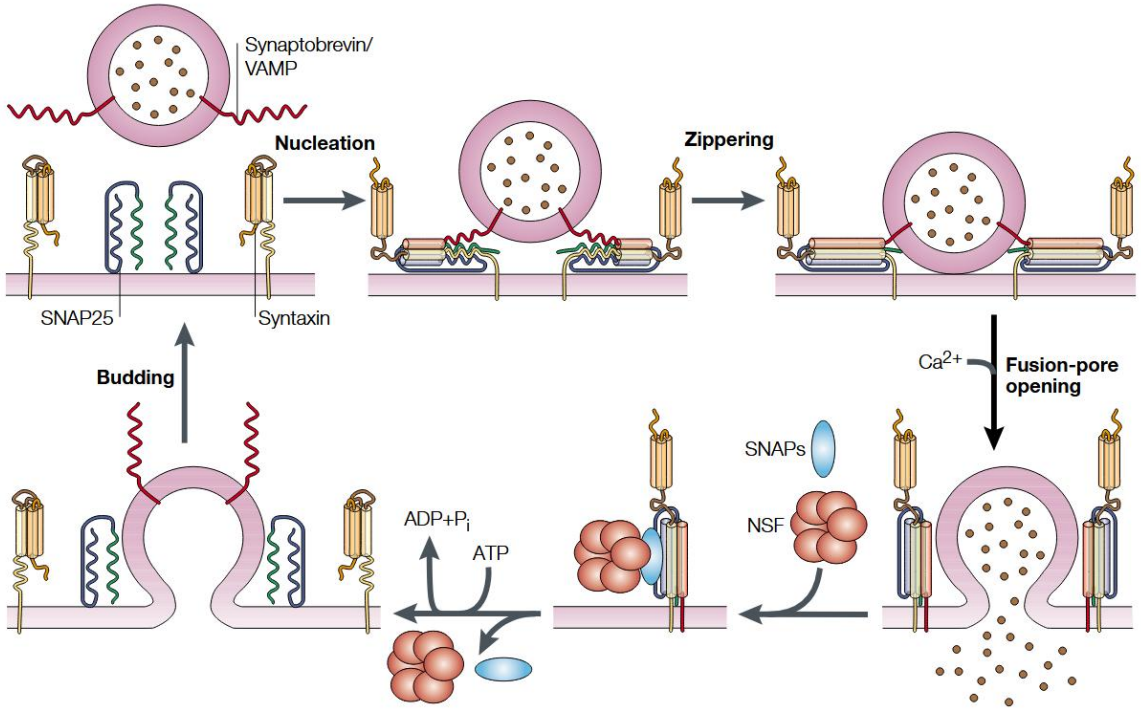

Figure 32. The SNARE cycle, from Rizo and Südhof (2002). A vesicle with its v-SNARE (e.g. VAMPs) interacts with two t-SNAREs (e.g. SNAP25 and syntaxin), forming a *trans*-SNARE complex. The zippering of the *trans*-SNARE complex catalyzes the formation of the fusion pore. After exocytosis, the *cis*-SNARE complex is disassembled through ATP hydrolysis. v-SNAREs are recycled by vesicle budding/endocytosis.

After exocytosis, the *cis*-SNARE complex needs to be disassembled and recycled. The disassembly of the *cis*-SNARE complex is mediated by NSF and SNAP. NSF is a hexameric ATPase of the family of ATPases Associated with diverse cellular Activities ATPases (AAA-ATPases). NSF, SNAP and the *cis*-SNARE complex are assembled into the so-called 20S particle. NSF uses the energy of ATP hydrolysis (38 k_BT) to unbundle the SNARE complex (Chang et al., 2012). The zipping energy is close to the energy used in the unzipping. However, zipping/unzipping of a SNARE complex presents a mechanical hysteresis (Fasshauer et al., 2002), suggesting that the unbundling by NSF could take a mechanical path that is different to the zipping. The mechanism of NSF unbundling is still poorly understood. After this step, v-SNAREs are recycled either by endocytosis, in the case where fusion takes place at the PM, or by budding of a vesicle for intracellular organelles. These molecular interactions define a "SNARE cycle" in which the exocytosis machinery can be re-used several times. In summary, the vesicle associates its v-SNAREs to the t-SNAREs of the target membrane. The SNARE interactions create a *trans*-SNARE complex. The full zipping of the SNARE complex catalyzes exocytosis. After exocytosis, the *cis*-SNARE complex is disassembled by NSF and SNAP through ATP hydrolysis. The recycling of v-SNAREs by vesicle budding closes the cycle (**Figure 32**) (Rizo and Südhof, 2002).

Box 2: Energy barrier of exocytosis

The energy barrier can be evaluated under simple hypothesis. Considering a vesicle with a radius R through 3 steps of exocytosis: i) vesicle + PM, ii) the vesicle just starting to fuse with the PM, iii) totally fused with the PM. The energy of the system is given by the Canham-Helfrich Hamiltonian (see chapter 3):

$$Step\ 1: \quad E = 4\pi(2\kappa_b + \kappa_G) \sim 400\ k_BT$$

$$Step\ 2: \quad E = 8\pi\kappa_b \sim 500\ k_BT$$

$$Step\ 3: \quad E = 0$$

With $\kappa_b = 20k_BT$ being the bending modulus and $\kappa_G = -\kappa_b/2$ the saddle splay modulus. The energy associated to the PM remains approximately constant, and can be therefore arbitrarily set to 0. In step 2, the energy associated to the Gaussian curvature is counted in the PM energy due to the Gauss-Bonnet theorem. We notice, that exocytosis is an exergonic process with $\Delta E = -400k_BT$. However the energy barrier is extremely high $E^{\ddagger} = 100k_BT$. The time scale is given by the Arrhenius law:

$$t = t_0 e^{\frac{E^{\ddagger}}{k_BT}}$$

With t_0 the time between successive attempts for crossing the energy barrier. Even with a small t_0 because the exponential is at the power 100, the spontaneous exocytosis rate is extremely slow and not compatible with life.

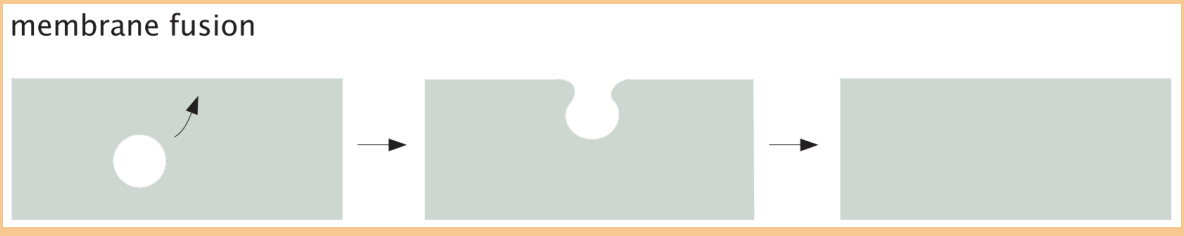

2.3. Experimental methods to explore exocytosis

The classical models of exocytosis include of course neurons (notably hippocampal neurons, neuro-muscular junctions and Calyx of Held), chromaffin cells (especially the phaeochromocytome PC12 cancer cell line), pancreatic β-cells, sea urchin eggs and immune cells (lymphocyte, mastocytes). In addition, new models have emerged such as the *Drosophila melanogaster* salivary gland (Gundelfinger et al., 2003; Tran and Ten Hagen, 2017). These exocytosis models have been explored through several methods: i) EM, ii) electrophysiological measurements, iii) membrane immunofluorescence, iv) medium dosage and v) live imaging by Total Internal Reflection Fluorescence Microscopy (TIRFM) (**Table 3**).

i) EM: EM was probably this first method used and gave important results especially, but not only, at synapses (Ichikawa, 1965; Ceccarelli et al., 1972; Heuser and Reese, 1973). This approach allows excellent spatial resolution, precise morphological information and can specifically detect cargos using immunogold labeling. However, it provides a poor temporal resolution, even if the dynamic of exocytosis can be inferred from pulse-chase experiments (Jamieson and Palade, 1967) or the observation of vesicles in different states (Ceccarelli et al., 1972).

ii) Electrophysiological measurements: The first electrophysiological method developed to measure exocytosis is the patch-clamp measure of membrane capacitance C_m (Fenwick et al., 1982). The capacitance is linearly proportional to the cell surface S:

$$C_m = \frac{\varepsilon_0 \varepsilon_r S}{h}$$

with ε_0 the vacuum permittivity, ε_r the relative membrane permittivity and h the membrane thickness. For a synaptic vesicle, and considering the membrane permittivity as equal to the one of parafilm ($\varepsilon_r = 2.2$ F.m^{-1}) and a membrane thickness of 5nm, a single vesicle fusion causes a capacitance increase of ~1-10 x 10^{-18} F. These attoFarad variations are detectable and the temporal profile of C_m can even distinguish the mode of exocytosis: kiss-and-run or full-collapse (He et al., 2006). A second method used carbon fiber electrodes as an electrochemical detector. The oxido-reduction reaction between released molecules and the electrode generates a current spike, indicating single exocytic event. This method is well adapted to chromaffin cells where the catecholamines can undergo oxidation reactions (Chow et al., 1992). These methods have an excellent temporal resolution, are able to resolve single exocytic events, however there is no spatial information (**Figure 33**). They can easily distinguish between several modes of exocytosis; however, they cannot probe for a specific type of cargo, except using specific amperometric methods for cargo oxidation.

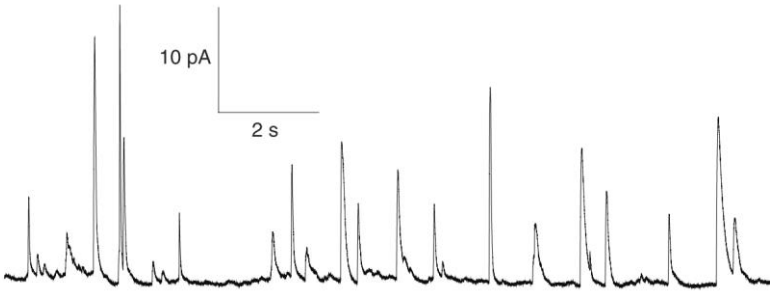

Figure 33. Amperometric recording of a chromaffin BON cell, from Bretou et al. (2014). Spikes indicate single exocytosis event.

iii) Membrane immunofluorescence: This method is commonly used due to its facility. It consists of the immunolabelling of a transmembrane cargo in non-permeabilized cells. The labeling intensity is believed to reflect the degree of exocytosis. However, for steady-state cells, the PM quantity of transmembrane cargo also depends on the rate of recycling, making these measures ambiguous. For regulated exocytosis, stimulation and an immediate fixation allows the specific measurement of exocytosis. Coupled with flow cytometry, this method can be also used in a high-throughput manner. This method is specific to a given pathway due to the antibody specificity.

iv) Medium dosage: This method is similar to the preceding one but adapted for soluble cargos. The protein quantification in the medium supernatant can provide information on the exocytosis rate. The quantification of low concentration molecules can be difficult; therefore, the activity assay of secreted enzymes is more common. However, this is quite limited to exocytosis of secreted enzymes, i.e. lysosomal exocytosis. Similarly, the quantification of exosomes in cell supernatant is used as a measure of MVBs exocytosis.

v) Live-imaging by TIRFM: The TIRFM exploits the physical principle of total reflection. When a light beam meets a medium with a different refractive index, it can be totally reflected if it has a specific angle. When total reflection occurs, an evanescent wave is emitted at the interface between the two media (**Figure 26**). This evanescent wave decreases exponentially and illuminates only 100 to 300nm allowing specific observations of the PM and its close vicinity when a cell is seeded on a coverslide. This method is therefore well suited for the detection of exocytosis (Schmoranzer et al., 2000). The development of pH sensitive fluorophores (pHluorin, pHtomato, etc.) improved drastically the method. In acidic vesicles, the signal is quenched. During fusion, protons are released allowing fluorescence emission. If the fluorophore is attached to a transmembrane protein (classically the C-terminal of a v-SNARE), the fusion step is followed by the 2D diffusion of the signal (**Figure 34**).

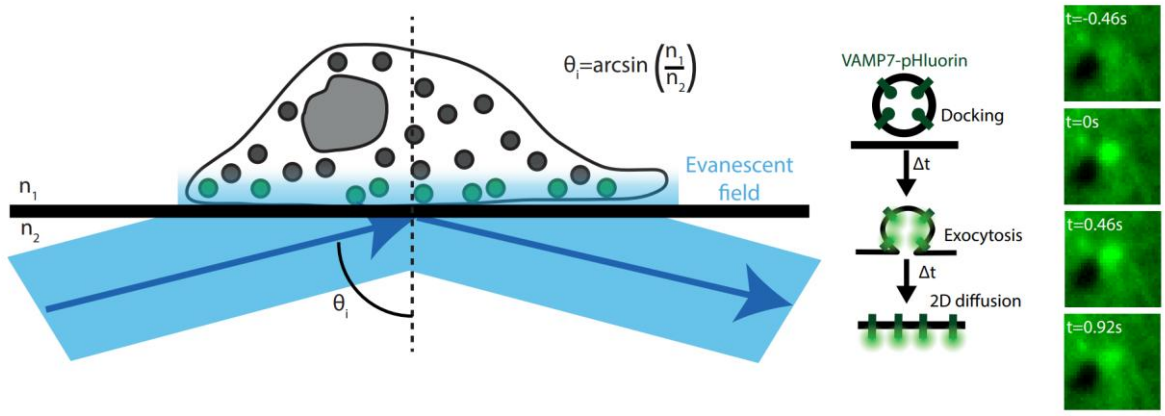

Figure 34. Principle of TIRFM of pH-sensitive fluorophore bound to acific compartments. When the exciting light beam meets the coverslip with a specific angle (θ_i), it can undergo total refraction emitting an evanescent wave at the medium interface. This wave decreases extremely rapidly, illuminating only 100-300nm at the ventral part of the sample. Coupled with pH-sensitive dyes, it allows easy detection of exocytic events. The pH-sensitive dye is quenched inside acidic vesicles and during fusion emits a signal due to proton release. Right images show TIRFM measurements of a single VAMP7-pHluorin exocytic event.

Using the fluorescence profile of single exocytic event, one can distinguish several modes of exocytosis such as full-collapse and kiss-and-run (Urbina et al., 2021). Unfortunately, this method only probes the ventral part of the cell. However, it has been demonstrated by TIRFM and capacitance recording, that ventral exocytosis correlates well with total exocytosis (Becherer et al., 2007). Lastly, this method is the only one that provides a good spatio-temporal resolution (Lachuer et al., 2020).

	EM	Electrophysiology	Membrane immunofluorescence	Medium dosage	Live-imaging TIRFM
Principle	Microscopy using an electron beam.	Membrane capacitance measurement or amperometric method using a carbon-fiber electrode as an electrochemical sensor.	Immunofluorescence of marker transmembrane proteins in non-permeabilized cells.	Dosage of a specific cargo (protein quantification or enzyme activity assay)	Specific illumination of the PM by the evanescent field; Combined with pH sensitive fluorophore (pHluorin, pHTomato).
Type of exocytosis	Constitutive and regulated	Constitutive and regulated	Mainly regulated	Constitutive and regulated	Constitutive and regulated
Mode of exocytosis	+/-	+++	---	---	+++
Spatial resolution	+++	---	+/-	---	++
Temporal resolution	--	+++	--	--	++
Cargo specificity	++	+/-	+++	+++	+++

Table 3. Methods to explore exocytosis.

2.4. Exocytosis regulation

Two types of exocytosis can be distinguished: constitutive and regulated (**Figure 35**). Whereas constitutive exocytosis never stops, regulated exocytosis is triggered by a stimulus. There are four main cell types with regulated exocytosis: neuronal, endocrine, exocrine and hematopoietic cells (Shitara and Weigert, 2015). Classical examples are the release of histamine by mastocytes triggered by an antigen or the release of catecholamines (adrenaline and neuradrenaline) by chromaffin cells in the medulla triggered by acetylcholine. In non-neuronal cells with regulated exocytosis, the secretory vesicles are often nammed Large Dense-Core Vesicles (LDCV) due to their EM aspect (Kasai et al., 2012).

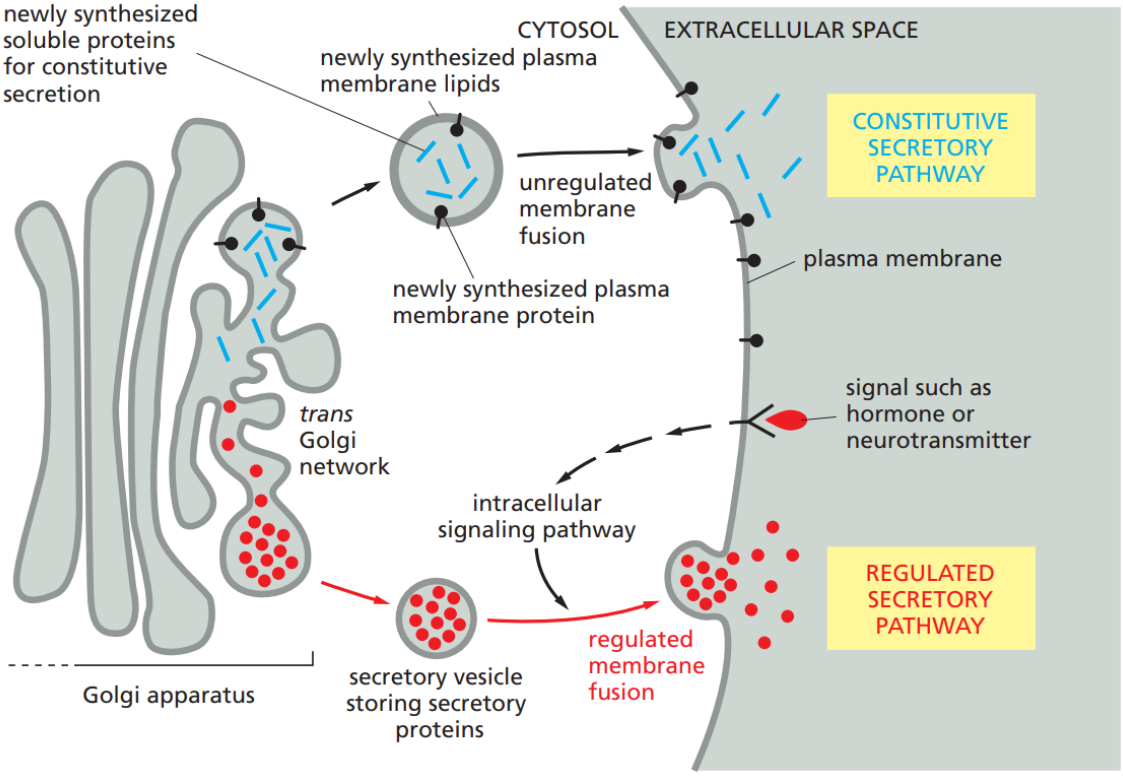

Figure 35. Constitutive and regulated exocytosis, from Molecular Biology of the Cell (6th edition). In constitutive exocytosis, as soon as a vesicle is ready, it starts to engage exocytosis. In regulated exocytosis, LDCVs are accumulated in the cytosol or docked to the PM but wait a stimulus to engage exocytosis.

Regulated exocytosis classically follows several steps: i) tethering, ii) docking, iii) priming and iv) fusion. The tethering step consists of the interaction of a PM tethering protein with, most of the time, a Rab protein on the vesicle. The docking step brings the vesicle in physical contact with the PM and retains it. The priming step consists of the biochemical operations rendering the vesicle competent for exocytosis. Primed vesicles can be immediately exocytosed after stimulation (Kasai et al., 2012). The fusion step is not stereotypical, and several kinds of exocytosis can be distinguished according to this final step: i) full-collapse, ii) kiss-and-run and iii) compound exocytosis (**Figure 36**).

These different kinds of exocytosis can co-exist in a single cell. For example, EM of frog neuromuscular junctions in '70s revealed two types of exocytosis: full-collapse (Heuser and Reese, 1973) and kiss-and-run (Ceccarelli et al., 1972). Full-collapse involves the enlargement of the fusion pore and total fusion of the vesicle membrane with the PM. In kiss-and-run exocytosis, the fusion pore is open but does not enlarge. Vesicle content is partially released through the fusion pore and the pore is then re-closed and the vesicle recycled. The compound exocytosis has been documented even before the kiss-and-run mechanism by EM in pancreatic acinar cells (Ichikawa, 1965). Compound exocytosis is either sequential exocytosis or multigranular. Sequential exocytosis is the fusion of a vesicle on a second vesicle that already started its exocytosis. New vesicles can start to fuse on this structure, creating a queue of several connected vesicles. Multigranular exocytosis consists first in the homotypic fusion of vesicles that are secondly secreted as a unique large structure. Although less frequent and less studied, compound exocytosis is present in many cell

types, including mast cells, lactotroph cells, pancreatic β-cells and even neurons. Compound exocytosis can involve >50% of the cell's LDCVs (Kasai et al., 2012; Tran and Ten Hagen, 2017). Other types of exocytosis can be distinguished. For example, in neuronal cells, Urbina et al. measured exocytosis by TIRFM using a VAMP2-pHluorin construct. The fluorescence profile of the exocytic events can easily distinguish full-collapse and kiss-and-run exocytosis. Using statistical classification tools on these intensity profiles, they propose to split these 2 obvious categories into 4 categories: delayed full-collapse, instantaneous full-collapse, delayed kiss-and-run, instantaneous kiss-and-run (Urbina et al., 2021).

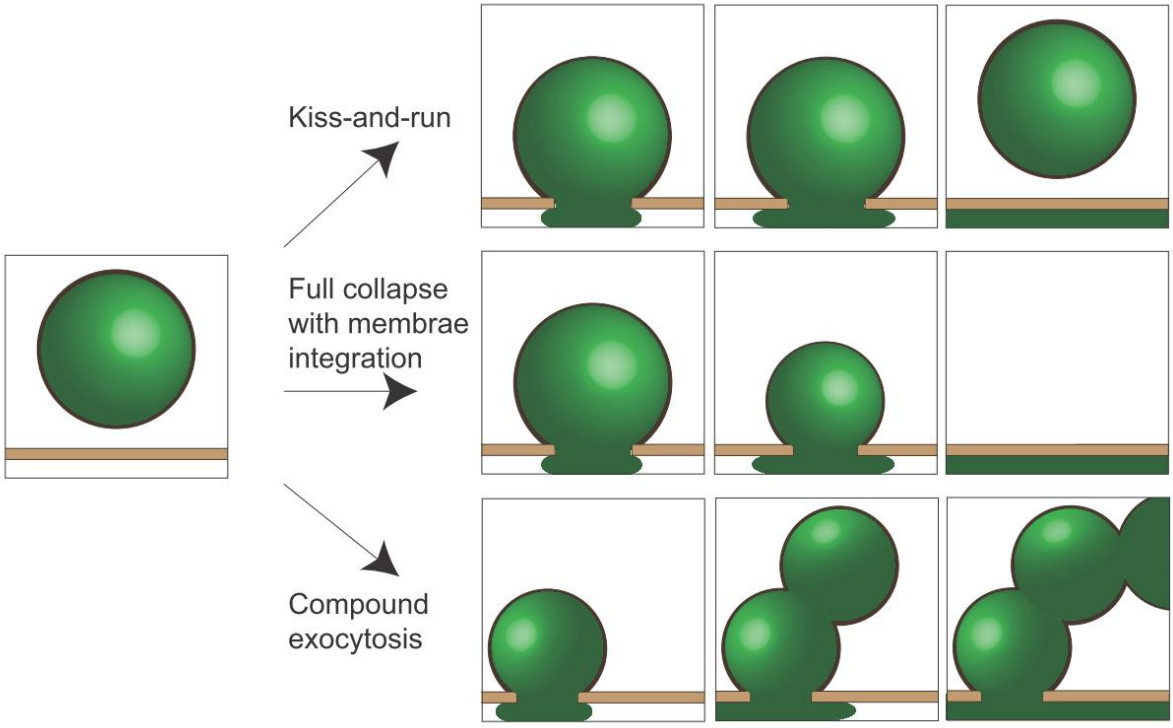

Figure 36. Modes of exocytosis, from Tran and Hagen (2017). Kiss-and-run exocytosis consists in the transitory and limited opening of the fusion pore. After a given time, the fusion pore is closed and the vesicle is detached from PM. Full-collapse exocytosis is the traditional exocytosis where the fusion pore enlarges and the vesicle totally fuses with the PM. Compound exocytosis consists either in the fusion of homotypically fused vesicles as a unit (multigranular exocytosis) or the sequential addition of a fusion site on a vesicle not yet collapsed (sequential exocytosis, as depicted on the figure).

Regulated exocytosis (and partially constitutive exocytosis) is regulated by diverse molecular factors influencing their spatio-temporal distribution. Physical factors will be excluded from this section because they are reviewed in chapter 3. The first regulatory factor is of course the presence of SNARE proteins and their fusion machinery, controlling the fusion event. Their presence can also be regulated by gene expression. For example, SNARE expression is tightly regulated during brain development (Urbina and Gupton, 2020). Among the other molecular factors, we can mainly distinguish: i) Ca^{2+}, ii) cytoskeleton, iii) lipids and iv) associated proteins.

i) **Ca^{2+}**: Ca^{2+} is a key regulator of exocytosis, especially in neurons where the action potential opens Voltage-Gated Ca^{2+} Channels (VGCC) raising the Ca^{2+} concentration from ~100nM to ~10-100µM. In neurons, the major Ca^{2+} sensors are proteins from the synaptotagmin family (Gundelfinger et al.,

2003). The mammalian synaptotagmin family consists of 16 isoforms. Synaptotagmin 1, 2 and 9 mediate Ca^{2+}-dependent synaptic vesicles exocytosis in neurons, and synaptotagmin 1 and 7 mediate LDCVs exocytosis in chromaffin cells (Pang and Südhof, 2010; Park and Ryu, 2018). The best known member of this family is synaptotagmin 1, a transmembrane proteins localized on synaptic vesicles or LCDVs. It includes two tandem C2 domains (C2A and C2B, characterized by a β-sandwich structure) at the cytosolic side. The C2A domain binds 3 Ca^{2+} and the C2B domain 2 Ca^{2+}. Bound Ca^{2+} are able to engage electrostatic interactions with negatively charged heads of lipids, creating a bridge between the vesicle and the PM and/or to engage interactions with SNAREs (Kasai et al., 2012; Park and Ryu, 2018). The mechanism by which Ca^{2+}-bound synaptotagmin 1 triggers exocytosis is still unclear. In neurons, complexins I and II are able to bind SNARE complexes and to block the zipping progression by taking the place of VAMP-2 C-terminal region in the complex. The functions of complexins are still controversial but in the most accepted model, Ca^{2+}-bound synaptotagmin removes complexins from the SNARE complex, allowing exocytosis (Park and Ryu, 2018).

Other Ca^{2+} sensors could play a role in Ca^{2+}-dependent exocytosis but these proteins remain difficult to identify with certitude. Candidate proteins should contain a C2-domain or an EF-hand (helice-loop-helice domain chelating 1 Ca^{2+}). For example, ferlin proteins (with 6 C2-domains including 2 domains with a Ca^{2+}-binding sequence) are required for exocytosis in sperm cells, muscle and hair cells (Pang and Südhof, 2010).

Interestingly, Ca^{2+} signaling does not only require proteins but also a special organelle organization. For example, in chromaffin cells, Ca^{2+} entry by VGCC induces a release of Ca^{2+} from the ER stock, a mechanism similar to the muscle “calcium-induced calcium release” mechanism. This increase in Ca^{2+} concentration leads to a risk of excitotoxicity. To buffer Ca^{2+} concentration and to limit Ca^{2+} in microdomains, a population of mitochondria is clustered close to exocytic sites. Mitochondria absorb Ca^{2+} through their mitochondrial Ca^{2+} uniporter (MCU), and additionally could provide energy for exocytosis (Villanueva et al., 2014). However, in pancreatic β-cells, the regulation of Ca^{2+} by mitochondria seems different. In β-cells, hyperglycemia triggers ATP production. ATP blocks ATP-sensitive K^+ channels causing depolarization and opening of VGCCs. During depolarization, mitochondria leave the cortical region. Indeed, using an optogenetic system, authors could induced cortical mitochondria localization that significantly reduced exocytosis, probably due to a strong buffering of Ca^{2+} (Griesche et al., 2019). This illustrates that the organization of intracellular organelles regulating local Ca^{2+} concentrations is cell type dependent, suggesting precise regulation by organelle positioning.

Despite the key role of Ca^{2+}, the minimal machinery required for exocytosis (SNARE and NSF-SNAP) is not Ca^{2+}-dependent, suggesting the possibility of Ca^{2+}-independent exocytosis. For example, Ca^{2+}-independent exocytosis has been reported in neurons (Zhang and Zhou, 2002; Zheng et al., 2009) and in chromaffin cells (Moya-Díaz et al., 2020). Surprisingly, in this second example, the Ca^{2+}-independent exocytosis still depends on the opening of VGCCs. Authors proposed a physical interaction between SNAREs and VGCCs to explain this result. However, these results should be take wih caution, since the use of a Ca^{2+}-chelator or Ca^{2+}-free medium does not prevent the mobilization of intracellular Ca^{2+} stocks in microdomains.

ii) Cytoskeleton: The main “cytoskeleton” regulator of exocytosis is cortical actin. Cortical actin has a dual role in exocytosis. It acts as a physical barrier blocking exocytosis but it also promotes exocytosis by vesicle tethering and by producing a force supporting vesicle collapse (Meunier and Gutiérrez,

2016). Cortical actin has different roles along the different steps of exocytosis: i) tethering, ii) docking and iii) fusion.

The first exocytosis step consists in the capture of the secretory vesicle by the cortical cytoskeleton. In chromaffin cells, cortical actin retains 2-4% of LCDVs (Papadopulos et al., 2013). Most of the time, this step is achieved by the processive actin-dependent motor protein myosin V. The Myosin V tail domain binds the vesicle and brings it close to the PM through its cargo-carrying processive activity (Meunier and Gutiérrez, 2016; Maschi et al., 2018; Miklavc and Frick, 2020). Using pull-down assays and mass spectrometry of secretory granules, myosin VI has also been identified as a tethering factor. Moreover this interaction is Ca^{2+}-dependent, highlighting again the role of Ca^{2+} in the regulation of exocytosis (Tomatis et al., 2013). The implication of myosin VI is supported by the mislocalization of synaptic vesicles in *Drosophila melanogaster* myosin VI mutants (Kisiel et al., 2011, 2014).

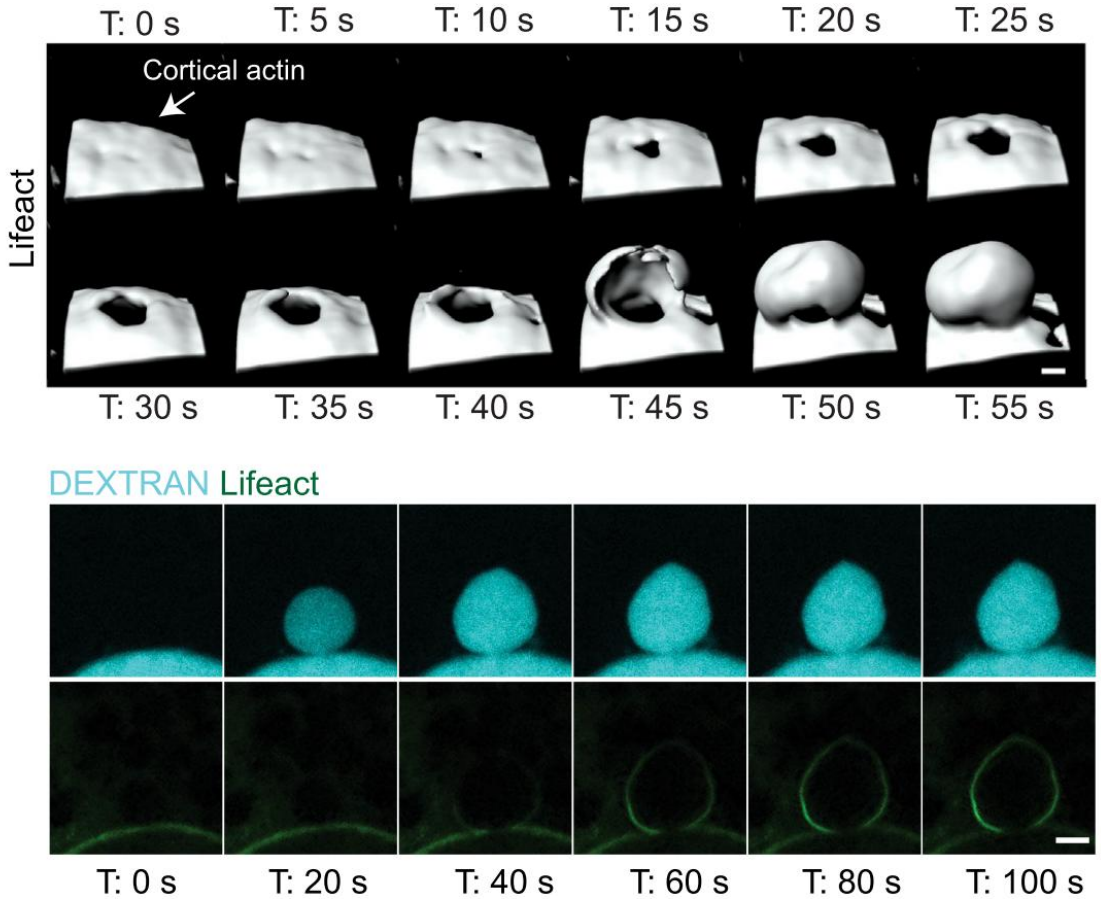

Figure 37. Visualization of the cortical actin during exocytosis of secretory vesicles in *Drosophila melanogaster* third-instar salivary glands, from Tran et al. (2015). Top: Reconstruction of the actin surface during exocytosis highlighting the depolymerization at the fusion site and the subsequent actin coating of the vesicle. Bottom: Salivary glands expressing Lifeact-GFP with a gland lumen filled with fluorescent dextran. It highlights that the opening of the fusion pore occurs before the actin coating of the vesicle. Scale bar = 5µm.

Next, the docking step requires actin remodeling. At rest, the cortical actin forms a dense layer of ~190nm thickness with a mesh size of ~100nm, blocking vesicles (Eghiaian et al., 2015; Li et al., 2018a). Drugs that disrupt cortical actin generally induce exocytosis (Miklavc and Frick, 2020) with

notable exceptions (Yuan et al., 2015; Carisey et al., 2018). However, a stabilization of cortical actin by jasplakinolide inhibits secretion (Carisey et al., 2018). These drug treatment experiments teach us that actin needs to stay dynamic to support exocytosis. This includes local switches between a polymerized state to tether and push vesicles, and a depolymerized state for docking. A rapid depolymerization of the actin cytoskeleton is observed before exocytosis (**Figure 37**) (Meunier and Gutiérrez, 2016; Tran and Ten Hagen, 2017). Depolymerization is induced by scinderin and/or the Myristoylated Akanine-Rich C Kinase Substrate (MARKS) regulated by PKC. Interestingly, both PKC and scinderin are activated by Ca^{2+} (Papadopulos et al., 2013). The remodeling of cortical actin creates open spaces around docking sites in 15-25s (Meunier and Gutiérrez, 2016). In mastocytes, Ca^{2+} oscillation causes oscillation of cortical actin correlating with cycles of exocytosis (Wollman and Meyer, 2012).

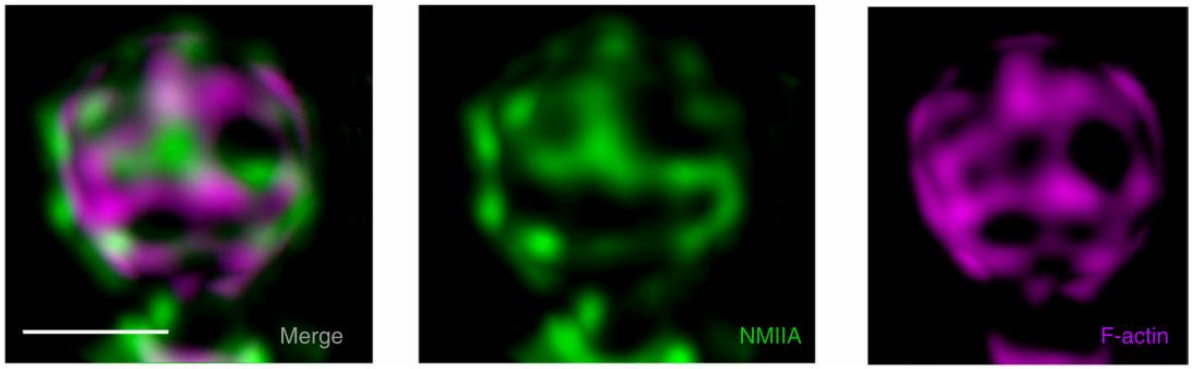

Figure 38. Actomyosin polyhedral structure of the exocytosis coat in mouse salivery gland, from Ebrahim et al. (2019). Fixed sample from mouse expressing GFP-NMIIA (Non-muscle Myosin IIa) and stained with phalloidin. Scale bar = 1µm.

Finally, during fusion, an actin coat is formed around the vesicle. The actin coating is a two step process including first polymerization of linear actin by formins (or its ortholog diaphanous in *Drosophila*) and then branching by Arp2/3 complex and WASP (Tran and Ten Hagen, 2017; Li et al., 2018a). Interestingly, membrane fusion seems to precede actin coating (**Figure 37**) (Sokac and Bement, 2006; Tran and Ten Hagen, 2017). The actin polymerization is dependent on the kinase Src in chromaffin cells (Olivares et al., 2014). Src is Ca^{2+}-dependent and could be also a regulator of myosin VI (Tomatis et al., 2013). Actin coat provides a plateform for the recruitment of other proteins such as myosin II and α-actinin. The actomyosin coat facilitates exocytosis by applying a force against the vesicle. Indeed myosin II-dependent contraction gives the force necessary to enlarge the fusion pore and leads to a full-collapse exocytosis (Li et al., 2018a). Myosin II inhibition by blebbistatin, or the expression of unphosphorylable myosin II mutants prevents fusion pore expansion, impairing cargo release (Ñeco et al., 2008; Berberian et al., 2009). Myosin Ib, Ic and Ie can also be recruited on the actin coat and promote contraction (Miklavc and Frick, 2020). It has been recently demonstrated that the acto-myosin coating of the vesicle follows a polyhedral organization and squeezes the vesicle in exocrine glands of live mice (**Figure 38**) (Ebrahim et al., 2019). The force of the acto-myosin coat controls the mode of exocytosis. When myosin II is inhibited, the fusion pore expansion is impaired and exocytosis can shift from a full-collapse mode to a kiss-and-run mode (Doreian et al., 2008). A high Ca^{2+} concentration also shifts the mode of exocytosis to kiss-and-run (Alés et al., 1999). This effect could be mediated by triggering actin depolymerization, impairing contractile activity and leading to the same phenotype than blebbistatin inhibition.

iii) **Lipids**: PtdIns(4,5)P_2 is the first lipid identified that regulates exocytosis. For example, it has been observed that direct addition of PtdIns(4,5)P_2 or over-expression of the kinase producing PtdIns(4,5)P_2 (phosphatidylinositol-4-phosphate-5-kinase I) increased exocytosis. Contrary, the overexpression of the phosphatase targeting PtdIns(4,5)P_2 (inositol 5-phosphatase domain of synaptojanin 1) blocks exocytosis almost completely (Milosevic et al., 2005). In cancer cells with non-regulated exocytosis, PtdIns(4,5)P_2 is also recruited at the fusion site (Stephens et al., 2019). How PtdIns(4,5)P_2 promotes exocytosis stays elusive. It interacts with synaptotagmin-1 and the t-SNARE syntaxin in a Ca^{2+}-dependent manner, and with the Ca^{2+}-dependent Activator Protein for Secretion (CAPS) (Ammar et al., 2013). It has been demonstrated that microdomains of PtdIns(4,5)P_2 are formed around syntaxin clusters and that these clusters correspond to fusion sites (Aoyagi et al., 2005; Umbrecht-Jenck et al., 2010; Honigmann et al., 2013). Moreover, PtdIns(4,5)P_2 stimulates actin polymerization by the activation of actin nucleators (Papadopulos et al., 2013; Tran et al., 2015; Tran and Ten Hagen, 2017; Miklavc and Frick, 2020). Indeed, PtdIns(4,5)P_2 diffusion from the PM to the vesicle precedes actin coating (**Figure 39**). PtdIns(4,5)P_2 levels at the PM require a precise spatio-temporal regulation. After exocytosis in mast cells, PtdIns(4,5)P_2 is depleted by phospholipase C (Hammond et al., 2006). In addition, MARKS has a PtdIns(4,5)P_2 binding domain, demonstrating a more complex role for this lipid than only promoting actin coating (Miklavc and Frick, 2020). One of the exocytosis regulators in chromaffin cells is the scaffolding protein annexin A2. With the support of actin, annexin A2 interacts with PtdIns(4,5)P_2, promotes lipid domain organization and exocytosis (Ammar et al., 2013; Gabel et al., 2015).

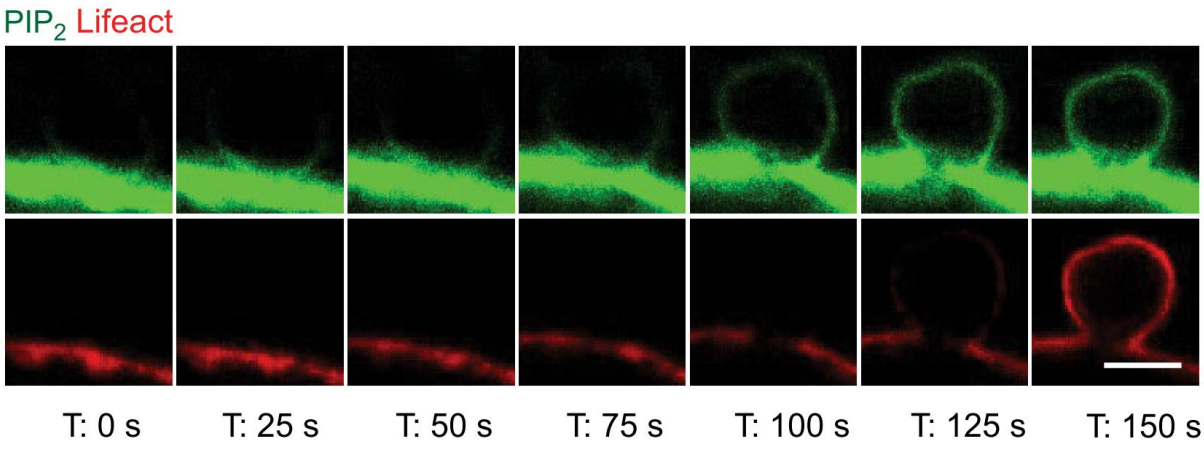

Figure 39. PtdIns(4,5)P_2 and actin coating in exocytosis of secretory vesicles from *Drosophila melanogaster* third-instar salivary glands, from Tran et al. (2015). The PtdIns(4,5)P_2 reporter is in green and actin is stained by Lifeact-RFP. The diffusion of PM PtdIns(4,5)P_2 in the vesicle membrane precedes actin coating. Scale bar: 5µm.

Cholesterol also plays a role in the regulation of exocytosis by concentrating t-SNAREs (Lang, 2007). However, cholesterol depletion by methyl-β-cyclodextrin has a facilitating role in some studies, while it inhibits exocytosis in other studies (Chamberlain et al., 2001; Linetti et al., 2010; Rituper et al., 2012; Xu et al., 2017; Rituper et al., 2020). These results should be taken with caution, since cholesterol depletion by methyl-β-cyclodextrin has broad effects that are sometimes difficult to interpret. The t-SNARE clustering by cholesterol could also promote the opening of the fusion pore and prevent pore flickering (Stratton et al., 2016).

iv) Associated proteins: Tethering factors are proteins responsible for the initial tether of a vesicle with a target membrane (Yu and Hughson, 2010), working upstream of SNARE complexes. Such as

the SNARE machinery, tethering factors are involved in both intracellular membrane fusion and exocytosis. As demonstrated by *in vitro* systems, tethering factors are not strictly necessary for exocytosis/fusion events (Ohya et al., 2009; Stroupe et al., 2009; Kliesch et al., 2017a). However, tethering factors could substantially accelerate their kinetics by vesicle capture but also by regulating SNARE complex assembly. Moreover, these tethering factors help to preserve the specificity of the target membrane, in addition to the one provided by SNARE pairings. Many of the described tethering factors are associated to intracellular fusion (e.g. Golgins associated to Golgi apparatus, HOPS and CORVET associated to the endolysosomal system) (Yu and Hughson, 2010). Tethering factors are classically divided into two groups: coiled-coil homodimers (e.g. Golgins) and Multisubunit Tethering Complexes (MTCs) (e.g. HOPS, CORVET and the exocyst). Exocyst is the only tethering factor directly involved in exocytosis. Exocyst is an evolutionary conserved octameric protein complex made of Sec3, Sec5, Sec6, Sec8, Sec10, Sec15, Exo70 and Exo84. With COG, Dsl1 and GARP, exocyst is a member of the Complex Associated with Tethering Containing Helical Rods (CATCHR) family. Interestingly, Sec3 (through a PH-like domain) and Exo70 (through basic residues in the C-terminus) can bind PtdIns(4,5)P_2. Moreover, in yeast, Sec6 binds to the v-SNARE Snc2 (Wu and Guo, 2015). Initial experiments by Schekman's lab demonstrated that mutations of these genes impaired exocytosis in yeast (Novick et al., 1980). In yeast, the ectopic recruitment of exocyst to mitochondria leads to a secretion defect and the mislocalization of secretory vesicles to mitochondria (Luo et al., 2014). In mammalian cells, Sec8 localizes at endosomal vesicles undergoing exocytosis, and stays associated to these vesicles until the dilation of the fusion pore (Rivera-Molina and Toomre, 2013). More recently, using high-speed imaging and correlation spectroscopy, it has been demonstrated that the exocyst is made of two tetramers oscillating between an octameric and monomeric state. These tetramers associate independently with the PM or the vesicle. This study also highlights that Sec3 leaves the complex before the fusion, whereas other subunits are disassembled after the fusion (Ahmed et al., 2018).

Other majtor regulators of exocytosis are Mammalian uncoordinated (Munc) proteins, Munc18-1 and Munc-13-1. Munc18-1 binds and shield syntaxin-1, preventing interactions with SNAREs. Munc13-1 catalyzes the transition from a syntaxin-1 Munc18-1-bound inactive closed conformation to an active open conformation in the presence of the SNAP25 and VAMP2. This complex sets the correct configuration of the SNARE proteins for fusion (Kasai et al., 2012; Wang et al., 2019). Interestingly, Munc13-1 contains multiple C2 domains, including a C2B domain that binds phospholipids in a Ca^{2+}-dependent manner (Kasai et al., 2012).

2.5. Spatial regulation of exocytosis

It has been noticed that exocytosis is spatially regulated in polarized cells. For example, exocytosis is oriented towards the apical pole of acinar cells (Jamieson and Palade, 1967) and towards the active zone in neurons (Südhof, 2012). However, if exocytosis is spatially regulated in non-polarized cell stayed an open question until the 2000s. The first study addressing this question argued that exocytosis of Golgi-derived vesicles is fairly random in its spatial distribution based on TIRFM observations (Schmoranzer et al., 2000). However, this result has been quickly contradicted. Keller et al. compared observed exocytosis maps to random simulations. This method revealed that observed fusion sites are more clustered than one would expect for a random distribution (Keller et al., 2001).

It reveals the need of quantitative methods to study the spatial regulation of exocytosis. Thus, the following studies especially used spatial statistics and demonstrated without ambiguity that Golgi-derived exocytosis is clustered in a large variety of cells, including epithelial cells, neurons, β-cells and melanoma cells (Sebastian et al., 2006; Yuan et al., 2015; Urbina et al., 2018; Fu et al., 2019). Strikingly, although all studies reveal universally that exocytosis is clustered, they report different levels of clustering.

Urbina et al. used cortical neurons in culture from mice embryos and observed their development during 72h. They found that the distribution of exocytosis is random at 24h but becomes clustered at 48h. Moreover, even at a given time point, the spatial distribution of exocytosis is different between the soma and the neurites. They completed their study by quantifying VAMP7+ and VAMP3+ exocytosis in melanoma cell lines. VAMP7+ exocytosis is much more clustered than VAMP3+ exocytosis, the latter being virtually random. These results demonstrate that the spatial regulation of exocytosis depends on cell location, cargo and even cell differentiation. Urbina et al. also explored the temporal distribution of exocytosis. Whereas neuronal exocytosis is temporally clustered after 48h in culture, melanoma exocytosis is temporally random for both cargos (VAMP3 and VAMP7) (Urbina et al., 2018). Sebastian et al. also reported a random temporal distribution of exocytosis (Sebastian et al., 2006). In addition, they did not find any coupling between temporal and spatial organization, meaning that these are two independent properties (Sebastian et al., 2006). However, this study is only based on 3 cells, and thus, drastically lacks stastical power. Interestingly, a spatial organization of exocytosis has been observed in multi-cellular systems of organotypic parotid gland (Warner et al., 2008). Unfortunately, this study lacks a precise quantitative measurement. The physiological significance of exocytosis clustering of exocytosis is still poorly understood. However, glucose stimulation of β-cells from type 2 diabetic patients leads to a random distribution of exocytosis whereas exocytosis is clustered in cells from healthy donors (Fu et al., 2019).

How is the clustering of exocytosis events achieved? In synapses, spatial organization is achieved through a specialized set of proteins in the active zone. Gundelfinger et al. proposed that “organizing elements” in the PM or at the cell cortex spatially regulate exocytosis (Gundelfinger et al., 2003). This hypothesis can be extended beyond the context of neurons. Gundelfinger et al. distinguished 3 types of organizing elements: lipids, cortical cytoskeleton and scaffolding proteins (**Figure 40**). Lipid components include the presence of PtdIns(4,5)P_2. Previous sections have summarized how PtdIns(4,5)P_2-rich domains are able to cluster t-SNAREs to promote exocytosis (Aoyagi et al., 2005; Umbrecht-Jenck et al., 2010; Honigmann et al., 2013). We have also reviewed the role of cortical actin in the regulation of exocytosis in the previous section (Meunier and Gutiérrez, 2016; Tran and Ten Hagen, 2017; Li et al., 2018a; Miklavc and Frick, 2020). Yuan et al. report that actin depolymerization by cytochalasin D totally abolishes exocytosis clustering. They also report that MT depolymerization by nocodazole leads to a similar effect (Yuan et al., 2015). MT (+) tips are dynamic targets of transported vesicles and could therefore organize local hot-spots of exocytosis. Interestingly, MT are coupled to FAs through Cytoplasmic Linker ASsociated Protein (CLASP) 1 and 2. This coupling is necessary for the localized MMPs exocytosis at FAs (Stehbens et al., 2014). Additionally, it has been observed that Rab6+ Golgi-derived vesicles are exocytosed at FAs (Fourriere et al., 2019). The last class of organizing elements includes “scaffolding proteins” in a large meaning. These could include FAs, as mentioned, but also t-SNAREs. It has been clearly demonstrated by super-resolution microscopy that t-SNAREs (SNAP-25 and syntaxin) cluster in nanometers domains, relying on lipid patterns (Rickman et al., 2010). Extracellular elements could also support the

formation of these organizing elements. Urbina et al. investigated this possibility in neuronal cell by using the MEC protein Netrin-1. TRIpartite Motif protein 9 (Trim9) is involved in the neuronal response to Netrin-1. Netrin-1 addition increases the spatial clustering in neurites and decreases it in soma. But in Trim9 KO condition, netrin-1 addition has no effect (Urbina et al., 2018). This result demonstrates that extracellular signals could change the spatial regulation of exocytosis through intracellular signaling pathways. However, most of the explored mechanisms (such as PtdIns(4,5)P_2 and t-SNAREs domains) explain clustering only at micrometric or sub-micrometric scale whereas the observed clustering is at the whole cell scale.

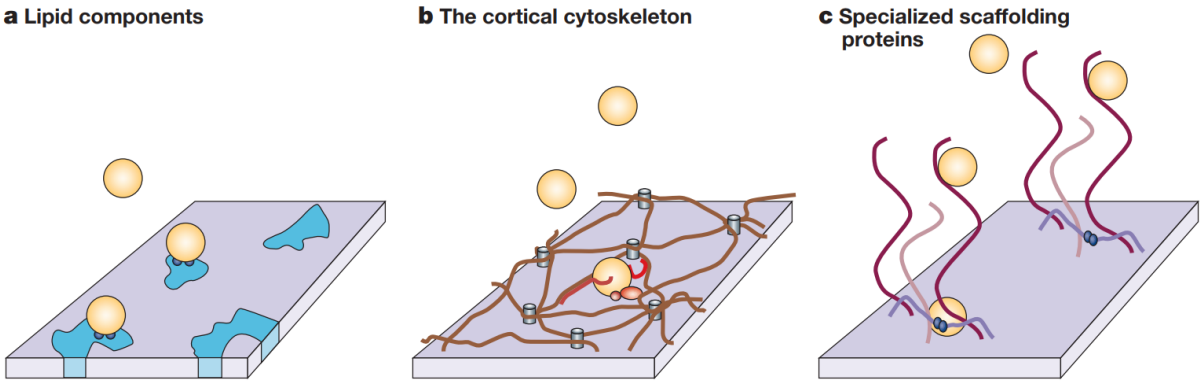

Figure 40. Organizing elements hypothesis, from Gundelfinger et al. (2003). 3 kinds of elements could organize spatially exocytosis: lipids, cortical cytoskeleton and scaffolding proteins.

3. Lysosomal exocytosis

3.1. Molecular machinery

Lysosomal exocytosis was first described in 1968 in the context of bone resorption by ostocleasts (Vaes, 1968). This pathway, viewed as an “unconventional secretion”, has been identified in diverse cells, and today it is recognized as being present in virtually all mammalian cell types. It requires the transport of lysosomes to the vicinity of PM. The molecular mechanisms of lysosomal trafficking have been already reviewed in previous sections. The fusion step requires the SNARE complex as in classical exocytosis. The lysosomal v-SNARE is VAMP7 (Martinez-Arca et al., 2000; Proux-Gillardeaux et al., 2007; Verderio et al., 2012), a SNARE that is insensitive to TeTx and BoNT (hence its other name TI-VAMP for Tetanus neurotoxin Insensitive Vesicle-Associated Membrane Protein) (Galli et al., 1998). VAMP7 is also associated to Golgi-derived vesicles in some cell types, especially in neurons where it promotes neurite outgrowth (Martinez-Arca et al., 2000; Chaineau et al., 2009). VAMP7 is characterized by the presence of a longin domain in its N-terminal region. The longin domain has an α-β-α sandwich structure and seems to have an inhibitory role on exocytosis. Moreover, this domain is also involved in the recycling and targeting of VAMP7 to lysosomes by interacting with the adaptin AP-3 (Daste et al., 2015). In epithelial cells, VAMP7 interacts with the t-SNAREs syntaxin 3 (Vogel et al., 2015) and 4 (Williams et al., 2014) found at the PM but also with syntaxins 7 and 8 (Chaineau et

al., 2009). Whereas syntaxin 3/4 are involved in exocytosis, syntaxin 7 and 8 are only involved in intracellular endosomal fusion events (Ward et al., 2000; Wade et al., 2001; Bogdanovic et al., 2002; Pryor et al., 2004). The formation of the SNARE complex requires SNAP23 (Tancini et al., 2020). In neuronal cells, VAMP7 is able to form a SNARE complex with syntaxin 1 and SNAP25 (Chaineau et al., 2009). Interestingly, a phosphoproteomic study revealed that SNAP23 is phosphorylated on the serin 110 during stimulated exocytosis. This phosphorylation is achieved by PKC. Therefore, lysosomal exocytosis can be activated by histamine, a stimulator of the H1HR-Gq pathway upstream of PKC (Verweij et al., 2018). Interestingly, exocytosis of the LRO lamellar bodies seems to be also controlled by PKC (Frick et al., 2001; Kittelberger et al., 2016). SNAREs are important to regulate the exocytosis rate but also for its spatial distribution. In polarized MDCK cells, lysosome exocytosis occurs at the basolateral membrane. This organization relies on the specific expression of Syntaxin 4 on the basolateral membrane (Xu et al., 2012). Surprisingly, the exocytosis of LROs seems to rely partially on other SNAREs, for example VAMP2 for lamellar bodies in type II pneumocyte, and VAMP8 for the exocytosis of dense and α granules in platelets (Ren et al., 2007; Jani et al., 2016). However, in platelets, VAMP7 plays a role in the exocytosis of LROs in addition to VAMP8 (Koseoglu et al., 2015). Finally, MVB exocytosis requires VAMP7 or the R-SNARE Ykt6 (Hessvik and Llorente, 2018).

Lysosomal exocytosis is believed to be Ca^{2+}-dependent (Jaiswal et al., 2002; Tancini et al., 2020). Ca^{2+} could be provided by the opening of PM channels. Alternatively, lysosomes could self-provide the Ca^{2+} needed for exocytosis by the opening of the lysosome-specific TRPML1 channel (Di Paola et al., 2018). Interestingly, TRPML1 expression is under the control of TFEB. TFEB overexpression promotes lysosomal exocytosis (Medina et al., 2011). Furthermore, TFEB is under the control of mTORC1, therefore a nutrient privation could promote exocytosis by mTORC1 inactivation. The major Ca^{2+} sensors for exocytosis are synaptotagmin proteins. Synaptotagmin VII has been identified for lysosomes (Tancini et al., 2020). A KO of synaptotagmin VII impairs cathepsin K secretion in osteoclats (Zhao et al., 2008). VAMP7+ mastocyte granules are also regulated by Ca^{2+} concentration. A computational model indicates that Ca^{2+} regulates PtdIns(4,5)P_2 levels at the PM, that in turn regulate actin polymerization at cell cortex (Wollman and Meyer, 2012). However a conflicting result reports that MVBs exocytosis is Ca^{2+}-independent (Verweij et al., 2018). These conflicting results could be due to different exocytosis pathways but also to experimental limitations in Ca^{2+} chelating as explained previously.

Several Rab proteins regulate lysosomal exocytosis. Rab7 is required for correct lysosomal trafficking, and thus, is essential for exocytosis (Pu et al., 2016; Cabukusta and Neefjes, 2018). But additional Rab proteins have been identified. In a screen for Rab proteins, Encarnação et al. identified Rab3a as a major regulator of lysosomal exocytosis. However, cell biology experiments reveal that Rab3a does not directly regulate exocytosis but rather lysosomal positioning. Rab3a silencing restricts lysosomes in the perinuclear region. Authors identified myosin II and Slp4-a as Rab3a effector and proposed that they could tether lysosomes to the cortical actin (Encarnação et al., 2016). The same team identified more recently Rab11 as a regulator of lysosomal exocytosis. Here again, the mechanism is largely indirect throught interaction between lysosomes with endosomes involving Rab3a, Rab11 and the GEF of Rab3a (named GRAP). This interaction would promote the GTP-bound form of Rab3a (Escrevente et al., 2021). Finally, Rab27b has been shown to positively regulate lysosome exocytosis in oligodendrocytes, but the molecular mechanism is not known (Shen et al., 2016). A similar effect has been described for Rab27a and Rab27b on exosome release (Ostrowski et al., 2010; Hessvik and Llorente, 2018). Interestingly, the trafficking of the LRO melanosome also involves Rab27 and Rab11

for the exocytosis step (Tarafder et al., 2014). In endothelial cells, the peripheral localization of LRO Weibel-Palade bodies also depends on Rab27, which couples these organelles to cortical actin through its effector MyRIP from one side and myosin Va on the other side (Nightingale et al., 2009; Rojo Pulido et al., 2011).

Myosins have also been identified as important regulators of lysosomal exocytosis. In sarcoma cells, LAMP1 interacts with myosin XI, and silencing of myosin XI and/or LAMP1 reduces lysosomal exocytosis rate (Machado et al., 2015). Here again, we do not know at which step(s) of trafficking and/or exocytosis these proteins are involved. Drug inhibition of myosin I clusters lysosomes at cell center and causes lysosomal swelling (Chinthalapudi et al., 2011). In type II pneumocytes, the treatment with the same drug causes a decrease in LRO lamellar body exocytosis. Using a dominant negative myosin Ic tail, authors highlight the implication of this myosin in exocytosis and report that it influences the vesicle compression rate by the actin coat (Kittelberger et al., 2016). The inhibition of myosin Ic also blocks the fusion between lysosomes and autophagosomes, but unfortunately the impact in lysosomal exocytosis has not been characterized (Brandstaetter et al., 2015; Zhang et al., 2019). Interestingly, a phosphoproteomic study identified myosin Ic as a putative regulator of MVB exocytosis. Indeed, histamine stimulation triggers exocytosis through PKC activation and myosin Ic could be a target of PKC (Verweij et al., 2018). PKC activation could regulate exocytosis through different pathways. In chromaffin cells, histamine stimulation activates PKC that in turn activates scinderin. The cortical actin disassembly by scinderin promotes exocytosis (Zhang et al., 1995). Myosin Ib is also involved in the coupling of lysosomes to actin, because a non functional myosin Ib causes perinuclear clustering and probably reduces lysosomal exocytosis (Cordonnier et al., 2001). The role of actin is not limited to the tethering of lysosomes/LROs to the cell cortex. The exocytosis of Weibel-Palade bodies in endothelial cells and of lamellar bodies in pneumocytes II requires the formation of a contractile acto-myosin II coating (Nightingale et al., 2011; Miklavc et al., 2012). In platelets, VARP interacts with Arp2/3 and VAMP7 at fusion sites in resting cells. This interaction is believed to promote actin coating when exocytosis is triggered (Koseoglu et al., 2015).

Similarly to conventional exocytosis, exocyst seems also required for lysosomal exocytosis. In B lymphocytes, a KD of the exocyst subunit Exo70 impairs lysosomal exocytosis (Sáez et al., 2019). Interestingly, exocyst is also required for melanosome exocytosis (Moreiras et al., 2020). LAMP1 is also an important regulator of exocytosis. Its cytosolic C-terminal domain is responsible for attachment to actin and myosin XI. Mutations in this domain decrease lysosomal exocytosis and induce a lysosomal perinuclear clustering (Machado et al., 2021).

3.2. Physiological functions

Lysosomal exocytosis primarily functions in secretion of digestive enzymes (Samie and Xu, 2014). These enzymes are essential for ECM remodeling. For example, they allow bone resorption by osteoclasts. Ostoclasts form a hole in the bone ECM called Howship's lacuna. The lacuna is enclosed by a sealing zone. Howship's lacuna is acidic due to the exocytosis of lysosomes, bringing the V-ATPase at the PM that pumps H^+ across the PM. A mutation in the subunit a3 of the V-ATPase causes osteopetrosis in human. The ClC-7 channel is also involved, probably by assuring the electroneutrality, similarly as it does in lysosomal acidification (Mindell, 2012; Lacombe et al., 2013).

Secreted enzymes activated by acidic pH, such as MMPs and more importantly cathepsin K which digest collagen I fibers. In addition to the role in ECM remodeling, lysosomal secretion can play a role in other cell types. For example, the secretion of LRO cytotoxic granules from cytotoxic T or natural killer lymphocytes at the immunological synapse releases perforin and granzyme, and leads to death of the attached cancer/infected cell (Peters et al., 1991; Trapani, 2012). In astrocytes, lysosomal exocytosis allows ATP release used for cell communication, promoting microglial cell migration (Dou et al., 2012). Lysosomes are also able to accumulate Cu^{2+} and Zn^{2+}, and lysosomal exocytosis allows the clearance of these toxic metals, especially in the liver (Tancini et al., 2020).

A special type of secretion through the exocytosis of MVBs leads to the release of exosomes (Kowal et al., 2014). Exosomes contain a variety of intracellular proteins (cytoskeletal proteins, growth factors and cytokines, heat shock proteins, Rabs, etc.) as well as nucleic acids (especially miRNA but also DNA, mRNA, lncRNA, tRNA, etc.). Additionaly, the exososome membrane contains transmembrane proteins such as tetraspanins (e.g. CD63), adhesion molecules, MHC and signaling receptors. Exosome secretion is important, because exosomes can mediate cell-cell communication. This communication is not restricted to short scales, since exosomes are found in diverse biological fluids (blood, urine, saliva, breast milk, etc.). When they reach their target cells, exosomes can either be internalized after binding to a surface receptor or triggers intracellular signaling. This new modality of cell-cell communication, still under investigation, has potentially broad effects (Gurung et al., 2021).

A second function of lysosomal exocytosis is the trafficking of transmembrane proteins to the PM. For example, lysosomal exocytosis is necessary to transport the myelin transmembrane protein P0 in Schwann cells and assure correct axonal myelination (Chen et al., 2012). Lysosomal exocytosis is also necessary for antigen presentation through the exposition of MHC-II at the PM (Geuze, 1998). It has been recently demonstrated that the uptake of antigens by B-lymhocytes is also dependent on VAMP7+ lysosomal exocytosis (Obino et al., 2017). However, the role of lysosomal exocytosis in the trafficking of transmembrane proteins is minor, since the majority of transmembrane proteins are directly targeted to PM by the anterograde Golgi secretory pathway. Whereas MHC-II needs to traffic to lysosomes to bind endocytosed antigens, the role of lysosomal P0 localization is elusive, especially since P0 can follow the classical Golgi secretory pathway (Chen et al., 2012).

Finally, lysosomal exocytosis is involved in diverse membrane remodeling functions. Its role in PMR has been already described in previous sections (Andrews and Corrotte, 2018). However, the role of lysosomal exocytosis in membrane remodeling is not restricted to PMR. The neurite outgrowth requires membrane inserted by exocytosis. It has been demonstrated that a pool of vesicles characterized by LAMP1+ and VAMP7+ is implicated in this process. Moreover, this process is Ca^{2+}- and synaptotagmin VII-dependent (Arantes and Andrews, 2006). Additionally, lysosomal exocytosis is required for phagocytosis. Phagocytosis includes a step of membrane elongations that form pseudopods. These pseudopods surround the target particle before engulfing it. This process requires membrane coming form lysosomal exocytosis. Here again, this process is VAMP7- and synaptotagmin VII- dependent. It is noteworhtly that the Ca^{2+} sensed by synaptotagmin VII could be self-provided by lysosomed because TRPML1 KO in macrophages causes phagocytosis defects (Huynh et al., 2007; Tancini et al., 2020).

3.3 Pathologies

The importance of lysosomal exocytosis is highlighted by its role in different pathologies. I will review only 3 pathologies, in which the role of lysosomal exocytosis is well documented and of a prime importance: i) cancer, ii) LSD and iii) intracellular infection.

i) Cancer: Cancer progression correlates with a relocalization of lysosomes to the cell periphery, which could potentially facilitate exocytosis (Mathur et al., 2022). Moreover, LAMP1 overexpression, viewed as a marker of lysosomal exocytosis, often correlates with cancer grade, metastasis probability and poor prognosis (e.g. breast and colon carcinoma, glioma and melanoma) (Machado et al., 2021). Several studies have shown that lysosomal exocytosis, especially at invadopodia, enhances cancer invasion (Hoshino et al., 2013; Machado et al., 2015). Some MMPs are secreted by this pathway and digest ECM, allowing cancer invasion. In particular, it has been demonstrated that the metalloprotease MT1-MMP plays a central role in ECM degradation (Castro-Castro et al., 2016). The secretion of MT1-MMP is dependent on the lysosomal v-SNARE VAMP7 (Steffen A et al., 2008). Additionally, lysosomal exocytosis activates Cancer Associated Fibroblast (CAFs) and immune cells (e.g. Tumor Associated Macrophages TAMs), endothelial cells and pericytes. These activated cells secrete ECM components (collagen, laminin, fibronectin, etc.) and proteases. This synergy creates a fibrotic desmoplastic tumor microenvironment, a hallmark of aggressive cancer (Machado et al., 2021). Moreover, MVBs exocytosis plays a specific role in cancer invasion: it releases exosomes that promote angiogenesis, immunosuppression and tumor progression (Osaki and Okada, 2019). Exosomes induce fibroblast differentiation into CAFs through the transport and release of TGFβ (Ringuette Goulet et al., 2018). Centrosome amplification, another hallmark of cancer, correlates with exosome secretion. More surprisingly, it also affects their nature. Exosomes extracted from Pancreatic Ductal AdenomaCarcinoma (PDAC) with centrosome amplification activates more efficiently pancreatic stellate cells (Adams et al., 2021).

Tumors are characterized by an acidosis around cells with an extracellular pH about 6.5. This acid environment is toxic leading to a Darwinian selection of resistant cells. LAMP2 over-expression at the PM promotes this acidic resistance in cancer cells, indicating an activation of lysosomal exocytosis (Damaghi et al., 2015; Funato et al., 2020).

Finally, lysosomal exocytosis is a factor of chemotherapy resistance. Most of the chemotherapeutics are lipophilic weak bases, which are properties of lysosomotropic drugs. Indeed, lysosomal exocytosis can efficiently clear lysosomotropic drugs. Moreover, some of the MultiDrug Resistance (MDR) transporters such as P-glycoproteins are also localized at the lysosomal membrane. Therefore, lysosomes can accumulate cytosolic drugs and exocyte them (Yamagishi et al., 2013; Machado et al., 2021). However, lysosomes can also be used as a therapeutic target. For example, the chemotherapeutic thiosemicarbazone Dp44mT accumulates in lysosomes and catalyzes ROS formation. ROS leads to the permeabilization of the lysosomal membrane and cell death (Machado et al., 2021).

ii) LSD: More than 70 LSDs are known, and most of them represent recessive genetics diseases. A mutation in a lysosomal gene can impair lysosomal functions, leading to the accumulation of undigested material. Although LSDs are individually rare, together they represent an incidence of 1 over 5000 live births, and are commonly associated with poor prognosis (Platt et al., 2018). MLIV is the only known LSD where the original defect is lysosomal exocytosis. MLIV is caused by mutations in

the TRPML1 gene (LaPlante et al., 2006). At the cellular scale, MLIV is characterized by an accumulation of gangliosides, phospholipids and mucopolysaccharides in lysosomes (Di Paola et al., 2018). However, in many LSDs, lysosomal exocytosis seems secondarily impaired, and an activation of this pathway seems to be a promising therapeutic strategy (Samie and Xu, 2014). Metachromatic leukodystrophy is a LSD caused by a deficiency in arylsulfatase A and characterized by an accumulation of sphingolipid sulfatide. It causes progressive demyelination, translated at the clinical level in muscle rigidity, developmental delays, convulsions, paralysis, dementia and even coma. The induction of lysosomal exocytosis by Ca^{2+} in mouse primary cells leads to the clearance of accumulated material (Klein et al., 2005). The activation of Ca^{2+} release by TRPML1, either by using drugs or by activating the TFEB transcriptional control, leads to the a clearance of accumulated material, as similarly observed in a large variety of LSDs (Medina et al., 2011; Shen et al., 2012; Tancini et al., 2020).

iii) **Intracellular infection**: Lysosomal exocytosis can promote the entry or exit of diverse pathogens. For example, the protist responsible of Chagas disease, *Trypanosoma cruzi*, invades diverse human cells including cardiomyocyte causing cardiomyopathy. To penetrate inside the cell, *T. cruzi* causes PM damage, activating the PMR pathway by Ca^{2+} entry. PMR pathway activation leads to lysosomal exocytosis, releasing ASM that transforms sphingomyelin in ceramide. Ceramides promote the endocytosis step of PMR. This endocytosis is exploited by *T. cruzi* for cell entry (Ireton et al., 2018). Adenoviruses, causing respiratory and intestinal diseases, exploit exactly the same pathway to penetrate inside cells. The capsid protein VI has a membrane lytic activity. It activates the PMR pathway and the endocytosis induced by ceramides promotes adenovirus entry (Ireton et al., 2018).

Intracellular pathogens can also use lysosomal exocytosis to promote their exit. It is the case for β-coronaviruses, a group of viruses including SARS-CoV-2 responsible for the COVID-19 pandemy. Murin coronavirus and SARS-CoV-2 are enriched in lysosomes once they penetrate inside the cell. The contaminated lysosomes are deacidified, leading to the inactivation of lysosomal enzymes. Moreover, the virus promotes lysosomal exocytosis (Ghosh et al., 2020). The expression of the SARS-CoV-2 ORF3a is sufficient to promote lysosomal exocytosis. The lysosomal exocytosis requires the classical SNARE complex syntaxin 4, SNAP23 and VAMP7. ORF3a interacts with VAMP7 through VPS39. Interestingly, the ORF3a from SARS-CoV has only two mutations compaired otoits SARS-CoV-2 homolog but does not promote lysosomal exocytosis (Chen et al., 2021).

This chapter highlights the physiological context of lysosomal exocytosis and its importance in pathological contexts. I demonstrated that exocytosis is regulated by different factors: cytoskeleton, lipids, Ca^{2+} and diverse proteins. However an important regulator of exocytosis is presented in the next chapter: membrane tension. My PhD work demonstrates that the organization of lysosomal exocytosis relies on the organization of membrane tension (**see results**).

Chapter 3

Membrane tension

"La science explique du visible compliqué par de l'invisible simple."

Reported quote from Jean Perrin in "Questions aux savants", Pierre-Henri Simon, 1969.

Chapter's summary:

Membrane tension is a key parameter of biological membranes, regulating many biological processes including exocytosis. Membrane tension is a physical quantity introduced in the context of the elastic membrane theory. In this theory, the membrane is described thanks to the so-called Canham-Helfrich Hamiltonian taking in consideration the energy due to membrane curvature. But additional factors can contribute such as the membrane tension. Membrane tension is classically measured by pulling membrane tethers but a mechanosensitive FLIM probe has been recently commercialized, the Flipper-TR. This probe allows a local measure of membrane tension in various conditions. This new tool will likely contribute to important debates about membrane tension such as its capacity to equalize. Indeed, if membranes were pure fluid lipid bilayers, then the tension is expected to equalize after a local perturbation resulting from membrane flow. The question remains controversial for many years but recent evidence using two-tethers experiments seems to demonstrate that membrane tension propagates extremely slowly and it should not be assumed that membrane tension is homogenous over the cell. Moreover, a high membrane tension leads to membrane rupture and homeostatic mechanisms regulate membrane tension: membrane reservoirs and folds, endocytosis/exocytosis balance, ionic channels regulating osmolarity and mTORC2 pathways. In turn, membrane tension regulates many cellular processes: endocytosis, mechanosensitive channels, cell migration, mitochondria fission, formation of ILVs, etc. Evidences also exist that membrane tension regulates exocytosis. While it is clear that membrane tension regulates the opening of fusion pores, its role in the other steps of exocytosis is less consensual. I review in this chapter recent evidences supporting the role of membrane tension in exocytosis.

1. Elastic membrane theory

1.1. Elasticity and curvature of biological membranes

Membrane tension represents the energetic cost of increasing the membrane area. It regulates many biological processes (cell migration, channel transport, endocytosis, etc.) including exocytosis. Membrane tension is a physical quantity introduced in the context of the elastic membrane theory presented in this chapter. The literature on membrane tension relies on different measurement methods reviewed in this chapter. I use a recent innovative FLIM probe to measure membrane tension in my PhD work (**see results**) that presents advantages compared to previous methods and allows a measurement of the spatial organization of membrane tension (**see the corresponding section in chapter 3**). The role of membrane tension in biological contexts is then reviewed with an emphasis on exocytosis.

Biological membranes exhibit a large diversity of shapes: from curved clathrin-coated pits to ER tubules. Knowing the physical parameters of the membrane, which shapes are possible and what would be the energetic cost/constraints associated? The lipid amphiphilic properties and their geometries are sufficient to spontaneously create different membrane shapes. This idea has been exploited in the seminal article of Israelachvili (Israelachvili et al., 1976). It can be assumed that amphiphilic lipids have a hydrophilic head with a surface area a, and a hydrophobic tail of length l and that the total volume of the molecule is v. Which geometries are possible for an aggregate of N molecules? If the aggregate is a sphere with a radius R, then $4\pi R^2 = Na$ and necessary $\frac{4}{3}\pi R^3 = Nv$. By making the ratio of the volume and the surface of the sphere, we obtain a relation for the radius of the sphere:

$$R = \frac{3v}{a}$$

We need to add a last condition on the lipid length l. To avoid the formation of a sphere with a hole in the middle, the condition $l \geq R$ is imposed, leading to the following relation:

$$P = \frac{v}{la} \leq \frac{1}{3} \quad \text{(Sphere)}$$

Thereby, when the dimensionless parameter P called packing parameter is inferior or equal to 1/3 the aggregate spontaneously self-organizes into a sphere (**Figure 41**). Now, we can repeat the same argument for a cylindrical geometry with a radius R and a length L. We have conditions for the surface ($2\pi RL = Na$) and for the volume ($\pi R^2 L = Nv$) leading to:

$$R = \frac{2v}{a}$$

Here again, to avoid a hole inside the cylinder, the condition $l \geq R$ is imposed. Therefore the packing parameter P needs to be inferior or equal to 1/2. We already know that a packing parameter inferior to 1/3 leads to a spherical geometry. Therefore:

$$\frac{1}{3} \leq P \leq \frac{1}{2} \quad \text{(Cylinder)}$$

Lastly, we can apply this argument to planar geometry with a thickness R and a side length L. We have conditions for the surface ($2L^2 = Na$) and the volume ($2RL^2 = Nv$) leading to:

$$R = \frac{v}{a}$$

By adding the condition $l \geq R$, we obtain:

$$\frac{1}{2} \leq P \leq 1 \quad \text{(Planar)}$$

Packing parameter superior to 1 leads to an inverted micellar structures. We can conclude from this simple model that the lipid geometry already controls a part of the membrane geometry.

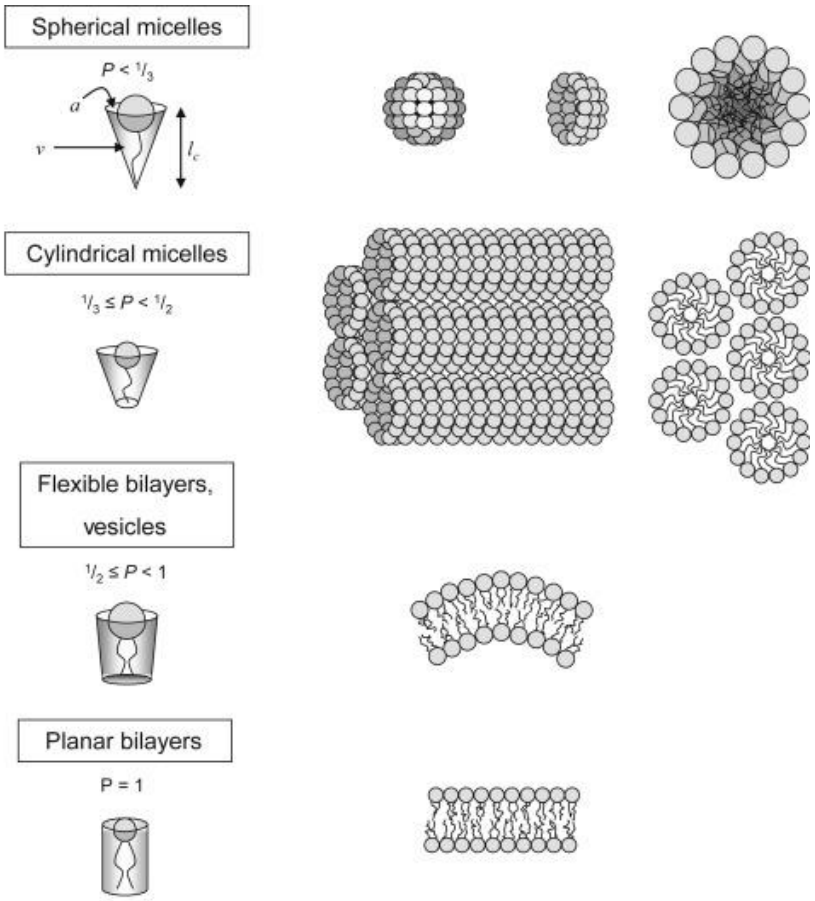

Figure 41. Packing parameter controls membrane organization, from Balazs and Godbey 2011.

The packing parameter is defined by the ratio between the surface occupied by the lipid head and the volume of the lipid tail. Most of the volume comes from the tail. Therefore a low packing parameter corresponds to a big head with a little tail, a shape usually described as an "ice-cone" known to create positive curvatures in membranes (Brown, 2012) (**Figure 42**). More sophisticated models lead to similar conclusions (Cooke and Deserno, 2006).

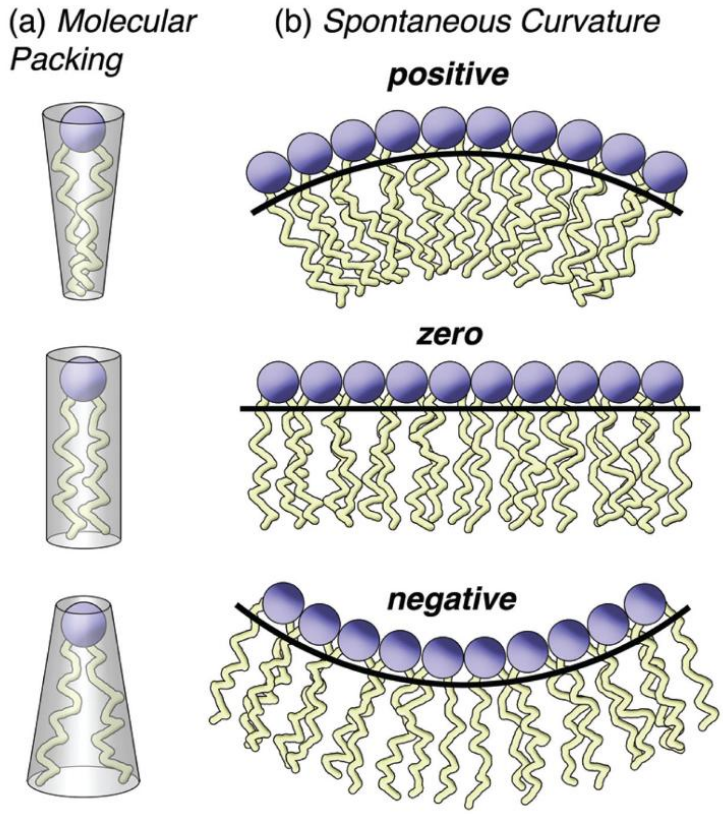

Figure 42. Packing parameter controls the membrane spontaneous curvature, from Brown (2012).

In addition to the membrane shape induced by lipid geometries, membranes can be deformed by physical constraints. Membranes can undergo 4 types of deformation (**Figure 43**):

- Thickness change: the thickness of the membrane changes.

- Stretching: the surface of the membrane increases (or decreases) by isotropic stretching.

- Shearing: a square patch of membrane is deformed into a parallelogram of equal area.

- Bending: the curvature of the membrane changes.

The energy associated to these deformations is derived from Hooke's law i.e. the membrane is seen as an array of springs modeling the interactions between lipids. Considering a patch of membrane with an optimal thickness w_0. This optimal value corresponds to the resting value when the membrane has no constraint. For example, $w_0 = 4 - 6$ nm for typical cellular membranes. External forces can change the thickness of the membrane creating a deformation $\Delta w = w - w_0$ with w the final thickness. The potential energy dE_w associated to this thickness modification in a small surface dA is given by the potential energy for a Hookian object:

$$dE_w = \frac{1}{2} K_w \left(\frac{\Delta w}{w_0}\right)^2 dA$$

with K_w the thickness modulus, in cellulo $K_w = 60k_BT$ nm^{-2} (Phillips et al., 2012). The total potential energy is obtained by integrating over the whole surface A of the membrane:

$$E_w = \frac{K_w}{2} \oiint \left(\frac{\Delta w}{w_0}\right)^2 dA$$

The energy associated to stretching can be derived similarly. Considering a small patch of membrane with a resting optimal surface dA_0 stretched until a final surface $d\mathrm{A}$, with $\Delta\mathrm{A} = d\mathrm{A} - \mathrm{dA}_0$. The potential energy for (isotropic) stretching E_s associated to the small surface dA_0 is given by the potential energy for a Hookian object:

$$dE_s = \frac{1}{2} K_s \left(\frac{\Delta A}{A_0}\right)^2 dA_0$$

With K_s the stretching modulus, in cellulo $K_s = 55 - 70k_BT$ nm^{-2} (Phillips et al., 2012). The total potential energy is obtained by integrating over the whole surface A_0 before stretching:

$$E_s = \frac{K_s}{2} \oiint \left(\frac{\Delta A}{A_0}\right)^2 dA_0$$

If areal strain is uniform:

$$E_s = \frac{1}{2} K_s \frac{\Delta A^2}{A_0}$$

Noteworthy, the biological membranes only support small variations of surface (~3-5%) before lysis, so called the rupture strain (Evans et al., 1976; Nichol and Hutter, 1996; Deserno, 2006; Sens and Plastino, 2015).

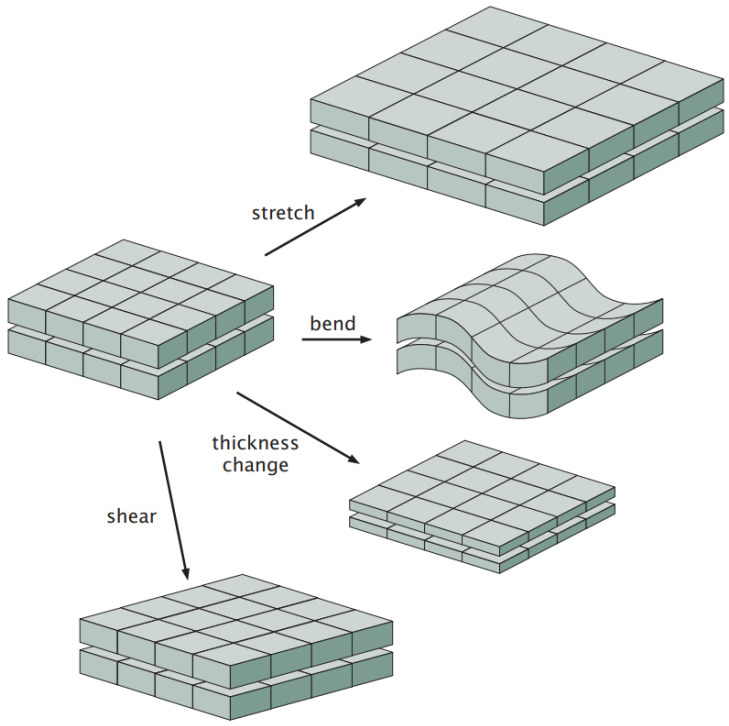

Figure 43. Deformations of the membrane, from Physical Biology of the Cell (2nd Edition). Membranes can undergo 4 types of deformation: stretching, bending, thickness change and shearing.

Shear stress displaces lipids relatively to each other keeping the area per lipid constant. For a Newtonian fluid (such as water or a pure lipid bilayer), there is no "resistance": lipid molecules flow. Due to the flow, the strain becomes infinity large, and therefore, the shear modulus would be infinite and cannot be defined (Deserno, 2006). However, the underlying cytoskeleton (e.g. spectrin network of red-blood cell) can retain the lipids and provide a shear modulus μ. For a parallelogram with a shear angle θ and a surface dA, the energy associated to shear stress is:

$$dE_{shear} = \frac{1}{2}\mu\theta^2 dA.$$

Finally, the bending energy has been introduced in 1970 by Peter Canham (Canham, 1970):

$$E_b = \oiint \frac{1}{2}\kappa_b(c_1^2 + c_2^2)dA$$

With c_1 and c_2 the principal curvatures of the membrane surface and κ_b the bending modulus of the membrane, in cellulo $\kappa_b = 10 - 20k_BT$ (Phillips et al., 2012). This equation is known as the Canham Hamiltonian. Hamiltonian refers to the total energy of the system i.e. the bending energy of a membrane representing its total energy. Of course, if the membrane is also stretched or has modifications in thickness, we should add these contributions to the Hamiltonian. In 1973, Wolfgang Helfrich proposed two modifications of this formula (Helfrich, 1973): i) the asymmetric composition of the bilayer can create a spontaneous curvature c_0 due to cone-shaped lipids, that should not be taken in consideration for the quantification of the energy, ii) an additional sensitivity for the Gaussian curvature $K_G = c_1c_2$. Therefore:

$$E_b = \oiint \frac{1}{2}\kappa_b(c_1 + c_2 - c_0)^2 + \kappa_G K_G dA$$

Where κ_G is the saddle splay modulus, in cellulo $\kappa_G \approx -\frac{\kappa_b}{2}$. The new term of Gaussian curvature can be easily calculated thanks to the Gauss-Bonnet theorem: for a surface without boundaries:

$$\oiint K_G dA = 4\pi(1 - g)$$

With g the genus of the surface, it represents how many holes it contains. Therefore, the Helfrich Hamiltonian can be re-written as:

$$E_b = \oiint \frac{1}{2}\kappa_b(c_1 + c_2 - c_0)^2 dA + \kappa_G 4\pi(1 - g)$$

As classic potential energies, membrane Hamiltonian is defined up to a constant. Therefore, in absence of spontaneous curvature and genus modification, Canham and Helfrich Hamiltonians are equivalent. We refer to them as Canham-Helfrich Hamiltonian. This Hamltonian can be used for example to compute the energy associated to a spherical vesicle of a radius R without spontaneous curvature. Because the two principal curvatures are constant and equal:

$$E_b = \frac{2\kappa_b}{R^2} \oiint dA + \kappa_G 4\pi$$

$$E_b = 4\pi(2\kappa_b + \kappa_G)$$

Surprisingly, the energy of a spherical vesicle does not depend on its radius.

1.2. Theoritical description of membrane tension

Membrane tension is a key mesoscopic parameter of biological membranes that represent the energetic cost of increasing the membrane area (in $J.m^{-2}$=$N.m^{-1}$ units). The stretching energy was already defined in the precedent section. However this stretching energy can be viewed as the reversible work required to stretch (or compress) the membrane from its optimal area A_0 to A_1 (and therefore $\Delta A = A_1 - A_0$) (Lipowsky, 2022):

$$E_s = \int_{A_0}^{A_1} \sigma(A)\, dA = \frac{1}{2} K_s \frac{\Delta A^2}{A_0}$$

With σ the membrane tension defined as:

$$\sigma = \frac{dE_s}{dA} = K_s \frac{\Delta A}{A_0}$$

Therefore, this quantity is directly related to the stretching energy:

$$E_s = \frac{1}{2}\sigma \Delta A$$

The more stretched the membrane is, the higher is its tension. Since the membrane can only undergo small variations before its lysis (∼3-5%), the lysis tension is around $\sim 10^4$ $pN.\mu m^{-1}$ (Deserno, 2006). Contrarily to the stress modulus, the membrane tension is not a constant and "reflects [membrane] intrinsic isotropic tangential stress" (Deserno, 2015). Thickness modifications and shear stresses are unusual constraints. Therefore the membrane Hamiltonian is often written as the sum of stretching and bending energies:

$$H' = \oiint \frac{1}{2}\kappa_b (c_1 + c_2 - c_0)^2 dA + \kappa_G 4\pi(1-g) + \oiint \frac{1}{2} K_s \left(\frac{\Delta A}{A_0}\right)^2 dA$$

The minimization of this quantity gives the geometry of the membranes. Lipowsky (Lipowsky, 2014, 2022) demonstrated that the following alternative Hamiltonian describes the same physics:

$$H = \oiint \frac{1}{2}\kappa_b (c_1 + c_2 - c_0)^2 dA + \kappa_G 4\pi(1-g) + \sigma \Delta A$$

where the elastic stretching energy has been replaced by a tension term. This Hamiltonian has several advantages: it is linear for the tension and the tension plays the role of a Lagrange multiplier (i.e. it satisfied certain constraints). This result can be interpreted in the context of linear response theory following Farago (Farago, 2011):

$$\delta E_s \approx \sigma \delta A$$

Therefore the membrane tension term can be interpreted as a linear approximation. Conserving the quadratic elastic term is possible but complicates the mathematical derivations (Farago and Pincus, 2003).

The membrane tension measures the difficulty to stretch the membrane from the current state of the membrane. The more stretched the membrane is, the harder it is to continue to stretch it

because the membrane tension increases. As explained by Sitarska and Diz-Muñoz, the membrane tension term "is a measure of the energetic cost of increasing the membrane area" keeping constant the number of lipids (Sitarska and Diz-Muñoz, 2020). Typical values range between 10 and 100 pN.µm^{-1} (**Table 4**).

Cell type	Membrane tension (pN.µm^{-1})
Neuron	2-40
Melanoma	40
Macrophage	40-200
Fibroblast	10-40
Sperm cell	50
Adenocarcinoma	40
Cardiomyocyte	50
Endothelial cell	35
Keratocyte	60-120
Bleb	10

Table 4. Typical values of membrane tension in different cell types from Pontes et al. (2017). The tether force is converted in membrane tension using $\kappa_b = 75 k_B T$.

1.3. Experimental techniques to measure membrane tension

The most common way to measure membrane tension is through the formation of a membrane tether, i.e. a long tube of membrane. A tether can be formed thanks to a dielectric coated bead. The bead coating, with antibodies for example, allows to bind it to the membrane. Then, the bead is trapped by optical tweezers. One can pull on the membrane by a displacement of the microscopic stage. The optical trap applies a spring force on the bead, the tether force f. This force creates the tether (**Figure 44**). The membrane tension is related to the tether force (**see box 3** for the derivation, following (Derényi et al., 2002; Brochard-Wyart et al., 2006)):

$$\sigma = \frac{f^2}{8\pi^2 \kappa_b}$$

For *in vitro* systems such as Giant Unilamellar Vesicles (GUVs), the measured tension could be a correct measurement of membrane tension. However, *in cellulo* the presence of the cortical cytoskeleton adds a level of complexity. Because of membrane-cytoskeleton interactions, the apparent membrane tension T (the one that is measured through the tether assay) is the sum of the in-plane membrane tension σ and the membrane–cytoskeleton adhesion energy per unit area and the cortical cytoskeleton tension γ (Keren, 2011). Therefore:

$$T = \sigma + \gamma$$

Especially, actin polymerizes inside tethers within minutes, challenging long-term measurements (Sitarska and Diz-Muñoz, 2020). Thereby, the equation should be corrected by:

$$T = \frac{f^2}{8\pi^2 \kappa_b}$$

Box 3: Measure of membrane tension by a membrane tether

What is the Hamiltonian associated to the tether? First, we can approximate the tether by a cylinder of radius r and with a length L. Since the topology is constant (i.e. not genus modification) we can drop out the Gaussian curvature term. The Hamiltonian takes in consideration the work given by the optical tweezers to create the tether. The displacement of the microscopic stage relatively to the bead creates a force f. For a tether of length L, the work is $-fL$, counted negatively because it is the exergonic part of the process driving tether formation. Therefore:

$$H_{tether} = \frac{\pi \kappa_b L}{r} + 2\pi r L\sigma - fL$$

The energy tends to be minimal. By minimizing the energy according to r:

$$\frac{\partial H_{tether}}{\partial r} = -\frac{\pi \kappa_b L}{r^2} + 2\pi L\sigma$$

$$\frac{\partial H_{tether}}{\partial r} = 0 \quad \Longrightarrow \quad r = \sqrt{\frac{\kappa_b}{2\sigma}}$$

By minimizing the energy according to L:

$$\frac{\partial H_{tether}}{\partial L} = \frac{\pi \kappa_b}{r} + 2\pi r\sigma - f$$

$$\frac{\partial H_{tether}}{\partial L} = 0 \quad \Longrightarrow \quad f = \pi\kappa_b\sqrt{\frac{2\sigma}{\kappa_b}} + 2\pi\sigma\sqrt{\frac{\kappa_b}{2\sigma}} \quad \Longrightarrow \quad f = 2\pi\sqrt{2\kappa_b\sigma}$$

Combining the expression of f and r, we obtain the unknown parameters κ_b and σ:

$$r = \sqrt{\frac{\kappa_b}{2\sigma}} \quad \Rightarrow \quad \sigma = \frac{\kappa_b}{2r^2}$$

$$f = 2\pi\frac{\kappa_b}{r} \quad \Rightarrow \quad \kappa_b = \frac{fr}{2\pi}$$

$$\Rightarrow \quad \sigma = \frac{f}{4\pi r}$$

Therefore, both membrane tension and the bending modulus can be measured with membrane tether. However, the measurement of tether radius is difficult because it is often below the resolution limit. Most studies assume a standard value of the membrane bending modulus $\kappa_b = 75k_BT$ and compute the membrane tension as follow (Pontes et al., 2017):

$$\sigma = \frac{f^2}{8\pi^2\kappa_b}$$

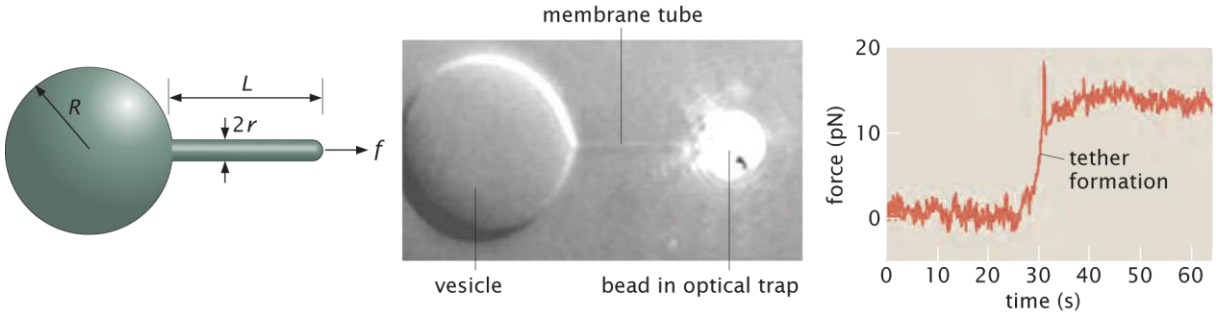

Figure 44. Measurment of the membrane tension through tether pulling, from Physical Biology of the Cell. On the left, a schematic representation of the experiment. A force f pulls a tether of length L and with a radius r from a cell/vesicle of radius R. In the middle, a micrograph of the experiment showing a vesicle and the coated bead in the optical trap pulling the tether. On the right, the time trace of a tether experiment. The optical trap force f increases suddenly corresponding to the tether formation, then the force stays fairly constant.

Membrane tension can be measured by other means. For example, a coated Atomic Force Microscopy (AFM) cantilever tip can be used to generate a tether. The measure is, in principle, identical to the tether generated by optical tweezers. Another possibility is to use micropipette aspiration (Pontes et al., 2017a). This method is helpful for spherical non-adherent cells. The idea is to bring a micropipette (radius ~ 10µm) close to the cell and to slightly aspirate it. The major part of the cell is outsite of the micropipette with a radius R_v and a minor part of the cell is aspirated inside the micropipette forming a cylinder caped with a hemi-sphere of radius R_1. Applying the Laplace-Young law, the tension is given by:

$$\sigma = 2\,\Delta P \left(\frac{1}{R_v} + \frac{1}{R_1}\right)$$

All these methods measure membrane tension at one localization and do not evaluate its putative heterogeneity. An alternative method is to measure membrane fluctuations by interferometry. Membrane tension can be inferred from fluctuations: the higher the tension is, the less important fluctuations become. This method has the advantage to be non-perturbative and to measure tension locally. However, fluctuations are also influenced by cortical cytoskeleton tension and this method requires calibration (Sens and Plastino, 2015; Biswas et al., 2019). As an alternative, Colom et al. have developed a fluorescent probe to measure the in-plane membrane tension locally. This probe is a mechanophore of the "flipper" family (Fin et al., 2012; Dal Molin et al., 2015; Soleimanpour et al., 2016; Colom et al., 2018). The Flipper-TR (also referred to as FliptR Fluorescent LIPid Tension Reporter) probe is a molecule made of two groups of aromatic rings separated by a mechanosenstive bond (**Figure 45**). Aromatic groups can turn around this bond. The probe has two possible states: either the two aromatic groups are orthogonal or parallel. Moreover, one of the groups is electron rich whereas the other is electron poor. The first group "pushes" electrons toward the other group that "pulls" on them. In the case that the groups are orthogonal, electrons are not “pushed” from one group to the other. The consequence is that each group has an individual independent electron conjugation. When the two-groups are parallel, they are electronically conjugated. This molecular system is called “push-pull”. This modification of the mesomeric state changes its optical properties, especially its fluorescence lifetime towards longer lifetimes in the case of a conjugated system (i.e. planar configuration). Flipper-TR is spontaneously incorporated into the PM. Under high membrane

tension, the molecules of the PM favor the planar configuration (longer fluorescence lifetime), whereas under low tension the probe is free to be in an orthogonal state (short fluorescence lifetime). Therefore, this planarizable probe can report local membrane tension through its fluorescence lifetime that can be measured by FLIM (Fluroescence-Lifetime Imaging Microscopy).

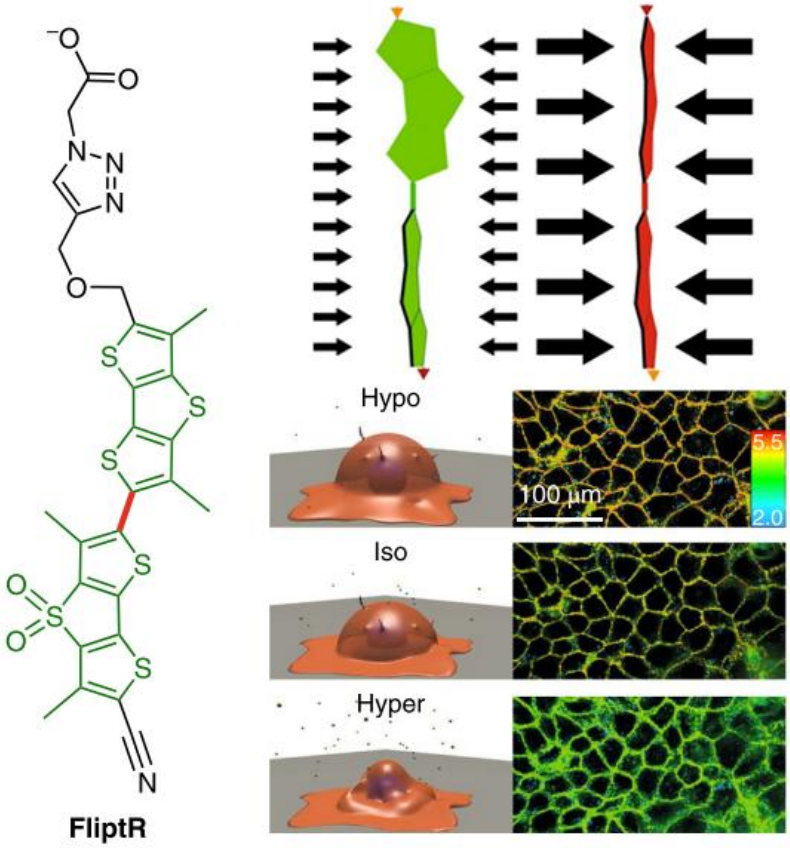

Figure 45. Principle of the Flipper-TR probe, from Colom et al. (2018). On the left, the Flipper-TR molecule with in green the two aromatic groups: the group on the top pushes electrons whereas the group on the bottom pulls electrons. In red the mechanosensitive bond. The top right panel shows how physical constrains such as membrane tension changes the conformation of the probe. A high membrane tension switches the probe from an orthogonal configuration to a planar one. On the bottom right panel, experimental measurements of the fluorescence lifetime (in ns) of the probe in different osmotic conditions. During hyper-osmotic shock, the membrane tension decreases and the fluorescence lifetime of the probe also decreases, whereas hypo-osmotic shock has opposite effects.

A second drawback of classical tether experiments it that the measurement of intracellular membrane tensions is very limited. By modifying the head-group of Flipper-TR, Goujon et al. developed flipper probes targeting mitochondria, ER and lysosomes (respectively referred to as mito-Flipper, ER-Flipper and Lyso-Flipper) (Goujon et al., 2019). More recently, a EE Flipper has been added at the Flipper family (Piazzolla et al., 2021). A HaloTagging strategy has been also developed to easily target Flipper-TR in the membranes of interest. In this HaloTag system, the head of the Flipper-TR has been replaced by a chloroalkane ligand forming the so-called HaloFlipper. In parallel, cells need to be transfected with a construct coding for a recombinant HaloTag protein fused with a resident protein marking the target compartment. The chloroalkane ligand spontaneously interacts with the active site of the HaloTag protein creating a covalent ester bond between Halo-Flipper and the recombinant protein (Straková et al., 2020). The latest advance in the Flipper story is the development of a Flipper probe that is able to probe at the same time membrane tension and membrane hydration, so-called HydroFlipper. The nitril group of Flipper is replaced by trifluoroketone group in HydroFlipper than can be hydrated. This hydratation changes optical properties of the probe, especially its fluorescence lifetime. Based on a tri-exponential fit of FLIM data, authors proposed a different index to quantify the tension and the hydration state of membranes (García-Calvo et al., 2022).

Other less successful attempts to develop fluorescent membrane tension probes have been made. Danylchuk et al. developed solvatochromic probes that are organelle specific (Danylchuk et al., 2021). These push-pull fluorophores change their emission spectrum in response to membrane hydration. This group of probes has the advantage to not require FLIM microscopy, but some experiments indicate that it is not at all specific for the membrane tension questioning its use. A second interesting approach is based on genetically encoded FRET membrane tension sensors (Li et al., 2018b). One fluorophore of the FRET pair is anchored to lipid raft domains through a Lyn kinase, while the other one is anchored in non-lipid raft regions through a K-Ras kinase. The two fluorophores are linked by an elastic linker derived from the spiker silk protein flagelliform. This linker plays the role of a microscopic spring. Under high membrane tension, the two fluorophores are distant reducing the FRET efficiency. Contradictory results have been reported between this FRET probe and Flipper-TR (Coomer et al., 2020). More work is required to carefully evaluate this probe.

1.4. Do membranes resist flow?

If membranes were pure fluid lipid bilayers (i.e. without transmembrane proteins), the tension would be expected to equalize after a local perturbation as a result of membrane flow. However, biological membranes are far from pure fluid lipid bilayers and contain plenty of transmembrane proteins connected to cortical cytoskeleton forming obstacles. The areal fraction ϕ of immobile obstacles is between 10 and 20% (Bussell et al., 1995; Shi et al., 2018). Both, theoretical and experimental studies, disagree on the capacity of membrane tension to be homogeneous and to equalize. Reviewing 24 studies, Cohen and Shi reported a factor 10^6 in the time scale of membrane propagation across studies (Cohen and Shi, 2020). Using a two-tether experiment, Shi et al. provide precious insights to the problem of membrane tension propagation (Shi et al., 2018). They demonstrated that membrane tension can vary substantially between two tethers separated by 5 to 15µm. This is the most direct evidence that membrane tension does not quickly propagate (**Figure 46**). However, the tension between two tethers generated from a bleb, lacking cortical cytoskeleton, quickly propagates and equilibrates. This result confirms the role of immobile transmembrane protein as obstacles to lipid flow.

Shi et al. developed a hydrodynamics model to explain these results (**See box 4**). They conclude that the membrane tension diffuses with a diffusion coefficient:

$$D_\sigma = \frac{kK_s}{\eta}$$

with k the Darcy permeability, a function of the areal fraction ϕ of immobile obstacles estimated by Fluorescence Recovery After Photobleaching (FRAP) ($k = 2 \times 10^{-6}$ µm^2), η the membrane viscosity ($\eta = 3 \times 10^{-3}$ pN.s.µm^{-1}) and K_s the stretching modulus ($K_s = 0.01 k_B T$ nm^{-2}) leading to a diffusion coefficient of $D_\sigma = 0.024$ µm^{-2}.s^{-1}. With such a low diffusion coefficient, the membrane tension requires tens of minutes to equilibrate over the cell scale. These results are coherent with experimental data; however, the stretching modulus used is much lower than typical values from the literature. With a standard stretching modulus of $K_s = 60 k_B T$ nm^{-2}, the diffusion coefficient becomes as high as $D_\sigma = 80$ µm^{-2}.s^{-1} leading to an opposite conclusion: lipids flow and rapidly equilibrate membrane tension. Values of $K_s = 60 k_B T$ nm^{-2} are obtained for purified lipid bilayers,

whereas micropipette aspiration of neutrophiles gives significant lower values about $K_s = 0.01 k_B T$ nm^{-2} (Needham and Hochmuth, 1992; Hochmuth, 2000). Cohen and Shi argue than if the stretching modulus was as high as for pure lipid bilayers, membranes would be almost inextensible for cellular forces. Moreover, based on experimental complex kinetics, authors argue that the stretching modulus is possibly not well defined in cellular contexts (Cohen and Shi, 2020).

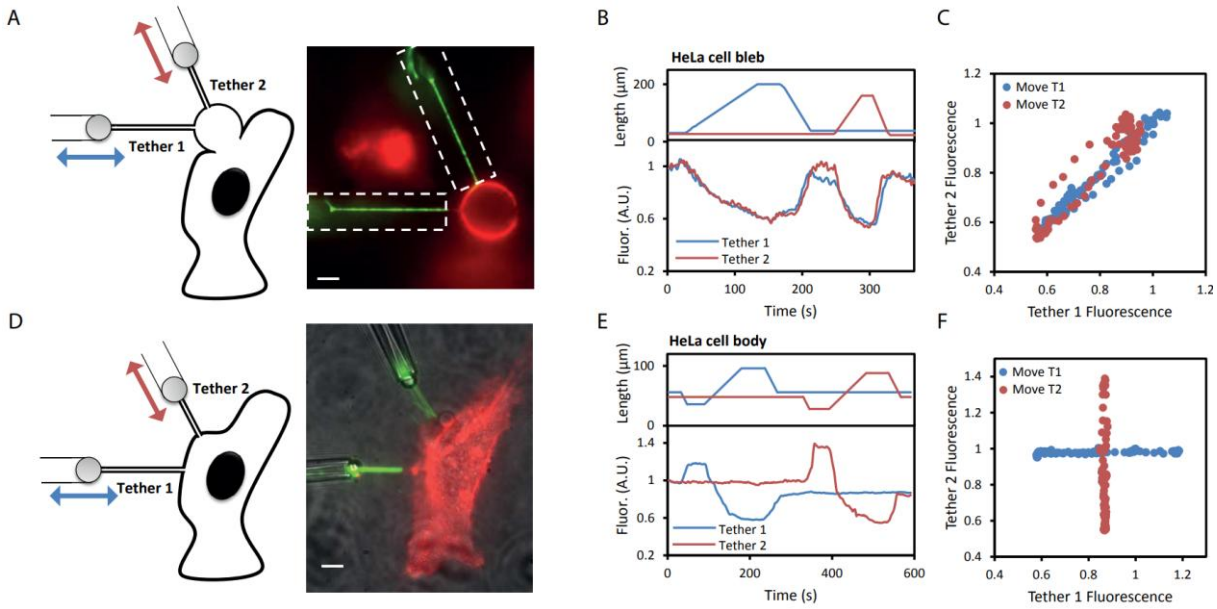

Figure 46. Two-tether experiment, from Shi et al. (2018). A) Schematic representation of the experiment and micrograph of the experiment with the bleb in red and the tether in green. B) Time trace of the experiment. The tether length and the fluorescence intensity are depicted. The fluorescence intensity is a proxy for the tether radius, inversely proportional to the tether force. C) Plot of the correlation between the fluorescence intensity of the two tethers showing a quick equalization in membrane tension. D-E) Same experiment on HeLa cell. Tether forces are independent showing that when the membrane is coupled to cortical cytoskeleton, the membrane tension does not equalized.

The heterogeneity in the time scale of tension propagation between cell lines could be due to differences in the Darcy permeability (Shi et al., 2018). Especially, the coupling with cortical cytoskeleton seems to be an important factor to create immobile obstacles, and could substantially vary between cell lines (Sitarska and Diz-Muñoz, 2020). Moreover, the heterogeneity of membrane tension was measured with Flipper-TR probe and clearly supports the hypothesis of low membrane tension propagation (Colom et al., 2018). Heterogeneity in membrane tension can be created in different ways. For example a front-to-rear gradient of membrane tension has been already observed in moving keratinocytes (Lieber et al., 2015), and is explained by friction between PM and actin tread milling as well as between PM and the substrate (Schweitzer et al., 2014). A reciprocal feedback between actin retrograde flow and membrane tension also probably exists through a balance of force mechanism (Sens and Plastino, 2015).

Box 4: Model of membrane flow and membrane tension propagation

Shi et al. used a Navier-Stokes equation to model lipid flow:

$$\rho\left(\frac{\partial\vec{v}}{\partial t}+\vec{v}\vec{\nabla}\vec{v}\right)=-\vec{\nabla}\sigma-\eta\vec{\nabla}^2\vec{v}+\vec{F}$$

With η the membrane viscosity, ρ the 2D lipid density and $\vec{v}$ the velocity field of lipid flow. The $\eta\vec{\nabla}^2\vec{v}$ term has a negative sign because membrane flows from low to high tension contrarily to liquid that flows from high to low pressure. The material derivative is null (i.e. velocities are small enough, the system is in a viscous-dominated regime and the inertial terms are neglected $\rho\left(\frac{\partial\vec{v}}{\partial t}+\vec{v}\vec{\nabla}\vec{v}\right)=0$) and in absence of external forces ($\vec{F}=0$), Navier-Stokes equation is simplified in:

$$\vec{\nabla}\sigma=-\eta\vec{\nabla}^2\vec{v}$$

However, to take in consideration immobile obstacles, this equation can be augmented with a drag term (Brinkman, 1949; Bussell et al., 1995):

$$\vec{\nabla}\sigma=-\eta\vec{\nabla}^2\vec{v}+\frac{\eta}{k}\vec{v}$$

With $\frac{\eta}{k}$ playing the role of a drag coefficient and k the Darcy permeability. The Darcy permeability is a function of areal fraction ϕ of immobile obstacles. A conservation of mass equation can be set for this system:

$$\frac{\partial\rho}{\partial t}+\vec{\nabla}(\rho\vec{v})=0$$

Lipid density can be written as the sum of a constant term plus a small perturbation $\rho=\rho_0+\delta\rho$. Neglecting variation of lipid density ($\delta\rho\ll\rho_0$):

$$\frac{\partial\rho}{\partial t}=-\rho_0\vec{\nabla}(\vec{v})$$

Membrane tension variation is given by:

$$\delta\sigma=K_s\frac{A-A_0}{A_0}$$

This equation can be rewritten in term of lipid density since $\rho=\frac{N_{lipid}}{A}$:

$$\delta\sigma=-K_s\frac{\delta\rho}{\rho}$$

Noteworthy, that I use a derivation different from authors and I obtained an equation for membrane tension variation that is slightly different. Considering that $\frac{\rho_0}{\rho} \approx 1$ and combining these equations:

$$\frac{\partial \sigma}{\partial \rho} = \frac{\partial \sigma}{\partial t}\frac{\partial t}{\partial \rho} = -\frac{K_s}{\rho} \quad \Rightarrow \quad \frac{\partial \sigma}{\partial t} = K_s \vec{\nabla}(\vec{v})$$

$$\vec{\nabla}\sigma = -\eta \vec{\nabla}^2 \vec{v} + \frac{\eta}{k}\vec{v} \quad \Rightarrow \quad \frac{K_s}{\eta}\vec{\nabla}^2\sigma = \left(\frac{1}{k} - \vec{\nabla}^2\right)\frac{\partial \sigma}{\partial t}$$

If the Darcy permeability is high, there is no drag and the equation is simply:

$$\vec{\nabla}^2 \frac{\partial \sigma}{\partial t} = -\frac{K_s}{\eta}\vec{\nabla}^2\sigma$$

Therefore the relaxation time is $\tau = \frac{\eta}{K_s} \sim 0.1$ms. However, if the drag dominates the equation can be simplified in a diffusion equation:

$$\frac{\partial \sigma}{\partial t} = \frac{kK_s}{\eta}\vec{\nabla}^2\sigma$$

Giving a membrane tension diffusion coefficient:

$$D_\sigma = \frac{kK_s}{\eta}$$

2. Biological applications

2.1. Membrane tension homeostasis

Membrane tension is directly related to the extension of a membrane. PM extensions/compressions occurs in plenty of biological situations: osmotic stress, migrating cells, formation of protrusions, mitosis, etc. It requires homeostatic processes to regulate the membrane tension and to avoid membrane rupture. The main regulatory mechanism is probably the existence of membrane reservoirs buffering elastic extension. They have been originally identified by Michael Sheetz's team, who noticed that the elongation of a membrane tether initially keeps tether force constant. The tether force relates to the membrane tension ($f \propto \sqrt{\sigma}$), therefore, a constant tether force indicates no stretching. They proposed that lipids are furnished by a membrane reservoir to buffer membrane tension (Raucher and Sheetz, 1999a). Caveolae have been identified to be one of these membrane reservoirs. Hypo-osmotic shock triggers the unfolding of caveolae and KO of caveolin-1 prevents buffering of membrane tension (Sinha et al., 2011). Interestingly, it has been proposed that the flattening of caveolae could release cavin proteins that could trigger the transcription of a gene regulatory network (Nassoy and Lamaze, 2012). However, caveolae represent only about 0.3% of the PM surface (Sinha et al., 2011), therefore, this buffer system has an efficiency that is limited to small variations. It indicates the existence of other membrane reservoirs. For example, cell spreading correlates with an increase in membrane tension and the unfolding of blebs and inwards folds (Gauthier et al., 2011). Whereas an increase of membrane tension correlates with unfolding of membrane reservoirs, a decrease of membrane tension promotes the formation of folding structures, especially blebs and Vacuole-Like Dilations (VLDs). VLDs are inward folds (sometimes as large as 10µm), connected or not with either the PM or actin. VLDs are observed during hyper-osmotic shock or during the recovery after a hypo-osmotic shock in neurons or fibroblast (Morris and Homann, 2001; Apodaca, 2002; Gauthier et al., 2012; Kosmalska et al., 2015) (**Figure 47**). The formation of different membrane reservoirs seem to depend on the type of physical constraints. For example, osmotic stress induces formation of VLDs, whereas physical compression induces the formation of tubular invaginations (Kosmalska et al., 2015).

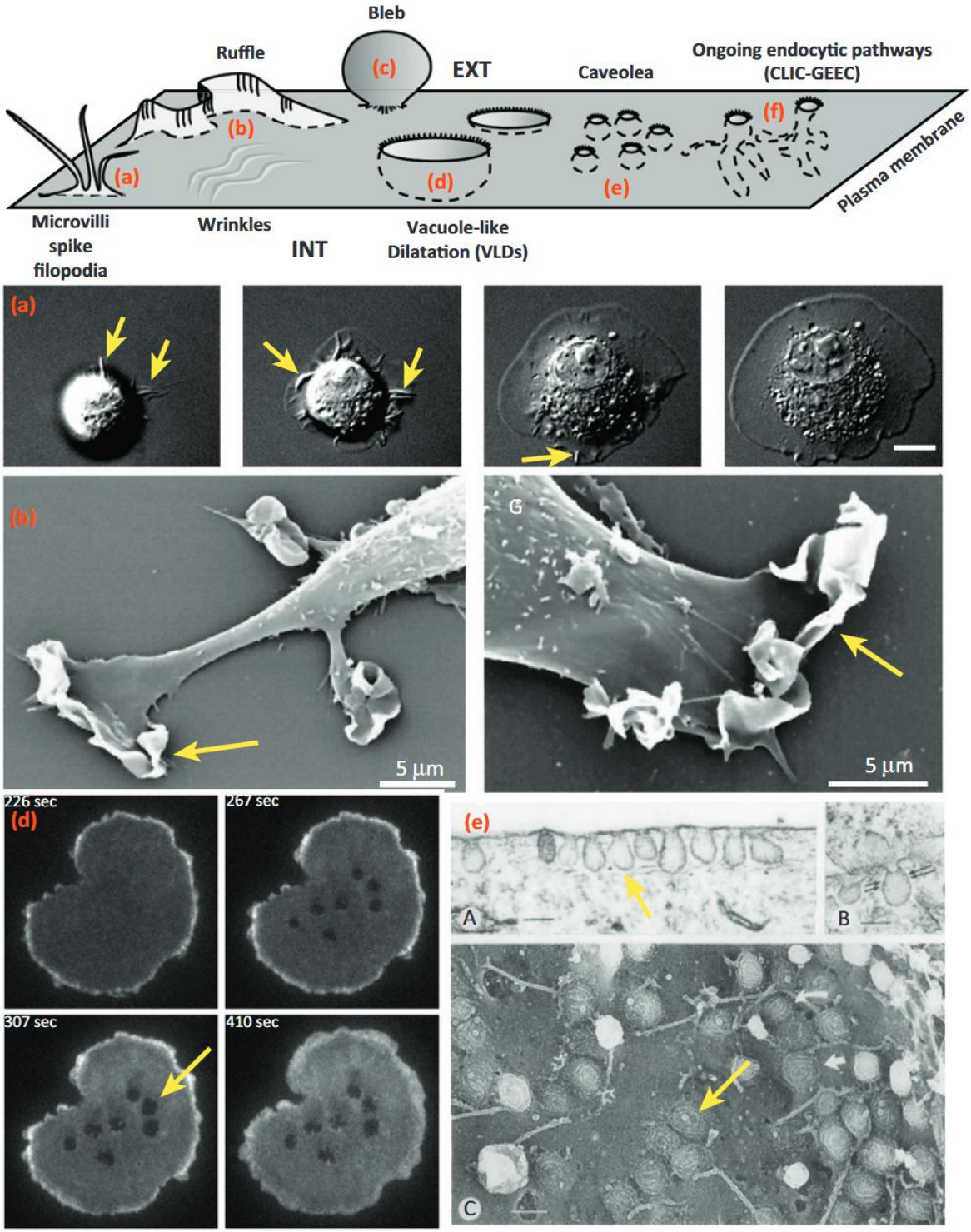

Figure 47. Membrane reservoirs, from Gauthier et al. (2012). Representation of the diversity of membrane reservoirs and the corresponding microscopic images. A. Microvilli and spikes during cell spreading. B. Membrane ruffles in fibroblast stimulated with growth factors. D. VLDs observed on the ventral membrane of a cell in isotonic condition after hypo-osmotic shock. E. Caveolae of a fibroblast cell.

Recently, Roffay et al. proposed an interesting statistical physical model of membrane folding/unfolding in response to membrane tension (Roffay et al., 2021). Considering a membrane with a surface A made of $N = A/a$ discrete small patches of size a. In the model, it is assumed than the folding is associated to the binding of proteins (such as caveolae associated protein) with a free energy G. The folding needs also to furnish work against the membrane tension. The potential energy associated to the unfolded state can be fixed arbitrary to 0. Therefore, the Boltzmann distribution gives the probability for a patch to be in a folded state:

$$P = \frac{e^{\frac{G-\sigma a}{k_B T}}}{1 + e^{\frac{G-\sigma a}{k_B T}}}$$

This model fits experimental data of cell volumes under osmotic shocks (Roffay et al., 2021). This model can be used to estimate the proportion of membrane patches in a folded state (**Figure 48**). Using parameters of the publication ($G = 1.5 k_B T$ and $a = 53\text{nm}^2$), we can predict that under classical membrane tension ($\sigma = 40\text{pN.µm}^{-1} \approx 0.01 k_B T\ \text{nm}^{-2}$) for a cell with a surface of $A = 1000\ \mu\text{m}^2$, the cell contains $n = NP \approx 13\,000\,000$ folded membrane patches. Noteworthy, these patches are not necessarily individual but they can be regrouped in larger structures such as VLDs.

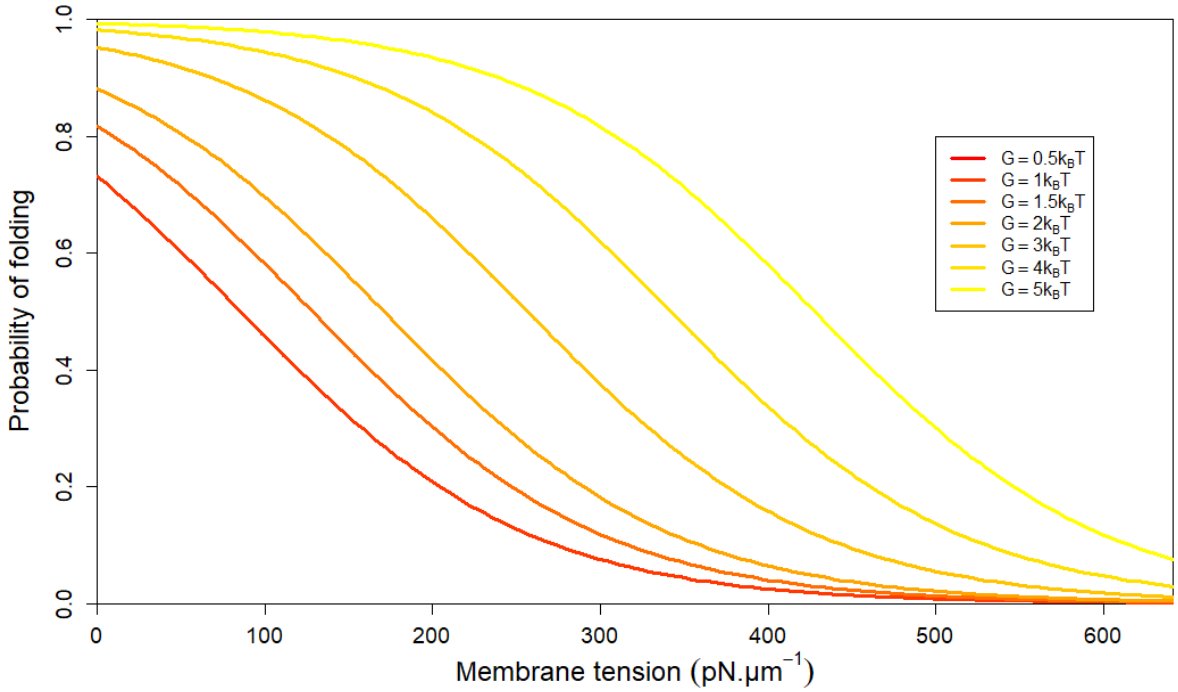

Figure 48. Computation of the folding probability of a membrane patch following the model of Roffay et al. (2021). Probability has been plotted for different coat protein binding energies G and with a patch size of $a = 53\text{nm}^2$ as in the publication. When membrane tension decreases the folding probability decreases. The increase of binding free energy switches the relation from a convex to a concave dependence. Noteworthly that this distribution corresponds actually to the Fermi-Dirac statistics.

Besides the regulation of membrane tension by unfolding of membrane reservoirs, membrane extension can be regulated by exocytosis and endocytosis. Already two decades ago, exocytosis was recognized as a regulator of membrane tension (Apodaca, 2002). For example, umbrella cells of the bladder have less intracellular vesicles when the bladder is full suggesting increase of exocytosis to gain surface area (Apodaca, 2002). In the context of cell spreading, the PM area increases by 40-60% and is accompanied by a massive exocytosis of vesicles enriched in glycosylphosphatidylinositol-anchored proteins in a MT independent manner (Gauthier et al., 2009). This massive exocytosis partially correlates with a decrease of membrane tension (Gauthier et al., 2011). However, there are some situations in which an increase of membrane tension inhibits exocytosis, this has been shown for mast cells degranulation or secretion of renin by juxtaglomerular cells (Apodaca, 2002). A defect in secretion has been also observed in HeLa and COS cells under hypotonic conditions, but it is due to an inhibition of the ER-Golgi anterograde transport and not due to an inhibition of exocytosis *per se* (Lee and Linstedt, 1999). Cell swelling also increases intracellular membrane tension, therefore COPI vesicle budding becomes mechanically more difficult. Conversely, endocytosis is thought to regulate membrane tension: by decreasing the number of PM lipids, it could increase membrane tension. A first study reported that an increase of membrane tension inhibits slow endocytosis (but not fast endocytosis) (Heidelberger et al., 2002). A second study confirmed this result, indicating inhibition of fast and slow endocytosis through an increase of membrane tension (Wu et al., 2017b). Authors explained this result by a theoretical model proposing that membrane tension increases the endocytosis energy barrier. This trend is also seen during the cell cycle: during mitosis, the membrane tension increases and the endocytosis rate decreases, but during interphase, membrane tension decreases and endocytosis increases (Raucher and Sheetz, 1999b). It seems that membrane tension inhibits the budding step of endocytosis. For example, the deformation of membrane by clathrin requires actin only at high membrane tensions (Boulant et al., 2011). This result has been confirmed *in vitro* with GUVs, because clathrin polymerization is reduced under high tension conditions (Saleem et al., 2015). A similar result has been reported for COPI coating (Manneville et al., 2008). However, the dynamin-induced fission is faster when membrane tension is high in GUVs (Morlot et al., 2012). Authors confirmed this *in vitro* result by showing that hyper-osmotic shock inhibits clathrin mediaded endocytosis *in cellulo*. Although the budding step is inhibited by membrane tension (Wu et al., 2017b), the fission step seems to be promoted (Morlot et al., 2012). Despite these contradictory studies (Morlot et al., 2012), it seems more accepted that membrane tension reduces endocytosis rate (Pontes et al., 2017a). However, it has been recently demonstrated that a dynamin independent CLathrin-Independent Carrier/GPI-Enriched Endocytic Compartment (CLIC/GEEC) endocytosis pathway regulates membrane tension (Thottacherry et al., 2018). This could partially explain the contradictory study based on dynamin activity (Morlot et al., 2012).

Therefore, a balance between endocytosis and exocytosis could regulate membrane tension. It has been originally observed that after a stimulation of exocytosis, membrane tension decreases and returns to its original value thanks to endocytosis (Dai et al., 1997). More recent literature supports that a balance between exocytosis and endocytosis at synapses regulates membrane tension (Lou, 2018). This hypothesis is supported by the fact that membrane tension diffuses quickly at synapses and can equilibrate within seconds (Gomis Perez et al., 2022). Therefore the decrease of membrane tension at the active zone can rapidly propagate to the so-called endocytic zone, a synaptic area encircling the active zone (Lou, 2018). The endocytosis/exocytosis balance is not restricted to neuronal cells. The existence of this balance to regulate membrane tension has been well demonstrated in *Arabidobsis thaliana*. In root meristem cells, a hypo-osmotic shock decreases

endocytosis and increases exocytosis, whereas hyper-osmotic shock has the opposite effect (Zwiewka et al., 2015). Recently, a theoretical paper descriped that a balance between exocytosis/endocytosis buffers membrane tension variations. This model assumes that endocytosis is inhibited by membrane tension and that exocytosis directly depends on the number of endocytic vesicles (Mao et al., 2021). Taken together, it seems that endocytosis/exocytosis balance regulates membrane tension, although the rules of the regulation are still unclear.

Instead of directly regulating membrane stretching, cells can also adapt by playing with the constraints generating membrane tension i.e. mainly cell volume and osmolarity. Indeed, osmolarity and cell volume are entangled. Their entanglement becomes clear in the Ponder-Boyle-Vant'Hoff equation (Roffay et al., 2021; Venkova et al., 2022) :

$$\Pi(V - V_{OI}) = \Pi_0(V_0 - V_{OI})$$

with Π the osmotic pressure, Π_0 the osmotic pressure under isotonic condition, V the cell volume, V_0 the cell volume under isotonic condition and V_{OI} the osmotically inactive cell volume corresponding roughly to the cell dry volume. The osmolarity and the volume are controlled by ionic channels (Syeda et al., 2016; Saha et al., 2018; Roffay et al., 2021; Venkova et al., 2022) and by the synthesis/degradation of small metabolites such as glycerol in yeast and amino acids in mammalian cells (Hohmann, 2002; Christoph et al., 2007). These mechanisms can be very efficient. Indded, the unicellular algae *Dunaliella salina* is able to survive in an environment with NaCl concentrations close to saturation (~5.5M), despite the absence of a rigid polysaccharide cell wall and thanks to glycerol synthesis (Chen and Jiang, 2009).

The cortical cytoskeleton plays also a role in the regulation of membrane tension, but its role is complex. As explained earlier, the membrane tension measurements take into account the lipid in-plane tension as well as a contribution from the cortical cytoskeleton tension. In addition to its own tension, the cortical cytoskeleton could regulate in-plane tension through interactions with the PM. These interactions are due to a physical coupling of actin with PM through different Membrane-to-Cortex Attachement (MCA) proteins such as ezrin (Kozlov and Chernomordik, 2015; Sitarska and Diz-Muñoz, 2020). The role of cortical cytoskeleton is revealed by experimental interferences with the actin cytoskeleton or associated proteins. For example, myosin Ia KO reduces significantly membrane tension (Nambiar et al., 2009), and myosin II activity reduces membrane tension by pulling actin bundles towards the cell interior (Kozlov and Chernomordik, 2015). Indeed, actin protrusions can deform the PM and increase membrane tension (Saha et al., 2018). Actin depolymerization invariably decreases the reported membrane tension (Pontes et al., 2017a). However, it is still unclear if these effects are only due to a reduction in the tension of the cortical cytoskeleton or also due to the interaction between PM lipids and the cortical cytoskeleton. The cortical cytoskeleton can play a direct role in the regulation of in-plane membrane tension by the regulation of cell shape. Keeping its volume constant, cells can change their shape to reduce their surface and reducing their stretching (Saha et al., 2018). For a constant volume, increasing the aspect ratio (ratio of the lengths of the two cell axis) increases the surface area. Therefore, the formation of membrane protrusions, such as a lamellipodium, by actin polymerization increases membrane tension. The elongation is stopped when the protrusive force of actin polymerization is stalled by the membrane tension (Sens and Plastino, 2015). It has been demonstrated that the regulation of membrane tension by the cytoskeleton is dominant in mobile keratocytes, since fusion with GUVs has only a minor effect on

membrane tension, whereas actin inhibition leads to a drastic decrease of membrane tension (Lieber et al., 2015).

Finally, it has been recently pointed out that mTORC2 emerges as a "key/master regulator of PM tension" (Riggi et al., 2020; Roffay et al., 2021). The mTORC2, like mTORC1, is organized around the mTOR kinase (**see chapter 2**), and is associated with a specific set of proteins: PROTOR1/2, mSIN1, mLST8 (also found in mTORC1) and DEPTOR (Liu and Sabatini, 2020). mTORC2 regulates a veriety of effectors (such as PKC) leading potentially to a large variety of effects (Riggi et al., 2020). In yeast, one of the membrane reservoirs is represented by eisosomes, invaginations of the PM forming a valley-shaped structure. In response to stretching, eisosomes flatten and release proteins that activate TORC2 (yeast homolog of mTORC2) (Berchtold et al., 2012). This pathway promotes sphingolipid synthesis. One can hypothesize that membrane tension regulation is achieved through a modification of the elastic modulus K_s mediated by a modification of the PM composition. The inhibition of TORC2 increases membrane tension when measured by Flipper-TR (Riggi et al., 2019). Conversely, a decrease in membrane tension induced by palmitoylcarnitine treatment decreases TORC2 activity and correlates with the formation of TORC2 clusters in PtdIns(4,5)P_2 domains (Riggi et al., 2018). Congruently, hypo-osmotic shock or stretching in mammalian cells activate mTORC2 (but not mTORC1) (Diz-Muñoz et al., 2016; Roffay et al., 2021). Moreover, inhibition of both mTORC1 and mTORC2 prevents changes of membrane tension after hypo-osmotic shock, contrary to the control situation, where membrane tension increases. In contrast, a specific inhibition of mTORC1 leads to an increase of membrane tension similarly to the control condition, confirming the specific role of mTORC2 in the regulation of membrane tension (Roffay et al., 2021). Lastly, it has been shown that mTORC2 is able to inhibit actin polymerization, therefore, membrane tension regulation could be through the regulation of actin (Saha et al., 2018).

2.2. Regulation of biological processes by membrane tension

Here I will brievly review three kind of biological processes regulated by membrane tension: i) transport through mechanosensitive channels, ii) cell migration and iii) intracellular membrane deformations.

i) Transport through mechanosensitive channels: Membrane tension is able to trigger the opening of some channels called Mechanosensitive Channels (MCs). Bacteria have two types of MCs to regulate the osmolarity, Large-conductance mechanosensitive channels MscL and Small-conductance mechanosensitive channels MscS. Eukaryotic MCs have additional functions such as touch sensation and the regulation of blood pressure. The mechanical gating of MCs has been explained by the force-from-lipid principle. The idea is that membrane forces, such as membrane tension, trigger a conformational change of the MC (Teng et al., 2015; Young et al., 2022). Most of the bacterial MCs are not conserved among vertebrates or lost their mechanosensitive properties (Parpaite and Coste, 2017). However in 2010, Piezo proteins were discovered in animals (Coste et al., 2010). Vertebrates have usually two Piezo genes: Piezo1 and Piezo2. Piezo is cation-permeable, and its activation depends on physical stimulations, especially membrane tension (Wu et al., 2017a). It has been recently demonstrated that local stretching of membranes can trigger Ca^{2+} influx through Piezo1. This Ca^{2+} influx is sufficient to trigger exocytosis (Shi et al., 2018). The channels from the two-pore domain

K^+ channels (K2P) TRAAK (TWIK-Related Arachidonic acid Activated K^+ channel, K2P4.1) and TREK (TWIK-RElated K^+ Channel 1, K2P2.1) are also activated by membrane tension (Beedle et al., 2015). The membrane tension required to open MCs in eukaryotic cell is 10 fold higher than the resting membrane tension (Shi et al., 2018).

ii) Cell migration: As explained earlier, high membrane tension inhibits lamellipodia formation by stalling actin polymerization (Sens and Plastino, 2015). A high membrane tension in *Caenorhabditis elegans* sperm cells restricts lamellipodia formation in one direction, thus increasing directional mobility (Batchelder et al., 2011). Similarly, the formation of protrusion correlates with an increase in membrane tension in neutrophils (Houk et al., 2012). Front-to-rear membrane tension gradients have been reported in moving keratocytes. Membrane tension is 30% higher at the leading edge (Lieber et al., 2015). A theoretical model based on mechanical stalling of actin was able to reproduce the observed cell shapes during migration (Keren et al., 2008). One study reports a contradictory behavior where hypo-osmotic shock increases cell velocity (Gabella et al., 2014), but Pontes et al. have given a different interpretation of these results. They emphasized that at short time scales the velocity is actually reduced (Pontes et al., 2017a). Membrane tension can regulates protrusion mechanically, and potentially also biochemically. Some data demonstrates that membrane tension inhibits actin polymerization through inhibition of WAVE, FBP17 and WASP/N-WASP by unclear biochemical signaling (possibly mTORC2 mediated) (Saha et al., 2018). By regulating the establishment of protrusions and actin dynamics membrane tension is an important regulator of cell migration. Moreover, it has been proposed that membrane tension could support cell migration by enhancing endocytosis at the rear and exocytosis at the front (Keren, 2011).

iii) Intracellular membrane deformations: Membrane tension is a physical parameter of all membranes, not only the PM. The membrane tension of intracellular organelles can regulate their physiology. It is challenging to measure the tension of intracellular membranes by classical methods. Fortunatelly, the development of the Flipper family should provide new tools to explore these questions. Some recent data document the role of intracellular membrane tension. The nucleus has been proposed to be a mechanosensitive organelle, and despite the absence of direct measurements, some authors have already predicted the importance of membrane tension for this organelle (Enyedi and Niethammer, 2017; Pontes et al., 2017a). For example, cell swelling increases the nuclear surface up to 60%. Similar to the PM, the nuclear envelope probably also has membrane reservoirs that could be ER membranes (Enyedi and Niethammer, 2017). Nuclear stretching translocates phospholipase A2 from the nucleoplasm to the nuclear envelope, which activates the inflammatory pathway. It seems to be a physical effect, a tensed membrane favored direct interactions with phospholipase A2 (Enyedi et al., 2016). Literature suggests that the nuclear envelope is stretched in various situations such as cell migration through confined channels or in the case of lamin mutations (Enyedi et al., 2016). Many questions remain unresolved concerning the mechanisms of the possible membrane tension gating of the nuclear pore. Moreover, mitochondrial membrane tension seems to control the probability of mitochondria fission. Once a mitochondrium starts to constrict, it undergoes fission, but sometimes this process is aborted. By measuring membrane tension through geometrical analysis (the membrane tension is linked to the constriction radius $\sigma = \frac{\kappa_b}{2r^2}$) and Flipper lifetime recording, Mahecic et al. demonstrated that the fission probability increases with mitochondrial membrane tension. They also demonstrated that the mitochondrial membrane tension for fission is regulated by MT and acto-myosin cytoskeleton (Mahecic et al., 2021). Another striking example comes from the formation of ILVs in endosomes.

The formation of ILVs is supported by the ESCRT machinery; ESCRT-0 recruits ESCRT-I which in turns recruits ESCRT-II. ESCRT-II is a nucleator triggering ESCRT-III filament polymerization. The ESCRT-III filaments enclose and compress cargos creating an inward membrane deformation leading to the formation of the ILV. Mercier et al. showed that a hypertonic shock reduces endosomal membrane tension measured by Flipper fluorescence lifetime (Mercier et al., 2020). This reduced membrane tension increases the recruitment of ESCRT-III on endosomal membranes, but does not change ESCRT-0 and ESCRT-I recruitment. GUV experiments demonstrate that this recruitment is due to a faster ESCRT-III polymerization rate. This higher recruitment is translated *in cellulo* by the formation of more ILVs, probably buffering the endosomal membrane tension.

2.3 Regulation of exocytosis

I have already presented in the precedent section that exocytosis regulates membrane tension. In the literature, it is a common claim that in turn membrane tension regulates exocytosis. However, the body of evidence supporting this claim is sparser than one could expect. As explained earlier, an increase in membrane tension partially correlates with an increase in exocytosis in the specific context of cell spreading (Gauthier et al., 2009, 2011). Other studies seem to go in the same direction (Apodaca, 2002). However, sometimes the induced exocytosis is observed at the time scales of hours, suggesting genetic regulation rather than a direct mechanical control. Therefore, these studies show limitations to infer a causal link between membrane tension and exocytosis. From the mechanical point of view, it is clear that membrane tension can drive the enlargement of the fusion pore (Chizmadzhev et al., 2000; Shillcock and Lipowsky, 2005; Kozlov and Chernomordik, 2015). The regulation of the membrane pore expansion however does not regulate exocytosis rate but the exocytosis mode. For example, it has been reported than actin depolymerization reduces membrane tension, increases the proportion of so called “kiss-and-stay” exocytosis events (fusion pore opens but vesicle does not collapse and keeps a Ω-profile for several seconds). Membrane tension additionally seems to increase the lifetime of full-collapse events. Moreover, hypo-osmotic shock rescues this phenotype confirming the mechanical role of membrane tension (Wen et al., 2016). Interesting data have been obtained from black lipid membranes, an *in vitro* system with a lipid bilayer covering a hole in a Teflon wall. In the black lipid membranes model, membrane tension induced by osmotic stress reduces fusion flickering and drives full fusion (Chanturiya et al., 1997) (**Figure 49**). This *in vitro* system also reports that the membrane tension required for fusion pore dilatation is about 1000 $pN.\mu m^{-1}$ (Kozlov and Chernomordik, 2015). This high tension threshold requires the participation of cortical actin *in cellulo* because in-plane membrane tension alone is usually far from this threshold (Wen et al., 2016; Shin et al., 2018).

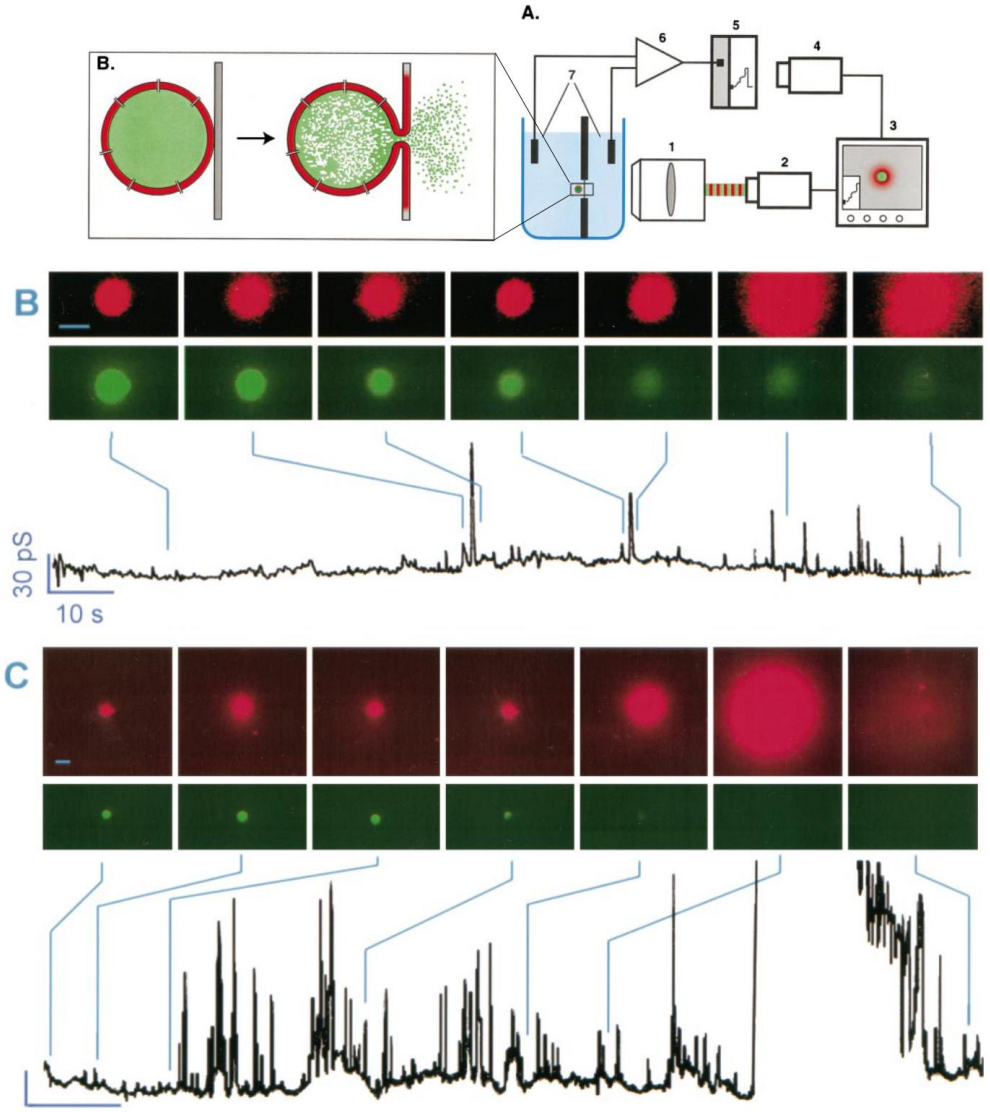

Figure 49. Measure of fusion pore opening in black lipid membrane, modified from Chanturiya et al. (1997). Top: Experimental setup, vesicle membrane is stained with a red dye whereas vesicle lumen is stained with a green dye. Electrical conductance and direct observation of the fusion pore are both recorded. Medium panel: Fusion pore flickering of an isotonic vesicle. The flickering is characterized by spike of conductance (see chapter 2 for details) and partial release of vesicle content. Bottom panel: Osmotically stressed vesicle with initial fusion pore flickering concluded by a full fusion event characterized by a large and durable increase of conductance and the complete release of vesicle content. The diffusion of the membrane dye does not require fusion pore opening but only hemifusion.

Specific data on the role of membrane tension in lysosomal exocytosis are still missing. A notable exception includes the role of lysosomal exocytosis during phagocytosis. The increase in membrane tension during pseudopod formation is followed by lysosomal exocytosis to complete the phagocytosis process (Wang and Galli, 2018). Interestingly, it has been demonstrated that the lysosomal v-SNARE VAMP7 is mechanosensitive. VAMP7+ exocytosis rate in fibroblastic Cos7 cells increases when cells are seeded on a substrate with a higher elastic modulus. Strikingly, VAMP2+ Golgi-derived exocytosis is not affected by substrate stiffness. Moreover, this regulation is integrin-dependent, since polylysine coating abolishes this effect. This mechanoregulation also dependent on

the longin domain of VAMP7. Authors proposed a tug-of-war mechanism where LRRK1 (an interactor of VAMP7 and dynein) and Varp (an interactor of VAMP7 and kinesin) compete for VAMP7 binding. On soft substrates, VAMP7 is preferentially bound by LRRK1 and transported to a perinuclear pool, decreasing exocytosis rate. On rigid substrates, VAMP7 is preferentially bound by Varp, supporting exocytosis (Wang et al., 2018b). Authors also reported that VAMP7+ exocytosis rate decreases during hyper-osmotic shock but this regulation is independent of VAMP7 longin domain. Its shows the existence of different regulatory mechanisms according to the physical stimulation and it confirms the role of membrane tension (Wang et al., 2018b). Other articles indicate that membrane tension could be regulated by actin/Cdc42. The rate of VAMP7+ exocytosis increases from 1.51 events/min to 17 events/min in fibroblastic Cos 7 cells expressing a constitutive active mutant of Cdc42. This positive regulation of exocytosis rate is actin-dependent (Alberts et al., 2006) and is associated with polarized activity in the cell (de Beco et al., 2018). Interestingly, the KD of Cdc42 or the expression of a dominant negative Cdc42 mutant decreases membrane tension in chromaffin BON cells. This decrease in membrane tension correlates with an impairment of exocytosis efficiency. But this inhibition of Cdc42 does not reduce exocytosis rate *per se*, rather it impairs fusion pore opening and shifts full-collapse exocytosis to kiss-and-run exocytosis (Bretou et al., 2014).

Therefore membrane tension is an interesting candidate to understand exocytosis properties. In addition to its role in the regulation of the mode of exocytosis and its putative role in the regulation of exoytosis rate, it could also regulate the spatial organization of exocytosis. Indeed, because lipids do not flow, membrane tension does not equalized itself and could create regions favoring exocytosis while others regions disadvantage exocytosis.

There is less data supporting that membrane tension is able to regulate exocytosis rate. From the theoretical point of view, it has been proposed that membrane tension could increase exocytosis rate through the exposure of lipid hydrophobic tails (Wang and Galli, 2018), but unfortunatelly there is lack of cellular experimental evidence. From the experimental side, it has been demonstrated that the local increase in membrane tension by applying a membrane tether triggers exocytosis (Shi et al., 2018). However, this mechanism is regulated through the opening of MCs (especially Piezo1) creating a Ca^{2+} flux. Therefore, cells without MCs, and exocytosis with a low sensitivity to Ca^{2+} should not be affected (Shi et al., 2018). The most direct evidence comes from an *in vitro* system demonstrating that membrane tension increases SNAREs efficiency (Kliesch et al., 2017b). Authors used system in which Large Unilamellar Vesicles (LUVs), equipped with synaptobrevins, are able to fuse with GUVs, equipped with syntaxin1A and SNAP-25. LUVs and GUVs are stained with different fluorescent dyes. The proportion of the dye coming from LUVs incorporated into GUVs is used as a measure for fusion efficiency. The fusion efficiency has been measured for different physical stretching conditions. The fusion activity seems to have a sigmoid dependence on membrane tension and is almost doubled when the threshold is crossed.

Chapter 4

Spatial statistics and spatial point patterns

"After years, I have deeply regretted that I did not proceed far enough at least to understand something of the great leading principles of mathematics, for men thus endowed seem to have an extra-sense"

Charles Darwin, "The Autobiography of Charles Darwin", chapter of "The Life and Letters of Charles Darwin, including an autobiographical chapter", 1887.

Chapter's summary:

In this technical chapter, I introduce spatial statistics as the field of statistics describing spatial point patterns and giving precious tools for many experimental studies including cell biology work. First and second-order properties of a spatial point pattern are defined in this chapter. Complete Spatial Randomness (CSR) process is introduced in the more general context of Poisson point process. Several methods to test the null hypothesis of CSR are explained: quadrats method, methods based on the nearest neighbor distance and fractal dimension test. The summary Ripley's functions are defined (K, L, H, J and g functions) and common limitations are discussed (edge effects, homogeneity hypothesis, missing points and noise). Statistical tests associated to Ripley's and some extensions of these functions (1D and 3D data, spatiotemporal data, polar analysis, multivariate data, marked data) are presented. Some models of point process are briefly described including the Cox and Newman-Scott processes. The conditional intensity function is introduced in the context of point process with interactions (i.e. Gibbs process) and the examples of hard-core and Strauss processes are presented. Two tools for the spatial analysis of continuous field are presented: Moran's I index and the variogram. Lastly, recent cell biology applications of these tools are briefly reviewed.

1. Probabilistic description of spatial point patterns

1.1. Spatial point patterns

Spatial statistics is a field of statistics interested in spatial data, especially patterns of points. The roots of this discipline are difficult to track. However, it is clear that historically epidemiology contributed a lot in the development of this field. For example, the pioneer Charles Picquet created a map of cholera outbreaks across 48 Paris districts in 1832 (in a report published in 1834). John Snow, inspired by Picquet, created a map of cholera deaths in London in 1854. These maps are constructed from the spatial localizations of death/outbreaks i.e. a spatial pattern of points. Spatial statistics brought important results in diverse fields, including ecology, geosciences, astronomy, economy, sociology and even crime mapping. The popularization of spatial statistics has been accompanied with the diffusion of software and codes. Especially, the incredible spatstat project, a package in the R language for analyzing spatial point patterns, became a reference for many communities. This package is the major source of this chapter (Baddeley et al., 2015). Exploring the spatial organization of exocytosis requires quantitative tools provided by spatial statistics. Indeed, exocytosis sites are small and can be seen as forming a pattern of points. The tools used to analyze such patterns are reviewed in this technical chapter.

A spatial point pattern is a dataset consigning spatial localizations of events (deaths, crimes, etc.) or things (trees, minerals, etc.). Independently of their nature, a spatial point pattern can be described as a dataset X:

$$X = \{x_1, x_2, \dots, x_n\}$$

where x_i (for i ranging from 1 to n) is a position vector. Points are included in a space region called a window W. The combination of a X and W is enough to define correctly the spatial point pattern. However, some datasets have additional information:

i) A multitype point pattern is defined by the combination of different spatial point patterns in the same observation window. This kind of data describes the co-distributions of different types of events (e.g. crimes and police station) and/or things (e.g. different tree species). It allows studying the interaction between different types of points.

ii) A marked point pattern is a spatial point pattern with only one type of points but each point has additional information called a mark (e.g. tree diameter).

iii) A spatial point pattern with covariate(s). Covariate is a continuous measure (e.g. altitude) over the whole observation window W. Covariate is formally described with a spatial function $Z(u)$:

$$\forall u \in W \qquad Z: u \longmapsto Z(u)$$

Notably, spatial point patterns should be distinguished from the point process, which is the probabilistic model generating a spatial point pattern (Baddeley et al., 2015).

1.2. First-oder property: intensity

Let $N(w)$ be the number of points inside the subregion $w \subset W$. The first-order property is the intensity $\lambda(u)$ (also called density) of the pattern defined as:

$$\lambda(u) = \lim_{du \to 0} \frac{E[N(du)]}{du}$$

where du is an elementary surface around u. Because du is small, it can only contain 1 or 0 point. Therefore, $E[N(du)]$ ranges between 0 and 1. The intensity can be used to compute the probability P to find one point at u:

$$P_u = \lambda(u)du$$

The integration of the intensity function over a region $w \subset W$ described the expected number of points in this region, also called intensity measure Λ:

$$\Lambda(w) = E[N(X \in w)] = \int_w \lambda(u)du$$

The intensity function allows the calculation of useful quantities. To measure a quantity $h(u)$ at the point's positions, one could use the Campbell's theorem:

$$E\left[\sum_{x_i \in W} h(x_i)\right] = \int_W h(u)\lambda(u)du$$

If the intensity function λ is constant over the observation window, the point process is said first-order stationary (or homogeneous) and the intensity function is noted $\bar{\lambda}$ (Marcon and Puech, 2009). If the intensity function is inhomogeneous, one could try to estimate it from an observed spatial point pattern. Usually, estimator of intensity function $\hat{\lambda}$ is achieved by a re-normalized Kernel Density Estimation (KDE):

$$\hat{\lambda}(u) = \frac{1}{b}\sum_{i=1}^{n} \kappa\left(\frac{\|u - x_i\|}{b}\right) e(u)$$

where b is the bandwidth (smoothing parameter), $e(u)$ an edge correction and κ a kernel i.e. a non-negative symmetric function with an area under the curve equal to 1. It is common to use a Gaussian kernel:

$$\kappa(x) = \frac{1}{\sqrt{2\pi}} e^{-\frac{x^2}{2}}$$

Note that contrary to a classical KDE, $\int_W \hat{\lambda}(u)du \neq 1$, the $\int_W \hat{\lambda}(u)du = n$. The simpler edge correction is to correct the intensity by the inverse of the proportion of the kernel outside the window W. Applying Campbell's theorem:

$$E\left[\hat{\lambda}(u)\right] = E\left[\frac{1}{b}\sum_{x_i \in W} \kappa\left(\frac{\|u - x_i\|}{b}\right) e(u)\right] = \frac{e(u)}{b}\int_W \kappa\left(\frac{\|u - v\|}{b}\right)\lambda(v)dv$$

Therefore, the estimator does not directly reflect the intensity function $\lambda(u)$, but a smoothed version of the intensity function.

1.3. Second-order property

The second-order property λ_2 is defined similarly to the first-order property but using the expected number of points at two locations u_1 and u_2:

$$\lambda_2(u_1, u_2) = \lim_{du_1, du_2 \to 0} \frac{E[N(du_1) \cap N(du_2)]}{du_1 du_2}$$

Therefore the probability P_{u_1,u_2} to find two points in two elementary areas du_1 and du_2 is:

$$P_{u_1,u_2} = \lambda_2(u_1, u_2)du_1 du_2$$

Using first-order property:

$$P_{u_1,u_2} = P_{u_1}P_{u_2}\frac{\lambda_2(u_1, u_2)}{\lambda(u_1)\lambda(u_2)}$$

The ratio between second-order property and first-order property is called pair correlation function g:

$$g(u_1, u_2) = \frac{\lambda_2(u_1, u_2)}{\lambda(u_1)\lambda(u_2)}$$

This pair correlation function is used to model the interactions between points. If the point distribution is independent:

$$P_{u_1,u_2} = P_{u_1}P_{u_2} \quad \Leftrightarrow \quad g(u_1, u_2) = 1$$

A hypothesis often made is that the pair correlation function depends only on the distance between points $r = u_1 - u_2$ (or is even constant) i.e. the function is invariant under translation. This property is called second-order stationary (Marcon and Puech, 2009). If the pair correlation function is also invariant under rotation (isotropy), it is only a function of $r = \|u_1 - u_2\|$. Hidden second-order stationary point processes are defined by a pair correlation function that only depends on a difference between points coordinates:

$$g(u_1, u_2) = g(u_1 \circ u_2)$$

where $\circ$ is a generalized subtraction operator, only defined by the following property (Hahn and Jensen, 2016):

$$u_1 \circ u_2 = -(u_2 \circ u_1)$$

Many hidden second-order stationary point processes can be easily transformed into classical second-order stationary point processes.

2. Complete spatial randomness and tests associated

2.1. Poisson point process

Let X be a spatial point pattern with n points over a window W and that this spatial point pattern is the result of a point process first- and second-order stationary, with a pair correlation function constant $g = 1$. In this situation, points do not interact and the probability to find a given point in the subregion w is given by a ratio of its surface over the total surface:

$$P(x_i \epsilon w) = \frac{|w|}{|W|}$$

where $|w|$denotes the surface (or volume for 3D data, or even hyper-volume for higher dimensions) of the subregion w. This point process is called Complete Spatial Randomness (CSR), defined by homogeneity (points do not have preferential locations) and independency (points are located independently of the others). Therefore, the localization of each point in the subregion w is a Bernoulli trial. The repetition of this trial leads to a binomial law:

$$P(N(X \in w) = k) = \binom{n}{k} P(x_i \epsilon w)^k \big(1 - P(x_i \epsilon w)\big)^{n-k}$$

$$P(N(X \in w) = k) = \binom{n}{k} \left(\frac{|w|}{|W|}\right)^k \left(1 - \frac{|w|}{|W|}\right)^{n-k}$$

When the number of points becomes high, the probability converges to a Poisson law due to the Poisson limit theorem:

$$\lim_{n \to \infty} P(N(X \in w) = k) = e^{-\gamma} \frac{\gamma^k}{k!}$$

with:

$$\gamma = n \frac{|w|}{|W|} = E[N(X \in w)]$$

Therefore, the CSR process is also called Poisson Point Process (PPP). Rigorously, CSR is a homogeneous PPP. Inhomogeneous PPPs are point processes, in which the parameter γ is not constant over space. In homogeneous PPP, the parameter of the Poisson law (i.e. its average) is simply given by:

$$\gamma = \int_W \lambda(u)\, du$$

Let F be a configuration of a spatial point pattern (e.g. all the points are in the lower half of the window W or each point has no neighbor at a distance inferior to an arbitrary value). The probability

to realize F can be estimated in the PPP model. First, the probability that the point process X contains n points is given by:

$$P(N(X) = n) = e^{-\int_W \lambda(u)du} \frac{\left(\int_W \lambda(u)\, du\right)^n}{n!}$$

The probability that these n points satisfy F is:

$$P(X \in F) = \sum_{n=0}^{\infty} P(X \in F | N(X) = n) P(N(X) = n)$$

The first term can be developed using PPP properties. The probability for point 1 to lie on the surface du_1 around u_1 is given by:

$$P(x_1 \in du_1) = \frac{\lambda(u_1)du_1}{\int_W \lambda(u)\, du}$$

Following the same logic, the probability that point 1 satisfies F is:

$$P(x_1 \in F) = \int_W \frac{\lambda(u_1)}{\int_W \lambda(u)\, du} 1_{u_1 \in F} du_1$$

For two points:

$$P(\{x_1, x_2\} \in F) = \int_W \int_W \frac{\lambda(u_2)\lambda(u_1)}{\left(\int_W \lambda(u)\, du\right)^2} 1_{\{u_1, u_2\} \in F} du_1 du_2$$

Therefore:

$$P(X \in F) = \sum_{n=0}^{\infty} \frac{e^{-\int_W \lambda(u)du}}{n!} \int_W \int_W \dots \int_W 1_{\{u_1, u_2, \dots, u_n\} \in F} \prod_{i=1}^{n} \lambda(u_i)\, du_1 du_2 \dots du_n$$

This property will be later helpful to define the probability density function of a point process.

Homogeneous PPP (i.e. CSR) is often the first hypothesis tested when a spatial point pattern is observed. CSR corresponds to a uniform point process without interactions and is therefore viewed as a "random" distribution. However, strictly speaking, CSR is a point process without special spatial structure and is not more "random" than other stochastic point processes. Diggle described two main deviations from the CSR pattern (Diggle, 2003): 1) clustering (i.e. point aggregation) and 2) dispersion (i.e. there is an inhibition volume around each point creating a regular organization of points) (**Figure 50**). In clustering, there is attraction between points reducing the distances between points, whereas in dispersion there is repulsion increasing distances between points. Of course, a spatial point pattern can be made of a mix between CSR, clustering and dispersion: points can have attraction in a region and repulsion in another region, or have repulsion at a given scale and attraction at another scale. This classification is originally proposed for homogeneous processes, and therefore, clustering/dispersing can only be due to point interactions. In the present manuscript, I extend this classification to inhomogeneous PPP. Consequently, clustering could be due to a region with higher intensity but without point interactions. This decision is supported by the technical

difficulty to distinguish between the realization of an inhomogeneous PPP and the realization of a point process with interactions.

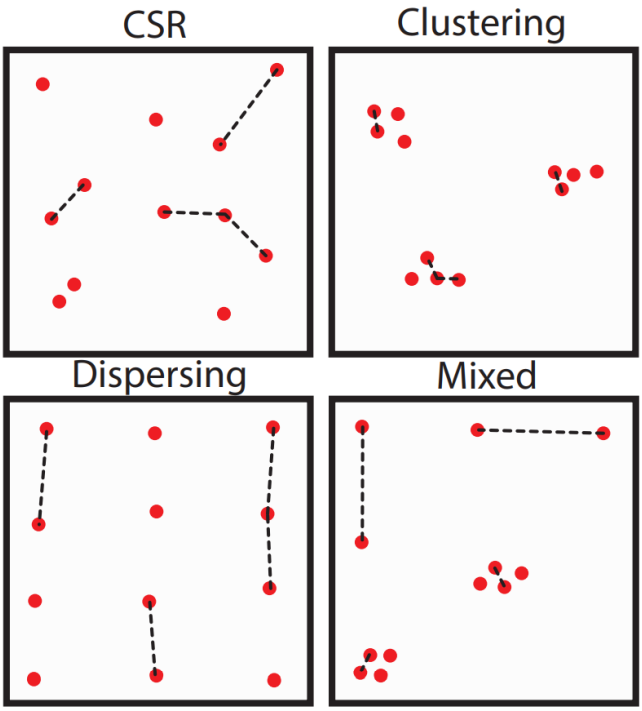

Figure 50. Different types of spatial point patterns. Diggle described two main deviations from the CSR pattern: clustering and dispersion.

2.2 Methods to test the CSR hypothesis

One of the basic questions is to know if an observed spatial point pattern is the result of a CSR point process. This CSR hypothesis can be evaluated by plenty of methods. I will review some of them: i) Quadrats method, ii) Nearest Neighbor Distance method and iii) Fractal dimension test.

i) Quadrats method: this is the easiest method. It consists of dividing the observation window W in m subregions called quadrats of equal size (noted w_i with i ranging from 1 to m) and to count the number of points in each quadrat (**Figure 51**). Under CSR hypothesis, the expected number of points in each quadrat follows a Poisson law and is equal to n/m in average. Of course, random fluctuations create small deviations around this expectation. The CSR hypothesis is evaluated by comparing for all the quadrats the difference between the expected number of points and the observed number of points with a χ^2 test. If the CSR hypothesis is rejected, an index of variation I is used to discriminate between clustering and dispersing:

$$I = \frac{\frac{1}{m-1}\left(\frac{n}{m} - \sum_{i=1}^{m} N(X \in w_i)\right)^2}{\frac{n}{m}}$$

This index is simply the variance of number of points per quadrat divided by the expected average number of points per quadrat. Under the CSR hypothesis, $I = 1$ because in a Poisson law the average is equal to the variance. In case of clustering, the variation between quadrats is high ($I > 1$) whereas in dispersing the variation is small ($I < 1$).

Figure 51. Quadrat counts for 3 types of spatial point patterns.

The Quadrats method has several drawbacks. Although a χ^2 test can theoretically be run in a bilateral way, most of the software packages only propose a unilateral test that only discriminates clustering and not dispersing. Secondly, the division of the observation window in equal size quadrats is difficult for observation windows with complicated geometries. This problem can be fixed by the division in unequal size quadrats and comparison of the intensity measure Λ in each quadrat instead of the number of points i.e. normalizing the number of points per quadrat surface. The most serious drawback is the choice of the number of quadrats i.e. their size. Too large quadrats lead to false negative results by missing the scale of clustering, whereas too small quadrats are not suitable for χ^2 testing and wrongly conclude to dispersing.

ii) Nearest Neighbor Distance method: The Nearest Neighbor Distance (NND) is the smallest distance from a given point to one of its neighbors according to a metric (usually Euclidean distance):

$$NND(x_i) = \min_{j \neq i} \|x_i - x_j\|$$

The probability that the NND of point x_i is superior to r is given by:

$$P(NND(x_i) > r) = P\left(N\left(X \backslash \{x_i\} \in \Omega_{x_i,r}\right) = 0\right)$$

where $\Omega_{x_i,r}$ is a circular subregion centered on x_i and with a radius r. In case of CSR, this probability can be easily computed using Poisson law:

$$P(NND > r) = e^{-\bar{\lambda}\pi r^2}$$

Rigorously, $\bar{\lambda}$ is the intensity function defined for the spatial point pattern $X \backslash \{x_i\}$. We can easily determine the NND cumulative distribution function:

$$F(r) = P(NND \leq r) = 1 - e^{-\bar{\lambda}\pi r^2}$$

and the probability density function:

$$f(r) = \frac{dF(r)}{dr} = 2\bar{\lambda}\pi r e^{-\bar{\lambda}\pi r^2}$$

The average is:

$$\mu_{NND} = \int_0^{\infty} 2\bar{\lambda}\pi r^2 e^{-\bar{\lambda}\pi r^2} dr$$

Using integration by parts:

$$\mu_{NND} = 2\bar{\lambda}\pi \left(\left[-\frac{r}{2\bar{\lambda}\pi} e^{-\bar{\lambda}\pi r^2} \right]_0^{\infty} + \frac{1}{4\bar{\lambda}\pi} \int_{-\infty}^{+\infty} e^{-\bar{\lambda}\pi r^2} dr \right)$$

$$\mu_{NND} = \sqrt{\frac{1}{4\bar{\lambda}}}$$

And the variance is:

$$V[NND] = E[NND^2] - E[NND]^2 = \int_0^{\infty} 2\bar{\lambda}\pi r^3 e^{-\bar{\lambda}\pi r^2} dr - \frac{1}{4\bar{\lambda}}$$

$$V[NND] = 2\bar{\lambda}\pi \left(\left[-\frac{r^2}{2\bar{\lambda}\pi} e^{-\bar{\lambda}\pi r^2} \right]_0^{\infty} + \int_0^{\infty} \frac{r}{\bar{\lambda}\pi} e^{-\bar{\lambda}\pi r^2} \right) - \frac{1}{4\bar{\lambda}}$$

$$V[NND] = 2\left[-\frac{1}{2\bar{\lambda}\pi} e^{-\bar{\lambda}\pi r^2} \right]_0^{\infty} - \frac{1}{4\bar{\lambda}} = \frac{1}{\bar{\lambda}\pi} - \frac{1}{4\bar{\lambda}}$$

$$V[NND] = \frac{4-\pi}{4\pi\bar{\lambda}}$$

For CSR point processes, the NND is equivalent to the Empty Space Distance (ESD) i.e. the minimal distance between an arbitrary location and the nearest point:

$$ESD(u) = \min\|x_i - u\|$$

Therefore, the distribution of ESD is the same as NND distribution under the CSR hypothesis. Skellam and Hopkins (Hopkins and Skellam, 1954) proposed to compare the NNDs and ESDs with an aggregation index:

$$A = \frac{\sum_{j=1}^{n} ESD(u_j)^2}{\sum_{i=1}^{n} NND(x_i)^2}$$

ESDs are generated from randomly selected locations. Skellam and Hopkins demonstrated that a derived statistics follows a β-distribution:

$$\frac{A}{1+A} \sim \beta(n, n)$$

If points are clustered, NNDs tend to be smaller than expected ($A > 1$) whereas in case of dispersing, points are well separated maximizing NNDs ($A < 1$).

An alternative popular method proposed by Clark and Evans (Clark and Evans, 1954) is to compare the average NND to its theoretical value in the so-called Clark-Evans index:

$$R = \frac{\frac{1}{n}\sum_{i=1}^{n} NND(x_i)}{\mu_{NND}} = \frac{\sqrt{4\bar{\lambda}}}{n}\sum_{i=1}^{n} NND(x_i)$$

A $R < 1$ suggests clustering whereas a $R > 1$ indicates dispersing. Deviation from $R = 1$ can be evaluated by the so-called Clark-Evans test. The Clark-Evans index approximately follows a normal distribution:

$$R \sim N\left(1, \frac{\frac{1}{\pi} - \frac{1}{4}}{n\bar{\lambda}}\right)$$

This result relies on the Central Limit Theorem (CLT). The Clark-Evans index can be computed using all the points, but it creates a bias in the normal approximation. Indeed, CLT requires independent observations, but two points may be mutually their nearest neighbor, so-called reflexive points. For the CSR point process, approximately 62.15% of the points are reflexive (Cox, 1981). Therefore, for a rigorous computation, the index should be evaluated on a randomly selected subset of points. However, it has been demonstrated that this correlation is weak and the introduced bias is minor (Donnelly, 1978).

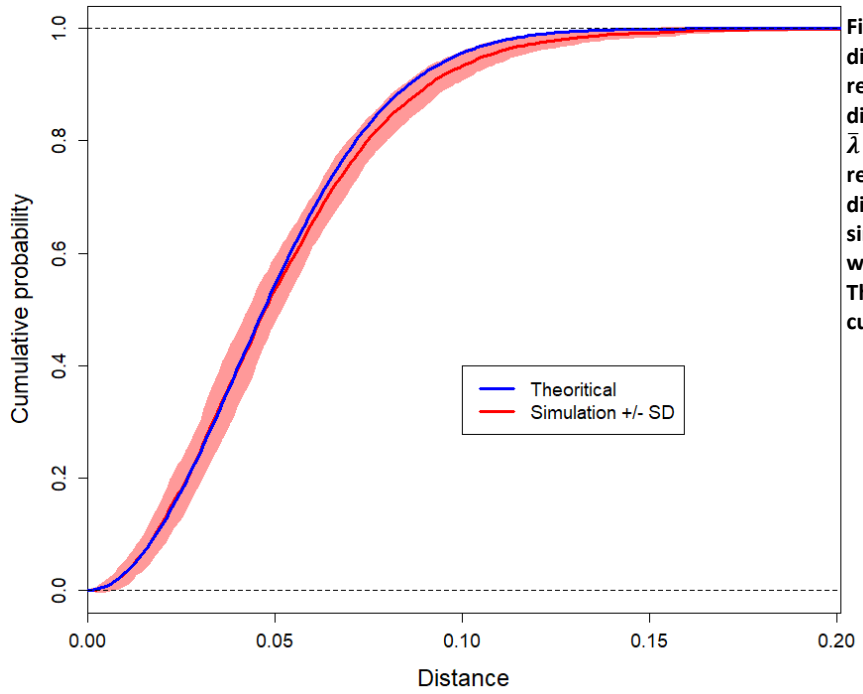

Figure 52. NND cumulative distribution. The blue curve represents the theoritical distribution for an intensity of $\bar{\lambda} = 100$ for CSR distribution. The red curve represents average distribution from Monte-Carlo CSR simulation on a rectangular windows with the same intensity. The difference between the two curves illustrates the edge effect.

Both the Skellam-Hopkins and Clark-Evans tests suffer of edge effects. Points close to window boundaries have artificially less neighbors, and thus a higher NND (**Figure 52**). These effects can be partially corrected by introducing a buffer area or by analytical corrections for well defined geometries. However, these solutions are never totally satisfying. The Monte-Carlo test provides a straightforward answer to these problems. The idea is to generate a Monte-Carlo CSR simulation of a spatial point pattern with the same number of points as observed and in the same window. Repeating simulations several times constructs an empirical distribution of the average NND for the observed window. Comparing the observed average NND to simulations allows the computation of a p-value and to reject CSR hypothesis.

Noteworthy, an observed average NND close to the theoretical one under the CSR hypothesis is not a proof of CSR (even at the threshold β of type II error risk). Indeed, some patterns with a mix of clustered and dispersed regions could have an average NND close to the average CSR NND. Therefore, a test on the full distribution on NNDs could be more powerful. A comparison between an observed distribution and theoretical distributions can be achieved by a Kolmogorov-Smirnov test, for example. An alternative is to use a Monte-Carlo test to compare the distributions, this strategy having the advantage to be edge correction free (Dixon, 2017).

Note that NNDs could be also helpful in the context of multitype spatial point patterns. Let X and Y be two different types of spatial point patterns. Let $F_{XY}(r)$ be the cumulative distribution of the minimal distances from a type X point, to a type Y point. If the types of points are independent, the function $F_{XY}(r)$ is totally equivalent to the cumulative distribution of ESD, so-called the void function $V_Y(r)$. Note that this void function $V_Y(r)$ takes only in consideration type Y points. Of course, we can define reciprocal functions $F_{YX}(r)$ and $V_X(r)$. If the two types are independents:

$$F_{XY}(r) = V_Y(r)$$

$$F_{YX}(r) = V_X(r)$$

Again these equalities can be tested by a Monte Carlo test. Noteworthy, these two equalities are independent ($F_{XY}(r) \neq F_{YX}(r)$ does not imply that $V_X(r) \neq V_Y(r)$ and reciprocally) and should be both tested (Dixon, 2017). If type X attracts type Y, we expect $F_{XY}(r) > V_Y(r)$ and $F_{YX}(r) > V_X(r)$.

A second straightforward way to deal with independence hypothesis of multitype spatial point patterns is the setting of a contingency table. One can quantify the number n_{XX} of type X points having a type X point as nearest neighbor; the number n_{XY} of type X points having a type Y point as nearest neighbor; n_{YY} and n_{YX}. Under the independency hypothesis, it is easy to calculate theoretical effectives:

$$n_{XX} = \frac{n_X(n_X - 1)}{n_X + n_Y - 1} \qquad and \qquad n_{XY} = \frac{n_X n_Y}{n_X + n_Y - 1}$$

$$n_{YY} = \frac{n_Y(n_Y - 1)}{n_X + n_Y - 1} \qquad and \qquad n_{YX} = \frac{n_Y n_X}{n_X + n_Y - 1}$$

The deviation from these theoretical effectives could be tested with a χ^2 test (with one degree of freedom). This procedure can be intuitively interpreted, if $n_{XX} > n_{XY}$ then type X points are segregated: they are more associated with type Y points than type X points (Dixon, 2017).

iii) Fractal dimension test: While previous methods are based on distances or quadrat counts, Caballero et al. recently proposed a method based on the box-counting method (Caballero et al., 2022). The box-counting method divides the space in non-overlapping squares with sides of length δ. $\Gamma(\delta)$ is the number of squares containing at least one point. For box-counting, the analog of fractal dimension D is defined as:

$$D = \lim_{\delta \to 0} \frac{\log\big(\Gamma(\delta)\big)}{\log\left(\frac{1}{\delta}\right)}$$

The probability to find at least one point in the square w_i with sides of length δ under CSR hypothesis is given by:

$$P(N(X \in w_i) > 0) = 1 - P(N(X \in w_i) = 0)$$

$$P(N(X \in w_i) > 0) = 1 - e^{-\bar{\lambda}\delta^2}$$

If the space is divided in m squares, we have:

$$E[\Gamma(\delta)] = \sum_{i=1}^{m} P(N(X \in w_i) > 0) = m\big(1 - e^{-\bar{\lambda}\delta^2}\big)$$

The expected value of the logarithm can be estimated by a first-order Taylor expansion with Δ a small fluctuation around the average:

$$E\big[\log\big(\Gamma(\delta)\big)\big] = E\big[\log\big(E[\Gamma(\delta)] + (E[\Gamma(\delta)] - \Delta)\big)\big]$$

$$E\big[\log\big(\Gamma(\delta)\big)\big] \approx \log(E[\Gamma(\delta)]) = \log\Big(m\big(1 - e^{-\bar{\lambda}\delta^2}\big)\Big)$$

leading to:

$$E[D] = \frac{\log\Big(m\big(1 - e^{-\bar{\lambda}\delta^2}\big)\Big)}{\log\left(\frac{1}{\delta}\right)}$$

with a high number of points, i.e. $\bar{\lambda} \to \infty$:

$$E[D] = \frac{\log(m)}{\log\left(\frac{1}{\delta}\right)}$$

Setting the total area $|W| = 1$:

$$m = \frac{1}{\delta^2} \quad \Rightarrow \quad E[D] = 2$$

The observed fractal dimension can be compared to this theoretical value. If the total area is normalized to 1, $D > 2$ indicates that more squares are needed to cover all the points than in the CSR scenario and suggesting dispersing, whereas $D < 2$ indicates clustering. Practically, D is not estimated for a particular δ but through a linear regression in a log-log plot:

$$\log\big(\Gamma(\delta_i)\big) = D \log\left(\frac{1}{\delta_i}\right)$$

The authors propose to do the linear fit not directly on this curve but on a straight line between the points corresponding to the minimum of partition ($m = 1$) and the maximum of partition (i.e. each square contains in average 1 point). They compute analytically the expected value of this fractal dimension under CSR hypothesis. To obtain a p-value, they propose to compute quantiles through Monte-Carlo simulations. This approach is computationally cheap, is independent on the metric chosen and independent on edge effects.

3. Summary Ripley's K functions

3.1. Ripley's K function:

Previous methods to test the CSR hypothesis reduced the spatial structure to one number (average NND, dispersion index, aggregation index, Clark-Evans Index, fractal dimension, etc.) missing the richness of a spatial structure that could change its properties according to the scale. Ripley's K function is probably the star of spatial statistics, because it avoids these problems. It also can be used as a test for the CSR hypothesis as well as a descriptive statistic. It has been introduced by Ripley in 1976 and 1977 (Ripley, 1976, 1977). The Ripley's K function is defined as:

$$K(r) = \frac{|W|}{n(n-1)} \sum_{i=1}^{n} \sum_{j \neq i} 1_{\|x_i - x_j\| \leq r}$$

This function quantifies the average number of points in a disk of radius r centered on one point (**Figure 53**). Under the CSR hypothesis:

$$\sum_{j \neq i} 1_{\|x_i - x_j\| \leq r} = E\left[N\left(X \backslash \{x_i\} \in \Omega_{x_{i,r}}\right)\right] = \pi r^2 \frac{n-1}{|W|}$$

Therefore:

$$K(r) = \pi r^2$$

A K function with values higher than πr^2 indicate that there are more points in the disk than expected under the CSR hypothesis, i.e. that there is clustering. Lower values indicate dispersing. Note that this function is not binary and may reveal clustering at one scale, and dispersing at another scale. Moreover, it gives information on the characteristic size of the clusters and inhibition length for dispersing (Dixon, 2014).

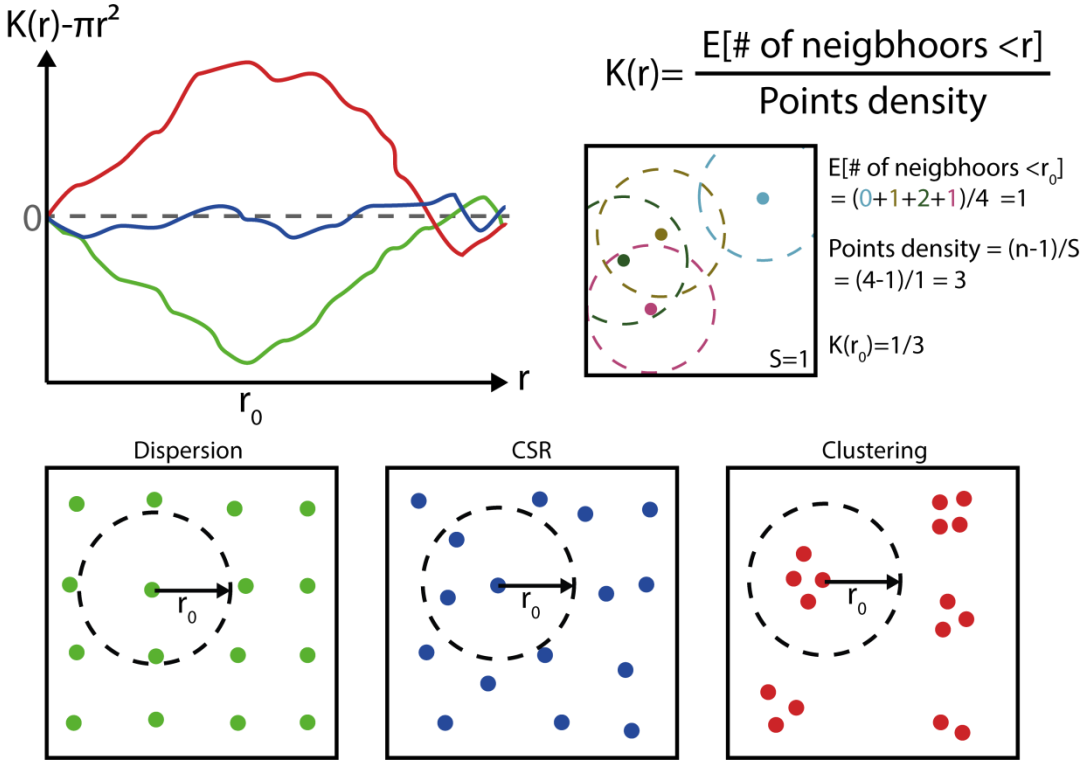

Figure 53 : Principle of the Ripley's K function. Ripley's K function for 3 types of spatial point patterns (dispersion, CSR and clustering). Right top part illustrates how Ripley's K function is calculated: average number of neighbors at a distance r divided by the density/intensity of points.

The variance of the Ripley's K function under the CSR hypothesis is not constant, it is proportional to r. This can complicate its interpretation. This is why a L function with unit variance has been proposed by Besag that is sometimes preferred (Besag, 1977):

$$L(r) = \sqrt{\frac{K(r)}{\pi}}$$

In the case of CSR, this function will be equal to r. Otherwise, the interpretation is the same as Ripley's K function. A centered version of the L function has been proposed (Ehrlich et al., 2004; Kiskowski et al., 2009), the so-called H function:

$$H(r) = L(r) - r$$

The analysis of Ripley's K function at large scales depends on what happens at short scale, because the evaluation is made in a disk and is subsequently cumulative. Therefore, the measure of the spatial structure at large scale could be attenuated by the short scale structure. Quantifying the number of points in a crown would remove the effect of short-scale points. For this purpose, one can derivate the Ripley's K function. The resultant function is the pair correlation function (**see box 5**):

$$g(r) = \frac{1}{2\pi r}\frac{dK(r)}{dr}$$

The expected value for this function under the CSR hypothesis is 1. The interpretation is the same as Ripley's L and K functions. However, because a crown contains less points than a disk (for the same radius r), this function has larger random fluctuations around the expected value in the case of CSR and could be practically difficult to use for spatial point patterns with a low number of points (Dixon, 2014).

Lastly, the J function is sometimes used as an uncommon alternative to Ripley's K function and pair correlation function. It is defined as a ratio between the cumulative distribution functions $F(r)$ of ESD and the cumulative distribution function $V(r)$ of NND:

$$J(r) = \frac{1 - V(r)}{1 - F(r)}$$

As explained earlier, for a CSR point process $V(r) = F(r)$ and therefore $J(r) = 1$. In clustering, NNDs decrease and ESDs increase, $V(r)$ increases faster and $F(r)$ increases slower, and then $J(r) < 1$ whereas in dispersing process $J(r) > 1$.

Box 5: Ripley's K function and pair correlation function

The Ripley's K function can be rewrite in terms of intensity:

$$K(r) = \frac{|W|}{n(n-1)} \sum_{i=1}^{n} \sum_{j \neq i} 1_{\|x_i - x_j\| \leq r} = \frac{|W|}{n(n-1)} \int_W \int_{\Omega_{u_1,r}} \lambda_2(u_1, u_2) du_2 du_1$$

With $\Omega_{u_1,r}$ a disk with a center u_1 and a radius r. One could introduce the pair correlation function. Under first and second-order stationary hypothesis, the pair correlation function is a function of the distance between points r and the intensity function $\bar{\lambda}$ is constant. We note $\bar{\lambda}'$ the intensity function of the spatial point pattern with the reference point excluded:

$$\bar{\lambda}' = \frac{n-1}{|W|}$$

Therefore the integral can be rewrite:

$$K(r) = \frac{|W|}{n(n-1)} \int_W \int_{\Omega_{u_1,r}} g(r = \|u_1 - u_2\|) \bar{\lambda}(u_1) \bar{\lambda}'(u_2) du_2 du_1$$

$$K(r) = \frac{|W|}{n(n-1)} \int_W \int_r g(r) \bar{\lambda}(u_1) 2\pi r \bar{\lambda}'(r) du_1 dr$$

$$K(r) = 2\pi \int_r r g(r) dr$$

Therefore:

$$g(r) = \frac{1}{2\pi r} \frac{dK(r)}{dr}$$

Ripley's K function (and associated functions) suffers from two important drawbacks: edge effects and homogeneity hypothesis. Because the observed area is finite, the points close to borders have fewer neighbors. To take into consideration this edge effect, several border corrections have been proposed. Therefore, the estimator of the Ripley's K function is calculated as:

$$\widehat{K}(r) = \frac{|W|}{n(n-1)} \sum_{i=1}^{n} \sum_{j \neq i} 1_{\|x_i - x_j\| \leq r} \, e(x_i, x_j, r)$$

with $e(x_i, x_j, r)$ the edge correction. The simplest method consists in eliminating situations where a part of the disk is outside of the observation window, creating a buffer zone around borders. The size of this buffer zone increases with r. This correction is sometimes referred as "border correction". This correction leads to a substantial loose of data. Alternative methods propose to give more weight to points close to borders. Ripley's K function counts the number of points is a disk of radius r. Under the CSR hypothesis, the region outside the observation window contains the same density of points. Therefore, the Ripley's K function can be corrected inversely proportional to the fraction of the disk outside the observation window. Let $|\Omega_{x,r} \cap W|$ be the surface of the disk inside the observation window, the correction is:

$$e(x_i, x_j, r) = \frac{\pi r^2}{|\Omega_{x_i,r} \cap W|}$$

a correction known as Besag's correction (Besag, 1977). Contrarily to Besag, Ripley's proposed to correct differently each point:

$$e(x_i, x_j, r) = \frac{2\pi r dr}{\left|\left(\Omega_{x_i, \|x_i - x_j\| + dr} - \Omega_{x_i, \|x_i - x_j\|}\right) \cap W\right|}$$

In the Ripley's isotropic correction, each point is corrected inversely proportional to the fraction of a crown of width dr and with an internal radius $\|x_i - x_j\|$ included in the window W (Ripley, 1977). Still based on isotropy, the translation correction proposes to translate the observation window W and to center it on the Ripley's disk. The correction is inversely proportional to the intersection between the observation windows before and after the translation. These methods, giving more weight to peripheral points, apply the principle of inverse probability weighting used in Horvitz-Thompson estimator. The selection of the correction is a difficult task and often requires a balance between computational time and performance. Complex observation windows can increase drastically the computation time of these corrections.

The second drawback of Ripley's K function is the requirement of homogeneity. Actually, Ripley's K function can be accurately calculated even for an inhomogeneous point process, but deviation from CSR cannot distinguish between point interactions and inhomogeneous process. Therefore, Ripley's K function can be correctly used but rejection of the CSR hypothesis indicates either point interactions or an inhomogeneous process. In some situations, one would like to distinguish between inhomogeneous process and interactions. For example, in epidemiology, we expect more cases in a city than in the country side just because of the number of habitants (i.e. inhomogeneity) and not necessarily due to contamination (i.e. interaction). In this example of an inhomogeneous process, we would like to investigate if the spatial distribution of cases is random by controlling the local density of habitants. This issue has been addressed by Diggle who proposed to compare the Ripley's K

function of cases to the Ripley's K function of control (Diggle and Chetwynd, 1991). The control Ripley's K function reflects the "natural" distribution of habitants and can be used to control inhomogeneity effects:

$$D = K_{case}(r) - K_{control}(r)$$

More recently, Marcon and Puech followed Diggle's strategy and proposed a function taking also into consideration weight for points (Marcon and Puech, 2009). However, these methods require the existence of cases and controls. There are many processes for which the controls cannot be sampled (or this concept does not even make sense in some situations). Therefore Diggle's solution is restricted to specific situations. To face this issue, Baddeley et al. (Baddeley et al., 2000) adapted the Ripley's K function for inhomogeneous processes with the following estimator:

$$\widehat{K}_{inhom}(r) = \frac{|W|}{\sum_{i=1}^{n} \hat{\lambda}(x_i)} \sum_{i=1}^{n} \sum_{j \neq i} \frac{1_{\|x_i - x_j\| \leq r}}{\hat{\lambda}(x_i)\hat{\lambda}(x_j)} e(x_i, x_j, r)$$

The term $\hat{\lambda}(x_i)\hat{\lambda}(x_j)$ counts the expected number of neighbor points separated by a distance $< r$ without interactions. Despite the apparent solution, the estimation of the intensities $\hat{\lambda}$ is challenging. The used of this function in empirical studies is still extremely limited (Floch et al., 2018). Interestingly, Hahn and Jensen developed new estimators similar to Ripley's K function for diverse inhomogeneous point processes (Hahn and Jensen, 2016). They propose to separate the spatial point pattern in quadrats. In each quadrat, a K function is computed. If the K function used is adapted to the point process, its estimation is independent on the quadrat's shape/intensity. A difference between K functions for low intensity quadrats and high intensity quadrats would reveal that the underlying model of the K function is incorrect. Differences between K functions is achieved with a permutation test (Hahn, 2012). Unfortunately, this permutation test requires at least 7 quadrats to possibility obtain a p-value below $\alpha = 5\%$. K function estimations require at least 20 points per quadrat. Therefore this test is not usable for patterns with less than 140 points and probably require >300 points to have a decent statistical power.

Comparing spatial point patterns across different conditions could be particularly relevant for experimental sciences. For this purpose, some tests have been developed to compare Ripley's K functions between conditions. A test based on a bootstrap approach has been proposed by Diggle et al. to compare groups of independent replicated experiments (Diggle et al., 1991, 2000). More recently, some limitation has been pointed out in this approach, and a test based on permutation has been published to compare two patterns divided in quadrats or two conditions with several replicates (Hahn, 2012).

Experimental data can add two difficulties to the estimation of Ripley's K function: i) missing points and ii) false positive points. Missing points are not a real issue, since Ripley's K function is invariant under random thinning i.e. if omitted points are randomly distributed (corresponding to a homogeneous PPP), the Ripley's K function is not affected by these omissions (Baddeley et al., 2015). False positive points correspond to points in the dataset that actually do not correspond to the event/object studied i.e. false positive. Under the reasonable hypothesis that noise corresponds to a PPP, it is easy to estimate how noise affects the spatial point pattern, especially its intensity function:

$$\lambda = \lambda_s + \lambda_n$$

with λ_s the signal intensity function and λ_n the noise intensity function. This superposition property is an immediate consequence of the independence property of the PPP (Baddeley et al., 2015). First, we can evaluate the bias introduced in an inhomogeneous PPP by a homogeneous PPP noise. The Ripley's K function is given by:

$$K(r) = \frac{|W|}{n(n-1)} \int_W \int_{\Omega_{u_1,r}} \lambda_2(u_1, u_2) du_1 du_2$$

$$K(r) = \frac{|W|}{n(n-1)} \int_W \int_{\Omega_{u_1,r}} \left(\lambda_s(u_1) + \bar{\lambda}_n\right)\left(\lambda_s(u_2) + \bar{\lambda}_n\right) du_1 du_2$$

$$K(r) = \frac{|W|}{n(n-1)} \left(\int_W \int_{\Omega_{u_1,r}} \lambda_s(u_1)\lambda_s(u_2) du_1 du_2 + \int_W \int_{\Omega_{u_1,r}} \bar{\lambda}_n^2 du_1 du_2 + \int_W \int_{\Omega_{u_1,r}} \lambda_s(u_1)\bar{\lambda}_n du_1 du_2 + \int_W \int_{\Omega_{u_1,r}} \lambda_s(u_2)\bar{\lambda}_n du_1 du_2 \right)$$

$$K(r) \approx \left(\frac{n_s}{n}\right)^2 K_s(r) + \left(\frac{n_n}{n}\right)^2 \pi r^2 + 2\frac{n_s n_n}{n^2} \pi r^2$$

Under correct experimental conditions, we expect $2\frac{n_s n_n}{n} \gg \left(\frac{n_n}{n^2}\right)^2$:

$$K(r) \approx \left(\frac{n_s}{n}\right)^2 K_s(r) + 2\frac{n_s n_n}{n^2} \pi r^2$$

To give the order of magnitude of the bias, assuming a proportion p of false positive points (noise), and that $K_s(r) = \alpha\, \pi r^2$ with α the strength of the clustering ($\alpha > 1$). Under these simplifying hypotheses, the bias is:

$$bias = \frac{K_s(r) - K(r)}{K_s(r)} = \frac{\alpha - (1-p)^2\alpha - 2p(1-p)}{\alpha}$$

Setting $\alpha = 3$ (similarly to our results (Lachuer et al., 2022) and $p = 5\%$ of false positives, the bias is about 9% (**Figure 54**). One can also use superposition theorem, to predict the bias introduced by a homogeneous PPP noise when the signal point process is first-order stationary with interactions. In this scenario:

$$\lambda_2(u_1, u_2) = \lambda_{s,2}(u_1, u_2) + \lambda_n^2 + 2\lambda_s\lambda_n$$

$$\Rightarrow \quad K(r) = \frac{\bar{\lambda}_s^2}{\left(\bar{\lambda}_s + \bar{\lambda}_n\right)^2} K_s(r) + \frac{\bar{\lambda}_n^2}{\left(\bar{\lambda}_s + \bar{\lambda}_n\right)^2} \pi r^2 + \frac{2\bar{\lambda}_s\bar{\lambda}_n}{\left(\bar{\lambda}_s + \bar{\lambda}_n\right)^2} \pi r^2$$

We obtain a result similar to the first scenario: the bias introduced is equivalent. The $2\lambda_s\lambda_n$ term is due to the fact that two situations are taken in consideration: point at u_1 is generated by the signal and point at u_2 by the noise, and inversely. Because these situations are equivalent we can sum them.

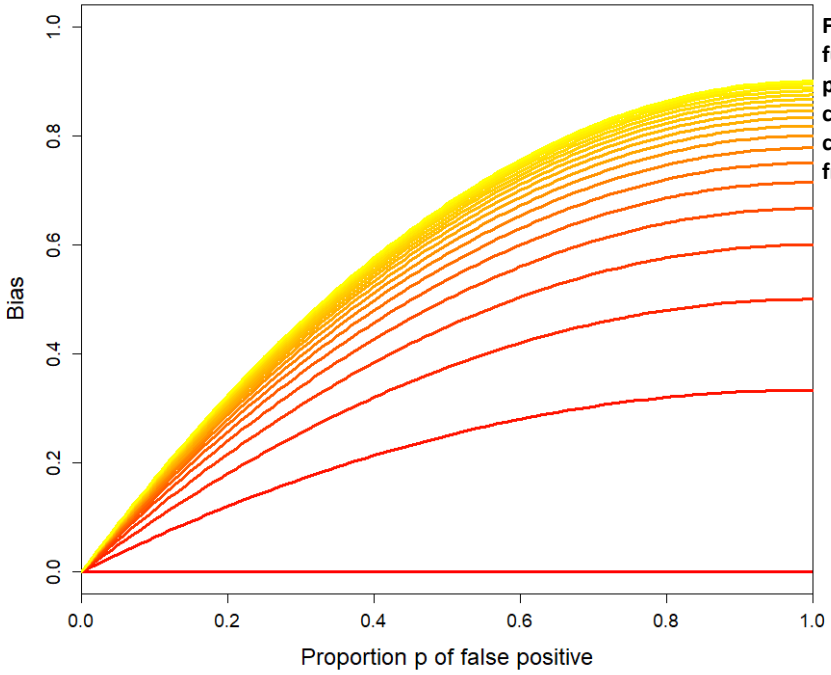

Figure 54. Bias of the Ripley's K function as a function of the proportion p of false positive. The color code represents the clustering level with a α ranging from 1 (red) to 10 (yellow).

3.2 Statistical test on Ripley's K function and other summary functions

Let $S(r)$ be one of the summary functions presented (Ripley's K, L, J, H, g). Deviation of an observed summary function from the theoretical one may be tested with a pointwise envelopes test (Baddeley et al., 2015). Monte-Carlo CSR simulations are run with the same number of points and over the same observation window. For each simulation, the summary function $S_i(r)$ is computed, for i ranging from 1 to m. These CSR simulations define upper and lower envelope boundaries:

$$Up(r) = \max\{S_1(r), S_2(r), \dots, S_m(r)\}$$

$$Low(r) = \min\{S_1(r), S_2(r), \dots, S_m(r)\}$$

The significance level associated is $\alpha = \frac{2}{m+1}$. The pointwise envelope test requires the a priori decision to evaluate the deviation of the observed summary function from envelopes at a particular distance r. Indeed, the probability for the observed summary function to deviate somewhere is higher than α under the CSR hypothesis. A difficulty known as multiple comparison problem, even if Ripley's K function values are correlated (i.e. it is not a repetition of independent testing) limiting the inflation of the type I error. This common misuse of the test can lead to false conclusions (Urbina et al., 2018). Because computations of the envelopes can be time-costly, some authors proposed analytical formulas to determine critical quantiles (Lagache et al., 2013; Yunta et al., 2014).

Alternative methods have been developed to avoid the a priori decision of a distance where simulations and observations are compared. One could compare the Maximum Absolute Deviation (MAD) between the observed summary function $S(r)$ and theoretical CSR values $S_{theo}(r)$:

$$MAD = \max|S(r) - S_{theo}(r)|$$

For example, theoretical summary function for Ripley's K function is $K_{theo}(r) = \pi r^2$. Here again, the MAD test is performed by comparing the observed MAD with Monte-Carlo CSR simulations. Notice than unlike pointwise envelope tests, the result of the MAD test is affected by the type of summary function chosen. Especially, the stabilization of the variance using L function provides a stronger statistical power (Baddeley et al., 2015).

Summarizing the difference between observed and simulated summary functions by the difference at one point, could miss information and give important weight to a single deviation. Therefore, the Diggle-Cressie-Loosmore-Ford test proposes to quantify the deviation as the integrated squared difference (similarly to the Cramér-von Mises test):

$$T = \int \left(S(r) - S_{theo}(r)\right)^2$$

Here again, the significance is provided by comparing observed T with Monte-Carlo CSR simulations (Baddeley et al., 2015).

3.3. Extensions of Ripley's K function

There are some interesting adaptations of the Ripley's K function. Most interesting extensions will be reviewed in this section: i) 1D and 3D adaptations, ii) Spatiotemporal Ripley's K function, iii) Sector Ripley's K function, iv) Multivariate Ripley's K function, v) Marked Ripley's K function.

i) 1D and 3D adaptation: Ripley's K function is usually used for 2D data such as protein localizations on PM or organelle localizations in flat cells, but it can be adapted for 1D and 3D data. For example a 1D version has been used to demonstrate that the distribution of cargos along the *Trypanosoma brucei* flagellum is a CSR (Yunta et al., 2014). The 1D version can also be used to describe the distribution of events over time. For example, this procedure has been used to analyze the distribution of exocytosis over time in cortical neurons (Urbina et al., 2018). 3D version of Ripley's K function has been also proposed (Baddeley et al., 1993; Jafari Mamaghani et al., 2010; Hansson et al., 2013).

ii) Spatiotemporal Ripley's K function: Diggle et al. introduced a spatiotemporal Ripley's K function, especially well adapted for epidemiological data. In addition to the spatial point pattern X, a spatiotemporal dataset contains temporal point pattern $T = \{t_1, t_2, \dots, t_n\}$ paired to spatial data. The spatiotemporal Ripley's K function is defined as:

$$K(r,\tau) = \frac{|W|}{n(n-1)} \sum_{i=1}^{n} \sum_{j \neq i} 1_{(\|x_i - x_j\| \leq r) \cap (\|t_i - t_j\| \leq \tau)}$$

Geometrically, it counts the number of neighbors in a spatiotemporal cylinder of radius r and with a height 2τ centered on one point. Under complete spatiotemporal randomness hypothesis:

$$K(r,\tau) = 2\pi r^2 \tau$$

But more interestingly, under the less restrictive hypothesis that spatial and temporal distributions are independent, spatiotemporal Ripley's K function can be written as the product of temporal and spatial Ripley's K function:

$$K(r,\tau) = K(r)K(\tau)$$

This result relies on probability independency. It suggests a natural statistic:

$$D = K(r,\tau) - K(r)K(\tau)$$

When temporal and spatial localizations co-cluster, $K(r)K(\tau)$ underestimates the statiotemporal Ripley's K function $K(r,\tau)$. Therefore, $D > 0$ indicates a positive spatio-temporal coupling: points spatially close are likely to be temporally close, and conversely. A $D < 0$ indicates a negative spatiotemporal coupling: points spatially close are likely to be temporally separated, and conversely. The significance is achieved by a Monte-Carlo test.

iii) Sector Ripley's K function: To test the isotropy hypothesis, it has been proposed to replace the Ripley's observation disk by an anisotropic shape such as a sector. The sector is defined by a diameter r and two angles θ and φ corresponding to the directions of the lines delimiting the sector. Under isotropy hypothesis:

$$K(r,\theta,\varphi) = \frac{\theta - \varphi}{2\pi} K(r)$$

Therefore, under this isotropy hypothesis, sector Ripley's K function is invariant when angles are modified while keeping the angle difference constant. An anisotropy can be detected by the evaluation of this function for different directions (Baddeley et al., 2015).

iv) Multivariate Ripley's K function: The multivariate form of the Ripley's K function is a particularly useful version. This function is used to investigate the interaction of (at least) two types of points, such as the distribution of two different proteins. It is interesting to know if these different types of points interact or not (co-cluster, inhibit each other). Considering a spatial point pattern made of two sub-spatial point pattern X and Y according to their types, the multivariate Ripley's K function is:

$$K_{XY}(r) = \frac{|W|}{n_X n_Y} \sum_{i=1}^{n_X} \sum_{j=1}^{n_Y} 1_{|x_i - y_j| \le r}$$

For m types of points, there is m^2 multivariate Ripley's K functions. With 2 types (X and Y) there are K_{XX}, K_{XY}, K_{YX} and K_{YY} (Dixon, 2014). The two cross-K functions give information on the interactions. If these functions are $> \pi r^2$, it indicates attraction between the two point types at distance r, whereas $< \pi r^2$ indicates repulsion. This tool has been used to study the co-clustering between H-Ras and K-Ras isoforms at the PM (Prior et al., 2003). It is also a tool used to measure colocalization on fluorescent microscopy images (Lagache et al., 2015).

v) Marked Ripley's K function: Let X be a marked spatial point pattern. One mark $\psi(x_i)$ is associated to each point. These marks can be organized in classes and the multivariate Ripley's K function can be used. However, for continuous marks, a specific Ripley's K function has been proposed (Guan, 2006):

$$K_{\psi}(r) = \frac{|\mathrm{W}|}{n(n-1)} \sum_{i=1}^{n} \sum_{j \neq i} \psi(x_j) 1_{|x_i - x_j| \le r}$$

Under the independency hypothesis, we have:

$$K_{\psi}(r) = \mu_{\psi} K(r)$$

where μ_{ψ} is the average value of the marks. Thereby, a plot of $K_{\psi}(r)$ as a function of $K(r)$ should be linear with a slope μ_{ψ}. Moreover, a formal test based on permutation has been proposed (Guan, 2006).

4. Models of point process

4.1. Cox processes

Statisticians have developed plenty of point process models. I will briefly review the two main classes of models: Cox processes and Gibbs processes (**Table 5**). Cox processes are PPPs with an inhomogeneous intensity function. Actually, in Cox processes, the intensity function is a random variable, therefore Cox processes are sometimes called double stochastic PPP: both intensity function and point localizations are stochastic (Cox, 1955). Application of this class of models to data supposes that the intensity function is influenced by unobservable parameters. However, the intensity function can be inferred from the observed point pattern. There is plenty of ways to generate a random intensity function but I will review two common examples of Cox processes: Newman-Scott process and Gaussian random field process.

The Newman-Scott processes have been initially developed to explain the distribution of the galaxies in the universe (Neyman and Scott, 1958). These models work in two steps: i) the generation of "parent points" following a PPP and ii) generation of "offspring points". These offspring points are organized in clusters around parent points. Newman-Scott processes can be illustrated with the most basic model: Matérn cluster process (**Figure 55**) (Matérn, 1986). The Matérn cluster process is constructed first by a homogeneous PPP with an intensity κ. Each point is a "parent" with a number of offspring drawn in a Poisson law with an average μ. These offspring points are randomly distributed in a disk of radius R centered on the parent. The spatial point pattern corresponding to the Matérn cluster process is formed only with offspring points (parent points are removed). This model has 3 parameters: κ, μ and R. This model exhibits clustering until the scale R with an average of μ points in each cluster. The Thomas process is similar to the Matérn process but instead of an uniform distribution of points in a disk of radius R, the localization of offspring points are drawn in an isotropic Gaussian distribution with a standard deviation σ centered on a parent point (**Figure 55**) (Thomas, 1949). Similarly to the Matérn cluster process, the Thomas process also has three parameters (κ, μ and σ) and also creates clusters.

The Gaussian random field process is constructed first by the discretization of the observed window W in pixels. A random number is drawn in a uniform law for each pixel of the discretized window. Then the resulting array is smoothed with a Gaussian kernel. The map generated by this process corresponds to the intensity function of the Cox process. This process is particularly interesting because it reflects the natural distribution of many parameters and generate both, hot-spots and cold-spots.

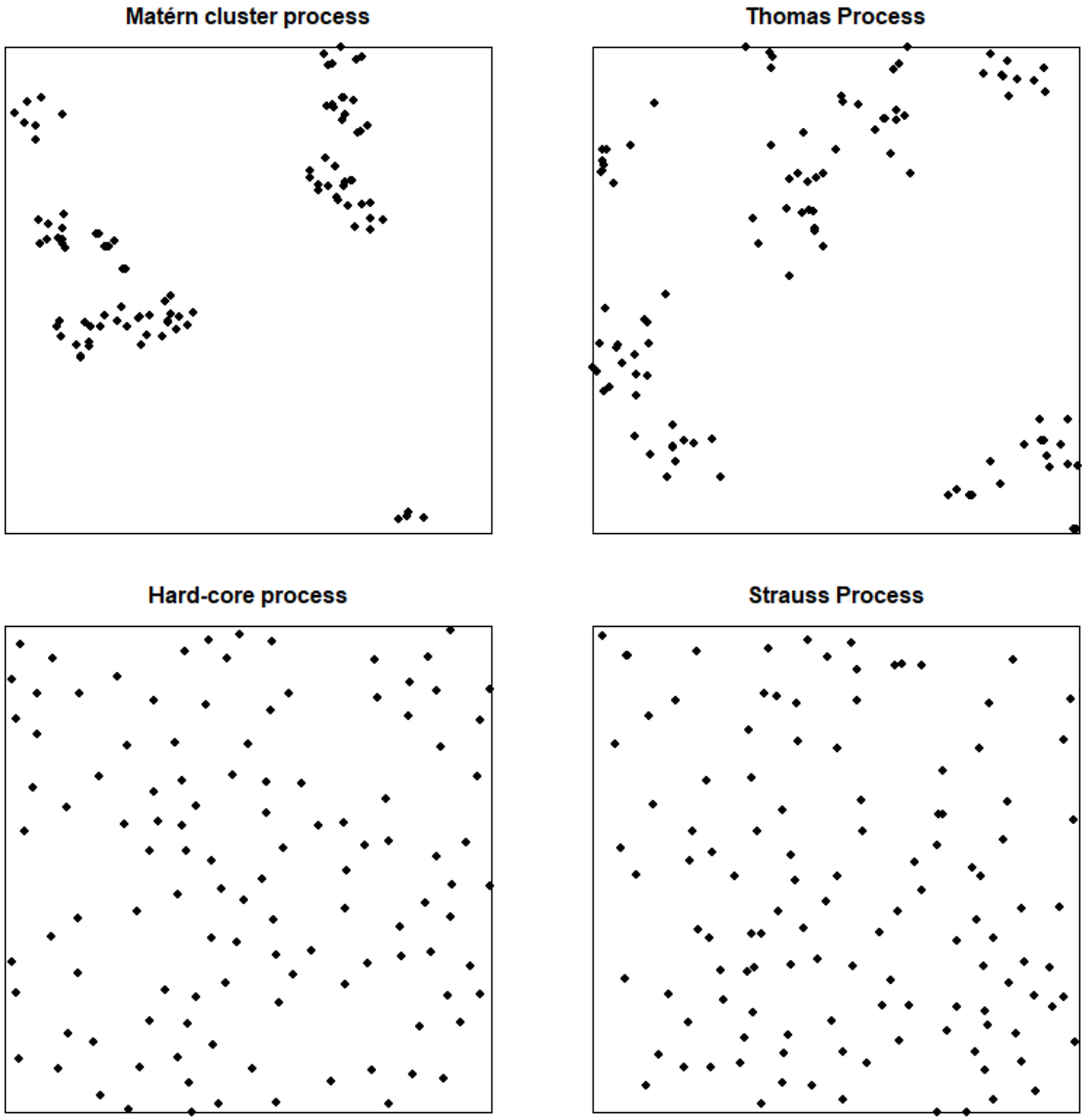

Figure 55. Different point processes. Top row illustrates the Cox process with two examples: Matérn cluster and Thomas processes. Both simulations have been realized with $\kappa = 10$ and $\mu = 10$ on a square window $|W| = 10$. For the Matérn cluster process, the scale $R = 0.05$ has been used creating small clusters with clear boundaries whereas boundaries of the Thomas process are blurry due to the Gaussian distribution ($\sigma = 0.05$). Bottom row illustrates the Gibbs process with two examples: Hard-core and Strauss processes. Both simulations have been realized with $\beta = 300$ and $R = 0.05$. For hard-core process, there is no pair of points with a distance $< R$ whereas it rarely occurs in the Strauss process (with an inhibition parameter $\gamma = 0.2$).

4.2. Gibbs processes

Gibbs processes are a class of models assuming interactions between points. More technically, these models are not fully characterized by the intensity function contrarily to PPP. Papangelou defined a conditional intensity $\lambda(u|X)$ (Papangelou, 1974). This conditional intensity can be interpreted as

follows: the probability to observe a point at u knowing the rest of the spatial point pattern X is given by $\lambda(u|X)du$. Contrarily to PPP that have the independency property, the Gibbs processes have $\lambda(u|X) \neq \lambda(u)$. Another important quantity to understand the Gibbs processes is the probability density $f(X)$. Similarly to the classical probability density, the spatial probability density $f(X)$ quantifies how much likely it is to obtain a spatial point pattern X with the point process Y. This is a relative value since the probability density for a point process Y is the probability to obtain X by Y divided by the probability to obtain X by a homogeneous PPP with an intensity equal to 1. Some probability densities are easy to calculate. For example, the probability for a PPP to localize n points at the coordinates given by X is:

$$P_{homogenous\ PPP}(X) = \frac{e^{-\int_W \lambda(u)du}}{n!} \prod_{i=1}^{n} \lambda(x_i)$$

We can compute the probability density of a homogeneous PPP with an intensity β:

$$f(X) = \beta^n e^{|W|(1-\beta)}$$

The probability density of an inhomogenous PPP with an intensity $\beta(u)$ is:

$$f(X) = e^{\int_W 1-\beta(u)du} \prod_{i=1}^{n} \beta(x_i)$$

The probability density allows specifying the conditional intensity:

$$\lambda(u|X) = \frac{f(X \cup \{u\})}{f(X)} \qquad \Leftrightarrow \qquad \lambda(u|X)f(X) = f(X \cup \{u\})$$

where $X \cup \{u\}$ corresponds to the addition of a point localized at u in the spatial point pattern. The second form of the relation have the same form than a classical conditional probability, therefore the conditional intensity can be interpreted as how likely it is to add a point at u knowing the rest of the pattern. For a model without interactions:

$$f(X \cup \{u\}) = f(X)\lambda(u) \qquad \Rightarrow \qquad \lambda(u|X) = \lambda(u)$$

With the help of these concepts, I will briefly define some of the main Gibbs processes: hard-core process and Strauss process. In a hard-core process, there is no couple of points with a distance inferior to a parameter h called the hard core diameter (**Figure 55**) (Berthelsen and Møller, 2002). It represents a distance of absolute repulsion. Therefore, the conditional intensity if:

$$\lambda(u|X) = \begin{cases} \beta & if \quad \min\limits_{x_i \epsilon X}(u - x_i) > h \\ 0 & if \quad \min\limits_{x_i \epsilon X}(u - x_i) \leq h \end{cases}$$

In an hard-core process, it is impossible to observe a NND inferior to h. This model is extremely restrictive and most of the inhibitions in experimental conditions are not absolute. The Strauss model lessens this absolute condition: it is unlikely that two points are closer than h but not impossible (**Figure 55**) (Strauss, 1975). The conditional intensity is:

$$\lambda(u|X) = \beta\gamma^{t(u,X,h)}$$

with $t(u, X, h)$ the number of points from X that are at a distance inferior to h from u. The parameter γ is the inhibition parameter and it is inferior to 1 (otherwise this process generates clustering but fails to define correctly a probability density and is therefore not used (Kelly and Ripley, 1976)). Noteworthy, we did not describe intensities of hard-core and Strauss processes. Actually, intensity functions of Gibbs processes are not trivial results. The intensity is given by a special case of the Georgii-Nguyen-Zessin formule (Nguyen and Zessin, 1977; Georgii, 1988; Baddeley et al., 2015):

$$\lambda(u) = E[\lambda(u|X)]$$

For a Strauss process:

$$\lambda(u) = \beta E\left[\gamma^{t(u,X,h)}\right]$$

underlying that β is not the intensity function of the Strauss process.

To conclude with, both hard-core and Strauss processes generate dispersing but Gibbs processes can also create clustering. These Gibbs processes with inhibition have interesting implications in physics. At equilibrium, gas molecules repel each other and have a spatial distribution corresponding to a Gibbs process. For a "billiard ball" model, it follows a hard-core process. Finally note that we only reviewed finite Gibbs models i.e. processes with a finite range of interaction h but infinite Gibbs models also exist.

<table>
<tr><th colspan="4">Class of model</th><th>Example(s)</th></tr>
<tr><td rowspan="4">PPP</td><td colspan="3">Homogeneous PPP</td><td>CSR</td></tr>
<tr><td rowspan="3">Inhomogeneous PPP</td><td colspan="2">Simple stochastic PPP</td><td>Determinist intensity function</td></tr>
<tr><td rowspan="2">Double stochastic PPP (Cox process)</td><td>Newman-Scott processes</td><td>Matérn cluster process
Thomas process</td></tr>
<tr><td>Others</td><td>Gaussian random field process</td></tr>
<tr><td rowspan="2">Gibbs</td><td colspan="3">Finite</td><td>Hard-core process
Strauss process</td></tr>
<tr><td colspan="3">Infinite</td><td>Infinite generalizations of Hard-core and Strauss processes</td></tr>
</table>

Table 5. Classification of point processes.

4.3. Model fitting

Once a spatial point pattern is observed, statistical inference by model fitting is interesting for making predictions and to understand the mechanisms causing the pattern. Classical models (Gibbs and Cox processes) can be fitted to the observed dataset. However, it is frequent to postulate that the distribution of points is actually influenced by the distribution of different factors. As an example, the distribution of trees can be explained by the local humidity. Considering the situation where m covariates that could influence the intensity are known ($\theta = \{Z_1(u), Z_2(u), \dots, Z_m(u)\}$). In an

inhomogeneous PPP model, the inhomogeneous intensity function could be a function of the different covariates. Therefore, the fit is given by:

$$\lambda_\theta(u) = f(\theta)$$

Most of the time, the fitting is treated through a loglinear model:

$$\lambda_\theta(u) = e^{f(\theta)}$$

This transformation is only a weak restriction on the different models that can be used, and has several technical advantages, such as to disallow negative intensity values. The fitting is based on the method of maximum likelihood (or its approximation the pseudolikelihood) (Baddeley et al., 2015). Model comparison can be made using the Akaike Information Criterion (AIC, or an analogous quantity when pseudolikelihood is used) quantifying the quality of the fit. AIC is given by:

$$AIC = 2k - 2\ln(L)$$

with k the number of model parameters and L the maximum likelihood. The lower AIC is, the better the fit is. The AIC increases when the number of parameters increases to penalize a lack of parsimony i.e. over-parameterization.

5. Others tools: Moran's I index and variogram

5.1. Moran's I index

The Moran's I index is a measure of the spatial auto-correlation proposed by Patrick Moran (**Figure 56**) (Moran, 1950). Let Z be a field of real values discretized in n sites. The index is computed as:

$$I = \frac{n}{\sum_{i=1}^{n}\sum_{j=1}^{n} w_{ij}} \frac{\sum_{i=1}^{n}\sum_{j=1}^{n} w_{ij}\,(Z_i - \mu)\big(Z_j - \mu\big)}{\sum_{i=1}^{n}(Z_i - \mu)^2}$$

with μ the average of Z values and w_{ij} weights from a square matrix W of size $n \times n$. The weight matrix reflects the distances between pair of sites. There are several strategies to choose this matrix. One can give a weight of 1 (before normalization) for pairs of sites that are immediate neighbors and 0 to the others, or a weight proportional to the inverse of the Euclidian distance between pair of sites. The weight matrix is usually conditioned to have a null diagonal, to be symmetric and to have a sum equal to 1. Counter-intuitively, when sites are independent, the first moment of Moran's I index is not equal to 0 (**Box 6**, note that the variance can also be analytically computed):

$$E[I] = -\frac{1}{n-1}$$

However, this value rapidly converges to 0 when n increases. If sites with similar values are spatially close (positive auto-correlation), the numerator sum tends to be higher, whereas repulsion of sites with similar values (negative auto-correlation) tends to decrease the numerator sum. The Moran's I index is bounded between -1 and 1. Values lower than $-1/(n-1)$ indicate negative auto-correlation whereas values higher than $-1/(n-1)$ indicate positive auto-correlation (**Figure 56**).

Positive (respectively negative) autocorrelation is sometimes named clustering (respectively dispersing) but this terminology should be distinguished from the one used for spatial point patterns.

Box 6: First moment of the Moran's I index

Let us compute the first moment of Moran's I index under independency hypothesis following a demonstration updated from the original publication (Moran, 1950):

$$E[I] = E\left[\frac{n}{\sum_{i=1}^{n}\sum_{j=1}^{n} w_{ij}} \frac{\sum_{i=1}^{n}\sum_{j=1}^{n} w_{ij}\,(Y_i-\mu)(Y_j-\mu)}{\sum_{i=1}^{n}(Y_i-\mu)^2}\right]$$

If the weight matrix is normalized to have a sum equal to 1:

$$E[I] = nE\left[\frac{\sum_{i=1}^{n}\sum_{j=1}^{n} w_{ij}\,(Y_i-\mu)(Y_j-\mu)}{\sum_{i=1}^{n}(Y_i-\mu)^2}\right]$$

Because Y variables are independent, all the pairs $(Y_i-\mu)(Y_j-\mu)$ can be regarded as equivalent (except when $i=j$) and receiving the same weight:

$$w = \frac{1}{n(n-1)}$$

Therefore:

$$E[I] = nE\left[\frac{\frac{1}{n(n-1)}\sum_{i=1}^{n}\sum_{j\neq i}(Y_i-\mu)(Y_j-\mu)}{\sum_{i=1}^{n}(Y_i-\mu)^2}\right]$$

$$E[I] = \frac{1}{n-1}E\left[\frac{\sum_{i=1}^{n}\sum_{j\neq i}(Y_i-\mu)(Y_j-\mu)}{\sum_{i=1}^{n}(Y_i-\mu)^2}\right]$$

This expression can be re-written under the form of a unique sum:

$$E[I] = \frac{1}{n-1}E\left[\frac{(\sum_{i=1}^{n}(Y_i-\mu))^2 - \sum_{i=1}^{n}(Y_i-\mu)^2}{\sum_{i=1}^{n}(Y_i-\mu)^2}\right]$$

We can easily note that $\sum_{i=1}^{n}(Y_i-\mu)=0$ and then:

$$E[I] = -\frac{1}{n-1}$$

A similar index has been proposed by Geary (Geary, 1954):

$$C = \frac{n-1}{\sum_{i=1}^{n}\sum_{j=1}^{n} w_{ij}} \frac{\sum_{i=1}^{n}\sum_{j=1}^{n} w_{ij}\left(Y_i-Y_j\right)^2}{2\sum_{i=1}^{n}(Y_i-\mu)^2}$$

Geary's C ranges between 0 and 2 and is interpreted in the other way around compared to Moran's I: a $C<1$ indicates clustering whereas a $C>1$ indicates dispersing. These indexes can be used to test

auto-correlation. Cliff and Ord demonstrated that Moran's I and Geary's C are asymptotically ($n \geq 50$) normally distributed (Cliff and Ord, 1981). Therefore a Z-test can be established (**Figure 56**):

$$Z = \frac{I - E[I]}{\sqrt{V[I]}} \sim N(0,1)$$

Practically, the computation of Moran's I index could be complicated for large fields. The weight matrix could be too large to be numerically tractable. Assuming that the observed field is a standard image with a resolution of 1024x1024 pixels, it requires a weight matrix with 1024^2 values. If weights are coded by simple precision float numbers, each of them requires 32bits, and the full matrix requires 32×1024^2bit = 4 Mio ≈ 4Mo. Thus, for larger images or dataset with several images, the size of the weight matrix can be a limitation. A strategy to stay computationally cheap is to randomly sample N sites from the field. This Monte-Carlo sampling scheme should achieve a good approximation of the Moran's I index preserving computer resources.

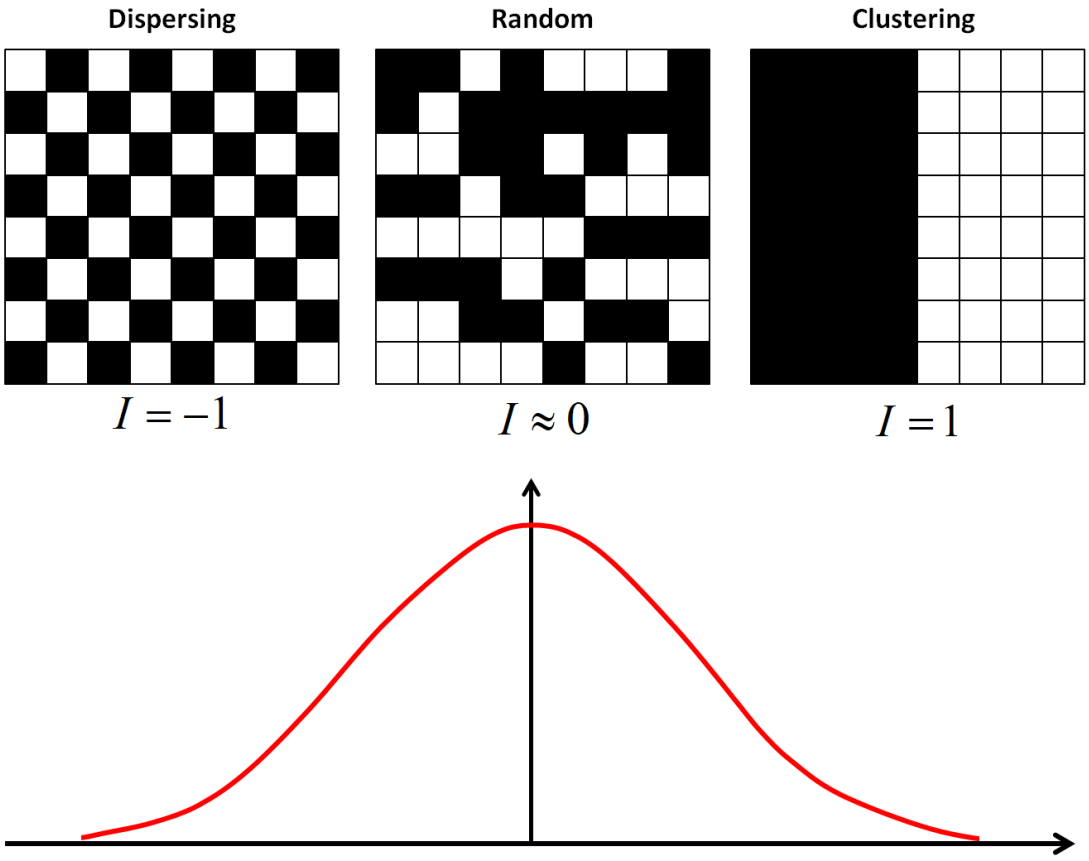

Figure 56. The Moran's I principle. 3 field organizations and the corresponding Moran's I. Lower plot represents the probability to observe the corresponding pattern under independency hypothesis.

5.2. Variogram

The variogram is the fundamental tool of geostatistics. It has been proposed by Georges Matheron in 1963, founding geostatistics (Matheron, 1963). Let $Z(u)$ be an isotropic random field, the variogram

quantifies the divergence as a function of the distances between two localizations (**Figure 57**). For isotropic random fields, the semi-variogram is defined as:

$$\gamma(h) = \frac{1}{2} E_{\|u_1 - u_2\| = h} \left[\left(Z(u_1) - Z(u_2) \right)^2 \right]$$

This quantity is analogous to the opposite of an auto-correlation function. The variogram name is a reference to its relationship with the variance. Noticing that $E_{\|u_1 - u_2\| = h}[Z(u_1) - Z(u_2)]^2 = 0$, we conclude that the semi-variogram is equivalent to the variance

$$\gamma(h) = \frac{1}{2} V_{\|u_1 - u_2\| = h}[Z(u_1) - Z(u_2)]$$

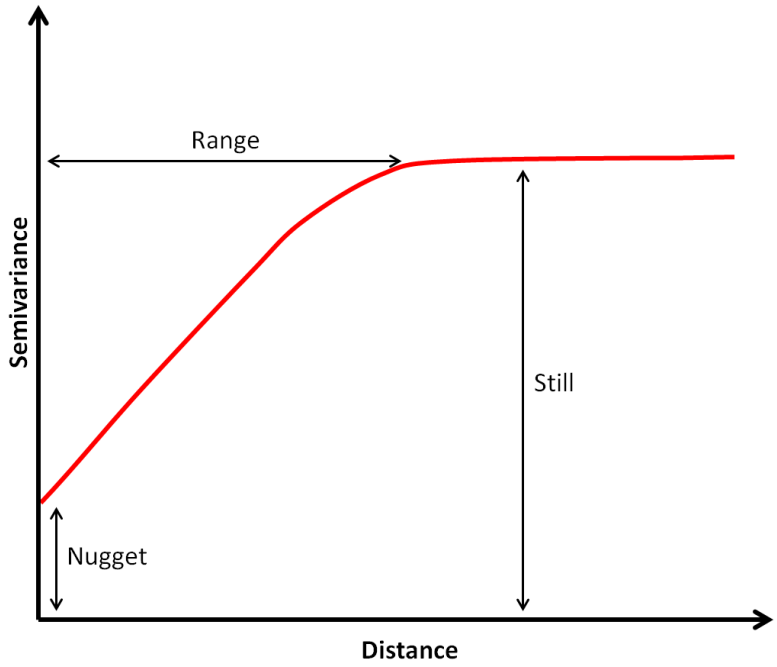

Figure 57. Typical variogram with its three parameters: the nugget, the still and the range.

The variogram curves are usually characterized by 3 parameters: the nugget, the still and the range (**Figure 57**) defined as:

$$nugget = \hat{\gamma}(0)$$

$$still = \lim_{h \to \infty} \hat{\gamma}\,(h)$$

$$still - \hat{\gamma}(range) < \varepsilon$$

The theoretical variogram is null when $h = 0$. However, experimental variogram can be positive. This is due to the intra-site variability but also to the estimator of the variogram:

$$\hat{\gamma}(h \pm \delta) = \frac{1}{2|Q(h \pm \delta)|} \sum_{i,j \in S(h \pm \delta)} \left(Z(u_i) - Z(u_j) \right)^2$$

with $Q(h \pm \delta)$ the list of the location pairs separated by a distance $h \pm \delta$. The estimator of the semi-variogram is discretized. Therefore, the nugget can be due to a brutal variation of a parameter at the

scale δ. The still represents the maximum divergence observed in the field, and the range is the distance necessary to reach a divergence that is extremely close to the still. It represents the distance necessary to cover the full diversity of the field. Most of the time, the divergence increases with the distance, and therefore variograms have a monotonic increase and converge to a limit. In this context, still and range are well defined. A Gaussian random field, such as many other fields, meets these properties. However some fields (e.g. periodic random fields) do not have still nor range and have a periodic variogram so-called “hole effect” (Pyrcz and Deutsch, 2003).

6. Applications

6.1. Ras isoforms distribution

In this section, I will review fruitful applications and refinements of spatial statistics in cell biology : i) the distribution of Ras isoforms , ii) Single Molecule Localization Microscopy and iii) Micropatterning.

Ras proteins are small GTPases associated to the PM. The Ras sub-family contains three isoforms (H-Ras, N-Ras and K-Ras) ubiquitously expressed in mammalian cells. H-Ras and K-Ras have the same effector-binding sites, and they interact with the same set of proteins *in vitro* (Parton and Hancock, 2004). However, these two isoforms generate different signaling outputs *in vivo*. The main hypothesis is that both isoforms are localized in different PM microdomains. Indeed, K-Ras and H-Ras are not homologous in their C-terminal regions that contain the membrane anchor domain. The C-terminal regions have different post-translational modifications according to the isoform (Parton and Hancock, 2004). In brilliant experiments, Prior et al. have investigated the spatial structure of K-Ras and H-Ras at the PM by immunogold EM and spatial statistics (Prior et al., 2003). Using a short-length construct of H-Ras containing the PM targeting motif, the authors showed that the short-length construct forms clusters of dozens of microns at the PM. Cholesterol depletion induced by methyl-β-cyclodextrin leads to a CSR distribution of the short-length H-Ras. Moreover, this short-length H-Ras co-clusters with GPI-proteins, suggesting that it clusters in lipid rafts. The authors have showed that constitutively activated H-Ras does no co-cluster with the short-length H-Ras. Taken together, these data indicate that H-Ras leaves lipid rafts when it is activated. Lastly, authors have showed, using multivariate Ripley’s K function, that K-Ras and H-Ras are clustered in different subdomains. This indicates that K-Ras and H-Ras have different roles, because they are localized in different PM microdomains. A second study by Pezzarossa et al. has also used spatial statistics to study the distribution of H-Ras at PM with super-resolution microscopy and photo-activated probes (Pezzarossa et al., 2015). They confirm that H-Ras is organized in clusters and that the coalescence of cholesterol domains at the PM, leads to an increase of H-Ras cluster size. They estimate that H-Ras clusters are mostly made of less than 10 H-Ras proteins.

6.2. Single Molecule Localization Microscopy

The recent development of super-resolution microscopy, and particularly Single Molecule Localization Microscopy (SMLM), has raised new challenges for spatial statistics. SMLM does not generate fluorescence intensity images but point clouds corresponding to molecule localizations. This point cloud is perfectly suitable for spatial statistics (Nicovich et al., 2017). Applying Ripley's analysis for cluster detection on SMLM data is common. Indeed, 50% of the papers describing SMLM cluster analysis between 2010 and 2019 used Ripley's K function or a related function (Khater et al., 2020). Especially, a local adaptation of Ripley's K function developed by Getis & Franklin is common (Getis and Franklin, 1987):

$$L_j(r) = \sqrt{\frac{|W|}{(n-1)}\sum_{i \neq j} 1_{\|x_i - x_j\| \leq r}}$$

This function corresponds to an analysis of the spatial structure around a unique point j using the L function. There is an easy relation between this local adaptation and the L function:

$$L(r) = \sqrt{\frac{1}{n\pi}\sum_{j=1}^{n} L_j(r)^2}$$

Spatial statistics have been mostly used to study the clustering of proteins at the PM. In the context of molecular clustering, the radius of the cluster could be approximated by the radius that corresponds to the maximum of the Ripley's K function (Kiskowski et al., 2009). In the context of SMLM, it has been reported that Ripley's K function analysis could underestimate the cluster size by a factor of 1.3 (Ruan et al., 2019).

6.3. Micropattern and density maps

One of the big challenges in the study of the spatial organization of the cell is to correctly take in consideration its shape. Edge corrections can circumvent biases introduced by the cell's geometry. Yet, the diversity of shapes increases the cell-to-cell variability. One way to reduce this variability is to culture cells on adhesive surface of well-defined shapes, so-called micropatterns. Micropatterns normalize the cell's shape and control the intracellular organization without impairing the functions of the cell (Théry et al., 2006a, 2006b). It facilitates the establishment of a stereotypical density map representing the distribution of organelles or proteins (Schauer et al., 2010b). This probabilistic density map is the 3D KDE of the point coordinates of organelles obtained by segmentation from cell images. This KDE approach produces a density f related to intensity function by:

$$f(u) = \frac{\lambda(u)}{n}$$

These maps can be used to compare spatial distributions of organelles or proteins between conditions. Especially, one can plot the minimal volume containing a given percentage (e.g. 90%) of

the density defining a “characteristic territory”. These territories can be qualitatively compared between conditions to detect change in the spatial organization of a given organelle. A robust test that is asymptotically normal under the null hypothesis has been developed to compare rigorously different conditions (Duong et al., 2012). This method is compatible with a high-throughput pipeline (Schauer et al., 2014). Recently, Pécot et al. have pointed out that the density map test is too sensitive (Pécot et al., 2018). Using also cells cultured on micropatterns, they propose to compare cells using a test based on Earth Mover’s Distance (EMD). Unfortunately, simulations reveal that this test does not have a uniform p-value distribution under the null hypothesis, leading to a specificity problem (Lachuer et al., 2020). The density map method has been nicely used and produced interesting results (Vonaesch et al., 2013; Grossier et al., 2014; Alanko et al., 2015). For example, density maps revealed a cellular dorso-ventral asymmetry in endocytic sites. Transferrin endocytosis sites are enriched at cell adhesions whereas epidermal growth factor endocytosis sites are restricted to the dorsal cell surface (Grossier et al., 2014). Moreover, comparison of density maps has recently been used to identify morphological changes of the Golgi complex after systematic depletion of myosin motors (Capmany et al., 2019).

Results

Lachuer et al. J Vis Exp. 2020

Quantifying Spatiotemporal Parameters of Cellular Exocytosis in Micropatterned Cells

"Nothing in the universe is contingent, but all things are conditioned to exist and operate in a particular manner by the necessity of the divine nature. [...]A thing can in no respect be called contingent, save in relation to the imperfection of our knowledge."

Baruch Spinoza, Ethics, Proposition XXIX and note to Proposition XXXIII (1677).

Abstract:

Live imaging of the pHluorin-tagged Soluble N-ethylmaleimide-sensitive-factor Attachment protein REceptor (v-SNARE) Vesicle-associated membrane protein 7 (VAMP7) by total internal reflection fluorescence microscopy (TIRFM) is a straightforward way to explore secretion from the lysosomal compartment. Taking advantage of cell culture on micropatterned surfaces to normalize cell shape, a variety of statistical tools was employed to perform a spatial analysis of secretory patterns. Using Ripley's K function and a statistical test based on the nearest neighbor distance (NND), we confirmed that secretion from lysosomes is not a random process but shows significant clustering. Of note, our analysis revealed that exocytosis events are also clustered in non-adhesion areas, indicating that adhesion molecules are not the only structures that can induce secretory hot spots at the plasma membrane. Still, we found that cell adhesion enhances clustering. In addition to precisely defined adhesive and non-adhesive areas, the circular geometry of these micropatterns allows the use of polar coordinates, simplifying analyses. We used Kernel Density Estimation (KDE) and the cumulative distribution function on polar coordinates of exocytosis events to identify enriched areas of exocytosis. In ring-shaped micropattern cells, clustering occurred at the border between the adhesive and non-adhesive areas. Our analysis illustrates how statistical tools can be employed to investigate spatial distributions of diverse biological processes.

Quantifying Spatiotemporal Parameters of Cellular Exocytosis in Micropatterned Cells

Hugo Lachuer[1,2,3], Pallavi Mathur[1,2,3], Kevin Bleakley[4], Kristine Schauer[1,2,3]

[1] Unité Mixte de Recherche 144 CNRS, Molecular Mechanisms of Intracellular Transport group, Institut Curie, 75005 Paris, France

[2] PSL Research University, Paris, France

[3] Sorbonne Université, Paris, France 4 INRIA, Université Paris-Sud, PSL

Corresponding Author: Kristine Schauer (kristine.schauer@curie.fr)

Citation: Lachuer, H., Mathur, P., Bleakley, K., Schauer, K. Quantifying Spatiotemporal Parameters of Cellular Exocytosis in Micropatterned Cells. J. Vis. Exp. (163), e60801, doi:10.3791/60801 (2020).

Date Published: September 16, 2020

DOI: 10.3791/60801

URL: jove.com/video/60801

Abstract

Live imaging of the pHluorin tagged Soluble N-ethylmaleimide-sensitive-factor Attachment protein REceptor (v-SNARE) Vesicle-associated membrane protein7 (VAMP7) by total internal reflection fluorescence microscopy (TIRFM) is a straightforward way to explore secretion from the lysosomal compartment. Taking advantage of cell culture on micropatterned surfaces to normalize cell shape, a variety of statistical tools were employed to perform a spatial analysis of secretory patterns. Using Ripley's K function and a statistical test based on the nearest neighbor distance (NND), we confirmed that secretion from lysosomes is not a random process but shows significant clustering. Of note, our analysis revealed that exocytosis events are also clustered in nonadhesion areas, indicating that adhesion molecules are not the only structures that can induce secretory hot spots at the plasma membrane. Still, we found that cell adhesion enhances clustering. In addition to precisely defined adhesive and nonadhesive areas, the circular geometry of these micropatterns allows the use of polar coordinates, simplifying analyses. We used Kernel Density Estimation (KDE) and the cumulative distribution function on polar coordinates of exocytosis events to identify enriched areas of exocytosis. In ring-shaped micropattern cells, clustering occurred at the border between the adhesive and nonadhesive areas. Our analysis illustrates how statistical tools can be employed to investigate spatial distributions of diverse biological processes.

Introduction

Exocytosis is a universal cellular process in which a vesicle fuses with the plasma membrane and releases its content. The vesicle can either fuse totally with the plasma membrane (full fusion) or create a fusion pore that stays open during a limited time (kiss-and-run)[1] . For instance, newly synthesized proteins are released into the extracellular medium from vesicles that come from the Golgi complex. This biosynthetic, anterograde pathway is primordial, especially in multicellular organisms, to secrete signaling peptides (e.g., hormones, neurotransmitters) and extracellular matrix components (e.g., collagen), as well as to traffic transmembrane proteins to the plasma membrane. Additionally, secretions can occur from different endosomes: 1) recycling endosomes in order to reuse transmembrane proteins; 2) multivesicular bodies (MVBs) to release exosomes; and 3) lysosomes for the release of proteolytic enzymes. Endosomal secretion has been shown to be important for neurite outgrowth, pseudopodia formation, plasma membrane repair, and ATP-dependent signaling[2].

To study exocytosis at the single cell level, several techniques have been employed. Patch-clamp allows for the detection of single exocytosis events with a high temporal resolution in a wide variety of living cells[3]. However, this method does not provide information on the localization of exocytosis events, nor from which compartment it occurs. Electron microscopy allows direct visualization of exocytic events with high spatial resolution, and in combination with immunolabeling provides information about the specificity of the compartments and molecules involved. A disadvantage of this approach is the lack of information on the dynamics of the process, as well as its inability to perform high-throughput studies. Light microscopy approaches such as total internal reflection fluorescence microscopy (TIRFM), which exploits the evanescent field to illuminate fluorophores at the vicinity of the coverslip (100 nm), provides good temporal and spatial resolution to study exocytosis events. However, this method is only compatible with adherent cells and can only be applied to the ventral/inferior part of cells.

Of note, the plasma membrane reveals significant heterogeneity based on adhesive complexes that are present only in restricted areas. This heterogeneity restricts, for instance, the uptake of different ligands[4]. Similarly, it has recently been reported that secretion from the Golgi complex is concentrated at “hot spots” in the plasma membrane[5]. Moreover, it is known that certain cargos are secreted through focal-adhesion-associated exocytosis[6]. Thus, special attention should be paid to the question of whether exocytosis events are randomly distributed in space, or whether they are concentrated at specific areas of the plasma membrane. Several statistical tools based on Ripley’s K function have been proposed to explore these questions[7,8,9]. Our approach combines these tools with micropatterning to control cell shape and plasma membrane heterogeneity. In addition to providing a means to distinguish between adhesive and nonadhesive areas, this technique also allows comparison across different cells and conditions and increases the power of statistical analyses.

Here we employ a variety of statistical tools to study the spatial distribution of exocytosis events from the lysosomal compartment monitored by TIRFM live cell imaging of VAMP7-pHluorin in ring-shaped micropattern- normalized hTert-RPE1 cells. It was confirmed that secretion from lysosomes is not a random process[8,9] and that exocytosis events exhibit clustering. Of note, we

found that exocytosis events are also clustered in nonadhesive areas, indicating that adhesion molecules are not the only structures that can induce secretory hot spots at the plasma membrane. Nevertheless, cell adhesion did enhance clustering. Consistently, our analysis identified enriched areas of exocytosis that were located at the border between the adhesive and nonadhesive areas.

Protocol

1. Preparation of micropatterned cells

1. Transfection of cells

1. One day before transfection, seed 2.5 x 10^6 hTERT-RPE1 cells into one well of a 12 well plate (2 x 2 cm)in 1 mL of medium.

2. On the day of transfection, prepare the transfection mixture with VAMP7-pHluorin plasmid (100 µL ofbuffer, 0.8 µg of DNA, 3 µL of transfection mixture). Incubate for 10 min.

NOTE: VAMP7 is a lysosomal v-SNARE, fused with aluminal pHluorin tag. The pHluorin probe is quenchedby low pH, but during exocytosis protons are releasedand pHluorin starts emitting a signal[10,11] .

3. Add the transfection mix to the cells in their medium.

4. Change the medium 4 h after adding the transfectionmix on the cells.

5. Use the cells for experiments during the next 24–48 h.

2. Micropattern preparation (photolithography method)

1. Wash the coverslips (25 mm of diameter) in ethanol and let them dry for 5 min.

2. Activate coverslips by illumination under deep UV for5 min.

3. Create a humid chamber by thoroughly humidifyinga paper towel on which a paraffin film is placed. Add drops (30 µL for 22 mm coverslip) of Poly-L-Lysine-graft-Polyethylene Glycol (PLL-g-PEG) solution (0.1 mg/mL, 10 mM HEPES, pH = 7.4) and place coverslips with the activated surface on them. Close the humid chamber with a top and incubate coverslipsfor 1h.

4. Wash coverslips 2x in PBS and 1x in distilled water and let them dry.

5. Wash the quartz photomask with distilled water and then with ethanol or propanol. Dry the photomask withfiltered airflow.

NOTE: The quartz photomask is coated on one side with antireflective chrome that contains holes in the form of micropatterns. A photomask containing ring-shaped micropatterns of 37 µm is used in this protocol. When deep UV is shined on the photomask, the light can only pass through these holes[12].

6. Expose the photomask (chrome-coated side) to deepUV for 5 min to clean the surface.

7. Add small water drops (10 µL for a 20 mm coverslip)on the chrome-coated side of the photomask. Placethe coverslip with their PLL-g-PEG-treated side on thedrop and dry the extra water. Make sure that no airbubbles form between the mask and the coverslips. NOTE: The capillary force of the water will immobilizethe coverslips.

8. Expose the photomask to deep UV for 5 min withthe non-chrome-coated side up (the coverslips are attached on the lower surface).

NOTE: The light can only pass through the holes andmodify the PLL-g-PEG-treated surface of coverslips below the photomask.

9. Remove the coverslips from the photomask by addingexcess water.

NOTE: Coverslips should quickly float off.

10. Incubate the coverslips in a solution of extracellularmatrix proteins (50 µg/mL of fibronectin, 5 µg/mL of fluorescent fibrinogen diluted in water) on paraffin filmin a humid chamber (as in step 1.2.3) for 1 h under alaminar flow hood to avoid contamination.

NOTE: The experiment can be paused at this point bystoring the coverslips in PBS at 4 °C.

3. Cell seeding on micropatterned surfaces

1. Use a magnetic coverslip holder that fits the size of the micropatterned coverslips to mount the coverslips.On the day of acquisition, heat the coverslip holderto 37 °C to avoid thermal shock for the cells during subsequent steps.

2. Prepare the pattern medium by supplementing DMEM/F12 medium with 20 mM HEPES and 2% of penicillin/streptomycin.

3. Place coverslips into the holder with the micropatterned side up and add pattern medium as soon as the coverslip is on the holder base. Add the seal and immobilize with the magnetic device. Fill thecoverslip holder with the pattern medium and close itwith the glass lid.

NOTE: Be quick, to not allow the coverslip to dry. Donot wash the coverslip holder with ethanol between experiments, because the seal might retain some ethanol, which can react with PLL-g-PEG and result in cell stress. Wash the coverslip holder only with soapy water. Moreover, the joint can be incubated inthe pattern medium at 37 °C for 1 h to dilute residual product.

4. Collect transfected hTERT-RPE1 cells by trypsinization (0.5 mL for one 12 well plate) and add 1 mL of 10% FBS DMEM/F12 medium.

5. Add 0.5 x 10^6 transfected hTERT-RPE1 cells to the coverslip holder and reclose it. Incubate for 10 min inthe incubator.

6. Wash the coverslip holder 5x with pattern medium toremove nonattached cells and residual FBS by addingthe pattern medium with one pipette and aspirating the medium with another pipette to create a washingflow. Always keep a small volume of pattern mediumin the coverslip holder to avoid drying of the cells on the micropatterned coverslip, which will lead to cell death.

7. Incubate in the incubator for 3 h to allow full cell spreading.

2. Acquisition of exocytosis data

1. Imaging of exocytosis events

1. Place coverslip holder under a TIRM. The signal hasto be detected by a sensitive camera set up with the best imaging format available.

NOTE: In this experiment, a 100x lens objective and an EMCCD camera with 512 x 512 pixel detection region was used giving rise to a pixel size of 160 nm.

2. Search for a cell expressing VAMP7-pHluorin that is fully spread (**Figure 1A**).

NOTE: Cells expressing VAMP7 are clearly identifiable, because they exhibit a green signal.

3. Change the angle of the laser until a TIRF anglethat allows the visualization of VAMP7-pHluorin exocytosis events is reached. Perform a 5 min acquisition at a frequency compatible with the exocytosis rate and time scale (typically 3 Hz, **Figure1D**) using the microscope software.

NOTE: hTERT-RPE1 cells have a lysosomal secretory rate of around 0.3 Hz on micropatterns. Lysosomal exocytosis has a typical duration of 1 s.It is characterized by a peak intensity followed by an exponential decay. The diffusion of the probe shouldbe evident at this time (**Figure 1B**, **C**).

4. For each cell, also perform an acquisition of themicropattern using the microscope software (**Figure 1A**).

2. Acquisition of exocytosis coordinates

1. Open the acquired movie with ImageJ/FIJI. Use **File**| **Import** | **Image Sequence**. Find exocytosis events by eye. An exocytosis event is characterized by the appearance of a bright signal that spreads outwards (**Figure 1**).

2. Use the point tool to mark the center of the exocytic event. Use **Analyze** | **Measure** to measure X andY coordinates, as well as the temporal coordinate (slice number). Perform these measurements for all exocytosis events of the movie.

3. Save the results (**Results** | **File** | **Save As**). Prepare a text file for each analyzed cell named "Results(cell_name).txt" that contains the slice, X coordinates, and Y coordinates for all exocytosisevents in that order.

The text file is supposed to look like this:

ID	X	Y	Feret's diameter	Radius
RPE1_WT_Cell1	167	136	230	115
RPE1_WT_Cell2	164	160	230	115

NOTE: Be careful to replace all commas with points.

4. Measure the center and diameter of each cell using the "**Oval Tool**". Fit a perfect circle (do not use an oval) and use "**Measure**" to obtain the X and Y coordinates and Feret's diameter.

5. Save each cell's identity (ID), X and Y coordinates, Feret's diameter, and radius (diameter/2) in a text file named "Sphericalparameter.txt".

The text file is supposed to look like this:

ID X Y Feret's diameter Radius

RPE1_WT_Cell1167 136 230 115

RPE1_WT_Cell2164 160 230 115

NOTE: Be careful to replace all commas with points.

6. Measure the thickness of the micropattern ring (adhesion length) with the straight tool and savethe cell ID, cell radius (from the file: "Spherical parameter.txt"), and adhesion length in a text file named "Pattern parameter.txt". Calculate the normalized adhesion length by dividing the adhesionlength by cell radius.

NOTE: Be careful to replace all commas by points.

The file should look like this:

ID	Cell radius	adhesion length	Normalized adhesion length
RPE1_WT_Cell1	115	34	0.295652174
RPE1_WT_Cell2	115	35	0.304347826

3. Single cell spatial analysis

1. R package and installation

NOTE: The R package for this analysis takes advantageof the Spatstat package[13] to compute the two-dimensional (2D) density and Ripley's K function. The code is open-source and uses text files that have been previously described.

1. Download and install R from https://www.r-project.org/ (version 3.5.2 was used in this analysis).

2. Download the package (and the demo dataset) from:https://github.com/GoudTeam/JoVE-paper

3. Install the package on R Studio using "**Tools**" using "**Install Packages**". Select "**Package Archive File (.zip; .tar.gz)**" for the category "**Install from:**" and choose the package file. Press "**Install**".

4. Load the package with the function "**library("ExocytosisSpatialAnalysis")**" by writing this command in R studio and pressing "**Enter**".

5. Run the package with the function "**ESA()**" by writingthis command in R studio and pressing "**Enter**". NOTE: A user interface will open.

6. Select the directory for the dataset (.txt files) and adirectory for output plots.

NOTE: Parameters of the analysis (see text below)can be changed through a user interface.

7. This script will automatically start and perform the analysis. It provides .pdf files of corresponding plots and .txt files containing numerical results.

Representative Results

The spatiotemporal characteristics of exocytosis events were analyzed from lysosomes visualized by VAMP7- pHluorin[10,11] in hTert-RPE1 cells. hTert-RPE1 cells are nontransformed cells that adopt well to micropatterning and have been extensively used in previous micropattern-based studies[4,14]. VAMP7 is a lysosomal v-SNARE[15] that was tagged with the super ecliptic pHluorin at its N-terminus and is located in the lumen of the lysosome. Inside the cell, the pHluorin probe was quenched by the low pH of the lysosome, but during exocytosis pHluorin started to emit a signal because the pH increased due to proton release. VAMP7- pHluorin was monitored by TIRFM live cell imaging on ring-shaped micropatterns (**Figure 1A**–**B**). The pHluorin signal exhibited a peak during exocytosis that represented the fast release of lysosomal protons followed by exponential decay,representing the 2D diffusion of the probe at the plasma membrane (**Figure 1C**). hTERT-RPE1 cells presented an important lysosomal secretion activity with an averaged exocytosis rate of 0.28 Hz (**Figure 1D**). However, high heterogeneity was observed in the exocytosis rate across cells (standard deviation of 0.15 Hz), indicating that there wasstrong cell-to-cell variability in secretion from the lysosomes.

Single cell spatial analysis to investigate whether exocytosis of lysosomes is random

It was possible to visualize the 2D distribution of exocytosis by KDE, as previously performed for endomembranous compartments[14], which could reveal differences in local densities (**Figure 2B**). This approach is pertinent for visualization of the average distribution of a population of cells, but less informative in single cells due to the limited number of events detected (tens versus the several thousandobtained by population-based analysis) and high cell-to- cell variability. For instance, this approach did not allow us to evaluate whether the distribution of exocytosis events followed a complete spatial randomness (CSR) behavior (i.e.,corresponded to a uniform point distribution in an observed region for a single cell). A points pattern follows a CSR behavior when the two following hypotheses are true: 1) each point's location is independent of that of the other points; and 2) the probability to find a point in a subregionis only dependent on the ratio between this subregion's area and the total area. There are three possible deviations from CSR: 1) clustering (i.e., aggregation); 2) dispersion(i.e., ordering with constant distance); or 3) a mixture of clustering and dispersion (**Figure 2C**). Ripley's K function was used to answer this question as in previous analyses[7,8,9] (**Figure 2D**). Ripley's K function is close to πr^2 (with d being the normalized distance from an event) in the case of CSR, but superior (respiratory inferior) to πr^2 in the case of clustering (respiratory dispersion). By subtracting πr^2 from Ripley's K function, the theoretical CSR curve should be at 0. Simulations of CSR cases were performed using the samenumber of points as the observed exocytosis events to assess the goodness-of-fit for the CSR case (gray envelope around the theoretical curve). The transformed Ripley's K function applied to the experimental data exhibited positive values outside the envelope, indicating clustering (**Figure 2D**).

To investigate if clustering of exocytosis events was dueto cell adhesion as previously reported[6] , we performed a similar analysis on data from exclusively the nonadhesive cell area in the center (**Figure 2A**, adhesive area in gray, nonadhesive cell center area in white). Of note, we found that exocytosis events in the nonadhesive area were also clustered (**Figure 2E**), indicating that adhesion molecules were not the only structures that induced secretory hot spotsat plasma membranes.

Because Ripley's K function is a descriptive statistic that doesnot provide a p-value, a statistical test was set up comparingcellular exocytosis events with CSR simulations. The nearestneighbor distance NND(i) method was used. NDD is definedas the minimal Euclidian distance between a point i and all other points. The average NND(i) from all exocytic eventsof one cell was computed and compared to CSR obtained with a high number of Monte Carlo simulations (**Figure 2F**). We found that the average NND of the single cell analyzedin **Figure 2F** was lower than the average of the simulated distribution of the CSR case, indicating closer neighbors on average and thus clustering. In the case of dispersion, a higher value for the average NND was expected (**Figure 2C**). This comparison allowed the calculation of a p-value for each cell. The p-value represents the percentage of simulations that exhibited a more extreme NND (in a two-sided way).To be precise, the unbiased p-value was computed as (k+1)/(N+1) with N being the total number of Monte-Carlosimulations (10,000), and k the number of these simulations that was more extreme than the observed measurent[16] . The histogram of all p-values was plotted for the total cell area (**Figure 2G**) and the nonadhesive cell area (**Figure 2I**). If H_0: "Exocytosis is a CSR process" was true, a uniform distribution of p-values was expected. If H_0 was false, a peakat a low p-value was expected. Performing a Kolmogorov-Smirnov test on the p-value histograms, a p-value inferior to 0.001 was obtained, showing a significant deviation from CSRin both cases (**Figures 2G** and **2I**). Moreover, a clustering coefficient of 0.955 for the total cell area and 1.000 for the nonadhesive cell area indicated that lysosomal exocytosis was a clustered process independent of cell adhesion. The clustering coefficient represents the percentage of cells that were closer to a clustering behavior than dispersion. This result was consistent with Ripley's K function.

To evaluate the role of cell adhesion in clustering, we compared the average NND in the nonadhesive area with that in the overall area for each individual cell (**Figure 2H**). Because the average NND was inversely proportional tothe surface density, we normalized the average NND of the nonadhesive area using homothety. The significantlylarger average NND of exocytosis events in the nonadhesive area indicated less clustering (**Figure 2H**). Thus, although secretion from lysosomes clusters in nonadhesive areas, celladhesion seemed to enhance clustering.

Spatial analysis of exocytosis events using polarcoordinates

The circular geometry of the ring-shaped micropattern allowed the use of the common polar coordinates, which simplified analyses, as previously found[17]. Each exocytosis event could thus be described by a modulus (distance from the origin, here the center of the lower plane of the cell) and an angle (according to a fixed arbitrary axis). Additionally, the modulus can be normalized by dividing it by the radiusof the cell. The histogram of exocytosis events was plotted according to the modulus for a representative cell (**Figure 3A**). This revealed a peak around the border between the adhesive/nonadhesive areas. A large variability between cellswas also observed. Therefore, we pooled n = 22 cells to obtainan average distribution of exocytosis events. However, in order to give the same statistical weight to each cell, the samenumber of events from each cell was randomly selected. This random selection did not change the overall patterns seen. To obtain a continuous average

distribution of the individual distributions of single cells, a KDE was used (**Figure 3B**). However, because the normalized modulus is between 0 and 1, edge conditions had to be taken into consideration. A beta kernel that changes shape next to edges was used[18]. An error band was computed with a bootstrap strategy. The observed average distribution was compared to a hypothetical CSR distribution that showed more events at a higher modulus, because the area increased with a higher modulus. Because the integral of a probability density should be one, the CSR distribution was 2r (with r the normalized radius, without units). A confidence band was computed around the theoretical curve using a large number of CSR Monte Carlo simulations (5,000 each). The 1^{st} and 99^{th} percentiles of the modulus distribution from these simulations were plotted. We found that the average distribution of exocytosis events deviated from the hypothetical one at $0.7r_{max}$, which corresponds to the beginning of the adhesive area of the cell.

We sought to test whether the observed distribution of the modulus was different from the theoretical one. Because average distributions, as in this case, cannot be accurately tested by a goodness-of-fit test (e.g., Kolmogorov-Smirnov) an alternative method proposed by Pecot et al. was employed. This method measures the difference between the variation across a population and the variation inside a population, and thus allows independent testing for each coordinate (i.e., modulus and angle)[17] . This test was used to compare our data to simulated data representing CSR exocytosis events (the same number of cells and exocytosis events as the observed data), and found a statistically significant difference in the variations ($p < 0.001$ with the Wilcoxon-Mann-Whitney test, $n = 22$ cells), indicating that the observed average exocytosis distribution was not CSR. However, when two CSR simulations (with 5,000 simulations each) were compared, we found that the p-value histogram did not show a uniform distribution, but exhibited a peak near 1, indicating that this test probably lacked sensitivity.

Because the KDE estimation relies on a non-trivial choice of kernel bandwidth and is sensitive to edge effects, the cumulative distribution function was also computed, which overcomes the problems inherent in KDE estimation (**Figure 3D**). This function is defined between 0 and 1 and does not contain any arbitrary parameters or biases (e.g., edge biases). Error and confidence bands were computed in the same way as for the modulus distribution. The cumulative distribution function confirmed that exocytosis events did not follow a CSR distribution but were overconcentrated at moduli around $0.7r_{max}$. This analysis thus allowed us to identify cellular areas where clustering occurred. An interesting question that this result raises is whether the overconcentration at $0.7r_{max}$ was because of the presence of adhesive/nonadhesive areas of the ring-shaped micropattern or an effect of peripheral/central secretion areas of cells.

As the average distribution of exocytosis events deviated from the CSR case in nonadhesive as well as adhesive areas, we also wondered where the exocytosis density was highest. The surface densities of exocytosis in adhesion and nonadhesion areas were computed and compared. We found that the surface density was lower in the adhesion area than in the nonadhesion area by a paired analysis (**Figure 3C**). This could be explained by the strong decrease of exocytosis at the cell periphery ($0.85 – 1r_{max}$, **Figure 3B**).

Discussion

We monitored exocytosis events from the lysosomal compartment by TIRFM live cell imaging of VAMP7-pHluorin in ring-shaped micropattern-normalized cells and performed a rigorous statistical analysis of the spatial parameters of exocytosis events. Employing the transformed Ripley's K function and a statistical test based on the nearest neighbor distance, we confirmed that secretion from lysosomes is not a random process[8,9]. Both statistical analyses convincingly showed that exocytosis events exhibit clustering (**Figures 2D** and **2G**). Applying similar tools to the nonadhesive cell area, we found that exocytosis events are also clusteredin nonadhesive areas (**Figures 2E** and **2I**). Thus, adhesion molecules that have been previously reported to allow clustering[6] are not the only structures that can induce secretory hot spots at the plasma membrane. However, cell adhesion enhanced clustering: the average nearest neighbor distance between exocytosis events was significantly larger in nonadhesive areas (**Figure 2H**). Consistently, our analysisbased on kernel density estimation and the cumulative distribution function identified enriched areas of exocytosis that were located at the border between the adhesive and nonadhesive areas in ring-shaped micropattern cells. More work is necessary to determine the molecular mechanisms underlying clustering, such as adhesion or a specific targeting of lysosome to this region. Interestingly, we observed high heterogeneity in the exocytosis rate across hTERT- RPE1 cells (standard deviation of 0.15 Hz for average exocytosis rate of 0.28 Hz, **Figure 1D**), indicating that secretion from lysosomes has high intercellular variation. Therefore, subpopulation analyses should be consideredin future work. It would be particularly interesting to investigate if this variation reflects the diversity of lysosomal compartments, differences in cargos, or dependence on exocytosis machinery.

These results illustrate how statistical tools can be employed to investigate spatial parameters of diverse biological processes. Moreover, micropatterns facilitate the study of the effect of cell adhesion in an unbiased manner with the help of different micropattern geometries (e.g., ring-shaped versus diskshaped). In particular, the use of round shapes facilitates analyses because polar coordinates can be employed. Because statistical tools require a certain amount of data to be meaningful, cells with more than 30 events wereused for our analysis. However, there is a possibility that cells with 30 or fewer events are meaningful. Thus, samplingcells with 30 or fewer events could be performed in order to obtain sufficient events for analysis to determine if this is the case. Similarly, it is difficult to estimate how many cells should be analyzed, particularly if there is strong intercellularvariation. One way to circumvent this is to randomly select the same number of events from each cell in order to give the same statistical weight to each cell when pooling them. However, we recommend that analyses on fewer than 15 cells be done with precaution. As average distributions of pooled cells cannot be accurately tested by goodness-of-fit tests (e.g., Kolmogorov-Smirnov) we employed a test statistic proposed by Pecot et al. that measures the difference in variations of populations[17]. Although this test allowed us to find a statistically significant difference in the variations inthe average distributions, we suspect that this test has low sensitivity because the p-value histogram was not flat (i.e., showed uniform distribution) when comparing different CSR simulations for p values close to 1. Therefore, this statistical procedure may need to be improved.

One drawback to our analyses is the manual detection of exocytosis events, which drastically reduces the speed of the analysis. Limitations in automatic detection are often due to strong heterogeneity in the unique and simple parameter being analyzed (e.g., intensity of exocytosis

events). Neural networks could be potentially powerful for automatic detection, because they can be trained to recognize many features.

The analysis presented here can be applied to other dynamic processes observed by TIRFM, such as secretion from other compartments and the distribution of the membrane microdomain or antigen presentation. Similar analyses can also be applied to fixed cells in order to study the spatial distribution of proteins. We hope that our work will enhance the increasing interest in spatial distribution analysis in cell biology.

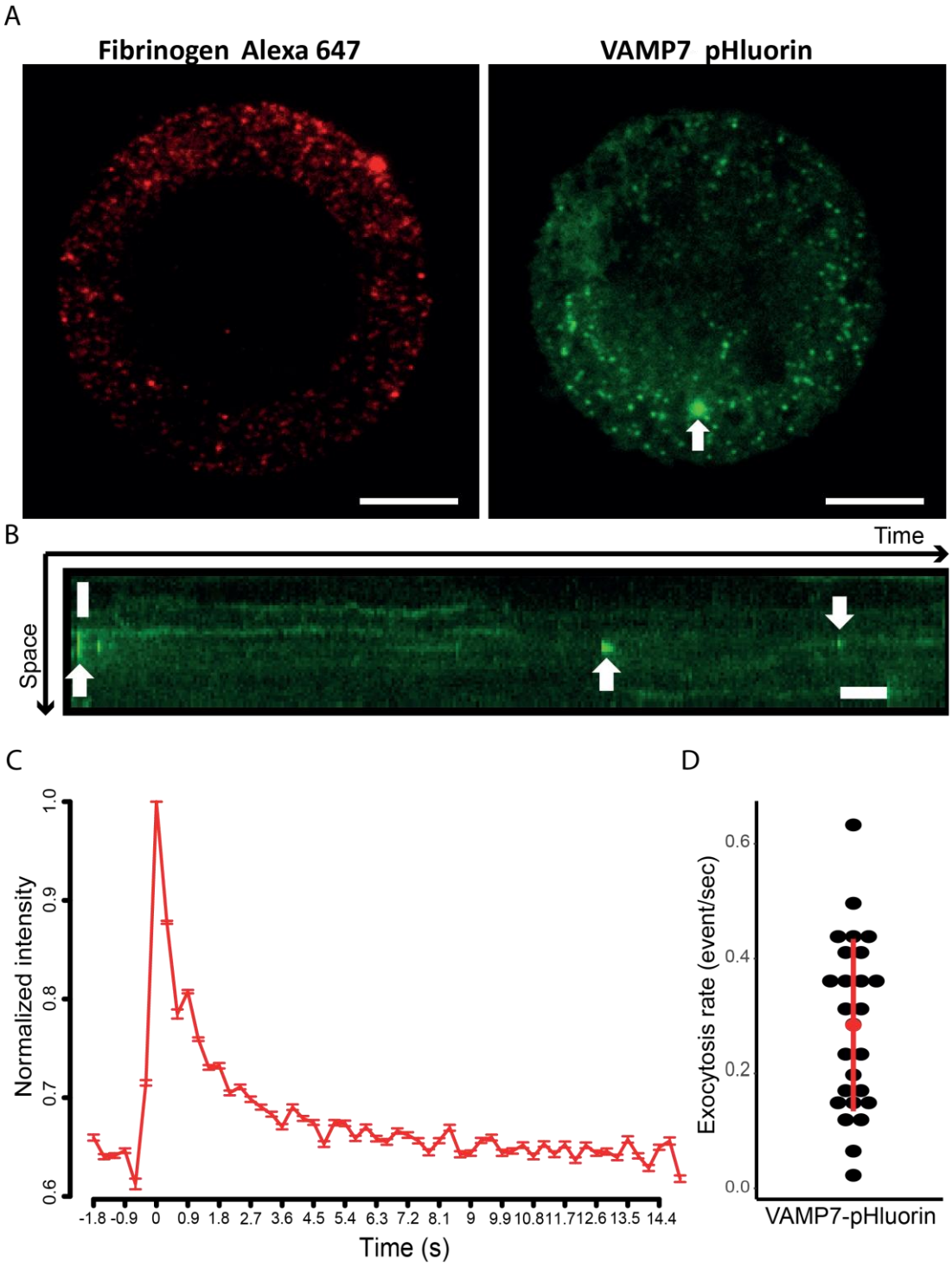

Figure 1. Exocytosis from lysosomes in hTert-RPE1 cells: (**A**) Ring-shaped micropattern (red) and adhesive hTert- RPE1 cell transfected with VAMP7-pHluorin (green) imaged by TIRFM. The arrow shows an exocytosis event. Scale bars = 10 µm. (**B**) Kymograph of exocytosis events. Arrows show exocytosis events. Scale bar = 2 µm, scale bar in time = 5s. (**C**) Normalized intensity profile of lysosomal exocytosis from 22 cells. Each point is an average of at least 1,530 exocytosis events. Data are presented ± SEM. (**D**) Exocytosis rate of the 22 cells. The average +/- standard deviation is plotted in red.

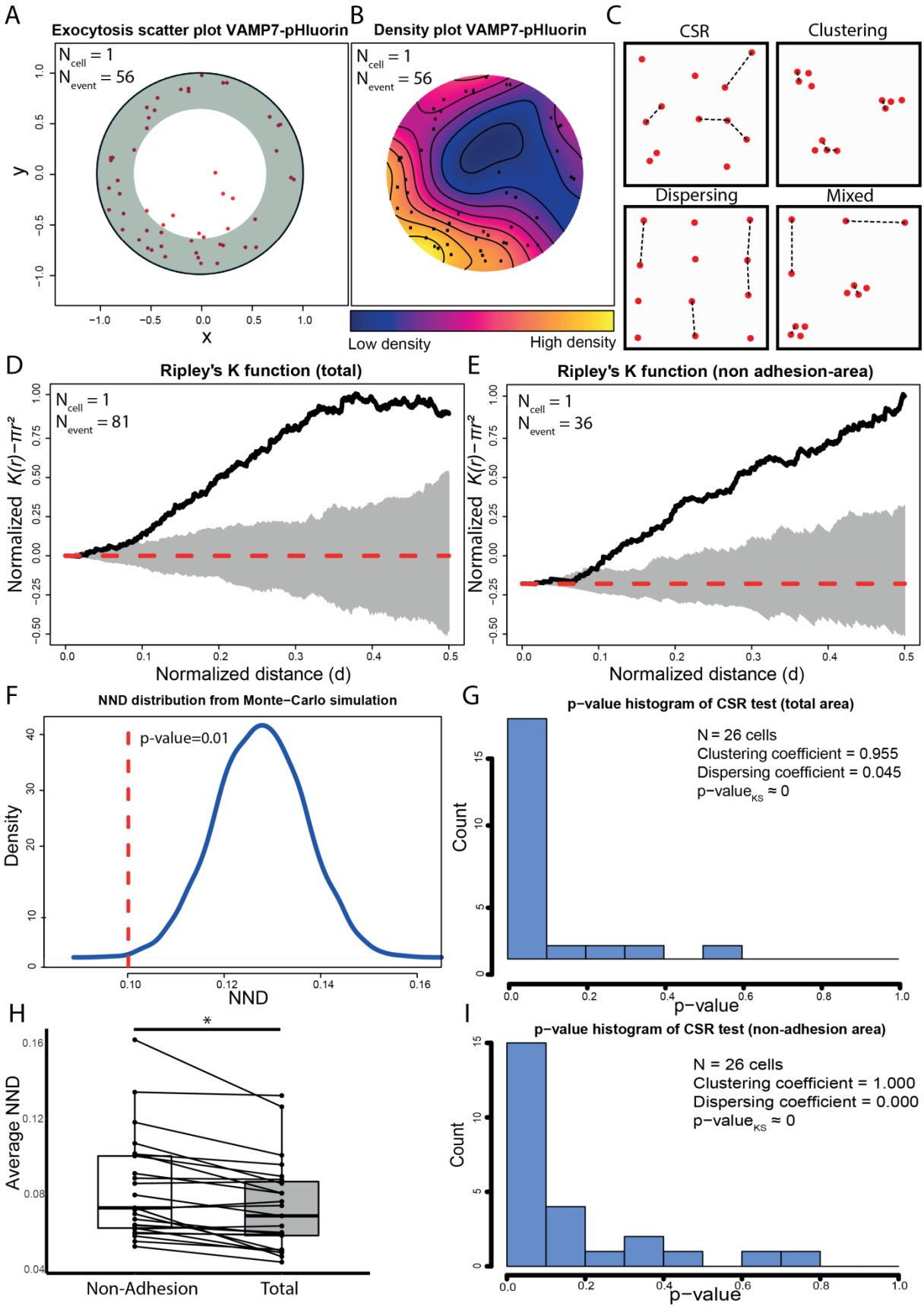
A
Exocytosis scatter plot VAMP7-pHluorin
N cell = 1
N event = 56
y
x
B
Density plot VAMP7-pHluorin
N cell = 1
N event = 56
Low density
High density
C
CSR
Clustering
Dispersing
Mixed
D
Ripley's K function (total)
N cell = 1
N event = 81
Normalized K(r)−πr²
Normalized distance (d)
E
Ripley's K function (non adhesion-area)
N cell = 1
N event = 36
Normalized K(r)−πr²
Normalized distance (d)
F
NND distribution from Monte−Carlo simulation
p-value=0.01
Density
NND
G
p−value histogram of CSR test (total area)
N = 26 cells
Clustering coefficient = 0.955
Dispersing coefficient = 0.045
p−value KS ≈ 0
Count
p−value
H
*
Average NND
Non-Adhesion
Total
I
p−value histogram of CSR test (non-adhesion area)
N = 26 cells
Clustering coefficient = 1.000
Dispersing coefficient = 0.000
p−value KS ≈ 0
Count
p−value

Figure 2. Spatial analysis of lysosomal exocytosis events. (**A**) Scatter plot of exocytosis events during 5 min acquisition. Each dot represents one exocytosis event. The adhesive area is shown in gray. (**B**) 2D kernel density estimation (KDE) of scatter plot of **A**. The color represents the local density of exocytosis events. (**C**) Schematic representation of possible point patterns. The four cases, Complete Spatial Randomness (CSR), Clustering, Dispersion, and Mixed are shown, and several nearest neighbor distances (NND) are plotted (dashed lines) to show how the average NND decreased in clustering and increased with dispersion. (**D**) Analysis of one representative cell using Ripley's K function. The red dashed line equals "Ripley's K function - πr^2" for CSR events, the gray envelope represents the estimated goodness-of-fit from Monte Carlo simulations with the same number of points as exocytosis events (N_{event} = 81). The black solid line equals "Ripley's Kfunction – πr^2" for observed exocytosis events (N_{event} = 81). Its positive deviation from the red curve out from the gray envelope indicates clustering of exocytosis events. Ripley's K function was normalized to have a maximum value of 1. (**E**) Analysis of the nonadhesive area of the same cell using Ripley's K function as in **D**. The positive deviation from the red curve outside the gray envelope indicates a clustering of exocytosis events in the nonadhesive area. (**F**) Comparison of the average NND distribution from one representative cell (red line) with the KDE of the CSR obtained from Monte Carlo simulations (blue curve). The p-value was calculated as the percentage of simulated values that were more extreme than the value observed. (**G**) p-value histogram obtained from the NND test as in **F** for n = 26 cells. The peak at low p-values means that the null hypothesis "exocytosis follows CSR" was rejected with a Kolmogorov-Smirnov test, indicating that lysosomal exocytosis was not CSR. (**H**) Box-plot of average NND from exocytosis events in nonadhesive areas (white) and total cell areas (gray). The two data points from the same cell are joined by a line. The average NND was bigger in the nonadhesive area, $p < 0.001$ with a paired Wilcoxon test (n = 25 cells), indicating significantly less clustering in the nonadhesive area. (**I**) Same as **G** for the nonadhesive area for n = 26 cells.

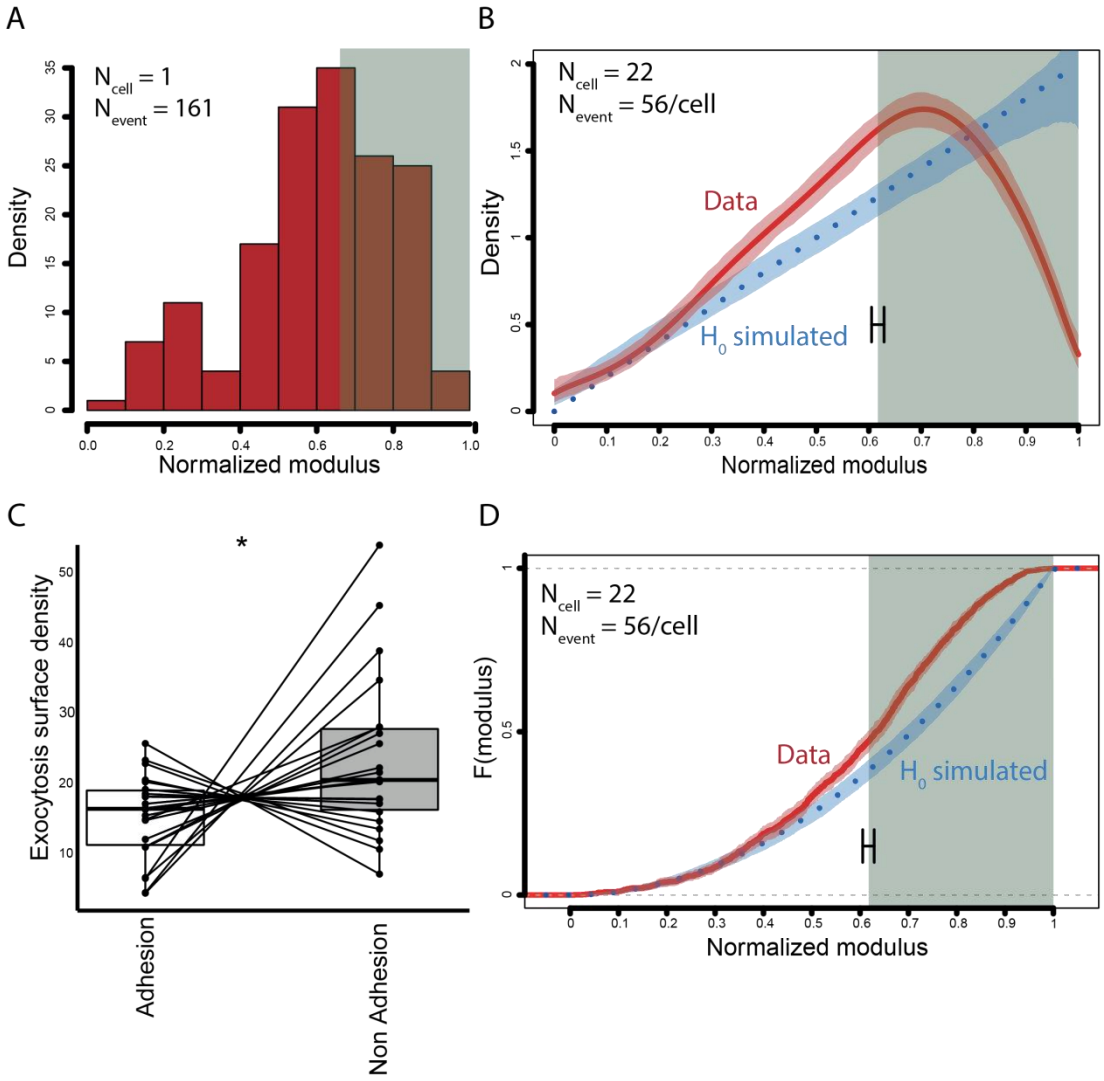

Figure 3. Spatial analysis of pooled lysosomal exocytosis events: (**A**) Histogram of the exocytosis events of one representative cell during a 5 min acquisition with n = 161 exocytosis events as a function of the normalized modulus; 0 represents the cell center and 1 the cell periphery. The adhesive area of the cell is shown in gray and corresponds to modulifrom 0.65–1 for the cells shown. There is a peak at the beginning of the adhesive area around moduli between 0.6 and 0.7. (**B**) KDE of the exocytosis events as a function of the normalized modulus for n = 22 cells with 56 events in each cell; 0 represents the cell center and 1 the cell periphery. The average adhesive area is shown in gray and corresponds on average to moduli from 0.61–1. The dashed blue curve is the theoretical curve expected in the case of CSR. This theoreticalcurve is accompanied by an envelope that represents the 1st–99th percentiles of CSR obtained using the Monte Carlo simulation. The KDE curve from the observed data is in red and accompanied by an error band generated by bootstrapping.The adhesive area is in gray +/- SEM. (**C**) Paired analysis of the surface densities in adhesion and nonadhesion areas. The exocytosis surface density was computed as the number of events per normalized area and per second. Here, *p < 0.05 from a paired student t-test (n = 22 cells). Normality was previously tested by a Shapiro-Wilk test. (**D**) Cumulative distribution function of the data in **B** (red line) and from Monte Carlo CSR simulations (dotted blue line). Envelopes were generated as in **B**. Note that the red line deviates from the theoretical CSR at around $0.7r_{max}$.

Disclosures

The authors have nothing to disclose.

Acknowledgments

We greatly acknowledge Thierry Galli (Center of Psychiatry and Neurosciences, INSERM) for providing the VAMP7- pHluorin plasmid. We thank Tarn Duong for advice on statistical analysis and members of the GOUD laboratoryfor fruitful discussions. The authors greatly acknowledgethe Cell and Tissue Imaging Facility (PICT-IBiSA @Burg, PICT-EM @Burg and PICT-IBiSA @Pasteur) and Nikon Imaging Center, Institut Curie (Paris), member of the French National Research Infrastructure France-BioImaging(ANR10-INBS-04). H.L. was supported by the Association pour la Recherche sur le Cancer (ARC) and P.M. received funding from the European Union's Horizon 2020 research and innovation programme under Marie Skłodowska-Curie grant agreement No 666003. This work was supported by grants from INFECT-ERA (ANR-14-IFEC-0002-04), the Labex CelTisPhyBio (ANR-10-LBX-0038) and Idex Paris Sciences et Lettres (ANR-10-IDEX-0001-02 PSL), as well as the Centre National de la Recherche Scientifique and InstitutCurie.

References

1. Wu, L.-G., Hamid, E., Shin, W., Chiang, H.-C. Exocytosis and endocytosis: modes, functions, and coupling mechanisms. *Annual Review of Physiology.* **76**, 301-331(2014).

2. Samie, M. A., Xu, H. Lysosomal exocytosis and lipid storage disorders. J*ournal of Lipid Research.* **55**, 995-1009 (2014).

3. Neher, E., Marty, A. Discrete changes of cell membrane capacitance observed under conditions of enhanced secretion in bovine adrenal chromaffin cells. *Proceedings of the National Academy of Sciences of the United Statesof America.* **79**, 6712-6716 (1982).

4. Grossier, J. P., Xouri, G., Goud, B., Schauer, K. Cell adhesion defines the topology of endocytosis and signalling. *The EMBO Journal.* **33,** 35-45 (2014).

5. Fourriere, L. et al. RAB6 and microtubules restrict proteinsecretion to focal adhesions. *Journal of Cell Biology.* **218**,2215-2231 (2019).

6. Wang, Y., McNiven, M. A. Invasive matrix degradation at focal adhesions occurs via protease recruitment bya FAK-p130Cas complex. *Journal of Cell Biology.* **196**, 375-385 (2012).

7. Lagache, T., Lang, G., Sauvonnet, N., Olivo-Marin, J. C. Analysis of the spatial organization of molecules with robust statistics. *PLoS One.* **12**, e80914 (2013).

8. Yuan, T., Lu, J., Zhang, J., Zhang, Y., Chen, L. Spatiotemporal Detection and Analysis of Exocytosis Reveal Fusion "Hotspots" Organized by the Cytoskeletonin Endocrine Cells. *Biophysical Journal.* **108**, 251-260 (2015).

9. Urbina, F. L., Gomez, S. M., Gupton, S. L. Spatiotemporalorganization of exocytosis emerges during neuronal shape change. *Journal of Cell Biology.* **217**, 1113-1128 (2018).

10. Martinez-Arca, S., Alberts, P., Zahraoui, A., Louvard, D., Galli, T. Role of Tetanus Neurotoxin Insensitive Vesicle- Associated Membrane Protein (Ti-Vamp) in VesicularTransport Mediating Neurite Outgrowth. *Journal of Cell Biology.* **149**, 889-900 (2000).

11. Alberts, P. et al. Cdc42 and Actin Control Polarized Expression of TI-VAMP Vesicles to Neuronal Growth Cones and Their Fusion with the Plasma Membrane. *Molecular Biology of Cell.* **17**, 1194-1203 (2006).

12. Azioune, A., Storch, M., Bornens, M., Théry, M., Piel, M. Simple and rapid process for single cell micro-patterning.*Lab on a Chip.* **9**, 1640-1642 (2009).

13. Baddeley, A. Rubak, E., Turner, R. *Spatial point Patterns:Methodology and Applications with R.* CRC Press, Indianapolis, IN. (2015).

14. Schauer, K. et al. Probabilistic density maps to study global endomembrane organization. *Nature Methods.* **7,** 560-566 (2010).

15. Advani, R.J. et al. Seven Novel Mammalian SNARE Proteins Localize to Distinct Membrane Compartments. *Journal of Biological Chemistry.* **273,** 10317-10324 (1998).

16. North, B. V., Curtis, D., Sham, P. C. A Note on the Calculation of Empirical P Values from Monte Carlo Procedures. *American Journal of Human Genetics.* **71**, 439-441 (2002).

17. Pecot, T., Zengzhen, L., Boulanger, J., Salamero, J., Kervrann, C. A quantitative approach for analyzing the spatio-temporal distribution of 3D intracellular events in fluorescence microscopy. *eLife.* **7**, e32311 (2018).

18. Chen, S. X. Beta kernel estimators for density functions. *Computational Statistics & Data Analysis.* **31**, 131-145 (1999).

Lachuer et al. bioRxiv, 2022

Membrane tension spatially organizes lysosomal exocytosis

"On doit exiger de moi que je recherche la vérité, mais non que je la trouve."

Denis Diderot, Pensées philosophiques (1746).

Abstract:

Lysosomal exocytosis is involved in many key cellular processes but its spatio-temporal regulation is poorly known. Using total internal reflection fluorescence microscopy (TIRFM) and spatial statistics, we observed that lysosomal exocytosis is not random at the adhesive part of the plasma membrane of RPE1 cells but clustered at different scales. Although the rate of exocytosis is regulated by the actin cytoskeleton, neither interfering with actin or microtubule dynamics by drug treatments alters its spatial organization. Exocytosis events partially co-appear at focal adhesions (FAs) and their clustering is reduced upon removal of FAs. Changes in membrane tension following a hypo-osmotic shock or treatment with methyl-β-cyclodextrin was found to increase clustering. To investigate the link between FAs and membrane tension, cells were cultured on adhesive ring-shaped micropatterns, which allows to control the spatial organization of FAs. By using a combination of TIRFM and fluorescence lifetime imaging microscopy (FLIM), we revealed the existence of a radial gradient in membrane tension. By changing the diameter of micropatterned substrates, we further showed that this gradient as well as the extent of exocytosis clustering can be controlled. Together, our data indicate that the spatial clustering of lysosomal exocytosis relies on membrane tension patterning controlled by the spatial organization of FAs.

Membrane tension spatially organizes lysosomal exocytosis

Hugo Lachuer[1], Laurent Le[2], Sandrine Lévêque-Fort[2], Bruno Goud[1], Kristine Schauer[1,3]

[1] Cell Biology and Cancer Unit, Institut Curie, PSL Research University, Sorbonne Université, CNRS UMR144, 75005 Paris, France

[2] Université Paris-Saclay, CNRS, Institut des Sciences Moléculaires d'Orsay, 91405, Orsay, France

[3] Tumor Cell Dynamics Unit, Inserm U1279, Gustave Roussy Institute, Université Paris-Saclay, 94800 Villejuif, France

Corresponding Author: Kristine Schauer (kristine.schauer@curie.fr)

Citation: Membrane tension spatially organizes lysosomal exocytosis Hugo Lachuer, Laurent Le, Sandrine Lévêque-Fort, Bruno Goud, Kristine Schauer bioRxiv 2022.04.22.489160; doi: https://doi.org/10.1101/2022.04.22.489160

Date Published: April 22, 2022

DOI: 10.1101/2022.04.22.489160

URL: https://www.biorxiv.org/content/10.1101/2022.04.22.489160v1

Abstract

Lysosomal exocytosis is involved in many key cellular processes but its spatio-temporal regulation is poorly known. Using total internal reflection fluorescence microscopy (TIRFM) and spatial statistics, we observed that lysosomal exocytosis is not random at the adhesive part of the plasma membrane of RPE1 cells but clustered at different scales. Although the rate of exocytosis is regulated by the actin cytoskeleton, neither interfering with actin or microtubule dynamics by drug treatments alters its spatial organization. Exocytosis events partially co-appear at focal adhesions (FAs) and their clustering is reduced upon removal of FAs. Changes in membrane tension following a hypo-osmotic shock or treatment with methyl-β-cyclodextrin was found to increase clustering. To investigate the link between FAs and membrane tension, cells were cultured on adhesive ring-shaped micropatterns, which allows to control the spatial organization of FAs. By using a combination of TIRFM and fluorescence lifetime imaging microscopy (FLIM), we revealed the existence of a radial gradient in membrane tension. By changing the diameter of micropatterned substrates, we further showed that this gradient as well as the extent of exocytosis clustering can be controlled. Together, our data indicate that the spatial clustering of lysosomal exocytosis relies on membrane tension patterning controlled by the spatial organization of FAs.

Introduction

Exocytosis is an evolutionary novelty shared among all eukaryotes (i.e. a synapomorphy) (Kloepper et al., 2007). It relies on the SNARE machinery probably inherited from an archaeal ancestor (Neveu et al., 2020). In addition to Golgi-derived vesicles along the secretory pathway, late endosomes, lysosomes and lysosome-related organelles also undergo exocytosis. Lysosomal exocytosis (referred to the secretion from late endosomes/lysosomes) is involved in the secretion of enzymes (Samie and Xu, 2014) and exosomes (Kowal et al., 2014). It supports plasma membrane repair (Andrews and Corrotte, 2018) as well as the remodeling of the microenvironment. Besides these general functions, lysosomal exocytosis fulfills specific roles in several cell types, such as the growth of neurites (Arantes and Andrews, 2006), axonal myelination (Chen et al., 2012), cell communication through ATP release in astrocytes (Dou et al., 2012), pseudopode formation in phagocytosis (Huynh et al., 2007), secretion of cytotoxic granules in lymphocytes (Peters et al., 1991), MHC-II antigen presentation (Geuze, 1998) and bone resorption in osteoclasts (Lacombe et al., 2013). It has a fundamental importance in several pathological contexts. For instance, lysosomal exocytosis is exploited by some β-coronavirus for their egress (Ghosh et al., 2020; Chen et al., 2021) or by cancer cells to enhance invasion through the secretion of metalloproteases, especially at invadopodia (Hoshino et al., 2013; Machado et al., 2015). Importantly, impairment of lysosomal exocytosis has been implicated in lysosomal storage disorders (LSDs) (LaPlante et al., 2006). Enhancing lysosomal exocytosis to release undigested lysosomal contents is a promising therapeutic strategy in these diseases (Samie and Xu, 2014).

Seminal work on exocytosis molecular machinery, particularly vesicular and target SNAREs that are critical for the fusion of secretory vesicles arriving at the plasma membrane (PM) (Novick et al., 1980; Söllner et al., 1993; Fernández-Chacón et al., 2001), uncovered key mechanisms that regulate the frequency of secretory events (Gundelfinger et al., 2003; Kasai et al., 2012). Exocytosis has been known to be polarized toward active zones in neuronal cells for a long time (Südhof, 2012). In recent years, the question has arisen where exocytosis takes place and how cells regulate secretion at specific cellular sites in non-neuronal cells. After some conflicting results (Schmoranzer et al., 2000; Keller et al., 2001), it has been now clearly demonstrated that exocytosis is not random but clustered even in non-polarized cells (Sebastian et al., 2006; Yuan et al., 2015; Urbina et al., 2018; Fu et al., 2019). Evidence also exists that lysosomal intracellular positioning is non-random (Schauer et al., 2010; Ba et al., 2018). Moreover, in polarized epithelial cells, lysosomal exocytosis is targeted to the basolateral membrane (Xu et al, 2012). However, the spatial regulation of exocytosis in non-polarized cells and its mechanisms have not been explored.

Lysosomal exocytosis relied on the VAMP7 (Martinez-Arca et al., 2000; Proux-Gillardeaux et al., 2007; Verderio et al., 2012), a v-SNARE insensitive to tetanus and botulinum neurotixines (hince its other names TI-VAMP for Tetanus neurotoxin Insensitive Vescile-Associated Membrane Protein) (Galli et al., 1998). In epithelial cells, VAMP7 interacts with the t-SNAREs syntaxin (STX) 3 (Vogel et al., 2015) and 4 (Williams et al., 2014) found at the PM but also with STX7. Whereas STX3/4 are involved in exocytosis, STX7 is only involved in intracellular endosomal fusion events (Ward et al., 2000; Wade et al., 2001; Bogdanovic et al., 2002).

In the present study, we use tools from spatial statistics to analyze live imaging data of fluorescent VAMP7 obtained by TIRFM on RPE1 cells undergoing lysosomal exocytosis. We report that spatial organization of lysosomal exocytosis is regulated by membrane tension gradient that relies on the spatial distribution of FAs.

Results

1) Exocytosis from lysosomes is not random

To monitor lysosomal exocytosis, we transfected RPE1 cells with a pHluorin construct of the v-SNARE VAMP7, VAMP7-pHluorin. The pHluorin signal is quenched in the lumen of acidic vesicles but unquenched during exocytosis when protons from the lysosomal lumen are released (F1A). Using dynamic TIRFM imaging, we manually detected exocytosis events characterized by a sudden increase in intensity followed by a decay clearly visualized in kymographs (F1B). The decrease in intensity corresponds to the 2D diffusion of VAMP7-pHluorin in the plane of the PM. Its diffusion kinetic can be fitted by a single decreasing exponential function with a half-life of about 1.69 ± 0.83s (S1A-S1B). Detected exocytosis can be represented by an intensity map where the intensity λ represents the local expected number of event/µm² (F1C). RPE1 cells display a high lysosomal exocytosis rate as several hundred exocytosis events in a typical cell could be observed within 5min, corresponding to an exocytosis rate of 39x10-5 ± 31x10-5 exocytosis/µm²/s (F1D). VAMP7 has been reported as a marker of the endosomal/lysosomal compartments. However, it substantially colocalizes with Golgi-derived vesicles in some cell types (Chaineau et al., 2009), especially in neuronal cells (Burgo et al., 2012). To confirm that VAMP7 specifically marks lysosomal exocytosis in RPE1 cells, we treated cells with Golgicide A, an inhibitor of the Arf1 GEF (Guanine nucleotide Exchange Factor) GBF1, which induces Golgi apparatus dispersion and inhibits the Golgi-derived vesicles secretion (Saenz et al., 2009). As shown in (F1E), Golgicide A did not significantly alter the exocytosis rate. Contrary, inhibition of the lysosomal V-type ATPase using Bafilomycin A1 significantly reduced the exocytosis rate (F1F). Lysosomal exocytosis can be stimulated by histamine through the G1q-PKC pathway (Verweij et al., 2018). As expected, treating RPE1 cells with histamine significantly increased the exocytosis rate (F1G) immediately after the addition of histamine (S1C). Taken together, these results demonstrate that VAMP7 exocytosis represents bona-fide lysosomal exocytosis in RPE1 cells.

The obtained exocytosis maps can be visualized as patterns of points (F1C). Such patterns can be the result of a uniformly random process (Complete Spatial Randomness, CSR) or reflects either clustering (i.e. aggregation) or dispersion (i.e. ordering with an inhibition surface around each point of exocytotic event) (Diggle, 1983; Lachuer et al., 2020). We obtained a large dataset of 183 cells showing 32 880 exocytosis events to test the CSR hypothesis and to characterize the spatio-temporal properties of lysosomal exocytosis. The observed spatio-temporal characteristics of exocytosis were compared to CSR Monte-Carlo simulations (see methods). First, we found that exocytosis events present a smaller nearest-neighbor distance (NND) than expected in the case of CSR, which indicates clustering at the scale of immediate neighbors (F1H). Moreover, events are more distant to cell borders than expected demonstrating that exocytosis is much less frequent close to cell borders (F1I). Events are also anisotropically distributed in the cells i.e. have a preferential direction (F1J). To explore this anisotropy, we seeded cells on rectangular micro-patterns forcing the orientation of cells into two possible directions (left or right) (S1D). Results confirmed anisotropy in exocytosis and showed that the secretory direction correlates with the Golgi-Nucleus axis (S1D).

The most pertinent tool to analyze a spatial structure is the Ripley's K function that measures the average number of neighbor events at a given scale. The average curve obtained from observed events significantly deviated from the expected one in case of CSR, indicating clustering of lysosomal exocytosis, even at the scale of several micrometers (F1K). The CSR envelope is not symmetric

around 0, reflecting a slight bias introduced by the boundary corrections in the computation of the Ripley's K function. Note that the treatment with Golgicide A, Bafilomycin A1 and histamine did not change the spatial organization of exocytosis (S1E-G), indicating that the rate and spatial patterning of exocytosis are independent features. We noticed a slight correlation between exocytosis rate and clustering (S1H). This correlation is not due to a bias in the measure, because Ripley's K function is independent on the number of events (Baddeley et al., 2015) and indeed, conserving an arbitrary percentage of the recorded events does not affect the Ripley's K function (S1I). We conducted a similar analysis for the temporal distribution of exocytosis events. The temporal Ripley's K function demonstrates a temporal clustering (S1J). However, a Fourier analysis revealed that this clustering is not due to a periodicity in the exocytosis rate (S1K). Lastly, we quantified the coupling between spatial and temporal dimensions using the spatio-temporal Ripley's K function (S1L), which provides information about the independency of the temporal and spatial coordinates. This analysis revealed that a substantial proportion of cells presents a spatio-temporal coupling and among cells with a significant coupling, 82.7% have a positive coupling i.e. events that are close in space are also more likely to be close in time. Together, our analysis confirmed that lysosomal exocytosis is a non-random process in space and time.

2) Lysosomal exocytosis is coupled to internal focal adhesions in a cytoskeleton-independent manner.

To investigate the mechanisms underlying the spatial clustering of lysosomal exocytosis events, we first tested whether the t-SNAREs interacting with VAMP7 show clustering, as proposed previously (Xu et al., 2012). Therefore we analyzed the spatial patterns of STX3 and STX4 (S2A-C). Although STX3/4 presented a significant clustering, it was much weaker than the one of exocytosis events, and did not recapitulate several features of VAMP7 exocytosis such as low frequency close to cell borders and a short scale clustering. Next, we focused on FAs, shown to be targeted by a subpopulation of lysosomes that were characterized to be the MAPK scaffold complex p14-MP1 (p14-MP1+) (Schiefermeier et al., 2014) as well as by Golgi-derived RAB6+ vesicles (Fourriere et al., 2019). We quantified the co-appearance of VAMP7-pHluorin with FAs using the FA protein paxillin (Paxillin-mCh) as a marker in co-transfected cells (F2A-B). The co-appearance index was significantly higher than expected from CSR Monte-Carlo simulations (F2B). Interestingly, VAMP7 lysosomal exocytosis only appeared at internal FAs, consistent with the observation that exocytosis frequency is low close to cell borders (F2A). To further test the role of FAs, we cultured cells on Poly-L-Lysine (PLL) substrates to inhibit the formation of FAs (S2D). Under this condition, the clustering of lysosomal exocytosis decreased significantly (F2C), indicating a role of FAs in the spatial organization of exocytosis. We noticed that exocytosis rate was significantly enhanced on PLL substrate, probably due to a smaller adhesive surface under this condition (S2E).

FAs are closely linked to both microtubules (MT) (+) ends (Stehbens and Wittmann, 2012; Stehbens et al., 2014; Seetharaman and Etienne-Manneville, 2019), and the cortical acto-myosin cytoskeleton (Miklavc and Frick, 2020). Surprisingly, MT depolymerization by nocodazole treatment did not reduce clustering (F2D) nor the exocytosis rate (F2E). Depolymerisation of F-actin by a low dose of cytochalasin D significantly reduced the exocytosis rate (F2G), however did not reduce lysosomal clustering (F2F). This suggested a role of actin in facilitating fusion of lysosomes with PM but not in the organization of exocytosis patterning. Moreover, myosin-2 (MYH9) inhibition by para-nitro-

blebbistatin treatment affected neither exocytosis clustering nor exocytosis rate (F2H-I). Taken together, these results demonstrate that FAs regulate lysosomal exocytosis patterns in a cytoskeleton-independent manner. Moreover, they confirm a targeting of lysosomal secretion events to internal FAs and exclusion from external ones.

3) Exocytosis clustering depends on membrane tension

We tested the role of physical parameters, such as membrane tension, known to regulate the exocytosis rate (Gauthier et al., 2011; Wen et al., 2016; Kliesch et al., 2017; Shi et al., 2018; Wang and Galli, 2018; Wang et al., 2018). We applied a hypo-osmotic shock and monitored VAMP7 exocytosis 15min after the shock. Hypo-osmotic shock causes cell swelling leading to an increased membrane tension. VAMP7+ exocytosis has been reported to be less frequent after hyper-osmotic shock (Wang et al., 2018) and hypo-osmotic shock decreased exocytosis rate in experimental and theoretical models (Zwiewka et al., 2015; Mao et al., 2021). Surprisingly, the hypo-osmotic shock significantly reduced the exocytosis rate in RPE1 cells (F3B). However, hypo-osmotic shock significantly increased the clustering of lysosomal exocytosis (F3A). It also increased the co-appearance between exocytosis events and FAs (F3C). To further confirm these results, we treated cells with methyl-β-cyclodextrin that depletes cholesterol from the PM, and thus has been proposed to affect membrane tension (Hissa et al., 2017; Biswas et al., 2019; Cox et al., 2021). Cyclodextrin treatment significantly increases clustering, similarly to hypo-osmotic shock treatment (F3D). Moreover, cyclodextrin treatment also decreases exocytosis rate (F3E) and increases the co-appearance between exocytosis events and FAs (F3F).

Next, we directly measured membrane tension using the Fluorescence Lifetime Imaging Microscopy (FLIM) probe Flipper-TR (Colom et al., 2018). The Flipper-TR intercalates in membranes, where the membrane microenvironment favors one of two possible molecular conformations of the Flipper-TR (planar or orthogonal). The two conformations display different fluorescence lifetimes. Higher local membrane tension leads to higher fluorescence lifetimes. We quantified fluorescence lifetime in living cells using a TIRF-FLIM device under different experimental conditions. We observed that the membrane tension at the ventral part of the cell is not homogeneous in cells seeded on fibronectin-coated surface. Interestingly, we found that membrane tension presents variability compatible with the micrometer scale of exocytosis clustering (F3G). Surprisingly, no major variation in the Flipper-TR fluorescence lifetime was observed following a hypo-osmotic shock or treatment with cyclodextrin (S3A-B). Because lysosomal clustering is regulated by FAs, we next quantified fluorescence lifetime in living cells seeded on PLL-coated surface. Despite their difference in exocytosis clustering, the average lifetime was again similar in these two conditions (F3H). Together, these results indicate that global membrane tension does not regulate clustering of exocytosis. However, cells grown on fibronectin showed clustering of similar lifetime values at several regions, whereas these values appeared more homogeneously distributed in cells on PLL (F3G). Thus, we measured the spatial auto-correlation using the Moran's index, which increases in case of clustering of pixels values. Moran's index was indeed significantly higher in cells plated on fibronectin than on PLL (F3I). This suggests that the spatial organization of lysosomal exocytosis is controlled by regional heterogeneity in membrane tension rather than the global tension at the whole cell level. Moreover, our results indicate that the presence of FAs favors a compartmentalization of membrane tension.

4) Intracellular coupling between exocytosis probability and membrane tension

A simultaneous observation of the Flipper-TR signal and exocytosis events is technically very challenging. Therefore, to correlate membrane tension and exocytosis events, we normalized RPE1 cell geometries using adhesive ring-shaped micropatterns. An advantage of micropatterned cells is the possibility to standardize the adhesive surface and FA distribution. On ring-shaped micropatterns (F4A), FAs are formed at the inner and outer borders of the ring mimicking the inner and peripheral FAs found in non-patterned cells (S4A-B). Using the Ripley's K function, we found that the clustering of lysosomal exocytosis also occurs in patterned cells, although significantly weaker than in non-patterned cells (F4B). Plotting the radial average density of exocytosis events demonstrated that cells exhibit an enrichment of events at half of the cell radius as the density deviated there from the expected CSR case (F4C). Moreover, exocytosis events are less frequent at cell borders similarly to non-patterned cells. Using the same micropatterns, we then measured membrane tension by TIRF-FLIM. Interestingly, cells displayed a radial gradient of membrane tension with lowest membrane tension values at the extreme cell border and in the center, and a linear increase in membrane tension for the center to the periphery (F4D-E). The Moran's index is lower in patterned cells than in non-patterned cells despite the presence of the gradient (S4C). Taken together with the PLL experiments, this result points out a correlation between clustering/compartmentalization of membrane tension and clustering of exocytosis. The cross-correlation between the normalized lifetime and the exocytosis probability demonstrates that the exocytosis probability increases with the membrane tension in a monotonous however non-linear manner (F4F). Note that the exocytosis probability is defined as the probability of exocytosis at a given place knowing that an event will occur. Therefore, it does not reflect the exocytosis rate but only its spatial distribution. The above results together indicate that exocytosis is favored at regions with high local membrane tension, and that these regions are spatially organized leading to clustering in these regions.

5) Strength of membrane tension gradient regulates clustering of lysosomal exocytosis

To further investigate the role of membrane tension in the spatial regulation of exocytosis, we established exocytosis and membrane tension maps of cells cultured on ring-shaped micropatterns of different sizes (F5A). The average membrane tension was found to be similar on all pattern sizes (S5A). However, the membrane tension gradient varied according to the pattern size (F5B), except for cells plated on small patterns that did not display any gradient. Consistently, the Moran's index increased from small to large micro-patterns (S5B). Interestingly, the absence of a gradient in the smallest size micropatterns correlates with a lower level of clustering of exocytosis events, whereas the presence of a gradient in the largest cell size correlates with higher clustering (F5C). On the other hand, the exocytosis rate (normalized to cell surface) was not significantly different regardless of the pattern sizes (S5C). These results confirm a role of the membrane tension gradient in the regulation of spatial exocytosis patterns.

Discussion

Our data demonstrate that lysosomal exocytosis is not random (i.e. CSR) but clustered in space and time with a positive coupling between spatial and temporal dimensions (Fig1). Lysosomal exocytosis occurs close to internal FAs and it is almost absent at cell borders. In agreement with this result, cells seeded on PLL, which inhibits the formation of FAs, display a decreased clustering of exocytic events (Fig2). Previous work described a targeting of lysosomes to FAs but exocytosis at these points was not demonstrated (Schiefermeier et al., 2014). Our data suggest that clustering does not rely on an intact cytoskeleton as the spatial pattern of lysosomal exocytosis was not perturbed upon treatment with drugs affecting the cytoskeleton (Fig2). The underlying mechanism supporting clustering of exocytotic events from lysosomes at FA is likely different from the exocytosis of Golgi-derived vesicles. Indeed, clustering of Golgi-derived vesicles was shown to be inhibited by both actin and microtubule depolymerization (Yuan et al., 2015). However, interfering with the actin cytoskeleton inhibits VAMP7-mediated exocytosis rate in neuronal cells (Gupton and Gertler, 2010). The involvement of the cytoskeleton in clustering of lysosomal and Golgi-derived exocytosis will then require further investigation in different cell types.

We found that interfering with membrane tension by hypo-osmotic shock and methyl-β-cyclodextrin treatments impact clustering of exocytosis, revealing for the first time a role of membrane tension in the spatial organization of exocytosis (Fig3). Our results complement previous data illustrating the role of membrane tension on the exocytosis rate (Wen et al., 2016; Kliesch et al., 2017; Shi et al., 2018; Wang and Galli, 2018; Wang et al., 2018; Cohen and Shi, 2020).

A previous study reported that in addition to changing total membrane tension, methyl-β-cyclodextrin treatment increases its heterogeneity (Biswas et al., 2019). In addition, transmembrane proteins such as FAs have been proposed to behave as obstacles to the lipid flow that equilibrates membrane tension (Cohen and Shi, 2020). Cells seeded on PLL reveal a more uniform membrane tension, confirming the role of FAs as obstacles. Together, our data suggest that an inhomogeneity of membrane tension induced by FAs leads to the accumulation of secretory events at these regions. This hypothesis is supported by experiments performed on micropatterns, which show that the symmetric arrangement of FAs leads to a well-defined gradient of membrane tension (Fig.4). Moreover, changing the micropattern diameter increases the strength of membrane tension gradient and exocytosis clustering (Fig.5). Interestingly, a gradient in membrane tension has been already observed in moving keratinocytes (Lieber et al., 2015). Such a gradient could result from the friction between plasma membrane and either actin treadmilling or the adhesion substrate (Schweitzer et al., 2014). In our experiments performed on non-migratory cells constrained by adhesion on micropatterns, only actin retrograde flow could potentially cause friction. Yet, experiments in non-patterned cells revealed that clustering is independent of the actin cytoskeleton. Thus, the above result could indicates that the diffusion of lipids in the plasma membrane is very slow, resulting in a stable gradient of membrane tension at the time scale of our experiments, similarly to what was previously observed in non-neuronal cells (Shi et al., 2018). Finally, the experiments on micropatterns revealed a positive coupling between exocytosis probability and membrane tension (Fig. 4). Of note, the absence of gradient in membrane tension observed in cells grown on small micropatterns does not totally abolish exocytosis clustering. This suggests that other mechanisms regulate clustering, such as for instance clustering of syntaxins. In conclusion, we propose that the spatial clustering of lysosomal exocytosis relies on the spatial organization of membrane tension, which is regulated by the presence and localization of FAs.

Figures

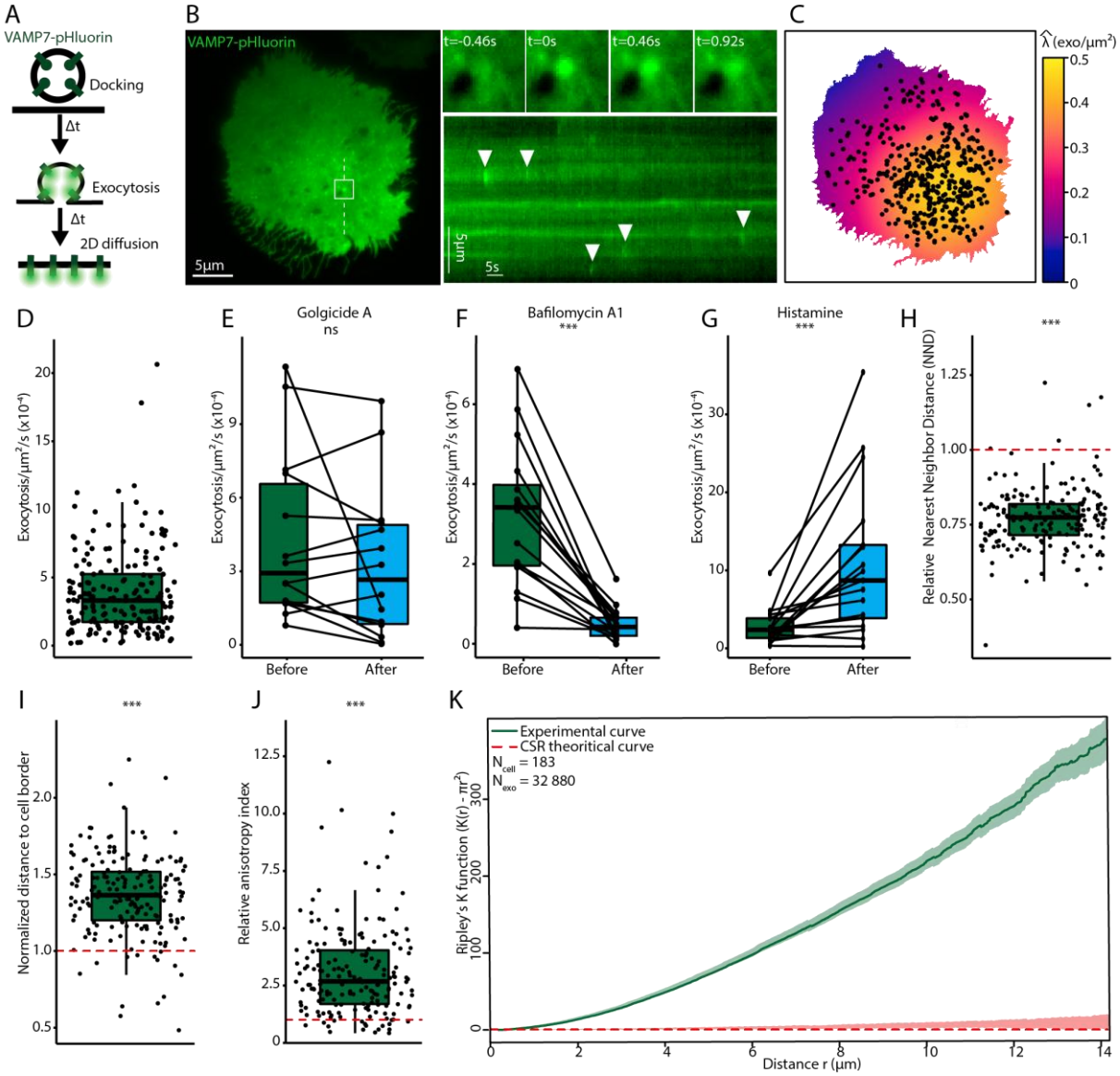

Figure 1. Lysosomal exocytosis is not random but clustered. A. Schematic representation of the exocytosis of a VAMP7-pHluorin+ vesicle: the low pH of the acidic lumen quenches the fluorescence of pHluorin. During exocytosis, protons are released and pHluorin starts to emit light. An exocytosis event is followed by the 2D diffusion of VAMP7-pHluorin at the plasma membrane. **B.** TIRFM image of VAMP7-pHluorin in a transfected RPE1 cell. The inset represents the field in the white square showing one exocytosis event at different time points, t=0 represents the beginning of the exocytosis event. A kymograph is plotted along the dashed white line and arrowheads indicate several observed exocytosis events. **C.** Exocytosis intensity map of the cell in B acquired during 5min. Black dots represent exocytosis events. The color code represents the estimation of the local intensity $\hat{\lambda}$ expressed in exocytosis/µm². **D.** Normalized exocytosis rate in RPE1 cells from n=183 cells (and

32.880 exocytosis events) from 34 independent experiments. ($3.9x10^{-4}$ ± $3.1x10^{-4}$ exocytosis/s/µm²). **E.** Exocytosis rate before and after Golgicide A (10µM, 30min) treatment; n=14 cells from 3 independent experiments. **F.** Exocytosis rate before and after bafilomycin A1 (100nM, 60min) treatment; n=16 cells from 3 independent experiments. **G.** Exocytosis rate before and after histamine (100µM, no incubation) treatment; n=17 cells from 3 independent experiments. **In E-G**, significance has been evaluated with paired Wilcoxon test, ns p>0.05 and ***p<0.001. **H.** Relative Nearest Neighbor Distance ($NND_{observed}/NND_{simulated}$) of basal exocytosis observed in D. **I.** Relative distance to cell borders ($distance_{observed}/distance_{simulated}$) of basal exocytosis observed in D. **J.** Relative anisotropy index ($anisotropy_{observed}/anistropy_{simulated}$) of basal exocytosis observed in D. 90% of the cells have a relative anisotropy index superior to 1. **In H-J**, the red dotted line represents expected value under CSR hypothesis and the significance of the deviation to CSR has been computed using a t-test. ***p<0.001. **K.** Average centered Ripley's K function ($K(r)-\pi r^2$) of 183 cells (and 32.880 exocytosis events) observed in D. Green curve represents the experimental results ± SEM and the red dotted line the expectation under CSR hypothesis. Red shade represents envelope containing 95% of CSR simulations.

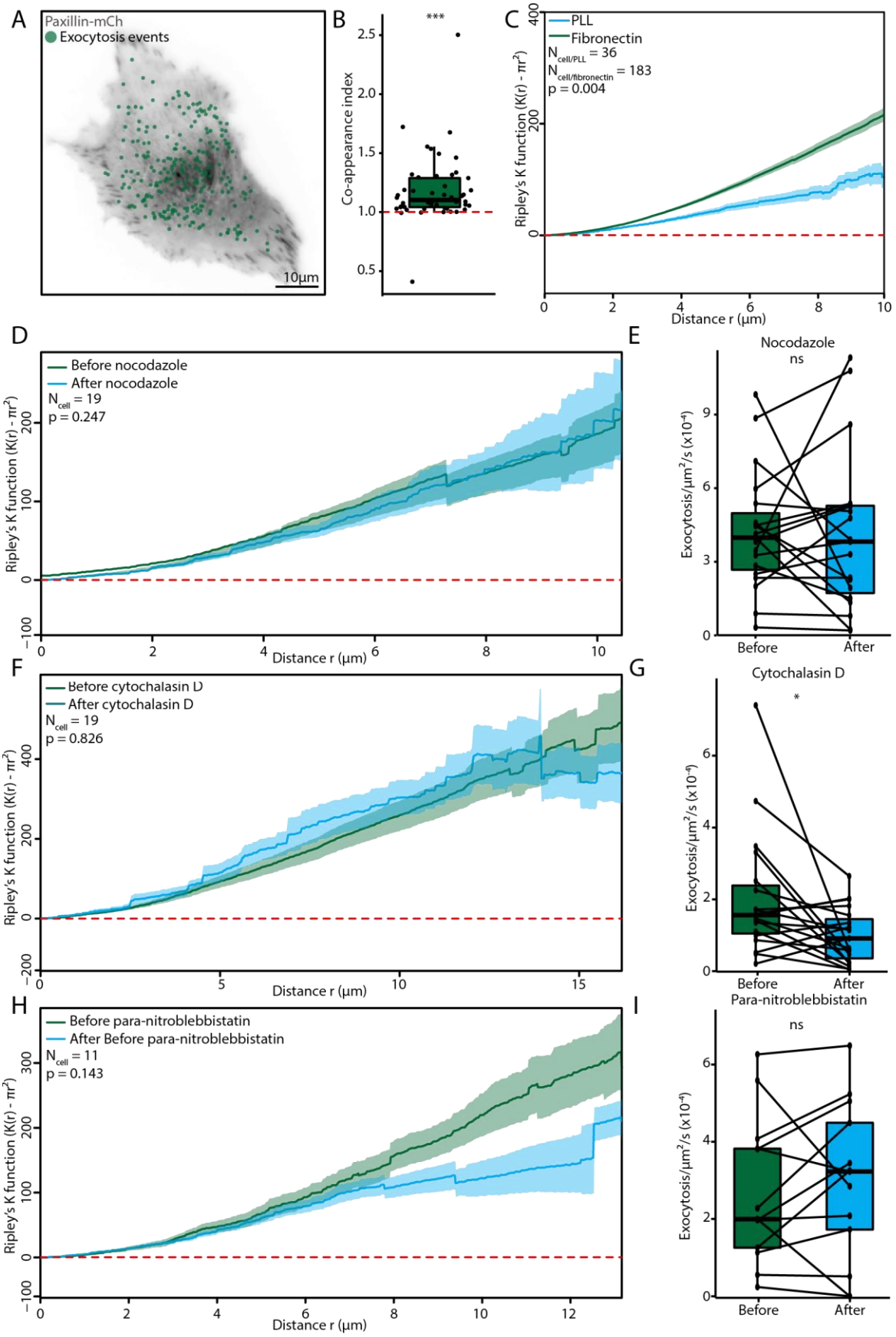
A
Paxillin-mCh
Exocytosis events
10µm
B
***
Co-appearance index
C
PLL
Fibronectin
N cell/PLL = 36
N cell/fibronectin = 183
p = 0.004
Ripley's K function (K(r) - πr²)
Distance r (µm)
D
Before nocodazole
After nocodazole
N cell = 19
p = 0.247
Ripley's K function (K(r) - πr²)
Distance r (µm)
E
Nocodazole
ns
Exocytosis/µm²/s (x10⁻⁴)
Before
After
F
Before cytochalasin D
After cytochalasin D
N cell = 19
p = 0.826
Ripley's K function (K(r) - πr²)
Distance r (µm)
G
Cytochalasin D
*
Exocytosis/µm²/s (x10⁻⁴)
Before
After
Para-nitroblebbistatin
H
Before para-nitroblebbistatin
After Before para-nitroblebbistatin
N cell = 11
p = 0.143
Ripley's K function (K(r) - πr²)
Distance r (µm)
I
ns
Exocytosis/µm²/s (x10⁻⁴)
Before
After

Figure 2. Lysosomal exocytosis is coupled to internal focal-adhesions in a cytoskeleton-independent manner. A. Merge from TIRFM live cell imaging of a paxillin-mCh/VAMP7-pHluorin co-transfected RPE1 cell: the gray scale image represents snapshot of paxillin-mCh intensity and green dots represent exocytosis events localization. **B.** Co-appearance index between exocytosis events and FAs. Red dashed line represents expected co-appearance in the case of CSR. The significance of the deviation to CSR has been computed using a t-test, ***p<0.001; n=49 cells from 4 independent experiments. **C.** Average spatial Ripley's K function ± SEM for cells seeded on fibronectin (green curve) and PLL (blue curve); 36 cells on PLL and 183 cells on fibronectin were analyzed from 3 and 34 independent experiments, respectively. **D.** Average spatial Ripley's K function ± SEM before (green) and after (blue) incubation with nocodazole (10µM, 60min). **E.** Exocytosis rate before and after nocodazole treatment (10µM, 60min). **D-E**: n=19 cells analyzed from 4 independent experiments. **F.** Average spatial Ripley's K function ± SEM before (green) and after (blue) cytochalasin D treatment (500nM, 60min). **G.** Exocytosis rate before and after incubation with cytochalasin D (500nM, 60min). **F-G**: 19 cells analyzed from 3 independent experiments. **H.** Average spatial Ripley's K function ± SEM before (green) and after (blue) para-nitro-blebbistatin treatment (20µM, 15min). **I.** Exocytosis rate before and after para-nitro-blebbistatin treatment (20µM, 15min). **H-I**: n=13 cells from 3 independent experiments were analyzed. In **C, D, F** and **H**, the significance of the difference between Ripley's K functions has been evaluated using a permutation test (see methods) and red-dashed line represents expectation in the case of CSR. In **E, G** and **I**, the significance has been evaluated using a paired Wilcoxon test, ns p>0.05, *p<0.05.

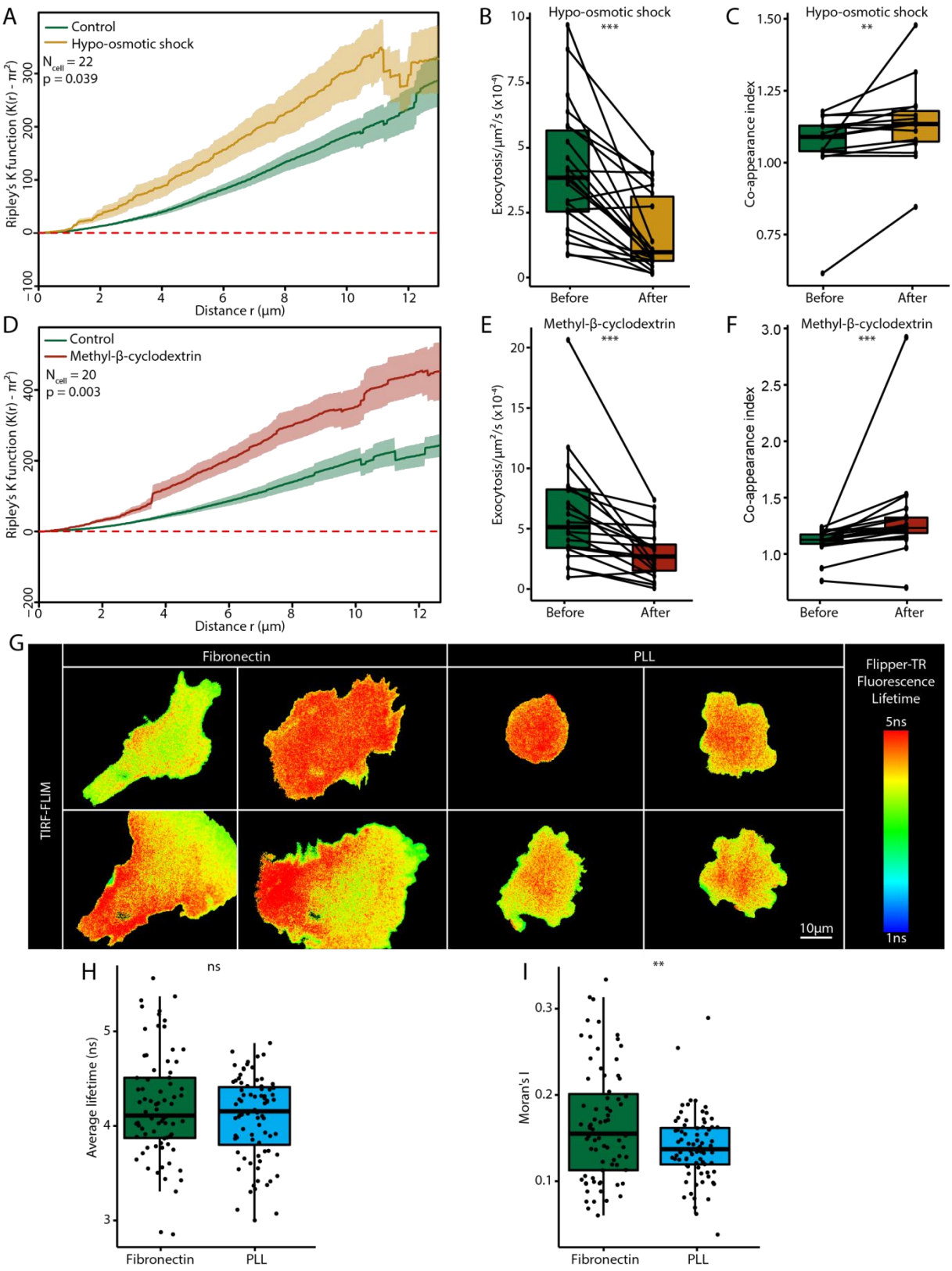

Figure 3. Membrane tension regulates lysosomal exocytosis clustering. A. Average spatial Ripley's K function ± SEM before (green) and after (yellow) hypo-osmotic shock (1:1 dilution, 15min). **B.** Exocytosis rate before and after hypo-osmotic shock. In **A** and **B**, 22 cells from 4 independent

experiments were analyzed. **C.** Co-appearance index between exocytosis spots and FAs before and after hypo-osmotic shock. 15 cells analyzed in 3 independent experiments. **D.** Average spatial Ripley's K function ± SEM before (green) and after (dark-red) β-methyl-cyclodextrin addition (5mM, 15min). **E.** Exocytosis rate before and after β-methyl-cyclodextrin addition. In **D** and **E**, 20 cells from 3 independent experiments were analyzed. **F.** Co-appearance index between exocytosis spots and FAs before and after β-methyl-cyclodextrin; 19 cells from 3 independent experiments were analyzed. In **A** and **D**, the significance of the difference between Ripley's K functions has been evaluated using a permutation test (see method) and red-dashed line represents expected curve in the case of CSR. In **B, C, E** and **F**, significance has been evaluated using paired Wilcoxon test, **p<0.01 and **p<0.001. **G.** TIRF-FLIM images of each 4 representative cells seeded on either fibronectin or PLL substrate, and incubated with Flipper-TR. The color code represents the Flipper-TR fluorescence lifetime. **H.** Average fluorescence lifetime per cell seeded on fibronectin and PLL substrate. **I.** Moran's I index per cell seeded on fibronectin and PLL substrate. In **H** and **I**, significance has been evaluated using t-test, ns p>0.05 and **p<0.01, 75 cells have been analyzed on fibronectin-coated surface, and 80 cells in PLL-coated, from 3 independent experiments.

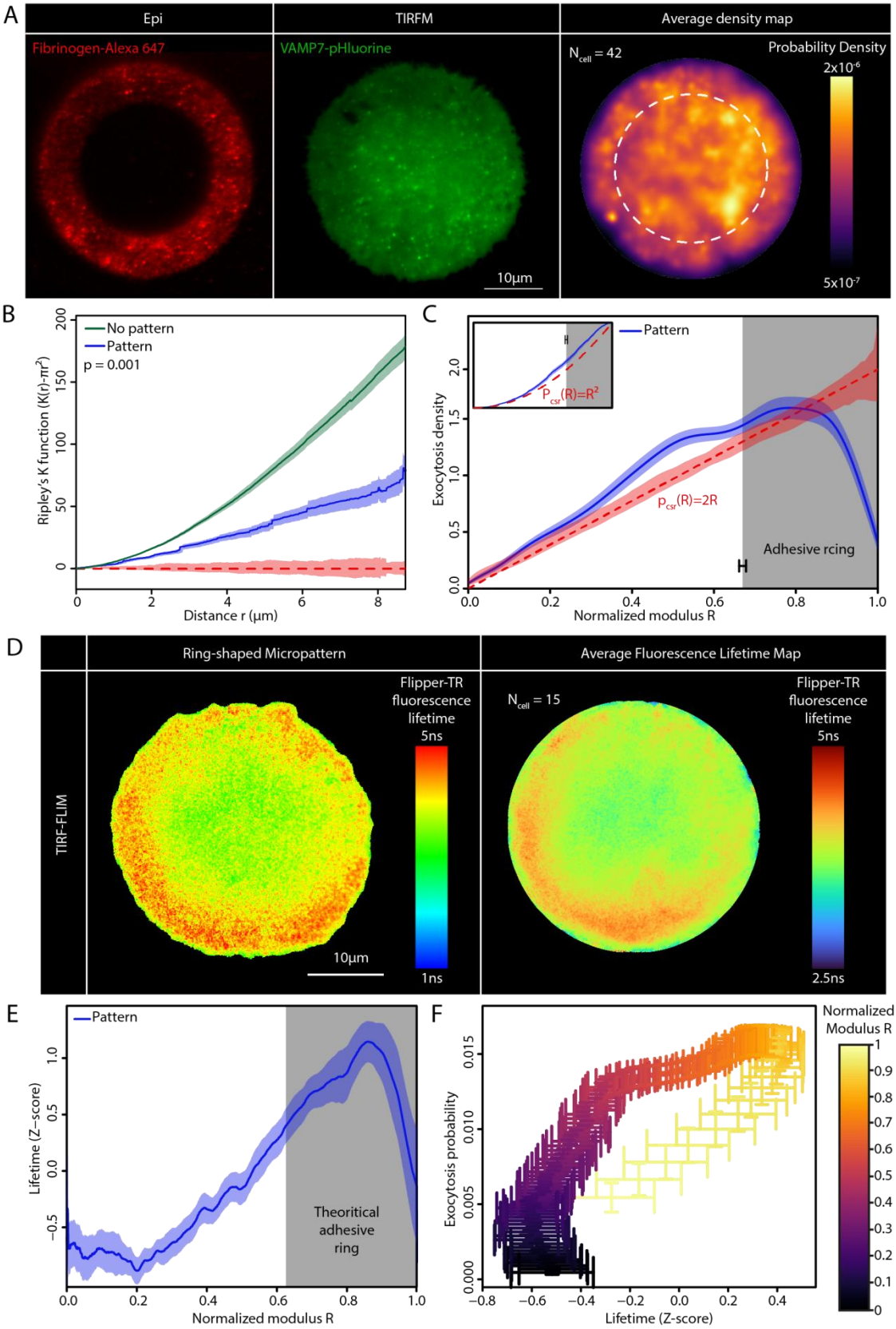

Figure 4. Coupling between membrane tension gradients and exocytosis probability. A. Representative epifluorescence image of a 37µm diameter ring-shaped micropattern stained with

fibrinogene-Alexa647 and a TIRFM image of VAMP7-pHluorin transfected cell cultured on it accompanied by the average exocytosis map from 42 cells. The color code represents the probability to observe exocytosis knowing that one event occurred. **B.** Average spatial Ripley's K function ± SEM of exocytosis in cells seeded on ring-shaped micropattern (blue) and non-patterned cells (green, same data as in F1K). The significance of the difference between Ripley's K functions has been evaluated using a permutation test (see method). **C.** Average radial-density ± SEM of exocytosis in cells seeded on ring-shaped micropattern. The modulus (distance to pattern center) is normalized to the cell radius, setting cell border at R=1. The gray rectangle represents the average position of the adhesive part of the micropattern ± SEM. The inset represents the same data but as a cumulative density function instead of probability density. **A-C**: 42 cells were analyzed from 9 independent experiments. In **B-C**, the red-dashed line represents expected curve in the case of CSR and red shade represents envelope containing 95% of CSR simulations. **D.** TIRF-FLIM image of a representative cell seeded on a ring-shaped micropattern and incubated with Flipper-TR, and average fluorescence lifetime map from TIRF-FLIM images of 15 cells. The color code represents Flipper-TR fluorescence lifetime. **E.** Radial average ± SEM of the Flipper-TR fluorescence lifetime. Fluorescence lifetime is presented under a Z-score form (see methods) and the modulus is normalized to the cell radius setting cell border at R=1. In **D** and **E**, 15 cells analyzed in 1 independent experiment. **F.** Coupling between exocytosis probability and membrane tension using data from **C** and **E**. The estimation of exocytosis probability at a given modulus R is based on the number of events normalized by the corresponding surface, contrarily to **C**. The color code corresponds to the normalized modulus R. Each point is associated to SEM for both axes.

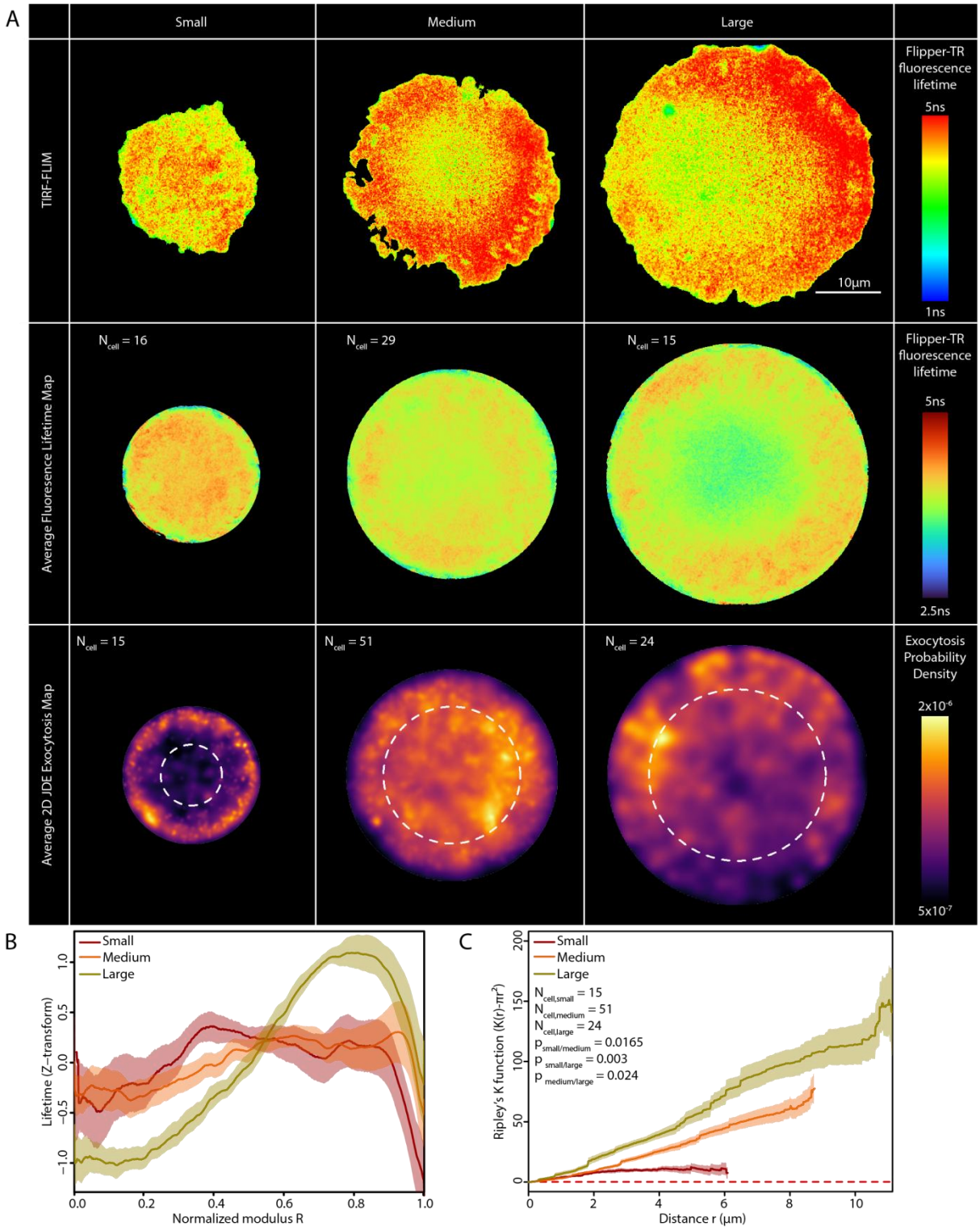

Figure 5. Strength of membrane tension gradient regulates clustering of lysosomal exocytosis. A. Representative images of cells seeded on ring-shaped micropattern of different diameters (classified as small ~25µm, medium ~35µm and large ~45µm) and incubated with Flipper-TR visualized by TIRF-FLIM (upper panel). The color code represents the Flipper-TR fluorescence lifetime. Average fluorescence lifetime maps for cells seeded on different diameters (middle panel), maps are an

average of FLIM images from n=16 (small), n=29 (medium) and n=15 (large) cells from 4 independent experiments. Color code represents Flipper-TR fluorescence lifetime. Average exocytosis maps (lower panel) from n=15 (small), n=51 (medium) and n=24 (large) cells from 11 independent experiments. The color code represents the probability of exocytosis. **B.** Radial averages ± SEM of the Flipper-TR fluorescence lifetime (data from **A**). Lifetime is presented under a Z-score form (see methods) and the modulus is normalized by the cell radius setting cell border at R=1 for the 3 conditions. **C.** Average spatial Ripley's K functions ± SEM of exocytosis in cells seeded on ring-shaped micropatterns with different diameters, small in dark red, medium in orange and large in yellow (data from **A**). The significance of the differences between Ripley's K functions has been evaluated using a permutation test (see methods) and p-values were corrected using Benjamini-Hochberg procedure. The red-dashed line represents expected curve under CSR hypothesis.

Supplemental figures

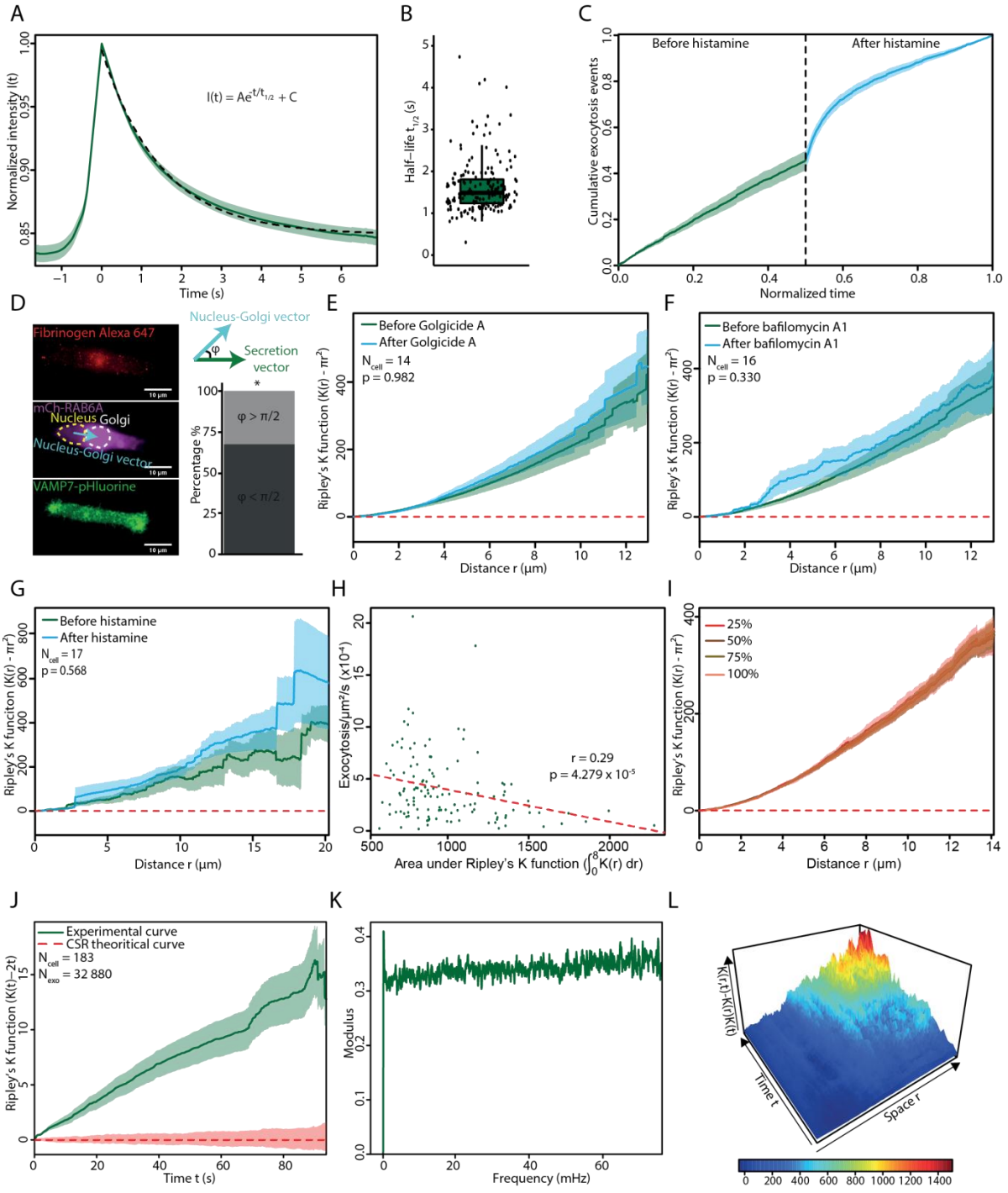

Figure S1. A. Exocytosis kinetics monitored by the normalized average fluorescence intensity (± SEM) at exocytosis event localization. Intensity has been normalized to 1 at t=0 observed at the beginning of the exocytosis event. The kinetic has been fitted by a single exponential function ($I(t) = Ae^{-\frac{t}{t_{1/2}}} + B$) represented by the black dashed line. The half-life extracted from this fit is $t_{1/2}$ = 1.48s. **B.** Half-life $t_{1/2}$ measured by the same fitting but cell by cell. Average half-life is 1.69 ± 0.83s. **C.**

Average cumulative exocytosis events after histamine addition: the y-axis represents the fraction of exocytosis events observed at a given time over the total number of exocytosis events recorded. Time is normalized between 0 and 1 and histamine (100µM) is added at 0.5 corresponding to the dashed black line. Green curve represents results before histamine and the blue one after histamine addition. Experimental curves are averages ± SEM; n=17 cells from 3 independent experiments. **D.** Anisotropy assay. VAMP7-pHluorin/mCh-RAB6A co-transfected cells are seeded on rectangular micropattern (visualized by fibrinogen Alexa647). Exocytosis axis was established by TIRFM and compared to the nucleus-Golgi axis. Histogram presents the percentage of cells with co-polarization and anti-polarization; n=42 cells from 4 independent experiments. Binomial test, *p<0.05. **E.** Average spatial Ripley's K function ± SEM before (green) and after (blue) Golgicide A (10µM, 30min) addition; n=14 cells from 3 independent experiments. **F.** Average spatial Ripley's K function ± SEM before (green) and after (blue) bafilomycin A1 (100nM, 60min) addition; n=16 cells from 3 independent experiments. **G.** Average spatial Ripley's K function ± SEM before (green) and after (blue) histamine (100µM, no incubation) addition; n=17 cells from 3 independent experiments**. E-G**. The significance of the difference between Ripley's K functions has been evaluated using a permutation test (see method) and red-dashed line represents expectation under CSR hypothesis. **H.** Correlation between the exocytosis rate and the clustering measured as the area under the Ripley's K function curve between 0µm and 8µm in control cells. Correlation has been evaluated using Pearson correlation (r=0.29) and t-test ($p=4.279x10^{-5}$) for correlation. **I.** Average Ripley's K function by keeping 25, 50, 75 and 100% of the events for each cell (artificial thinning). Curves represent averages ± SEM and red-dashed line represents expectation under CSR hypothesis. **J.** Average centered temporal Ripley's K function (K(t)-2t). Green curve represents the experimental average ± SEM and the red dashed line the expectation under CSR hypothesis. Red shade represents envelope containing 95% of CSR simulations. **K.** Fourier analysis of the temporal distribution of exocytosis events. Curve represents the average modulus of FFT. **L.** Median spatio-temporal Ripley's K function (K(r,t)) subtracted by the product of the spatial and the temporal Ripley's K function (K(r) and K(t)). An independency test has been made cell by cell. Among significant cells, 82.7% present a positive spatiotemporal coupling (and 62.8% among all cells). In **A-B** and **H-L**, 183 cells from 34 independent experiments were analyzed.

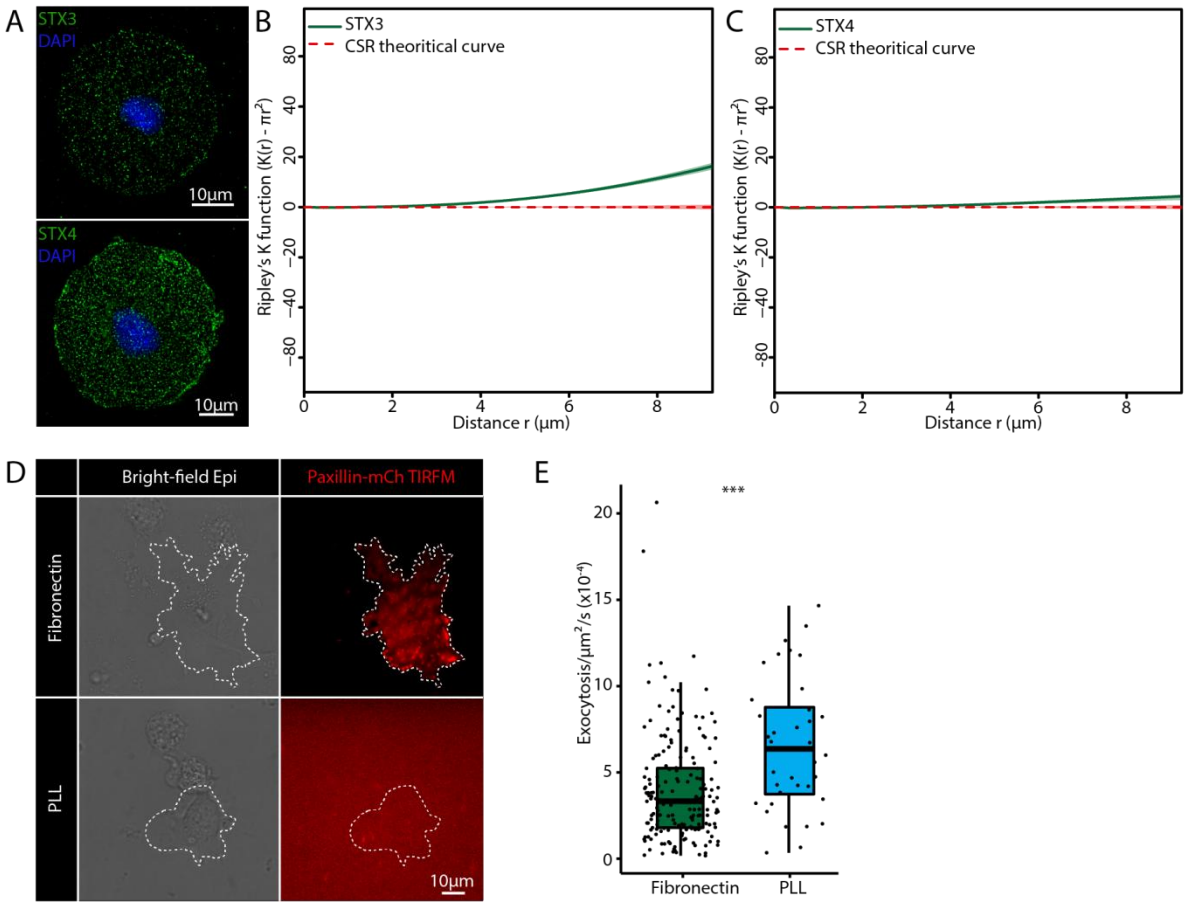

Figure S2. A. STX3/4 immunofluorescence of representative fixed cells seeded on ring-shaped micropattern. **B.** Average Ripley's K function ± SEM of STX3 segmented spots from 28 cells. **C.** Average Ripley's K function ± SEM of STX4 segmented spots from 30 cells. In **B** and **C,** red-dashed line represents expected curve in the case of CSR, and the red shade represents the envelope containing 95% of CSR simulations. **D.** Bright-field and TIRFM images of paxillin-mCh transfected cells seeded on fibronectin or PLL substrate. The cell counters of transfected cells are marked by white dashed lines. **F.** Exocytosis rate for cells seeded on fibronectin or PLL substrate. 36 cells on PLL and 183 cells on fibronectin were analyzed from 3 and 34 independent experiments, respectively. The significance has been evaluated using a t- test, ***p<0.001.

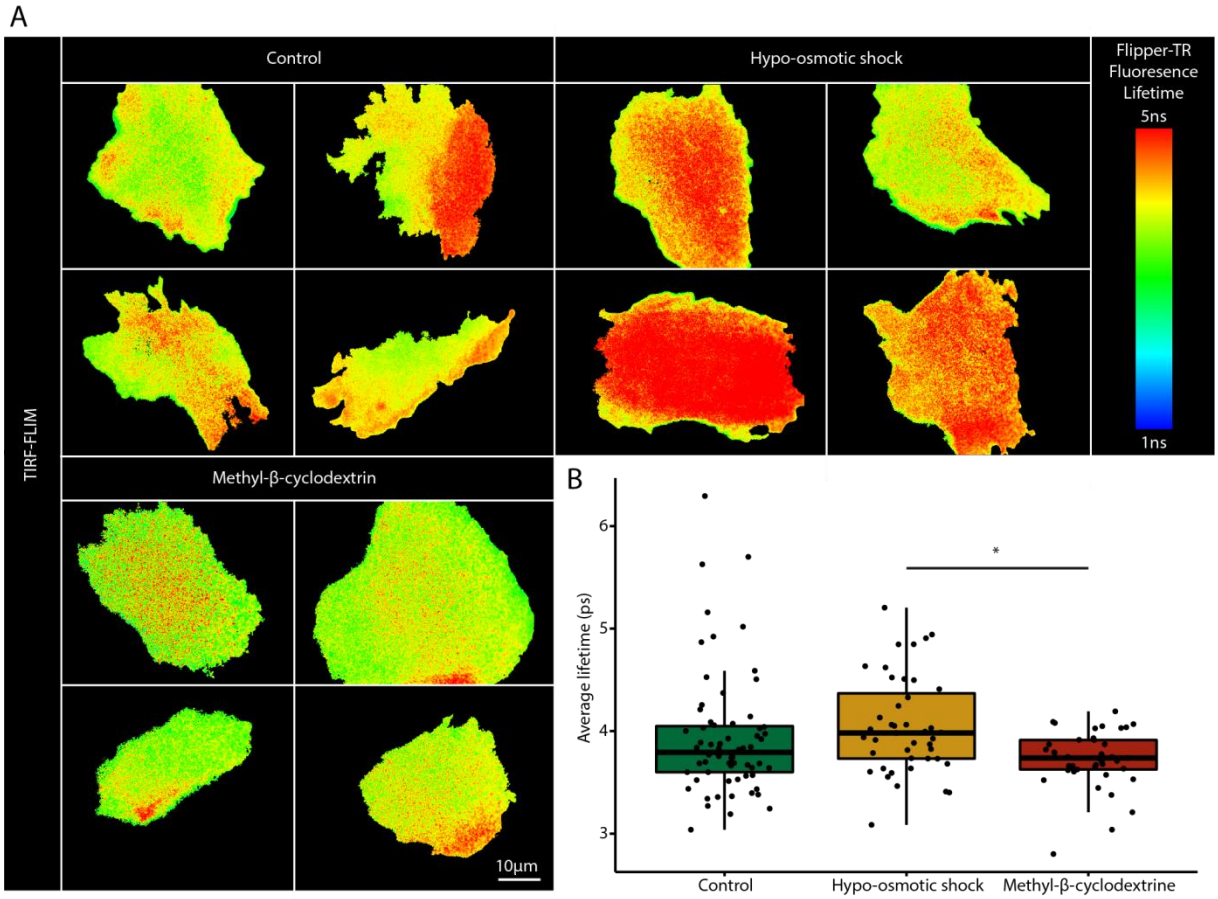

Figure S3. A. TIRF-FLIM images of 4 representative cells in each condition: control, hypo-osmotic shock (1:1 dilution, 15min) and β-methyl-cyclodextrin (5mM, 15min), all incubated with Flipper-TR. The color code represents the Flipper-TR fluorescence lifetime. **B.** Average fluorescence lifetime per cell in 3 conditions: control, hypo-osmotic shock and β-methyl-cyclodextrin. The significance has been evaluated using Kruskal-Wallis test and a *post-hoc* Dunn's test, *p<0.05, 67 cells were analyzed in control condition, 43 in hypo-osmotic shock condition, and 41 cells in β-methyl-cyclodextrin, from 5, 3 and 3 independent experiments, respectively.

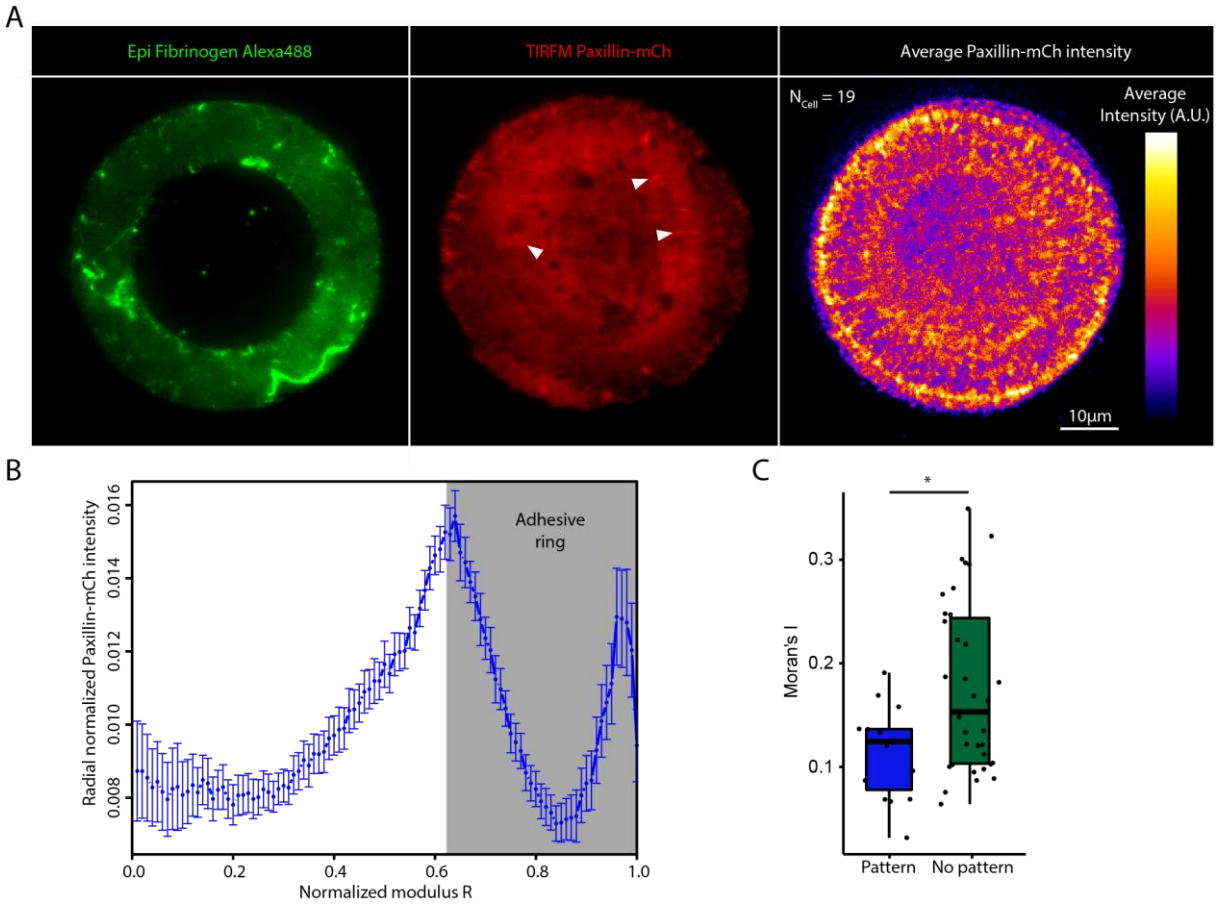

Figure S4. A. Representative epifluorescence image of a 37µm diameter ring-shaped micropattern stained with fibrinogene-Alexa488 and a TIRFM image of paxillin-mCh transfected cells. Arrowheads show internal FAs. On the right, average paxillin signal (from 19 cells) after denoising. **B.** Average paxillin radial intensity ± SEM. The modulus is normalized to the cell radius setting cell border at R=1. The intensity is normalized to obtain a total equal to 1, 19 cells were analyzed. **C.** Moran's index for cells seeded on micropattern or non-patterned fibronectin coated classical culture, 15 cells from one independent experiment and 42 cells from 9 independent experiments were analyzed, respectively. The significance has been evaluated using unpaired Wilcoxon test, *p<0.05.

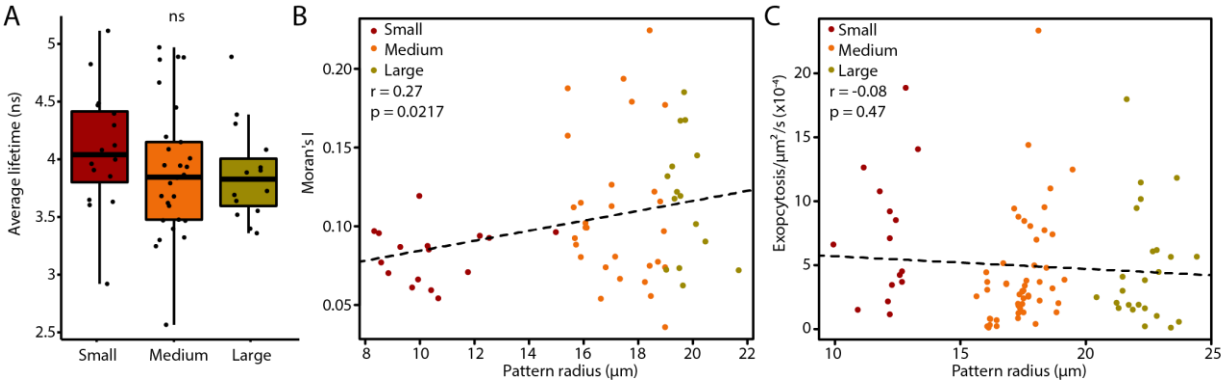

Figure S5. A. Average Flipper-TR fluorescence lifetimes per cell seeded on ring-shaped micropatterns with different diameters: small, medium and large. Significance has been evaluated using Kruskal-Wallis test, ns p>0.05. **B.** Correlation between the Moran's index per cell and the cell radius (cell seeded on ring-shaped micropatterns). Correlation has been evaluated using Pearson correlation (r=0.27) and t-test (p=0.0217) for correlation. In **A** and **B**, 60 cells from 5 independent experiments were analyzed. **C.** Correlation between the exocytosis rate per cell and the cell radius (cell seeded on ring-shaped micropatterns). Correlation has been evaluated using Pearson correlation (r=-0.08) and t-test (p=0.47) for correlation. 90 cells were analyzed from 11 independent experiments.

Materials and Methods

Cell culture: hTERT-immortalized retinal pigment epithelial cell line (hTERT RPE-1) were cultivated in DMEM/F12 media (Gibco, catalog # 21041-025) complemented with 10% Fetal Bovine Serum (Eurobio, catalog # CVFSVF00-01) (without antibiotics). Cells were maintained at 37°C with 5% CO2 in a humidified incubator.

Transfection: Cells were transfected with the following constructs: (Chaineau et al., 2008), mCh-Rab6A and Paxillin-mCh (Fourriere et al., 2019). Cells are transfected with 800ng of DNA (or 2x400ng for co-transfection) using the JetPrime kit (Polyplus). Cells were imaged 24h after transfection.

Drug treatments: Cells were treated with the following drugs with the given concentration and incubation time: Golgicide A 10µM 30min (Merck, catalog # G0923), Bafilomycin A1 100nM 1h (MedChemExpress, catalog # HY-100558), Histamine 100µM no incubation (Merck, catalog # H7125), Nocodazole 10µM 1h (Merck, catalog # M1404), Cytochalasin D 500nM 1h (Merck, catalog # C8273), Para-nitroblebbistatin 20µM 15min (Cayman Chemical Company, item 24171), β-methyl-cyclodextrin 5mM 15min (Merck, catalog # C4555). Hypo-osmotic shocks were made by adding water in the media with a volume ratio of 1:1 and cells were imaged 15min after. For all drug conditions, a paired design has been used: the same cell is imaged before and after the treatment.

Micropatterning: We followed the photolithography micropatterning protocol from Azioune *et al*. (Azioune et al., 2010). Briefly, coverslips (1.5H ThorLabs, Catalog # CG15XH1) were oxidized by plasma-cleaner (Harrick Plasma) during 5min. Coverslips were PEG-coated by incubating them on a drop of PLL-g-PEG (Surface Solutions, PLL(20)-g[3.5]- PEG(2)) (0.1mg/ml diluted in water, 10mM HEPES, pH=7.4) in a moiety chamber during 1h. After coating, patterns were printed using a deep UV lamp (Jelight Company Inc, catalog # 342-220) with radiation passing through a photomask (DeltaMask) during 5min. Finally, patterns were fibronectin-coated by incubating coverslips on a drop of fibronectin (Merck/Sigma, catalog # F1141) (50µg/ml diluted in water) and fibrinogen-Alexa647 (Molecular Probes, Invitrogen, catalog # F35200) (or fibrinogen-Alexa488) (5µg/ml) in a moiety chamber during 1h. Coverslips were conserved at 4°C in PBS.

Cell seeding on micropatterns was described in Lachuer et al. (Lachuer et al., 2020). Briefly, coverslips were maintained in magnetic chamlides for live imaging or kept in a P6 wells for fixation. ~200 000 trypsinized (Thermo Ficher, catalog # 12605010) cells were added in the chamlide chamber. After 10min incubation in 37°C incubator, cells were attached to the substrate. Cells were washing using DMEM/F12 media with 20mM HEPES (Gibco, catalog # 15630-056) (+ 2% penicillin/streptomycin (Gibco, catalog # 15140-122) if cells were used for lived-imaging). Cells were incubated at least 3h in the incubator until full spreading on the micropattern. Cells were imaged the same day.

Different geometries of micropatterns were used. In figure 4 and S2, ring-shaped micropatterns with a diameter of 37µm were employed. In figure 5, 3 sizes of ring-shaped micropatterns were used, with diameters of 25µm, 35µm and 45µm. For all sizes, the thickness of the adhesive ring was 7µm. Figure 5 also includes data of figure 4. Despite these theoretical sizes, a variation in the measured cell diameter was observed likely due to UV diffraction during the printing. The actual dimensions were systematically measured. During analysis, cells with diameter inferior to 20µm were categorized as “Small”, between 20µm and 38µm as “medium” and superior to 38µm as “large”. In figure S1, rectangular micropattern has dimensions of 9x40µm.

Microscopy:

TIRFM: Non-patterned cells were seeded in fluorodishes (World Precision Instrument) coated with fibronectin (or PLL (Merck P4707)). DMEM/F12 media + 20mM HEPES was used for imaging. Patterned cells were prepared as described. Acquisition was made using an inverted Nikon TIRFM equipped with an EMCCD camera (efficiency 95%) with a 100x objective (pixel size = 0.160µm). The following lasers were used 491nm, 561nm and 642nm. Time-lapse of VAMP7-pHluorin was acquired with a frame rate of 1 image every 300ms during 5min. Frame rate was set according to the half-life of exocytosis events. Due to microscopic device delay, the actual frame rate was computed using the computer time of saved files.

TIRF-FLIM: Images were acquired on a homemade setup based on a x100 1.49 Nikon Objective Objective (Blandin et al., 2009; Marquer et al., 2011). A 2MHz supercontinuum laser source (SC450 HE-PP Fianium) was filtered (Excitation filter 482-18, Dichroic Di01-R488, Emission filter Long Pass 488, Semrock) within the microscope cube to match the dye excitation/emission spectra. The average power in the back focal place of the objective was between 30 and 100 µW depending on the experiment. The TIRF angle was finely controlled thanks to a motorized stage which allows one to adjust the pulsed beam focalization in the back focal plane of the TIRFM objective. Fluorescence images were detected thanks to a time-resolved detection based on the use of a high-rate imager (Kentech Ltd., UK) optically relayed to a charge-coupled device camera (ORCA AG, Hamamatsu, binning 2x2). This intensifier was synchronized with the laser pulse through a programmable delay line (Kentech, precision programmable 50 Ω delay line), which enables us to open temporal gates with 1 ns width at different times after the pulse, thus sampling the fluorescence decay. Each time gated image corresponds to an average of 10 images (10 x 250 ms). FLIM maps were thus produced by recording a series of 17 time-gated fluorescence intensity images and fitting the data for each image pixel to a single exponential decay model by use of a standard nonlinear least-squares fitting algorithm.

Flipper-TR: Cells were prepared as for classical TIRFM. 15min before acquisition, Flipper-TR was added in the media (Spirochrome, Catalog # SC020) (Colom et al., 2018) at a concentration of 1µM. If used, drugs were added with Flipper-TR. Cells were not washed as recommended. Due to the high variability of the fluorescence lifetime, a z-score transformation was applied when specified. For each cell, the average µ and standard-deviation σ of the fluorescence lifetime was computed. Then, each lifetime pixel xi value was reduced and centered:

$$z_i = \frac{x_i - \mu}{\sigma}$$

Immunofluorescence: Cells were fixed with 4% PFA (Euromedex, catalog # 15710) during 15min and quenched with a 50mM NH4Cl solution. After PBS washing, cells were permeabilized (and blocked) with a PBS Saponin (MP Biomedicals, catalog # 102855) (0.5g/l) BSA (Merck, catalog # 10735094001) (1g/l). Coverslips were incubated during 1h in a moiety chamber at RT with primary antibodies diluted in a PBS 2% BSA solution. After PBS washing, coverslips were incubated with a secondary antibody (400x) conjugated with a fluorophore following the same protocol. Finally, coverslips were mounted with Mowiol (Biovaley, catalog # MWL4-88-25) and DAPI (Merck, catalog # D8417). The following primary antibodies were used: Syntaxin 3 (100x) (Merck/Sigma, catalog # S5547), Syntaxin 4 (1000x) (BD Transduction Laboratories, Material # 610439). The following secondary antibodies were used: Mouse A488 (Interchim 715-545-151) and Rabbit A488 (Interchim, 711-545-152).

Sample were imaged using an inverted videomicroscope with deconvolution (Delta Vision – Applied Precision) equipped with Xenon lamp. Acquisition was made at 100x (pixel size = 65nm). Images acquired were deconvolved using softworx (enhanced ratio method).

Statistical analysis: All statistical analysis were made with R (R Core Team (2021)) with the help of the following packages: spatsat (Baddeley et al., 2015), raster, viridis, ggplot2, dunn.test, ape (Paradis and Schliep, 2019), imager, pracma, circular, ggpur, evmix (Hu and Scarrott, 2018), splancs, OpenImageR, minpack.lm.

Hypothesis testing: The number of cells and the number of independent repetition is indicated in the legend. Since our cells are mostly isolated when imaged, we performed only single cells analysis, each cell is considered as independent, setting the sample size. The statistical test used is indicated in the legend. Tests are always conducted in a two-sided manner and a multiple comparison correction is applied when needed. We mainly used non-parametric test (Wilcoxon test, Kruskal-Wallis test), and a parametric test (Student t-test) only when the sample size was high (n>30). Paired tests were used for all experiments where the same cell is imaged before and after treatment. Finally, correlation was measured by Pearson correlation coefficient and tested with a t-test.

Intensity map: The intensity function λ is defined by:

$$E[x \in S] = \int_S \lambda(u) du$$

With x a pattern of points, u coordinates, S a region of the observation window, and E[x∈n] the expected number of points in S. The intensity map was computed using spatstat function density() with Jones-Diggle improved edge correction. The intensity map can be interpreted and normalized as a density map by dividing it by the total number of points.

Monte-Carlo CSR simulations: Monte-Carlo simulations were used for 3 purposes: i) normalization and ii) generation of CSR 95% envelopes.

i) Several measures used depend on the cell geometry and the number of exocytosis events. Therefore, we normalized observed values by CSR simulated values. For each cell, a high number (n=100) of Monte-Carlo simulations was run to generate CSR exocytosis maps associated with the same number of exocytosis events and the same cell geometry. The ratio between observed and average simulated values allows classifying cells in two categories: more extreme or less extreme than CSR compared to the observed measure.

ii) Monte-Carlo simulations were used to generate CSR envelopes. Some measures (mainly Ripley's K function) were averaged over a population of cells; therefore CSR simulations were run in the same way: Monte-Carlo CSR simulations were run for the full population of cells and the evaluated quantity is averaged over the different simulated cells. This procedure was repeated a high number of times (n=100). The CSR envelope contains 95% of these simulations.

Nearest Neighbor Distance: The Nearest Neighbor Distance (NND) of a given exocytosis event is the distance to the closest exocytosis event. These distances give information on the short scale spatial structure. NND was used to test CSR hypothesis according to the procedure presented in Lachuer *et al.* (Lachuer et al., 2020) and detailed in the Monte-Carlo section. Simulated average NND are compared to the observed NND. This allowed to classify the cell as clustered

($NND_{observed}$<$NND_{simulated}$), or dispersed ($NND_{observed}$>$NND_{simulated}$). Note that temporal NND were treated similarly to spatial NND, just by reducing the dimension of the analysis.

Ripley's K function: For a point pattern X={x_1, x_2, …, x_n} where each x is point coordinates observed in an area **|S|**, the Ripley's K function (Ripley, 1976; Dixon, 2014) is defined as:

$$K(r) = \frac{|\Omega|}{n(n-1)} \sum_{i=1}^{n} \sum_{j \neq i} 1_{|x_i - x_j| \leq r}$$

This function quantifies the average number of points in a disk of radius r centered on one point. In case of CSR, this function should be close to πr^2. Therefore we always substrate πr^2 to K(r), a positive value indicates clustering whereas a negative value indicates dispersing. The spatial Ripley's K function was computed using spatstat function Kest() with the best edge correction possible. Ripley's K function was computed between 0 and a quarter of the cell size to avoid edge effects. All Ripley's K functions plotted are an average of a population of Ripley's K functions (+/- SEM). A permutation test (with 999 permutations) based on a Studentized distance is used to compare populations thanks to the sptatstat function studpermu.test() (Hahn, 2012). Finally, a CSR 95% envelope was computed with Monte-Carlo simulations (see corresponding section).

Temporal Ripley's K function K(t) is the reduction of the 2D spatial Ripley's K function in 1D. Therefore the expected value under CSR hypothesis is 2t. K(t) was computed by our own function using the Ripley's edge correction following (Yunta et al., 2014). Temporal Ripley's K function was treated in the same way as the spatial one to generate the CSR 95% envelope and for the averaging.

Spatio-temporal Ripley's K function K(r,t) is the 3D extension of the spatial Ripley's K function that evaluates the number of neighbors in a cylinder of a radius r and a half height t (Diggle et al., 1995). K(r,t) was computed using the splancs function stkhat(). The median K(r,t) was computed (averaging is avoided due to the generation of aberrant values by splancs). In absence of spatio-temporal coupling (i.e. independency of the temporal and spatial point coordinates):

$$D = K(r,t) - K(r)K(t) = 0$$

Thereby the independency can be evaluated by the D statistics. It can be statistically tested using a permutation test (1000 permutations) using the splancs function stmctest().

Distance to cell border: Distance to cell border was computed using imager function distance_transform(). For each cell, the distance to cell border at exocytosis sites was measured. The distribution was computed using Kernel Density Estimation (KDE). The distribution depicted is a distribution averaged over multiples cells +/-SEM. The 95% CSR envelope was computed by Monte-Carlo simulations (see corresponding section). The solid blue line represents the average of the simulated densities.

The significance at the single cell level was accessed using Monte-Carlo simulations (see corresponding section). Observed cell border distances were divided by the average simulated cell border distances allowing a classification of the cells into two categories: borders-avoiding (ratio<1) or borders-linking (ratio>1).

Anisotropy: The cell was cut in 30 angular sections (from the center of mass). An angle θ_i was associated to each section. The number of exocytosis event was computed in each section and

divided by the surface of the corresponding section giving a coefficient w_i (normalized by the sum of the coefficients). The anisotropy/polarization measurement is based on the average resultant length computed as:

$$R = \frac{1}{n}\sqrt{\left(\sum_{i=1}^{30} w_i cos(\theta_i)\right)^2 + \left(\sum_{i=1}^{30} w_i sin(\theta_i)\right)^2}$$

This polarization index ranged between 0 and 1. The significance was accessed using Monte-Carlo simulations (see corresponding section). Observed average resultant lengths were divided by the average simulated resultant length allowing a classification of the cells into two categories: polarized (ratio>1) or non-polarized (ratio<1).

Exocytosis-FA co-appearing index: The average paxillin fluorescence intensity was measured at the locations of exocytosis event. The significance was accessed using Monte-Carlo simulations (see corresponding section). The comparison of the observed average intensity with simulated ones allows classifying cells with a colocalization index (I_{obs}/I_{sim}) under two categories: co-appearing ($I_{obs}/I_{sim}>1$), no-co-appearing ($I_{obs}/I_{sim}<1$).

Modulus distribution: On micropatterns, exocytosis events were described with polar coordinates (with the origin at the center of the pattern). The modulus is the distance between an event and the center (normalized by the cell radius). For each cell a modulus distribution was computed using Kernel Density Estimation (KDE). To avoid boundary effects, an asymmetric beta kernel was used (Chen, 1999) using the evmix function dbckden(). The depicted modulus distribution is an average over the population +/- SEM. This distribution can be compared to the expected distribution in case of CSR:

$$p_{CSR}(r) = 2r$$

The 95% CSR envelope was computed using Monte-Carlo simulations (see corresponding section). Despite beta edge correction, the simulations do not fit perfectly p_{csr}. In order to avoid any bias due to kernels, we also conducted the same analysis using empirical cumulative distributions. The empirical cumulative distribution P_{CSR} under CSR hypothesis is:

$$P_{CSR}(r) = \int_0^1 p_{CSR}(x)\,dx = r^2$$

Fourier analysis: Fourier analysis was conducted using Fast Fourier Transform function fft(). The spectrum of modulus was computed for each cell between 0 and Nyquist frequency. Modulus spectrum were averaged over the cell population.

Moran'I: Moran's I evaluates the spatial auto-correlation (Moran, 1950). We used it to evaluate the spatial structure of lifetime measurement. For an image of N pixels, the Moran's I is defined as:

$$I = \frac{N}{\sum_{i=1}^{N}\sum_{j=1}^{N} w_{i,j}} \frac{\sum_{i=1}^{N}\sum_{j=1}^{N} w_{i,j}(x_i - \bar{x})\left(x_j - \bar{x}\right)}{\sum_{i=1}^{N}(x_i - \bar{x})^2}$$

With x_i the i^{th} pixel value, $\bar{x}$ the average pixel values, and w_{ij} the inverse of the Euclidian distance between pixel i and j. This index is superior to -1/(N-1) in case of pixel clustering and inferior to in

case of regular spacing (*i.e.* pixels with similar values are regularly separated). A decreased of the Moran's I should be perceived as a spatial decorrelation *i.e.* pixels are less clustered. Moran's I index was computed using ape function Moran.I() using a random subsample of pixels (Monte-Carlo random sampling scheme) to keep a decent computation time.

Image analysis:

Exocytosis detection: Exocytosis events were detected manually (because automatization failed to reach our exigency level). However some events were probably missed (false negative). This is not a problem, because Ripley's K function is invariant under random thinning (Baddeley et al., 2015). It is also likely that some events did not correspond to exocytosis (false positive). Due to the superposition principle (Baddeley et al., 2015), the experimental Ripley's K function is the sum of the exocytosis Ripley's K function and the one of false annotation. Therefore, under the assumption that these false annotations are random, possible false annotations could only slightly underestimates clustering.

Half-life: Fluorescence intensity was measured at exocytosis event localizations in a window of 1.12µm centered on the event through time. The intensity was divided by the intensity at the beginning of the event normalizing the exocytosis peak at 1. The intensity profile of all events in a cell was averaged. The intensity was fitted on this averaged profile over 20 frames (~8s) with a single exponential function:

$$I(t) = Ae^{-t/t_{1/2}} + B$$

With $t_{1/2}$ the half-life. The fitting was performed with the minpack.lm function nlsLM(). The profile depicted is the average over multiple cells. The half-life obtained from this average curve is close to the lifetime averaged over multiple cells.

Segmentation: Cell segmentation to obtain mask or segmentation of syntaxin patches was perforled using manual thresholding with ImageJ software.

Acknowledgements

We are grateful to Sabine Bardin, Pallavi Mathur, David Pereira, Tarn Duong, Mathieu Coppey and Pierre Sens for fruitful discussions and/or help at the bench. We also thank Mathieu Piel lab for sharing photomasks, Thierry Galli for the VAMP7-pHluorin plasmid and syntaxin antibodies, and Marc Tramier and Giulia Bertolin for testing Flipper-TR with their FAST-FLIM. Finally, we thank (again) Thierry Galli and Christophe Lamaze for critical reading of the manuscript. The authors greatly acknowledge the Nikon Imaging Centre @ Institut Curie-CNRS, member of the French National Research Infrastructure France-BioImaging (ANR10-INSB-04). This work was supported by ARC (Association pour la Recherche sur le Cancer) PhD fellowship and FRM (Fondation Recherche Médicale) PhD extension fellowship.

Declaration of Interests

The authors declare no competing interests.

References

Andrews, N.W., and Corrotte, M. (2018). Plasma membrane repair. Curr. Biol. 28, R392–R397. https://doi.org/10.1016/j.cub.2017.12.034.

Arantes, R.M.E., and Andrews, N.W. (2006). A Role for Synaptotagmin VII-Regulated Exocytosis of Lysosomes in Neurite Outgrowth from Primary Sympathetic Neurons. J. Neurosci. 26, 4630–4637. https://doi.org/10.1523/JNEUROSCI.0009-06.2006.

Azioune, A., Carpi, N., Tseng, Q., Théry, M., and Piel, M. (2010). Protein micropatterns: A direct printing protocol using deep UVs. Methods Cell Biol. 97, 133–146. https://doi.org/10.1016/S0091-679X(10)97008-8.

Ba, Q., Raghavan, G., Kiselyov, K., and Yang, G. (2018). Whole-Cell Scale Dynamic Organization of Lysosomes Revealed by Spatial Statistical Analysis. Cell Rep. 23, 3591–3606. https://doi.org/10.1016/j.celrep.2018.05.079.

Baddeley, A., Rubak, E., and Turner, R. (2015). Spatial Point Patterns: Methodology and Applications with R (Boca Raton ; London ; New York: Chapman and Hall/CRC).

Biswas, A., Kashyap, P., Datta, S., Sengupta, T., and Sinha, B. (2019). Cholesterol Depletion by MβCD Enhances Cell Membrane Tension and Its Variations-Reducing Integrity. Biophys. J. 116, 1456–1468. https://doi.org/10.1016/j.bpj.2019.03.016.

Blandin, P., Lévêque-Fort, S., Lécart, S., Cossec, J.C., Potier, M.-C., Lenkei, Z., Druon, F., and Georges, P. (2009). Time-gated total internal reflection fluorescence microscopy with a supercontinuum excitation source. Appl. Opt. 48, 553–559. https://doi.org/10.1364/ao.48.000553.

Bogdanovic, A., Bennett, N., Kieffer, S., Louwagie, M., Morio, T., Garin, J., Satre, M., and Bruckert, F. (2002). Syntaxin 7, syntaxin 8, Vti1 and VAMP7 (vesicle-associated membrane protein 7) form an active SNARE complex for early macropinocytic compartment fusion in Dictyostelium discoideum. Biochem. J. 368, 29–39. https://doi.org/10.1042/BJ20020845.

Burgo, A., Proux-Gillardeaux, V., Sotirakis, E., Bun, P., Casano, A., Verraes, A., Liem, R.K.H., Formstecher, E., Coppey-Moisan, M., and Galli, T. (2012). A Molecular Network for the Transport of the TI-VAMP/VAMP7 Vesicles from Cell Center to Periphery. Dev. Cell 23, 166–180. https://doi.org/10.1016/j.devcel.2012.04.019.

Chaineau, M., Danglot, L., Proux-Gillardeaux, V., and Galli, T. (2008). Role of HRB in clathrin-dependent endocytosis. J. Biol. Chem. 283, 34365–34373. https://doi.org/10.1074/jbc.M804587200.

Chaineau, M., Danglot, L., and Galli, T. (2009). Multiple roles of the vesicular-SNARE TI-VAMP in post-Golgi and endosomal trafficking. FEBS Lett. 583, 3817–3826. https://doi.org/10.1016/j.febslet.2009.10.026.

Chen, S.X. (1999). Beta kernel estimators for density functions. Comput. Stat. Data Anal. 31, 131–145. https://doi.org/10.1016/S0167-9473(99)00010-9.

Chen, D., Zheng, Q., Sun, L., Ji, M., Li, Y., Deng, H., and Zhang, H. (2021). ORF3a of SARS-CoV-2 promotes lysosomal exocytosis-mediated viral egress. Dev. Cell 56, 3250-3263.e5. https://doi.org/10.1016/j.devcel.2021.10.006.

Chen, G., Zhang, Z., Wei, Z., Cheng, Q., Li, X., Li, W., Duan, S., and Gu, X. (2012). Lysosomal exocytosis in Schwann cells contributes to axon remyelination. Glia 60, 295–305. https://doi.org/10.1002/glia.21263.

Cohen, A.E., and Shi, Z. (2020). Do Cell Membranes Flow Like Honey or Jiggle Like Jello? BioEssays 42, 1900142. https://doi.org/10.1002/bies.201900142.

Colom, A., Derivery, E., Soleimanpour, S., Tomba, C., Molin, M.D., Sakai, N., González-Gaitán, M., Matile, S., and Roux, A. (2018). A fluorescent membrane tension probe. Nat. Chem. 10, 1118–1125. https://doi.org/10.1038/s41557-018-0127-3.

Cox, C.D., Zhang, Y., Zhou, Z., Walz, T., and Martinac, B. (2021). Cyclodextrins increase membrane tension and are universal activators of mechanosensitive channels. Proc. Natl. Acad. Sci. U. S. A. 118, e2104820118. https://doi.org/10.1073/pnas.2104820118.

Diggle, P. (1983). Statistical Analysis of Spatial Point Patterns (Academic Press).

Diggle, P.J., Chetwynd, A.G., Häggkvist, R., and Morris, S.E. (1995). Second-order analysis of space-time clustering. Stat. Methods Med. Res. 4, 124–136. https://doi.org/10.1177/096228029500400203.

Dixon, P.M. (2014). Ripley's K Function. In Wiley StatsRef: Statistics Reference Online, (John Wiley & Sons, Ltd), p.

Dou, Y., Wu, H., Li, H., Qin, S., Wang, Y., Li, J., Lou, H., Chen, Z., Li, X., Luo, Q., et al. (2012). Microglial migration mediated by ATP-induced ATP release from lysosomes. Cell Res. 22, 1022–1033. https://doi.org/10.1038/cr.2012.10.

Fernández-Chacón, R., Königstorfer, A., Gerber, S.H., García, J., Matos, M.F., Stevens, C.F., Brose, N., Rizo, J., Rosenmund, C., and Südhof, T.C. (2001). Synaptotagmin I functions as a calcium regulator of release probability. Nature 410, 41–49. https://doi.org/10.1038/35065004.

Fourriere, L., Kasri, A., Gareil, N., Bardin, S., Bousquet, H., Pereira, D., Perez, F., Goud, B., Boncompain, G., and Miserey-Lenkei, S. (2019). RAB6 and microtubules restrict protein secretion to focal adhesions. J. Cell Biol. 218, 2215–2231. https://doi.org/10.1083/jcb.201805002.

Fu, J., Githaka, J.M., Dai, X., Plummer, G., Suzuki, K., Spigelman, A.F., Bautista, A., Kim, R., Greitzer-Antes, D., Fox, J.E.M., et al. (2019). A glucose-dependent spatial patterning of exocytosis in human β-cells is disrupted in type 2 diabetes. JCI Insight 5, 127896. https://doi.org/10.1172/jci.insight.127896.

Galli, T., Zahraoui, A., Vaidyanathan, V.V., Raposo, G., Tian, J.M., Karin, M., Niemann, H., and Louvard, D. (1998). A novel tetanus neurotoxin-insensitive vesicle-associated membrane protein in SNARE complexes of the apical plasma membrane of epithelial cells. Mol. Biol. Cell 9, 1437–1448. https://doi.org/10.1091/mbc.9.6.1437.

Gauthier, N.C., Fardin, M.A., Roca-Cusachs, P., and Sheetz, M.P. (2011). Temporary increase in plasma membrane tension coordinates the activation of exocytosis and contraction during cell spreading. Proc. Natl. Acad. Sci. 108, 14467–14472. https://doi.org/10.1073/pnas.1105845108.

Geuze, H.J. (1998). The role of endosomes and lysosomes in MHC class II functioning. Immunol. Today 19, 282–287. https://doi.org/10.1016/S0167-5699(98)01269-9.

Ghosh, S., Dellibovi-Ragheb, T.A., Kerviel, A., Pak, E., Qiu, Q., Fisher, M., Takvorian, P.M., Bleck, C., Hsu, V.W., Fehr, A.R., et al. (2020). β-Coronaviruses Use Lysosomes for Egress Instead of the Biosynthetic Secretory Pathway. Cell 183, 1520-1535.e14. https://doi.org/10.1016/j.cell.2020.10.039.

Gundelfinger, E.D., Kessels, M.M., and Qualmann, B. (2003). Temporal and spatial coordination of exocytosis and endocytosis. Nat. Rev. Mol. Cell Biol. 4, 127–139. https://doi.org/10.1038/nrm1016.

Gupton, S.L., and Gertler, F.B. (2010). Integrin signaling switches the cytoskeletal and exocytic machinery that drives neuritogenesis. Dev. Cell 18, 725–736. https://doi.org/10.1016/j.devcel.2010.02.017.

Hahn, U. (2012). A Studentized Permutation Test for the Comparison of Spatial Point Patterns. J. Am. Stat. Assoc. 107, 754–764. https://doi.org/10.1080/01621459.2012.688463.

Hissa, B., Oakes, P.W., Pontes, B., Ramírez-San Juan, G., and Gardel, M.L. (2017). Cholesterol depletion impairs contractile machinery in neonatal rat cardiomyocytes. Sci. Rep. 7, 43764. https://doi.org/10.1038/srep43764.

Hoshino, D., Kirkbride, K.C., Costello, K., Clark, E.S., Sinha, S., Grega-Larson, N., Tyska, M.J., and Weaver, A.M. (2013). Exosome secretion is enhanced by invadopodia and drives invasive behavior. Cell Rep. 5, 1159–1168. https://doi.org/10.1016/j.celrep.2013.10.050.

Hu, Y., and Scarrott, C. (2018). evmix: An R package for Extreme Value Mixture Modeling, Threshold Estimation and Boundary Corrected Kernel Density Estimation. J. Stat. Softw. 84, 1–27. https://doi.org/10.18637/jss.v084.i05.

Huynh, K.K., Kay, J.G., Stow, J.L., and Grinstein, S. (2007). Fusion, Fission, and Secretion During Phagocytosis. Physiology 22, 366–372. https://doi.org/10.1152/physiol.00028.2007.

Kasai, H., Takahashi, N., and Tokumaru, H. (2012). Distinct initial SNARE configurations underlying the diversity of exocytosis. Physiol. Rev. 92, 1915–1964. https://doi.org/10.1152/physrev.00007.2012.

Keller, P., Toomre, D., Díaz, E., White, J., and Simons, K. (2001). Multicolour imaging of post-Golgi sorting and trafficking in live cells. Nat. Cell Biol. 3, 140–149. https://doi.org/10.1038/35055042.

Kliesch, T.-T., Dietz, J., Turco, L., Halder, P., Polo, E., Tarantola, M., Jahn, R., and Janshoff, A. (2017). Membrane tension increases fusion efficiency of model membranes in the presence of SNAREs. Sci. Rep. 7, 12070. https://doi.org/10.1038/s41598-017-12348-w.

Kloepper, T.H., Kienle, C.N., and Fasshauer, D. (2007). An Elaborate Classification of SNARE Proteins Sheds Light on the Conservation of the Eukaryotic Endomembrane System. Mol. Biol. Cell 18, 3463–3471. https://doi.org/10.1091/mbc.E07-03-0193.

Kowal, J., Tkach, M., and Théry, C. (2014). Biogenesis and secretion of exosomes. Curr. Opin. Cell Biol. 29, 116–125. https://doi.org/10.1016/j.ceb.2014.05.004.

Lachuer, H., Mathur, P., Bleakley, K., and Schauer, K. (2020). Quantifying Spatiotemporal Parameters of Cellular Exocytosis in Micropatterned Cells. J. Vis. Exp. JoVE https://doi.org/10.3791/60801.

Lacombe, J., Karsenty, G., and Ferron, M. (2013). Regulation of lysosome biogenesis and functions in osteoclasts. Cell Cycle Georget. Tex 12, 2744–2752. https://doi.org/10.4161/cc.25825.

LaPlante, J.M., Sun, M., Falardeau, J., Dai, D., Brown, E.M., Slaugenhaupt, S.A., and Vassilev, P.M. (2006). Lysosomal exocytosis is impaired in mucolipidosis type IV. Mol. Genet. Metab. 89, 339–348. https://doi.org/10.1016/j.ymgme.2006.05.016.

Lieber, A.D., Schweitzer, Y., Kozlov, M.M., and Keren, K. (2015). Front-to-Rear Membrane Tension Gradient in Rapidly Moving Cells. Biophys. J. 108, 1599–1603. https://doi.org/10.1016/j.bpj.2015.02.007.

Machado, E., White-Gilbertson, S., van de Vlekkert, D., Janke, L., Moshiach, S., Campos, Y., Finkelstein, D., Gomero, E., Mosca, R., Qiu, X., et al. (2015). Regulated lysosomal exocytosis mediates cancer progression. Sci. Adv. 1, e1500603. https://doi.org/10.1126/sciadv.1500603.

Mao, F., Yang, Y., and Jiang, H. (2021). Endocytosis and exocytosis protect cells against severe membrane tension variations. Biophys. J. 120, 5521–5529. https://doi.org/10.1016/j.bpj.2021.11.019.

Marquer, C., Devauges, V., Cossec, J.-C., Liot, G., Lécart, S., Saudou, F., Duyckaerts, C., Lévêque-Fort, S., and Potier, M.-C. (2011). Local cholesterol increase triggers amyloid precursor protein-Bace1 clustering in lipid rafts and rapid endocytosis. FASEB J. Off. Publ. Fed. Am. Soc. Exp. Biol. 25, 1295–1305. https://doi.org/10.1096/fj.10-168633.

Martinez-Arca, S., Alberts, P., Zahraoui, A., Louvard, D., and Galli, T. (2000). Role of tetanus neurotoxin insensitive vesicle-associated membrane protein (TI-VAMP) in vesicular transport mediating neurite outgrowth. J. Cell Biol. 149, 889–900. https://doi.org/10.1083/jcb.149.4.889.

Miklavc, P., and Frick, M. (2020). Actin and Myosin in Non-Neuronal Exocytosis. Cells 9, 1455. https://doi.org/10.3390/cells9061455.

Moran, P.A.P. (1950). Notes on Continuous Stochastic Phenomena. Biometrika 37, 17–23. https://doi.org/10.2307/2332142.

Neveu, E., Khalifeh, D., Salamin, N., and Fasshauer, D. (2020). Prototypic SNARE Proteins Are Encoded in the Genomes of Heimdallarchaeota, Potentially Bridging the Gap between the Prokaryotes and Eukaryotes. Curr. Biol. CB 30, 2468-2480.e5. https://doi.org/10.1016/j.cub.2020.04.060.

Novick, P., Field, C., and Schekman, R. (1980). Identification of 23 complementation groups required for post-translational events in the yeast secretory pathway. Cell 21, 205–215. https://doi.org/10.1016/0092-8674(80)90128-2.

Paradis, E., and Schliep, K. (2019). ape 5.0: an environment for modern phylogenetics and evolutionary analyses in R. Bioinformatics 35, 526–528. https://doi.org/10.1093/bioinformatics/bty633.

Peters, P.J., Borst, J., Oorschot, V., Fukuda, M., Krähenbühl, O., Tschopp, J., Slot, J.W., and Geuze, H.J. (1991). Cytotoxic T lymphocyte granules are secretory lysosomes, containing both perforin and granzymes. J. Exp. Med. 173, 1099–1109. https://doi.org/10.1084/jem.173.5.1099.

Proux-Gillardeaux, V., Raposo, G., Irinopoulou, T., and Galli, T. (2007). Expression of the Longin domain of TI-VAMP impairs lysosomal secretion and epithelial cell migration. Biol. Cell 99, 261–271. https://doi.org/10.1042/BC20060097.

Ripley, B.D. (1976). The Second-Order Analysis of Stationary Point Processes. J. Appl. Probab. 13, 255–266. https://doi.org/10.2307/3212829.

Saenz, J.B., Sun, W.J., Chang, J.W., Li, J., Bursulaya, B., Gray, N.S., and Haslam, D.B. (2009). Golgicide A reveals essential roles for GBF1 in Golgi assembly and function. Nat. Chem. Biol. 5, 157–165. https://doi.org/10.1038/nchembio.144.

Samie, M.A., and Xu, H. (2014). Lysosomal exocytosis and lipid storage disorders. J. Lipid Res. 55, 995–1009. https://doi.org/10.1194/jlr.R046896.

Schauer, K., Duong, T., Bleakley, K., Bardin, S., Bornens, M., and Goud, B. (2010). Probabilistic density maps to study global endomembrane organization. Nat. Methods 7, 560–566. https://doi.org/10.1038/nmeth.1462.

Schiefermeier, N., Scheffler, J.M., de Araujo, M.E.G., Stasyk, T., Yordanov, T., Ebner, H.L., Offterdinger, M., Munck, S., Hess, M.W., Wickström, S.A., et al. (2014). The late endosomal p14-MP1 (LAMTOR2/3) complex regulates focal adhesion dynamics during cell migration. J. Cell Biol. 205, 525–540. https://doi.org/10.1083/jcb.201310043.

Schmoranzer, J., Goulian, M., Axelrod, D., and Simon, S.M. (2000). Imaging Constitutive Exocytosis with Total Internal Reflection Fluorescence Microscopy. J. Cell Biol. 149, 23–32. .

Schweitzer, Y., Lieber, A.D., Keren, K., and Kozlov, M.M. (2014). Theoretical Analysis of Membrane Tension in Moving Cells. Biophys. J. 106, 84–92. https://doi.org/10.1016/j.bpj.2013.11.009.

Sebastian, R., Diaz, M.-E., Ayala, G., Letinic, K., Moncho-Bogani, J., and Toomre, D. (2006). Spatio-temporal analysis of constitutive exocytosis in epithelial cells. IEEE/ACM Trans. Comput. Biol. Bioinform. 3, 17–32. https://doi.org/10.1109/TCBB.2006.11.

Seetharaman, S., and Etienne-Manneville, S. (2019). Microtubules at focal adhesions – a double-edged sword. J. Cell Sci. 132, jcs232843. https://doi.org/10.1242/jcs.232843.

Shi, Z., Graber, Z.T., Baumgart, T., Stone, H.A., and Cohen, A.E. (2018). Cell Membranes Resist Flow. Cell 175, 1769-1779.e13. https://doi.org/10.1016/j.cell.2018.09.054.

Söllner, T., Whiteheart, S.W., Brunner, M., Erdjument-Bromage, H., Geromanos, S., Tempst, P., and Rothman, J.E. (1993). SNAP receptors implicated in vesicle targeting and fusion. Nature 362, 318–324. https://doi.org/10.1038/362318a0.

Stehbens, S., and Wittmann, T. (2012). Targeting and transport: How microtubules control focal adhesion dynamics. J. Cell Biol. 198, 481–489. https://doi.org/10.1083/jcb.201206050.

Stehbens, S.J., Paszek, M., Pemble, H., Ettinger, A., Gierke, S., and Wittmann, T. (2014). CLASPs link focal-adhesion-associated microtubule capture to localized exocytosis and adhesion site turnover. Nat. Cell Biol. 16, 561–573. https://doi.org/10.1038/ncb2975.

Südhof, T.C. (2012). The Presynaptic Active Zone. Neuron 75, 11–25. https://doi.org/10.1016/j.neuron.2012.06.012.

Urbina, F.L., Gomez, S.M., and Gupton, S.L. (2018). Spatiotemporal organization of exocytosis emerges during neuronal shape change. J. Cell Biol. 217, 1113–1128. https://doi.org/10.1083/jcb.201709064.

Verderio, C., Cagnoli, C., Bergami, M., Francolini, M., Schenk, U., Colombo, A., Riganti, L., Frassoni, C., Zuccaro, E., Danglot, L., et al. (2012). TI-VAMP/VAMP7 is the SNARE of secretory lysosomes contributing to ATP secretion from astrocytes. Biol. Cell 104, 213–228. https://doi.org/10.1111/boc.201100070.

Verweij, F.J., Bebelman, M.P., Jimenez, C.R., Garcia-Vallejo, J.J., Janssen, H., Neefjes, J., Knol, J.C., de Goeij-de Haas, R., Piersma, S.R., Baglio, S.R., et al. (2018). Quantifying exosome secretion from single cells reveals a modulatory role for GPCR signaling. J. Cell Biol. 217, 1129–1142. https://doi.org/10.1083/jcb.201703206.

Vogel, G.F., Klee, K.M.C., Janecke, A.R., Müller, T., Hess, M.W., and Huber, L.A. (2015). Cargo-selective apical exocytosis in epithelial cells is conducted by Myo5B, Slp4a, Vamp7, and Syntaxin 3. J. Cell Biol. 211, 587–604. https://doi.org/10.1083/jcb.201506112.

Wade, N., Bryant, N.J., Connolly, L.M., Simpson, R.J., Luzio, J.P., Piper, R.C., and James, D.E. (2001). Syntaxin 7 Complexes with Mouse Vps10p Tail Interactor 1b, Syntaxin 6, Vesicle-associated Membrane Protein (VAMP)8, and VAMP7 in B16 Melanoma Cells*. J. Biol. Chem. 276, 19820–19827. https://doi.org/10.1074/jbc.M010838200.

Wang, G., and Galli, T. (2018). Reciprocal link between cell biomechanics and exocytosis. Traffic 19, 741–749. https://doi.org/10.1111/tra.12584.

Wang, G., Nola, S., Bovio, S., Bun, P., Coppey-Moisan, M., Lafont, F., and Galli, T. (2018). Biomechanical Control of Lysosomal Secretion Via the VAMP7 Hub: A Tug-of-War between VARP and LRRK1. IScience 4, 127–143. https://doi.org/10.1016/j.isci.2018.05.016.

Ward, D.M., Pevsner, J., Scullion, M.A., Vaughn, M., and Kaplan, J. (2000). Syntaxin 7 and VAMP-7 are soluble N-ethylmaleimide-sensitive factor attachment protein receptors required for late endosome-lysosome and homotypic lysosome fusion in alveolar macrophages. Mol. Biol. Cell 11, 2327–2333. https://doi.org/10.1091/mbc.11.7.2327.

Wen, P.J., Grenklo, S., Arpino, G., Tan, X., Liao, H.-S., Heureaux, J., Peng, S.-Y., Chiang, H.-C., Hamid, E., Zhao, W.-D., et al. (2016). Actin dynamics provides membrane tension to merge fusing vesicles into the plasma membrane. Nat. Commun. 7, 12604. https://doi.org/10.1038/ncomms12604.

Williams, K.C., McNeilly, R.E., and Coppolino, M.G. (2014). SNAP23, Syntaxin4, and vesicle-associated membrane protein 7 (VAMP7) mediate trafficking of membrane type 1-matrix metalloproteinase (MT1-MMP) during invadopodium formation and tumor cell invasion. Mol. Biol. Cell 25, 2061–2070. https://doi.org/10.1091/mbc.E13-10-0582.

Xu, J., Toops, K.A., Diaz, F., Carvajal-Gonzalez, J.M., Gravotta, D., Mazzoni, F., Schreiner, R., Rodriguez-Boulan, E., and Lakkaraju, A. (2012). Mechanism of polarized lysosome exocytosis in epithelial cells. J. Cell Sci. 125, 5937–5943. https://doi.org/10.1242/jcs.109421.

Yuan, T., Lu, J., Zhang, J., Zhang, Y., and Chen, L. (2015). Spatiotemporal detection and analysis of exocytosis reveal fusion “hotspots” organized by the cytoskeleton in endocrine cells. Biophys. J. 108, 251–260. https://doi.org/10.1016/j.bpj.2014.11.3462.

Yunta, M.L., Lagache, T., Santi-Rocca, J., Bastin, P., and Olivo-Marin, J.-C. (2014). A statistical analysis of spatial clustering along cell filaments using Ripley’s K function. In 2014 IEEE 11th International Symposium on Biomedical Imaging (ISBI), pp. 541–544.

Zwiewka, M., Nodzyński, T., Robert, S., Vanneste, S., and Friml, J. (2015). Osmotic Stress Modulates the Balance between Exocytosis and Clathrin-Mediated Endocytosis in Arabidopsis thaliana. Mol. Plant 8, 1175–1187. https://doi.org/10.1016/j.molp.2015.03.007.

Discussion

Discussion

***Summary*.** The analysis of our data with the tools of spatial statistics demonstrate that lysosomal exocytosis is not random (i.e. CSR) but clustered. Exocytosis events are regrouped and avoid cell borders. They partially appear at internal FAs in a cytoskeleton-independent manner, but are related to membrane tension. Removing FAs reduces clustering, whereas perturbations of membrane tension increase it. Moreover, in the absence of FAs, membrane tension seems less compartmentalized. Manipulating FAs by seeding cells on ring-shaped micropatterns revealed the existence of a radial gradient of membrane tension. Using this micropatterning system, we demonstrate that exocytosis probability correlates with local membrane tension. Finally, by changing the micropattern diameter, we controlled the strength of the membrane tension gradient and the exocytosis clustering. Taken together, we propose that the spatial organization of exocytosis relies on the distribution of membrane tension. The intracellular correlation between membrane tension and exocytosis confirms a claim of the literature: exocytosis probability increases with membrane tension. In a non-homogeneous PM, some regions could favor exocytosis whereas others are unfavorable. The direct prediction of this hypothesis is that the compartmentalization of membrane tension directly correlates with the organization of exocytosis.

***Framework to investigate spatial organization of exocytosis*.** In addition to the challenge to record exocytosis events, already solved by the development of TIRFM and pH-sensitive probes, the investigation of the spatial organization of exocytosis required a pertinent cell model. Models for the exocytosis of vesicles derived from the Golgi apparatus are already well documented (**see chapter 2**), but cell models of lysosomal exocytosis are rare. RPE1 cells seem to be a good model for investigating lysosomal exocytosis due to their high exocytosis rate, likely resulting from their phagocytic activity (Kwon and Freeman, 2020). The large variations in the exocytosis rate observed from one cell to another could be explained by the fact that RPE1 cells conserve a circadian rhythm in culture regulating many cellular processes (e.g. phagocytosis) (Ikarashi et al., 2017).

In addition to these biological considerations, the investigation of spatial organization of exocytosis required quantitative measurements. Spatial statistics provides many useful tools (**see chapter 4**) easily usable in experimental studies (Ripley's K function, NND), whereas others required more development (inhomogeneous Ripley's K function). However, the application of these tools to cell biology data raises some specific challenges. First, it requires handling data with several repetitions. We propose to simply average individual Ripley's K functions and to compare conditions thanks to the permutation test developed by Hahn (Hahn, 2012). In addition to comparison between conditions, a method to compare observed data and a model of point process (especially CSR) is required. We proposed to achieve this comparison by comparing observed data with simulations (Monte-Carlo simulations for CSR). This method has the advantage to fix the problem of edge effects that are important for complex geometries such as cell fractal shape. Indeed, by comparing spatial point patterns in the same geometry, the bias potentially introduced by edge effects equally affects observed point patterns and the simulations, keeping the comparison bias-free.

The role of the cell substrate and FAs. Our work illustrates the importance of the cell substrate in exocytosis. Cells seeded on PLL display an increased exocytosis rate, but a decreased clustering of exocytic events. The increased exocytosis rate (normalized to surface units) could be explained by a reduction of the membrane spreading, while keeping the number of lysosomes per cell constant.

Interestingly, in neurons, poly-D-lysin coating decreases VAMP7+ exocytosis rate compared to laminin coating. This decrease of lysosomal exocytosis seems to be due to a lack of poly-D-lysin-mediated FA signaling (Gupton and Gertler, 2010). Precautions should be taken when comparing neuronal and non-neuronal cell types, because VAMP7+ vesicles can be Golgi-derived in neurons (Martinez-Arca et al., 2000; Chaineau et al., 2009). Another study in a non-neuronal cell-type reveals that VAMP7+ exocytosis depends on the substrate elasticity. However, the cell sensibility to substrate elasticity appears only on laminin coated but not polylysin coated substrates (Wang et al., 2018b). The role of the substrate mechanics (elasticity) and biochemistry (coating) in the regulation of VAMP7 exocytosis rate is still unclear and deserves more attention in future studies.

Our study clearly demonstrates that lysosomal exocytosis sites appear at (or close to) internal FAs. Interestingly, it has been demonstrated that a subpopulation of lysosomes positive for the MAPK scaffold complex p14-MP1 is specifically targeted to FAs (Schiefermeier et al., 2014). However, it has not been directly shown that these lysosomes are exocytosed at FAs, although their targeting is necessary for correct FA remodeling during cell migration. A previous study demonstrated that Golgi-derived vesicles are exocytosed at FAs, but peripheral ones (Fourriere et al., 2019). The distinction between different sub-populations of FAs according to their distances to the cell edge has been already proposed in the literature (Berginski et al., 2011; Pageon et al., 2013). These different sub-populations have different properties, e.g. internal FAs display higher disassembly rates than peripheral ones whether newly formed FAs preferentially localized close to cell edge (Berginski et al., 2011).

The appearance of exocytic events at FAs is a correlation and does not explain causally the non-random organization of lysosomal exocytosis. How the cell specifies the targeting of vesicles to different sub-populations of FAs is an interesting issue for future studies. Our data suggest that this targeting is cytoskeleton independent. However, we observed a decrease of exocytosis rate when actin is depolymerized, a result in good agreement with the literature (Gupton and Gertler, 2010; Yuan et al., 2015). On the other hand, the clustering of exocytic Golgi-derived vesicles is totally inhibited upon actin or MT depolymerization (Yuan et al., 2015). Noteworthy that we treated cells with cytoskeleton drugs within the same timescale than Yuan et al. (i.e. ~15/20min for cytochalasin D, and 1h for nocodazole). This suggests that the cytoskeleton does not play the same role in the spatial organization of Golgi-derived vesicles and lysosomal exocytosis. One possibility is that the transport of lysosomes is less dependent on MTs (only about 30% of lysosomes are transported by MTs) (Ba et al., 2018) than that of Golgi-derived vesicles. Moreover, lysosomal exocytosis pathway keeps a pool of vesicle that can be secreted after stimulation contrarily to constitutive Golgi exocytosis. Indeed, TIRFM reveals that many lysosomal vesicles are docked at PM (Jaiswal et al., 2002). Therefore it is possible that these vesicles are already patterned and exocyted during drug treatment. Longer drugs treatments are needed to consume this possibly pre-patterned pool and see how the spatial structure of the new vesicles is affected.

The role of membrane tension. Interfering with membrane tension by hypo-osmotic shock and methyl-β-cyclodextrin increases clustering of exocytosis, revealing for the first time a role of membrane tension in the spatial organization of exocytosis. Note that our experimental procedure includes an incubation time of 15 min after the hypo-osmotic shock. In fact, the organization of lysosomal exocytosis is not immediately affected after a hypo-osmotic shock (data not shown). It has been recently shown that an osmotic shock immediately induces a peak of membrane tension, but even after the peak, membrane tension remains higher than its steady-state value for minutes

(Roffay et al., 2021). My interpretation is that during the peak, tension increases uniformly over cell surface and the organization of membrane tension is not altered. Given the fact that clustering of exocytosis results from inhomogeneity of PM tension, this could explain why the spatial structure of lysosomal exocytosis is unchanged. In a few minutes, regulating mechanisms locally reduce membrane tension (membrane unfolding, actin remodeling, etc.), leading to a new organization of membrane tension. This hypothesis could be directly tested by measuring membrane tension with Flipper-TR. However, an osmotic shock may interfere with the capacity of Flipper-TR to be incorporated in membranes. In addition, the treatment with methyl-β-cyclodextrin significantly reduces the fluorescence signal, probably by extruding Flipper-TR from membranes. The Moran's I is biased under these conditions and cannot be used to measure membrane tension organization. However, a previous study has reported an increase in membrane tension heterogeneity after methyl-β-cyclodextrin treatment (Biswas et al., 2019). Corroborating the role of membrane tension organization, we observed that cells seeded on PLL present less organization in membrane tension. This could be explained by the absence of FAs that are obstacle to the lipid flow that equilibrates membrane tension (Cohen and Shi, 2020).

Our micropattern strategy revealed an intracellular coupling between local exocytosis probability and local membrane tension. It was already known that exocytosis probability correlates with membrane tension (Wen et al., 2016; Kliesch et al., 2017b; Shi et al., 2018; Wang and Galli, 2018; Cohen and Shi, 2020). However, our results are the first in the literature to present an intra-cellular correlation leading to spatial organization of exocytosis.

Our study is hypothesis free about the origin and the maintenance of membrane tension gradients. However, a similar gradient has been already observed in moving keratinocytes (Lieber et al., 2015). It is explained by friction between PM and actin tread milling as well as between PM and substrate (Schweitzer et al., 2014). In non-migratory cells constrained on micropatterns, only actin retrograde flow could participate in the establishment of membrane tension by friction. Due to the very slow diffusion of membrane tension (Shi et al., 2018), even after cytochalasin D treatment, the gradient should be stable within the time scale of our experiments. With the membrane tension diffusion coefficient measured by Shi et al. in HeLa cells ($D_\sigma = 0.024\ \mu m^2.s^{-1}$) and for a cell with typical size of $\Delta x = 30\mu m$, membrane tension equilibrates within the time scales of hours ($\tau = \frac{\Delta x^2}{4D_\sigma} \sim 2 - 3h$). All these mechanisms depend on the FA topography, and studying the crosstalk between FA topography and membrane tension is a promising issue still poorly explored (Delanoë-Ayari et al., 2004; Pontes et al., 2017b).

The need of modeling. Our data revealed the existence of a temporal clustering of lysosomal exocytosis and a positive coupling between spatial and temporal structures. These empirical results are of interest for theorists. Indeed, this spatio-temporal coupling suggests models relying on PDEs with time and space variables. Indeed, convection-diffusion models presented in chapter 1 can create spatio-temporal coupling. Spatio-temporal models of exocytosis are still rare. An important exception is a model based on the diffusion of Ca^{2+} that triggers exocytosis (Segura et al., 2000). Interestingly, some Ca^{2+} permeable channels (e.g. Piezo1) are known to be membrane tension sensitive. However, the triggering role of Ca^{2+} in lysosomal exocytosis is debated (Jaiswal et al., 2002; Verweij et al., 2018). Mechanical models are rare with the notable exception of Mao *et al.*, in which endocytosis and exocytosis are regulated by membrane tension (Mao et al., 2021). However, in this model, only endocytosis is directly regulated by membrane tension whereas exocytosis is indirectly

regulated by endocytosis through the number of vesicles. Moreover, it does not include spatial dimensions, but it provides an interesting framework for further developments. The lack of spatial and mechanical models can be attributed to the absence of empirical data. Our work participates in the effort of empirical description needed by theorists.

***Physiological significance of clustered exocytosis*.** The non-random distribution of exocytosis events can be interrogated: which function is supported by this organization? While the polarized secretion in special cell types such as neurons or acinar cells has an obvious adaptative purpose, the clustering of lysosomal exocytosis in weakly polarized cells is more mysterious. Noteworthy, the organization of exocytosis events in polarized cells is limited to a small region (synapse or apical side) and works as an all-or-nothing process: there is no exocytosis of synaptic vesicle outside the synapse. It is different from our observations that present an organization of exocytosis at the whole-cell scale relying on the spatial organization of membrane tension.

A membrane tension gradient has been already observed in the context of cell migration (Lieber et al., 2015). The membrane tension was measured to be ~30% higher at the leading edge than at the rear. Interestingly, it has been shown that α5β1 integrins are endocytosed and recycled toward PM during cell migration (Dozynkiewicz et al., 2012). Therefore, membrane tension gradient during cell migration could spatially organize exocytosis for integrin recycling. However, this model faces several limitations. First, the measured membrane tension gradient corresponds to the dorsal PM, but it is likely that such gradient also exists on the ventral side where integrins are exocytosed. Indeed, the gradient is explained by friction between PM and actin treadmilling, but also between PM and adhesion substrate (Schweitzer et al., 2014). The second issue is that integrins are recycled toward the cell rear where membrane tension is lower (Dozynkiewicz et al., 2012), in conflict with our results. However, it has been proposed that endocytosed fibronectin is not digested in lysosomes but secreted at the leading edge of migrating cells (Sung et al., 2011). This targeting at the cell front fits our data and could be regulated by membrane tension. The differential regulation according to the cargo (fibronectin or integrin) is puzzling but could also results from cell type variation (Dozynkiewicz et al. used A2780 ovarian cancer cell line, and Sung et al. used HT1080 fibrosarcoma cell line).

A second example is the phagocytosis process. Phagocytosis starts with the formation of pseudopods, locally increasing membrane tension. This step is followed by lysosomal exocytosis, decreasing membrane tension and allowing the engulfment of the foreign target (Wang and Galli, 2018). Membrane tension could be the spatial signal to target lysosomes to the phagocytosis site. Additionally, the exocytosis of lysosomes could start the digestion of the foreign particle. It potentially could give an evolutionary advantage in the defense against pathogens. The regulation of lysosomal exocytosis by membrane tension also would make sense in the context of plasma membrane repair (PMR). It has been already proposed that lysosomes are the exocytosed organelles during PMR, because the secretion of enzymes and acidity can kill a potential aggressor (Andrews and Corrotte, 2018). The dedication of lysosomes to PMR, from this putative early evolutionary step, makes advantageous the acquisition of a membrane tension sensibility for exocytosis in a subsequent evolutionary step. Indeed, a high membrane tension leads to PM rupture. The detection of region with high membrane tension followed by local lysosomal exocytosis could prevent membrane rupture.

***Evolutionary considerations*.** Further speculations (if not "just-so stories"): one can be skeptical about the premise of the question: does non-random exocytosis have an adaptative value in terms of

evolution? The paleontologist Adolf Seilacher proposed three dimensions to explain the evolutionary origin of a biological treat: adaptative value, phylogenetic inertia, and architectural constraints (Seilacher, 1970). The phylogenetic axis evaluates a kind of evolutionary inertia: a treat can be not adaptative, because it is the result of an evolutionary tinkering through generations. As a possible example, one can wonder why it is the lysosome that is exocytosed in case of plasma damage by a bacterial attack. It has probably no advantage in organisms with an immune system but unicellular ancestors could use it as a way to attack the bacteria (Andrews and Corrotte, 2018). Therefore, this treat has currently no adaptative value in animals; it is a phylogenetic inheritance of a treat that was adaptative in the past. The third axis measures the architectural constraints. Seilacher emphasizes on developmental constraints (e.g. the female hymen is, at least partially, the result of developmental constraints) but we can extend it to physical constraints (e.g. patterns of mollusk shells are only due to physical constraints of the shell formation). Of course, many biological treats have a composite origin made of the three dimensions put forward by Seilacher. In a famous article, Gould and Lewontin used the Seilacher's triangle to criticize the adaptationist program, the view claiming that all traits are adaptations (Gould et al., 1979). In a nutshell, they extended the Seilacher argument on physical constraints with a legendary analogy: "The great central dome of St Mark's Cathedral in Venice presents in its mosaic design a detailed iconography expressing the mainstays of Christian faith. […] Spandrels –the tapering triangular spaces formed by the intersection of two rounded arches at right angles – are necessary architectural by-products of mounting a dome on rounded arches. […] The design is so elaborate, harmonious and purposeful that we are tempted to view it as the starting point of any analysis, as the cause in some sense of the surrounding architecture. But this would invert the proper path of analysis". In other words, some biological treats can look as adaptative but are actually just by-products of physical constraints and not the result of a selection. Although the architectural analysis of Gould and Lewontin has been contradicted, these biological treats are named spandrels. I argue that the non-random organization of lysosomal exocytosis is a spandrel: it confers no advantage and it is the result of the physical constraints faced by the cell. According to our model, the non-random organization of exocytosis is the consequence of i) a non-homogeneous membrane tension and ii) an exocytosis dependence on membrane tension. According to the model proposed by Shi et al., the non-homogeneous membrane tension is due to a resistance to lipid flow provided by a high amount of immobile proteins (Shi et al., 2018; Cohen and Shi, 2020). The exocytosis dependence on membrane tension is due to several factors. Membrane tension accelerates pore expansion in a purely mechanical way (Chizmadzhev et al., 2000; Shillcock and Lipowsky, 2005; Kozlov and Chernomordik, 2015) without genetic control. Additionally, SNARE proteins seem to display membrane tension sensitivity (Kliesch et al., 2017b) but we do not know if this is the result of a selective pressure. If such sensitivity confers an advantage, it is likely to regulate membrane tension by exocytosis. Indeed, cell rupture by osmotic stress is susceptible to drastically affect the cell survival. Therefore, conditions i and ii are met without invoking any selective pressure for a non-random organization of exocytosis. This reasoning has also the advantage to respect the principle of parsimony: it does not require any additional evolutionary explanation for its apparition. Even if the question cannot be answered in a definitive way yet, it seems more reasonable to consider the clustering of lysosomal exocytosis as a spandrel, at least awaiting for further data.

***Future developments*.** My work indicates that membrane tension spatially regulates exocytosis. Are there other physical parameters affecting exocytosis probability? Membrane curvature is an interesting possibility. Since many proteins are sensitive to membrane curvature, it could affect exocytosis probability by regulating the recruitment of these proteins. By seeding cells on small

fluorescent beads, we artificially induced membrane curvature. Our preliminary results show that there is a correlation between exocytosis sites and beads localization (data not shown). These data could contribute to explain the appearance of exocytic events at FAs, because FAs locally induce membrane curvature. Moreover, the bending modulus itself could also regulate the kinetics of exocytosis. A high bending modulus favors the collapse of the opened exocytic vesicle to reduce curvature. This hypothesis could be experimentally tested by the incorporation of polyunsaturated lipids in the membrane, which reduces the bending modulus without affecting membrane tension (Pinot et al., 2014).

The spatial statistics framework presented in this thesis could be used to study numerous cellular processes and should not be restricted to the qualitative analysis of the Ripley's K function. For example, using spatial statistics, it has been shown that endocytosis spots are spatially clustered (Ehrlich et al., 2004; Lagache et al., 2013). Unfortunately, these authors did not perform any spatio-temporal analysis, did not compare several conditions, did not co-analyze different types of endocytosis sites, and neither fit their data with spatial statistics models. The spatial clustering of endocytosis is particularly interesting because membrane tension also controls endocytosis probability (Raucher and Sheetz, 1999a; Heidelberger et al., 2002; Manneville et al., 2008; Saleem et al., 2015; Pontes et al., 2017b; Wu et al., 2017c), and the spatio-temporal distribution of clathrin-coated pits (Willy et al., 2017). The same mechanism of membrane tension compartmentalization that spatially organizes exocytosis could also explain the spatial structure of endocytosis. However, this would be in a mirror-manner, because endocytosis is inhibited by high membrane tension, whereas exocytosis is favored.

Many publications highlight the role of PM tension in the regulation of biological processes, but the importance of organelle membrane tension is poorly known. Classical tether experiments do not allow probing the tension of intracellular membranes. However, the recent development of intracellular probes of the Flipper family is a promising way (Goujon et al., 2019). Thanks to these tools, it has been shown that mitochondrial membrane tension regulates fission (Mahecic et al., 2021), and that endosomal membrane tension regulates the formation of ILVs (Mercier et al., 2020). Many questions involving intracellular membrane tension deserve to be explored: is the interaction between two organelles dependent on their tension? Does membrane tension of an organelle correlate with their spatial localization in the cell? How the membrane tension of an organelle affects its functions?

Bibliography

Adams, S.D., Csere, J., D'angelo, G., Carter, E.P., Romao, M., Arnandis, T., Dodel, M., Kocher, H.M., Grose, R., Raposo, G., et al. (2021). Centrosome amplification mediates small extracellular vesicle secretion via lysosome disruption. Curr. Biol. CB *31*, 1403-1416.e7. https://doi.org/10.1016/j.cub.2021.01.028.

Ahmed, S.M., Nishida-Fukuda, H., Li, Y., McDonald, W.H., Gradinaru, C.C., and Macara, I.G. (2018). Exocyst dynamics during vesicle tethering and fusion. Nat. Commun. *9*, 5140. https://doi.org/10.1038/s41467-018-07467-5.

Aits, S., and Jaattela, M. (2013). Lysosomal cell death at a glance. J. Cell Sci. *126*, 1905–1912. https://doi.org/10.1242/jcs.091181.

Akter, F., Ponnaiyan, S., Kögler-Mohrbacher, B., Bleibaum, F., Damme, M., Renard, B.Y., and Winter, D. (2020). Multi cell line analysis of lysosomal proteomes reveals unique features and novel lysosomal proteins. BioRxiv 2020.12.21.423747. https://doi.org/10.1101/2020.12.21.423747.

Alanko, J., Mai, A., Jacquemet, G., Schauer, K., Kaukonen, R., Saari, M., Goud, B., and Ivaska, J. (2015). Integrin endosomal signalling suppresses anoikis. Nat. Cell Biol. *17*, 1412–1421. https://doi.org/10.1038/ncb3250.

Alberts, P., Rudge, R., Irinopoulou, T., Danglot, L., Gauthier-Rouvière, C., and Galli, T. (2006). Cdc42 and actin control polarized expression of TI-VAMP vesicles to neuronal growth cones and their fusion with the plasma membrane. Mol. Biol. Cell *17*, 1194–1203. https://doi.org/10.1091/mbc.e05-07-0643.

Alés, E., Tabares, L., Poyato, J.M., Valero, V., Lindau, M., and Alvarez de Toledo, G. (1999). High calcium concentrations shift the mode of exocytosis to the kiss-and-run mechanism. Nat. Cell Biol. *1*, 40–44. https://doi.org/10.1038/9012.

Ammar, M., Kassas, N., Chasserot-Golaz, S., Bader, M.-F., and Vitale, N. (2013). Lipids in Regulated Exocytosis: What are They Doing? Front. Endocrinol. *4*. .

Ampah, K.K., Greaves, J., Shun-Shion, A.S., Asnawi, A.W., Lidster, J.A., Chamberlain, L.H., Collins, M.O., and Peden, A.A. (2018). S-acylation regulates the trafficking and stability of the unconventional Q-SNARE STX19. J. Cell Sci. *131*, jcs212498. https://doi.org/10.1242/jcs.212498.

Andrews, N.W., and Corrotte, M. (2018). Plasma membrane repair. Curr. Biol. *28*, R392–R397. https://doi.org/10.1016/j.cub.2017.12.034.

Andrews, N.W., Almeida, P.E., and Corrotte, M. (2014). Damage control: cellular mechanisms of plasma membrane repair. Trends Cell Biol. *24*, 734–742. https://doi.org/10.1016/j.tcb.2014.07.008.

Aon, M., Cortassa, S., and Lloyd, D. (2011). Chaos in Biochemistry and Physiology. https://doi.org/10.1002/3527600906.MCB.201100001.

Aoyagi, K., Sugaya, T., Umeda, M., Yamamoto, S., Terakawa, S., and Takahashi, M. (2005). The activation of exocytotic sites by the formation of phosphatidylinositol 4,5-bisphosphate microdomains at syntaxin clusters. J. Biol. Chem. *280*, 17346–17352. https://doi.org/10.1074/jbc.M413307200.

Apodaca, G. (2002). Modulation of membrane traffic by mechanical stimuli. Am. J. Physiol. Renal Physiol. *282*, F179-190. https://doi.org/10.1152/ajprenal.2002.282.2.F179.

Arantes, R.M.E., and Andrews, N.W. (2006). A Role for Synaptotagmin VII-Regulated Exocytosis of Lysosomes in Neurite Outgrowth from Primary Sympathetic Neurons. J. Neurosci. *26*, 4630–4637. https://doi.org/10.1523/JNEUROSCI.0009-06.2006.

Avci, B., Brandt, J., Nachmias, D., Elia, N., Albertsen, M., Ettema, T.J.G., Schramm, A., and Kjeldsen, K.U. (2022). Spatial separation of ribosomes and DNA in Asgard archaeal cells. ISME J. *16*, 606–610. https://doi.org/10.1038/s41396-021-01098-3.

Ba, Q., Raghavan, G., Kiselyov, K., and Yang, G. (2018). Whole-Cell Scale Dynamic Organization of Lysosomes Revealed by Spatial Statistical Analysis. Cell Rep. *23*, 3591–3606. https://doi.org/10.1016/j.celrep.2018.05.079.

Baddeley, A., Rubak, E., and Turner, R. (2015). Spatial Point Patterns: Methodology and Applications with R (Boca Raton ; London ; New York: Chapman and Hall/CRC).

Baddeley, A.J., Moyeed, R.A., Howard, C.V., and Boyde, A. (1993). Analysis of a Three-Dimensional Point Pattern with Replication. J. R. Stat. Soc. Ser. C Appl. Stat. *42*, 641–668. https://doi.org/10.2307/2986181.

Baddeley, A.J., Møller, J., and Waagepetersen, R. (2000). Non- and semi-parametric estimation of interaction in inhomogeneous point patterns. Stat. Neerlandica *54*, 329–350. https://doi.org/10.1111/1467-9574.00144.

Baier, null, and Sahle, null (1998). Homogeneous and Spatio-temporal Chaos in Biochemical Reactions With Feedback Inhibition. J. Theor. Biol. *193*, 233–242. https://doi.org/10.1006/jtbi.1998.0695.

Bainton, D.F. (1981). The discovery of lysosomes. J. Cell Biol. *91*, 66s–76s. .

Baker, R.W., Jeffrey, P.D., Zick, M., Phillips, B.P., Wickner, W.T., and Hughson, F.M. (2015). A direct role for the Sec1-Munc18-family protein Vps33 as a template for SNARE assembly. Science *349*, 1111–1114. https://doi.org/10.1126/science.aac7906.

Balch, W.E., Dunphy, W.G., Braell, W.A., and Rothman, J.E. (1984). Reconstitution of the transport of protein between successive compartments of the Golgi measured by the coupled incorporation of N-acetylglucosamine. Cell *39*, 405–416. https://doi.org/10.1016/0092-8674(84)90019-9.

Bame, K.J., and Rome, L.H. (1985). Acetyl coenzyme A: alpha-glucosaminide N-acetyltransferase. Evidence for a transmembrane acetylation mechanism. J. Biol. Chem. *260*, 11293–11299. https://doi.org/10.1016/S0021-9258(17)39179-2.

Bandyopadhyay, D., Cyphersmith, A., Zapata, J.A., Kim, Y.J., and Payne, C.K. (2014). Lysosome Transport as a Function of Lysosome Diameter. PL0S ONE *9*, e86847. https://doi.org/10.1371/journal.pone.0086847.

Bard, J., and Lauder, I. (1974). How well does Turing's theory of morphogenesis work? J. Theor. Biol. *45*, 501–531. https://doi.org/10.1016/0022-5193(74)90128-3.

Batchelder, E.L., Hollopeter, G., Campillo, C., Mezanges, X., Jorgensen, E.M., Nassoy, P., Sens, P., and Plastino, J. (2011). Membrane tension regulates motility by controlling lamellipodium organization. Proc. Natl. Acad. Sci. U. S. A. *108*, 11429–11434. https://doi.org/10.1073/pnas.1010481108.

Baum, M., Erdel, F., Wachsmuth, M., and Rippe, K. (2014). Retrieving the intracellular topology from multi-scale protein mobility mapping in living cells. Nat. Commun. *5*, 4494. https://doi.org/10.1038/ncomms5494.

Baumert, M., Maycox, P.R., Navone, F., De Camilli, P., and Jahn, R. (1989). Synaptobrevin: an integral membrane protein of 18,000 daltons present in small synaptic vesicles of rat brain. EMBO J. *8*, 379–384. .

Becherer, U., Pasche, M., Nofal, S., Hof, D., Matti, U., and Rettig, J. (2007). Quantifying Exocytosis by Combination of Membrane Capacitance Measurements and Total Internal Reflection Fluorescence Microscopy in Chromaffin Cells. PLOS ONE *2*, e505. https://doi.org/10.1371/journal.pone.0000505.

de Beco, S., Vaidžiulytė, K., Manzi, J., Dalier, F., di Federico, F., Cornilleau, G., Dahan, M., and Coppey, M. (2018). Optogenetic dissection of Rac1 and Cdc42 gradient shaping. Nat. Commun. *9*, 4816. https://doi.org/10.1038/s41467-018-07286-8.

Beedle, A.E., Williams, A., Relat-Goberna, J., and Garcia-Manyes, S. (2015). Mechanobiology—chemical origin of membrane mechanical resistance and force-dependent signaling. Curr. Opin. Chem. Biol. *29*, 87–93. https://doi.org/10.1016/j.cbpa.2015.09.019.

Benincà, E., Ballantine, B., Ellner, S.P., and Huisman, J. (2015). Species fluctuations sustained by a cyclic succession at the edge of chaos. Proc. Natl. Acad. Sci. *112*, 6389–6394. https://doi.org/10.1073/pnas.1421968112.

Berberian, K., Torres, A.J., Fang, Q., Kisler, K., and Lindau, M. (2009). F-Actin and Myosin II Accelerate Catecholamine Release from Chromaffin Granules. J. Neurosci. *29*, 863–870. https://doi.org/10.1523/JNEUROSCI.2818-08.2009.

Berchtold, D., Piccolis, M., Chiaruttini, N., Riezman, I., Riezman, H., Roux, A., Walther, T.C., and Loewith, R. (2012). Plasma membrane stress induces relocalization of Slm proteins and activation of TORC2 to promote sphingolipid synthesis. Nat. Cell Biol. *14*, 542–547. https://doi.org/10.1038/ncb2480.

van Bergeijk, P., Hoogenraad, C.C., and Kapitein, L.C. (2016). Right Time, Right Place: Probing the Functions of Organelle Positioning. Trends Cell Biol. *26*, 121–134. https://doi.org/10.1016/j.tcb.2015.10.001.

Berginski, M.E., Vitriol, E.A., Hahn, K.M., and Gomez, S.M. (2011). High-Resolution Quantification of Focal Adhesion Spatiotemporal Dynamics in Living Cells. PLOS ONE *6*, e22025. https://doi.org/10.1371/journal.pone.0022025.

Berthelsen, K.K., and Møller, J. (2002). A primer on perfect simulation for spatial point processes. Bull. Braz. Math. Soc. *33*, 351–367. https://doi.org/10.1007/s005740200019.

Besag, J. (1977). Comments on Ripley's Paper. J. R. Stat. Soc. *B 39*, 193–195. .

Binder, B., Goede, A., Berndt, N., and Holzhütter, H.-G. (2009). A Conceptual Mathematical Model of the Dynamic Self-Organisation of Distinct Cellular Organelles. PLOS ONE *4*, e8295. https://doi.org/10.1371/journal.pone.0008295.

Birbaumer, M., and Schweitzer, F. (2011). Agent-Based Modeling of Intracellular Transport. Eur. Phys. J. B *82*, 245–255. https://doi.org/10.1140/epjb/e2011-20283-x.

Biswas, A., Kashyap, P., Datta, S., Sengupta, T., and Sinha, B. (2019). Cholesterol Depletion by MβCD Enhances Cell Membrane Tension and Its Variations-Reducing Integrity. Biophys. J. *116*, 1456–1468. https://doi.org/10.1016/j.bpj.2019.03.016.

Blagodatski, A., Sergeev, A., Kryuchkov, M., Lopatina, Y., and Katanaev, V.L. (2015). Diverse set of Turing nanopatterns coat corneae across insect lineages. Proc. Natl. Acad. Sci. *112*, 10750–10755. https://doi.org/10.1073/pnas.1505748112.

Block, M.R., Glick, B.S., Wilcox, C.A., Wieland, F.T., and Rothman, J.E. (1988). Purification of an N-ethylmaleimide-sensitive protein catalyzing vesicular transport. Proc. Natl. Acad. Sci. U. S. A. *85*, 7852–7856. .

Blum, J.J., and Reed, M.C. (1988). The transport of organelles in axons. Math. Biosci. *90*, 233–245. https://doi.org/10.1016/0025-5564(88)90068-5.

Blum, J.J., and Reed, M.C. (1989). A model for slow axonal transport and its application to neurofilamentous neuropathies. Cell Motil. Cytoskeleton *12*, 53–65. https://doi.org/10.1002/cm.970120107.

Bock, J.B., Matern, H.T., Peden, A.A., and Scheller, R.H. (2001). A genomic perspective on membrane compartment organization. Nature *409*, 839–841. https://doi.org/10.1038/35057024.

Bogdanovic, A., Bennett, N., Kieffer, S., Louwagie, M., Morio, T., Garin, J., Satre, M., and Bruckert, F. (2002). Syntaxin 7, syntaxin 8, Vti1 and VAMP7 (vesicle-associated membrane protein 7) form an active SNARE complex for early macropinocytic compartment fusion in Dictyostelium discoideum. Biochem. J. *368*, 29–39. https://doi.org/10.1042/BJ20020845.

Bonifacino, J.S., and Neefjes, J. (2017). Moving and positioning the endolysosomal system. Curr. Opin. Cell Biol. *47*, 1–8. https://doi.org/10.1016/j.ceb.2017.01.008.

Bonifacino, J.S., and Rojas, R. (2006). Retrograde transport from endosomes to the trans-Golgi network. Nat. Rev. Mol. Cell Biol. *7*, 568–579. https://doi.org/10.1038/nrm1985.

Boulant, S., Kural, C., Zeeh, J.-C., Ubelmann, F., and Kirchhausen, T. (2011). Actin dynamics counteract membrane tension during clathrin-mediated endocytosis. Nat. Cell Biol. *13*, 1124–1131. https://doi.org/10.1038/ncb2307.

Boya, P., Reggiori, F., and Codogno, P. (2013). Emerging regulation and functions of autophagy. Nat. Cell Biol. *15*, 713–720. https://doi.org/10.1038/ncb2788.

Brandstaetter, H., Kishi-Itakura, C., Tumbarello, D.A., Manstein, D.J., and Buss, F. (2015). Loss of functional MYO1C/myosin 1c, a motor protein involved in lipid raft trafficking, disrupts autophagosome-lysosome fusion. Autophagy *10*, 2310–2323. https://doi.org/10.4161/15548627.2014.984272.

Brangwynne, C.P., Koenderink, G.H., MacKintosh, F.C., and Weitz, D.A. (2009). Intracellular transport by active diffusion. Trends Cell Biol. *19*, 423–427. https://doi.org/10.1016/j.tcb.2009.04.004.

Braulke, T., and Bonifacino, J.S. (2009). Sorting of lysosomal proteins. Biochim. Biophys. Acta *1793*, 605–614. https://doi.org/10.1016/j.bbamcr.2008.10.016.

Bretou, M., Jouannot, O., Fanget, I., Pierobon, P., Larochette, N., Gestraud, P., Guillon, M., Emiliani, V., Gasman, S., Desnos, C., et al. (2014). Cdc42 controls the dilation of the exocytotic fusion pore by regulating membrane tension. Mol. Biol. Cell *25*, 3195–3209. https://doi.org/10.1091/mbc.E14-07-1229.

Bretou, M., Sáez, P.J., Sanséau, D., Maurin, M., Lankar, D., Chabaud, M., Spampanato, C., Malbec, O., Barbier, L., Muallem, S., et al. (2017). Lysosome signaling controls the migration of dendritic cells. Sci. Immunol. *2*, eaak9573. https://doi.org/10.1126/sciimmunol.aak9573.

Bright, N.A., Davis, L.J., and Luzio, J.P. (2016). Endolysosomes Are the Principal Intracellular Sites of Acid Hydrolase Activity. Curr. Biol. CB *26*, 2233–2245. https://doi.org/10.1016/j.cub.2016.06.046.

Brochard-Wyart, F., Borghi, N., Cuvelier, D., and Nassoy, P. (2006). Hydrodynamic narrowing of tubes extruded from cells. Proc. Natl. Acad. Sci. *103*, 7660–7663. https://doi.org/10.1073/pnas.0602012103.

Brose, N., Petrenko, A.G., Südhof, T.C., and Jahn, R. (1992). Synaptotagmin: a calcium sensor on the synaptic vesicle surface. Science *256*, 1021–1025. https://doi.org/10.1126/science.1589771.

Brown, M.F. (2012). Curvature Forces in Membrane Lipid-Protein Interactions. Biochemistry *51*, 9782–9795. https://doi.org/10.1021/bi301332v.

Bussell, S.J., Koch, D.L., and Hammer, D.A. (1995). Effect of hydrodynamic interactions on the diffusion of integral membrane proteins: diffusion in plasma membranes. Biophys. J. *68*, 1836–1849. https://doi.org/10.1016/S0006-3495(95)80360-7.

Buxbaum, A.R., Haimovich, G., and Singer, R.H. (2015). In the right place at the right time: visualizing and understanding mRNA localization. Nat. Rev. Mol. Cell Biol. *16*, 95–109. https://doi.org/10.1038/nrm3918.

Caballero, Y., Giraldo, R., and Mateu, J. (2022). A spatial randomness test based on the box-counting dimension. AStA Adv. Stat. Anal. https://doi.org/10.1007/s10182-021-00434-4.

Cabukusta, B., and Neefjes, J. (2018). Mechanisms of lysosomal positioning and movement. Traffic Cph. Den. *19*, 761–769. https://doi.org/10.1111/tra.12587.

Calizo, R.C., Bell, M.K., Ron, A., Hu, M., Bhattacharya, S., Wong, N.J., Janssen, W.G.M., Perumal, G., Pederson, P., Scarlata, S., et al. (2020). Cell shape regulates subcellular organelle location to control early Ca2+ signal dynamics in vascular smooth muscle cells. Sci. Rep. *10*, 17866. https://doi.org/10.1038/s41598-020-74700-x.

Canham, P.B. (1970). The minimum energy of bending as a possible explanation of the biconcave shape of the human red blood cell. J. Theor. Biol. *26*, 61–81. https://doi.org/10.1016/S0022-5193(70)80032-7.

Cao, Q., Zhong, X.Z., Zou, Y., Zhang, Z., Toro, L., and Dong, X.-P. (2015). BK Channels Alleviate Lysosomal Storage Diseases by Providing Positive Feedback Regulation of Lysosomal Ca2+ Release. Dev. Cell *33*, 427–441. https://doi.org/10.1016/j.devcel.2015.04.010.

Capmany, A., Yoshimura, A., Kerdous, R., Caorsi, V., Lescure, A., Del Nery, E., Coudrier, E., Goud, B., and Schauer, K. (2019). MYO1C stabilizes actin and facilitates the arrival of transport carriers at the Golgi complex. J. Cell Sci. *132*, jcs225029. https://doi.org/10.1242/jcs.225029.

Carisey, A.F., Mace, E.M., Saeed, M.B., Davis, D.M., and Orange, J.S. (2018). Nanoscale Dynamism of Actin Enables Secretory Function in Cytolytic Cells. Curr. Biol. *28*, 489-502.e9. https://doi.org/10.1016/j.cub.2017.12.044.

Carlton, J.G., Jones, H., and Eggert, U.S. (2020). Membrane and organelle dynamics during cell division. Nat. Rev. Mol. Cell Biol. *21*, 151–166. https://doi.org/10.1038/s41580-019-0208-1.

Castro-Castro, A., Marchesin, V., Monteiro, P., Lodillinsky, C., Rossé, C., and Chavrier, P. (2016). Cellular and Molecular Mechanisms of MT1-MMP-Dependent Cancer Cell Invasion. Annu. Rev. Cell Dev. Biol. *32*, 555–576. https://doi.org/10.1146/annurev-cellbio-111315-125227.

Ceccarelli, B., Hurlbut, W.P., and Mauro, A. (1972). Depletion of vesicles from frog neuromuscular junctions by prolonged tetanic stimulation. J. Cell Biol. *54*, 30–38. https://doi.org/10.1083/jcb.54.1.30.

Chaineau, M., Danglot, L., and Galli, T. (2009). Multiple roles of the vesicular-SNARE TI-VAMP in post-Golgi and endosomal trafficking. FEBS Lett. *583*, 3817–3826. https://doi.org/10.1016/j.febslet.2009.10.026.

Chamberlain, L.H., Burgoyne, R.D., and Gould, G.W. (2001). SNARE proteins are highly enriched in lipid rafts in PC12 cells: Implications for the spatial control of exocytosis. Proc. Natl. Acad. Sci. *98*, 5619–5624. https://doi.org/10.1073/pnas.091502398.

Chang, L.-F., Chen, S., Liu, C.-C., Pan, X., Jiang, J., Bai, X.-C., Xie, X., Wang, H.-W., and Sui, S.-F. (2012). Structural characterization of full-length NSF and 20S particles. Nat. Struct. Mol. Biol. *19*, 268–275. https://doi.org/10.1038/nsmb.2237.

Chanturiya, A., Chernomordik, L.V., and Zimmerberg, J. (1997). Flickering fusion pores comparable with initial exocytotic pores occur in protein-free phospholipid bilayers. Proc. Natl. Acad. Sci. *94*, 14423–14428. https://doi.org/10.1073/pnas.94.26.14423.

Chen, H., and Jiang, J.-G. (2009). Osmotic responses of Dunaliella to the changes of salinity. J. Cell. Physiol. *219*, 251–258. https://doi.org/10.1002/jcp.21715.

Chen, D., Zheng, Q., Sun, L., Ji, M., Li, Y., Deng, H., and Zhang, H. (2021). ORF3a of SARS-CoV-2 promotes lysosomal exocytosis-mediated viral egress. Dev. Cell *56*, 3250-3263.e5. https://doi.org/10.1016/j.devcel.2021.10.006.

Chen, G., Zhang, Z., Wei, Z., Cheng, Q., Li, X., Li, W., Duan, S., and Gu, X. (2012). Lysosomal exocytosis in Schwann cells contributes to axon remyelination. Glia *60*, 295–305. https://doi.org/10.1002/glia.21263.

Chinthalapudi, K., Taft, M.H., Martin, R., Heissler, S.M., Preller, M., Hartmann, F.K., Brandstaetter, H., Kendrick-Jones, J., Tsiavaliaris, G., Gutzeit, H.O., et al. (2011). Mechanism and Specificity of Pentachloropseudilin-mediated Inhibition of Myosin Motor Activity. J. Biol. Chem. *286*, 29700–29708. https://doi.org/10.1074/jbc.M111.239210.

Chizmadzhev, Y.A., Kuzmin, P.I., Kumenko, D.A., Zimmerberg, J., and Cohen, F.S. (2000). Dynamics of Fusion Pores Connecting Membranes of Different Tensions. Biophys. J. *78*, 2241–2256. https://doi.org/10.1016/S0006-3495(00)76771-3.

Chow, R.H., von Rüden, L., and Neher, E. (1992). Delay in vesicle fusion revealed by electrochemical monitoring of single secretory events in adrenal chromaffin cells. Nature *356*, 60–63. https://doi.org/10.1038/356060a0.

Christoph, K., Beck, F.-X., and Neuhofer, W. (2007). Osmoadaptation of Mammalian Cells – An Orchestrated Network of Protective Genes. Curr. Genomics *8*, 209–218. .

Chu, B.-B., Liao, Y.-C., Qi, W., Xie, C., Du, X., Wang, J., Yang, H., Miao, H.-H., Li, B.-L., and Song, B.-L. (2015). Cholesterol transport through lysosome-peroxisome membrane contacts. Cell *161*, 291–306. https://doi.org/10.1016/j.cell.2015.02.019.

Clark, P.J., and Evans, F.C. (1954). Distance to Nearest Neighbor as a Measure of Spatial Relationships in Populations. Ecology *35*, 445–453. https://doi.org/10.2307/1931034.

Clary, D.O., and Rothman, J.E. (1990). Purification of three related peripheral membrane proteins needed for vesicular transport. J. Biol. Chem. *265*, 10109–10117. .

Clary, D.O., Griff, I.C., and Rothman, J.E. (1990). SNAPs, a family of NSF attachment proteins involved in intracellular membrane fusion in animals and yeast. Cell *61*, 709–721. https://doi.org/10.1016/0092-8674(90)90482-t.

Cliff, A.D., and Ord, J.K. (1981). Spatial processes: Models and applications.

Cohen, A.E., and Shi, Z. (2020). Do Cell Membranes Flow Like Honey or Jiggle Like Jello? BioEssays *42*, 1900142. https://doi.org/10.1002/bies.201900142.

Cohn, Z.A. (1963). The fate of bacteria within phagocytic cells. I. The degradation of isotopically labeled bacteria by polymorphonuclear leucocytes and macrophages. J. Exp. Med. *117*, 27–42. .

Collins, M.P., and Forgac, M. (2018). Regulation of V-ATPase Assembly in Nutrient Sensing and Function of V-ATPases in Breast Cancer Metastasis. Front. Physiol. *9*. .

Collins, T.J., Berridge, M.J., Lipp, P., and Bootman, M.D. (2002). Mitochondria are morphologically and functionally heterogeneous within cells. EMBO J. *21*, 1616–1627. https://doi.org/10.1093/emboj/21.7.1616.

Colom, A., Derivery, E., Soleimanpour, S., Tomba, C., Molin, M.D., Sakai, N., González-Gaitán, M., Matile, S., and Roux, A. (2018). A fluorescent membrane tension probe. Nat. Chem. *10*, 1118–1125. https://doi.org/10.1038/s41557-018-0127-3.

Cooke, I.R., and Deserno, M. (2006). Coupling between Lipid Shape and Membrane Curvature. Biophys. J. *91*, 487–495. https://doi.org/10.1529/biophysj.105.078683.

Coomer, C.A., Carlon-Andres, I., Iliopoulou, M., Dustin, M.L., Compeer, E.B., Compton, A.A., and Padilla-Parra, S. (2020). Single-cell glycolytic activity regulates membrane tension and HIV-1 fusion. PLoS Pathog. *16*, e1008359. https://doi.org/10.1371/journal.ppat.1008359.

Cordonnier, M.-N., Dauzonne, D., Louvard, D., and Coudrier, E. (2001). Actin Filaments and Myosin I Alpha Cooperate with Microtubules for the Movement of Lysosomes. Mol. Biol. Cell *12*, 4013–4029. .

Corradetti, M.N., Inoki, K., Bardeesy, N., DePinho, R.A., and Guan, K.-L. (2004). Regulation of the TSC pathway by LKB1: evidence of a molecular link between tuberous sclerosis complex and Peutz-Jeghers syndrome. Genes Dev. *18*, 1533–1538. https://doi.org/10.1101/gad.1199104.

Coste, B., Mathur, J., Schmidt, M., Earley, T.J., Ranade, S., Petrus, M.J., Dubin, A.E., and Patapoutian, A. (2010). Piezo1 and Piezo2 are essential components of distinct mechanically activated cation channels. Science *330*, 55–60. https://doi.org/10.1126/science.1193270.

Cox, D.R. (1955). Some Statistical Methods Connected with Series of Events. J. R. Stat. Soc. Ser. B Methodol. *17*, 129–164. .

Cox, T.F. (1981). Reflexive Nearest Neighbours. Biometrics *37*, 367–369. https://doi.org/10.2307/2530424.

Cullen, P.J., and Steinberg, F. (2018). To degrade or not to degrade: mechanisms and significance of endocytic recycling. Nat. Rev. Mol. Cell Biol. *19*, 679–696. https://doi.org/10.1038/s41580-018-0053-7.

Dai, J., Ting-Beall, H.P., and Sheetz, M.P. (1997). The secretion-coupled endocytosis correlates with membrane tension changes in RBL 2H3 cells. J. Gen. Physiol. *110*, 1–10. https://doi.org/10.1085/jgp.110.1.1.

Dal Molin, M., Verolet, Q., Colom, A., Letrun, R., Derivery, E., Gonzalez-Gaitan, M., Vauthey, E., Roux, A., Sakai, N., and Matile, S. (2015). Fluorescent Flippers for Mechanosensitive Membrane Probes. J. Am. Chem. Soc. *137*, 568–571. https://doi.org/10.1021/ja5107018.

Dalmasso, G., Zapata, P.A.M., Brady, N.R., and Hamacher-Brady, A. (2017). Agent-Based Modeling of Mitochondria Links Sub-Cellular Dynamics to Cellular Homeostasis and Heterogeneity. PLOS ONE *12*, e0168198. https://doi.org/10.1371/journal.pone.0168198.

Damaghi, M., Tafreshi, N.K., Lloyd, M.C., Sprung, R., Estrella, V., Wojtkowiak, J.W., Morse, D.L., Koomen, J.M., Bui, M.M., Gatenby, R.A., et al. (2015). Chronic acidosis in the tumour microenvironment selects for overexpression of LAMP2 in the plasma membrane. Nat. Commun. *6*, 8752. https://doi.org/10.1038/ncomms9752.

Danylchuk, D.I., Jouard, P.-H., and Klymchenko, A.S. (2021). Targeted Solvatochromic Fluorescent Probes for Imaging Lipid Order in Organelles under Oxidative and Mechanical Stress. J. Am. Chem. Soc. *143*, 912–924. https://doi.org/10.1021/jacs.0c10972.

Daste, F., Galli, T., and Tareste, D. (2015). Structure and function of longin SNAREs. J. Cell Sci. *128*, 4263–4272. https://doi.org/10.1242/jcs.178574.

De Duve, C. (1965). Function of microbodies (peroxisome). J. Cell Biol.

De Duve, C., Pressman, B.C., Gianetto, R., Wattiaux, R., and Appelmans, F. (1955). Tissue fractionation studies. 6. Intracellular distribution patterns of enzymes in rat-liver tissue. Biochem. J. *60*, 604–617. .

Decker, C.J., and Parker, R. (2012). P-bodies and stress granules: possible roles in the control of translation and mRNA degradation. Cold Spring Harb. Perspect. Biol. *4*, a012286. https://doi.org/10.1101/cshperspect.a012286.

Decroly, O., and Goldbeter, A. (1982). Birhythmicity, chaos, and other patterns of temporal self-organization in a multiply regulated biochemical system. Proc. Natl. Acad. Sci. U. S. A. *79*, 6917–6921. https://doi.org/10.1073/pnas.79.22.6917.

Delanoë-Ayari, H., Kurdi, R.A., Vallade, M., Gulino-Debrac, D., and Riveline, D. (2004). Membrane and acto-myosin tension promote clustering of adhesion proteins. Proc. Natl. Acad. Sci. *101*, 2229–2234. https://doi.org/10.1073/pnas.0304297101.

Delevoye, C., Marks, M.S., and Raposo, G. (2019). Lysosome-related organelles as functional adaptations of the endolysosomal system. Curr. Opin. Cell Biol. *59*, 147–158. https://doi.org/10.1016/j.ceb.2019.05.003.

Derényi, I., Jülicher, F., and Prost, J. (2002). Formation and Interaction of Membrane Tubes. Phys. Rev. Lett. *88*, 238101. https://doi.org/10.1103/PhysRevLett.88.238101.

Deserno, M. (2006). Fluid lipid membranes – a primer.

Deserno, M. (2015). Fluid lipid membranes: From differential geometry to curvature stresses. Chem. Phys. Lipids *185*, 11–45. https://doi.org/10.1016/j.chemphyslip.2014.05.001.

Desnick, R.J., and Schuchman, E.H. (2002). Enzyme replacement and enhancement therapies: lessons from lysosomal disorders. Nat. Rev. Genet. *3*, 954–966. https://doi.org/10.1038/nrg963.

Di Paola, S., Scotto-Rosato, A., and Medina, D.L. (2018). TRPML1: The Ca(2+)retaker of the lysosome. Cell Calcium *69*, 112–121. https://doi.org/10.1016/j.ceca.2017.06.006.

Diggle, P.J. (2003). Statistical Analysis of Spatial Point Patterns (London: Hodder Education Publishers).

Diggle, P.J., and Chetwynd, A.G. (1991). Second-order analysis of spatial clustering for inhomogeneous populations. Biometrics *47*, 1155–1163. .

Diggle, P.J., Lange, N., and Benes, F.M. (1991). Analysis of Variance for Replicated Spatial Point Patterns in Clinical Neuroanatomy. J. Am. Stat. Assoc. *86*, 618–625. https://doi.org/10.2307/2290390.

Diggle, P.J., Mateu, J., and Clough, H.E. (2000). A Comparison between Parametric and Non-Parametric Approaches to the Analysis of Replicated Spatial Point Patterns. Adv. Appl. Probab. *32*, 331–343. .

Dillon, R., Maini, P.K., and Othmer, H.G. (1994). Pattern formation in generalized Turing systems. J. Math. Biol. *32*, 345–393. https://doi.org/10.1007/BF00160165.

Dinh, A.-T., Theofanous, T., and Mitragotri, S. (2005). A model for intracellular trafficking of adenoviral vectors. Biophys. J. *89*, 1574–1588. https://doi.org/10.1529/biophysj.105.059477.

Dinh, A.-T., Pangarkar, C., Theofanous, T., and Mitragotri, S. (2006). Theory of Spatial Patterns of Intracellular Organelles. Biophys. J. *90*, L67–L69. https://doi.org/10.1529/biophysj.106.082875.

Dinh, A.-T., Pangarkar, C., Theofanous, T., and Mitragotri, S. (2007). Understanding Intracellular Transport Processes Pertinent to Synthetic Gene Delivery via Stochastic Simulations and Sensitivity Analyses. Biophys. J. *92*, 831–846. https://doi.org/10.1529/biophysj.106.095521.

Dixon, P.M. (2014). Ripley's K Function. In Wiley StatsRef: Statistics Reference Online, (John Wiley & Sons, Ltd), p.

Dixon, P.M. (2017). Nearest Neighbor Methods: Overview with Examples. In Wiley StatsRef: Statistics Reference Online, (John Wiley & Sons, Ltd), pp. 1–17.

Diz-Muñoz, A., Thurley, K., Chintamen, S., Altschuler, S.J., Wu, L.F., Fletcher, D.A., and Weiner, O.D. (2016). Membrane Tension Acts Through PLD2 and mTORC2 to Limit Actin Network Assembly During Neutrophil Migration. PLOS Biol. *14*, e1002474. https://doi.org/10.1371/journal.pbio.1002474.

Donnelly, K. (1978). Simulations to determine the variance and edge-effect of total nearest neighbour distance. In Simulation Studies in Archaeology, p.

Doreian, B.W., Fulop, T.G., and Smith, C.B. (2008). Myosin II activation and actin reorganization regulate the mode of quantal exocytosis in mouse adrenal chromaffin cells. J. Neurosci. Off. J. Soc. Neurosci. *28*, 4470–4478. https://doi.org/10.1523/JNEUROSCI.0008-08.2008.

Dou, Y., Wu, H., Li, H., Qin, S., Wang, Y., Li, J., Lou, H., Chen, Z., Li, X., Luo, Q., et al. (2012). Microglial migration mediated by ATP-induced ATP release from lysosomes. Cell Res. *22*, 1022–1033. https://doi.org/10.1038/cr.2012.10.

Dozynkiewicz, M.A., Jamieson, N.B., Macpherson, I., Grindlay, J., van den Berghe, P.V.E., von Thun, A., Morton, J.P., Gourley, C., Timpson, P., Nixon, C., et al. (2012). Rab25 and CLIC3 collaborate to promote integrin recycling from late endosomes/lysosomes and drive cancer progression. Dev. Cell *22*, 131–145. https://doi.org/10.1016/j.devcel.2011.11.008.

Dunphy, W.G., Pfeffer, S.R., Clary, D.O., Wattenberg, B.W., Glick, B.S., and Rothman, J.E. (1986). Yeast and mammals utilize similar cytosolic components to drive protein transport through the Golgi complex. Proc. Natl. Acad. Sci. U. S. A. *83*, 1622–1626. .

Duong, T., Goud, B., and Schauer, K. (2012). Closed-form density-based framework for automatic detection of cellular morphology changes. Proc. Natl. Acad. Sci. *109*, 8382–8387. https://doi.org/10.1073/pnas.1117796109.

Durand, S., Feldhammer, M., Bonneil, E., Thibault, P., and Pshezhetsky, A.V. (2010). Analysis of the biogenesis of heparan sulfate acetyl-CoA:alpha-glucosaminide N-acetyltransferase provides insights into the mechanism underlying its complete deficiency in mucopolysaccharidosis IIIC. J. Biol. Chem. *285*, 31233–31242. https://doi.org/10.1074/jbc.M110.141150.

de Duve, C. (1983). Lysosomes revisited. Eur. J. Biochem. *137*, 391–397. .

Ebrahim, S., Chen, D., Weiss, M., Malec, L., Ng, Y., Rebustini, I., Krystofiak, E., Hu, L., Liu, J., Masedunskas, A., et al. (2019). Dynamic polyhedral actomyosin lattices remodel micron-scale curved membranes during exocytosis in live mice. Nat. Cell Biol. *21*, 933–939. https://doi.org/10.1038/s41556-019-0365-7.

Eden, E.R., Burgoyne, T., Edgar, J.R., Sorkin, A., and Futter, C.E. (2012). The relationship between ER-multivesicular body membrane contacts and the ESCRT machinery. Biochem. Soc. Trans. *40*, 464–468. https://doi.org/10.1042/BST20110774.

Eghiaian, F., Rigato, A., and Scheuring, S. (2015). Structural, mechanical, and dynamical variability of the actin cortex in living cells. Biophys. J. *108*, 1330–1340. https://doi.org/10.1016/j.bpj.2015.01.016.

Ehrlich, M., Boll, W., Van Oijen, A., Hariharan, R., Chandran, K., Nibert, M.L., and Kirchhausen, T. (2004). Endocytosis by random initiation and stabilization of clathrin-coated pits. Cell *118*, 591–605. https://doi.org/10.1016/j.cell.2004.08.017.

Elferink, L.A., Trimble, W.S., and Scheller, R.H. (1989). Two vesicle-associated membrane protein genes are differentially expressed in the rat central nervous system. J. Biol. Chem. *264*, 11061–11064. .

Eme, L., Spang, A., Lombard, J., Stairs, C.W., and Ettema, T.J.G. (2017). Archaea and the origin of eukaryotes. Nat. Rev. Microbiol. *15*, 711–723. https://doi.org/10.1038/nrmicro.2017.133.

Encarnação, M., Espada, L., Escrevente, C., Mateus, D., Ramalho, J., Michelet, X., Santarino, I., Hsu, V.W., Brenner, M.B., Barral, D.C., et al. (2016). A Rab3a-dependent complex essential for lysosome positioning and plasma membrane repair. J. Cell Biol. *213*, 631–640. https://doi.org/10.1083/jcb.201511093.

Enyedi, B., and Niethammer, P. (2017). Nuclear membrane stretch and its role in mechanotransduction. Nucleus *8*, 156–161. https://doi.org/10.1080/19491034.2016.1263411.

Enyedi, B., Jelcic, M., and Niethammer, P. (2016). The Cell Nucleus Serves as a Mechanotransducer of Tissue Damage-Induced Inflammation. Cell *165*, 1160–1170. https://doi.org/10.1016/j.cell.2016.04.016.

Erie, C., Sacino, M., Houle, L., Lu, M.L., and Wei, J. (2015). Altered lysosomal positioning affects lysosomal functions in a cellular model of Huntington's disease. Eur. J. Neurosci. *42*, 1941–1951. https://doi.org/10.1111/ejn.12957.

Eroumé, K., Vasilevich, A., Vermeulen, S., Boer, J. de, and Carlier, A. (2021). On the influence of cell shape on dynamic reaction-diffusion polarization patterns. PLOS ONE *16*, e0248293. https://doi.org/10.1371/journal.pone.0248293.

Escrevente, C., Bento-Lopes, L., Ramalho, J.S., and Barral, D.C. (2021). Rab11 is required for lysosome exocytosis through the interaction with Rab3a, Sec15 and GRAB. J. Cell Sci. *134*, jcs246694. https://doi.org/10.1242/jcs.246694.

Eskelinen, E.-L. (2006). Roles of LAMP-1 and LAMP-2 in lysosome biogenesis and autophagy. Mol. Aspects Med. *27*, 495–502. https://doi.org/10.1016/j.mam.2006.08.005.

Evans, E.A., Waugh, R., and Melnik, L. (1976). Elastic area compressibility modulus of red cell membrane. Biophys. J. *16*, 585–595. .

Farago, O. (2011). Mechanical surface tension governs membrane thermal fluctuations. Phys. Rev. E *84*, 051914. https://doi.org/10.1103/PhysRevE.84.051914.

Farago, O., and Pincus, P. (2003). The effect of thermal fluctuations on Schulman area elasticity. Eur. Phys. J. E Soft Matter *11*, 399–408. https://doi.org/10.1140/epje/i2003-10049-y.

Fasshauer, D., Sutton, R.B., Brunger, A.T., and Jahn, R. (1998). Conserved structural features of the synaptic fusion complex: SNARE proteins reclassified as Q- and R-SNAREs. Proc. Natl. Acad. Sci. U. S. A. *95*, 15781–15786. .

Fasshauer, D., Antonin, W., Subramaniam, V., and Jahn, R. (2002). SNARE assembly and disassembly exhibit a pronounced hysteresis. Nat. Struct. Biol. *9*, 144–151. https://doi.org/10.1038/nsb750.

Fenwick, E.M., Marty, A., and Neher, E. (1982). A patch-clamp study of bovine chromaffin cells and of their sensitivity to acetylcholine. J. Physiol. *331*, 577–597. https://doi.org/10.1113/jphysiol.1982.sp014393.

Fernandez, I., Araç, D., Ubach, J., Gerber, S.H., Shin, O., Gao, Y., Anderson, R.G.W., Südhof, T.C., and Rizo, J. (2001). Three-Dimensional Structure of the Synaptotagmin 1 C2B-Domain: Synaptotagmin 1 as a Phospholipid Binding Machine. Neuron *32*, 1057–1069. https://doi.org/10.1016/S0896-6273(01)00548-7.

Fernández-Chacón, R., Königstorfer, A., Gerber, S.H., García, J., Matos, M.F., Stevens, C.F., Brose, N., Rizo, J., Rosenmund, C., and Südhof, T.C. (2001). Synaptotagmin I functions as a calcium regulator of release probability. Nature *410*, 41–49. https://doi.org/10.1038/35065004.

Fin, A., Vargas Jentzsch, A., Sakai, N., and Matile, S. (2012). Oligothiophene Amphiphiles as Planarizable and Polarizable Fluorescent Membrane Probes. Angew. Chem. Int. Ed. *51*, 12736–12739. https://doi.org/10.1002/anie.201206446.

Floch, J.-M., Marcon, E., and Puech, F. (2018). Les configurations de points. In Manuel d'analyse Spatiale. Théorie et Mise En Oeuvre Pratique Avec R, p.

Fofonjka, A., and Milinkovitch, M.C. (2021). Reaction-diffusion in a growing 3D domain of skin scales generates a discrete cellular automaton. Nat. Commun. *12*, 2433. https://doi.org/10.1038/s41467-021-22525-1.

Fourriere, L., Kasri, A., Gareil, N., Bardin, S., Bousquet, H., Pereira, D., Perez, F., Goud, B., Boncompain, G., and Miserey-Lenkei, S. (2019). RAB6 and microtubules restrict protein secretion to focal adhesions. J. Cell Biol. *218*, 2215–2231. https://doi.org/10.1083/jcb.201805002.

Frick, M., Eschertzhuber, S., Haller, T., Mair, N., and Dietl, P. (2001). Secretion in Alveolar Type II Cells at the Interface of Constitutive and Regulated Exocytosis. Am. J. Respir. Cell Mol. Biol. *25*, 306–315. https://doi.org/10.1165/ajrcmb.25.3.4493.

Friedman, A., and Craciun, G. (2005). A model of intracellular transport of particles in an axon. J. Math. Biol. *51*, 217–246. https://doi.org/10.1007/s00285-004-0285-3.

Fu, J., Githaka, J.M., Dai, X., Plummer, G., Suzuki, K., Spigelman, A.F., Bautista, A., Kim, R., Greitzer-Antes, D., Fox, J.E.M., et al. (2019). A glucose-dependent spatial patterning of exocytosis in human β-cells is disrupted in type 2 diabetes. JCI Insight *5*, 127896. https://doi.org/10.1172/jci.insight.127896.

Fukuda, R., McNew, J.A., Weber, T., Parlati, F., Engel, T., Nickel, W., Rothman, J.E., and Söllner, T.H. (2000). Functional architecture of an intracellular membrane t-SNARE. Nature *407*, 198–202. https://doi.org/10.1038/35025084.

Funato, Y., Yoshida, A., Hirata, Y., Hashizume, O., Yamazaki, D., and Miki, H. (2020). The Oncogenic PRL Protein Causes Acid Addiction of Cells by Stimulating Lysosomal Exocytosis. Dev. Cell *55*, 387-397.e8. https://doi.org/10.1016/j.devcel.2020.08.009.

Gabel, M., Delavoie, F., Demais, V., Royer, C., Bailly, Y., Vitale, N., Bader, M.-F., and Chasserot, S. (2015). Annexin A2-dependent actin bundling promotes secretory granule docking to the plasma membrane and exocytosis. J. Cell Biol. *210*, 785–800. https://doi.org/10.1083/jcb.201412030.

Gabella, C., Bertseva, E., Bottier, C., Piacentini, N., Bornert, A., Jeney, S., Forró, L., Sbalzarini, I.F., Meister, J.-J., and Verkhovsky, A.B. (2014). Contact Angle at the Leading Edge Controls Cell Protrusion Rate. Curr. Biol. *24*, 1126–1132. https://doi.org/10.1016/j.cub.2014.03.050.

Galli, T., Zahraoui, A., Vaidyanathan, V.V., Raposo, G., Tian, J.M., Karin, M., Niemann, H., and Louvard, D. (1998). A novel tetanus neurotoxin-insensitive vesicle-associated membrane protein in SNARE complexes of the apical plasma membrane of epithelial cells. Mol. Biol. Cell *9*, 1437–1448. https://doi.org/10.1091/mbc.9.6.1437.

García-Calvo, J., López-Andarias, J., Maillard, J., Mercier, V., Roffay, C., Roux, A., Fürstenberg, A., Sakai, N., and Matile, S. (2022). HydroFlipper membrane tension probes: imaging membrane hydration and mechanical compression simultaneously in living cells. Chem. Sci. *13*, 2086–2093. https://doi.org/10.1039/D1SC05208J.

Garner, R.M., Molines, A.T., Theriot, J.A., and Chang, F. (2022). Vast heterogeneity in cytoplasmic diffusion rates revealed by nanorheology and Doppelgänger simulations. 2022.05.11.491518. https://doi.org/10.1101/2022.05.11.491518.

Gauthier, N.C., Rossier, O.M., Mathur, A., Hone, J.C., and Sheetz, M.P. (2009). Plasma Membrane Area Increases with Spread Area by Exocytosis of a GPI-anchored Protein Compartment. Mol. Biol. Cell *20*, 3261–3272. https://doi.org/10.1091/mbc.e09-01-0071.

Gauthier, N.C., Fardin, M.A., Roca-Cusachs, P., and Sheetz, M.P. (2011). Temporary increase in plasma membrane tension coordinates the activation of exocytosis and contraction during cell spreading. Proc. Natl. Acad. Sci. *108*, 14467–14472. https://doi.org/10.1073/pnas.1105845108.

Gauthier, N.C., Masters, T.A., and Sheetz, M.P. (2012). Mechanical feedback between membrane tension and dynamics. Trends Cell Biol. *22*, 527–535. https://doi.org/10.1016/j.tcb.2012.07.005.

Geary, R.C. (1954). The Contiguity Ratio and Statistical Mapping. Inc. Stat. *5*, 115–146. https://doi.org/10.2307/2986645.

Georgii, H.-O. (1988). Gibbs Measures and Phase Transitions (Berlin ; New York: Walter De Gruyter Inc).

Getis, A., and Franklin, J. (1987). Second-Order Neighborhood Analysis of Mapped Point Patterns. Ecology *68*, 473–477. https://doi.org/10.2307/1938452.

Geuze, H.J. (1998). The role of endosomes and lysosomes in MHC class II functioning. Immunol. Today *19*, 282–287. https://doi.org/10.1016/S0167-5699(98)01269-9.

Ghosh, S., Dellibovi-Ragheb, T.A., Kerviel, A., Pak, E., Qiu, Q., Fisher, M., Takvorian, P.M., Bleck, C., Hsu, V.W., Fehr, A.R., et al. (2020). β-Coronaviruses Use Lysosomes for Egress Instead of the Biosynthetic Secretory Pathway. Cell *183*, 1520-1535.e14. https://doi.org/10.1016/j.cell.2020.10.039.

Glick, B.S., and Rothman, J.E. (1987). Possible role for fatty acyl-coenzyme A in intracellular protein transport. Nature *326*, 309–312. https://doi.org/10.1038/326309a0.

Gomis Perez, C., Dudzinski, N.R., Rouches, M., Landajuela, A., Machta, B., Zenisek, D., and Karatekin, E. (2022). Rapid propagation of membrane tension at retinal bipolar neuron presynaptic terminals. Sci. Adv. *8*, eabl4411. https://doi.org/10.1126/sciadv.abl4411.

Gou, J., Edelstein-Keshet, L., and Allard, J. (2014). Mathematical model with spatially uniform regulation explains long-range bidirectional transport of early endosomes in fungal hyphae. Mol. Biol. Cell *25*, 2408–2415. https://doi.org/10.1091/mbc.e14-03-0826.

Goujon, A., Colom, A., Straková, K., Mercier, V., Mahecic, D., Manley, S., Sakai, N., Roux, A., and Matile, S. (2019). Mechanosensitive Fluorescent Probes to Image Membrane Tension in Mitochondria, Endoplasmic Reticulum, and Lysosomes. J. Am. Chem. Soc. *141*, 3380–3384. https://doi.org/10.1021/jacs.8b13189.

Gould, S.J., Lewontin, R.C., Maynard Smith, J., and Holliday, R. (1979). The spandrels of San Marco and the Panglossian paradigm: a critique of the adaptationist programme. Proc. R. Soc. Lond. B Biol. Sci. *205*, 581–598. https://doi.org/10.1098/rspb.1979.0086.

Greer, W.L., Riddell, D.C., Gillan, T.L., Girouard, G.S., Sparrow, S.M., Byers, D.M., Dobson, M.J., and Neumann, P.E. (1998). The Nova Scotia (Type D) Form of Niemann-Pick Disease Is Caused by a G3097→T Transversion in NPC1. Am. J. Hum. Genet. *63*, 52–54. https://doi.org/10.1086/301931.

Griesche, N., Sanchez, G., Hermans, C., and Idevall-Hagren, O. (2019). Cortical mitochondria regulate insulin secretion by local Ca2+ buffering in rodent beta cells. J. Cell Sci. *132*, jcs228544. https://doi.org/10.1242/jcs.228544.

Grissom, J.H., Segarra, V.A., and Chi, R.J. (2020). New Perspectives on SNARE Function in the Yeast Minimal Endomembrane System. Genes *11*, E899. https://doi.org/10.3390/genes11080899.

Gross, S.P., Vershinin, M., and Shubeita, G.T. (2007). Cargo Transport: Two Motors Are Sometimes Better Than One. Curr. Biol. *17*, R478–R486. https://doi.org/10.1016/j.cub.2007.04.025.

Grossier, J.-P., Xouri, G., Goud, B., and Schauer, K. (2014). Cell adhesion defines the topology of endocytosis and signaling. EMBO J. *33*, 35–45. https://doi.org/10.1002/embj.201385284.

Grünbaum, D. (2000). Advection-Diffusion Equations for Internal State-Mediated Random Walks. SIAM J. Appl. Math. *61*, 43–73. .

Guan, Y. (2006). Tests for Independence between Marks and Points of a Marked Point Process. Biometrics *62*, 126–134. .

Guardia, C.M., Farías, G.G., Jia, R., Pu, J., and Bonifacino, J.S. (2016). BORC Functions Upstream of Kinesins 1 and 3 to Coordinate Regional Movement of Lysosomes along Different Microtubule Tracks. Cell Rep. *17*, 1950–1961. https://doi.org/10.1016/j.celrep.2016.10.062.

Guardia, C.M., Pace, R.D., Sen, A., Saric, A., Jarnik, M., Kolin, D.A., Kunwar, A., and Bonifacino, J.S. (2019). Reversible association with motor proteins (RAMP): A streptavidin-based method to manipulate organelle positioning. PLOS Biol. *17*, e3000279. https://doi.org/10.1371/journal.pbio.3000279.

Gundelfinger, E.D., Kessels, M.M., and Qualmann, B. (2003). Temporal and spatial coordination of exocytosis and endocytosis. Nat. Rev. Mol. Cell Biol. *4*, 127–139. https://doi.org/10.1038/nrm1016.

Gupton, S.L., and Gertler, F.B. (2010). Integrin signaling switches the cytoskeletal and exocytic machinery that drives neuritogenesis. Dev. Cell *18*, 725–736. https://doi.org/10.1016/j.devcel.2010.02.017.

Gurung, S., Perocheau, D., Touramanidou, L., and Baruteau, J. (2021). The exosome journey: from biogenesis to uptake and intracellular signalling. Cell Commun. Signal. *19*, 47. https://doi.org/10.1186/s12964-021-00730-1.

Hahn, U. (2012). A Studentized Permutation Test for the Comparison of Spatial Point Patterns. J. Am. Stat. Assoc. *107*, 754–764. https://doi.org/10.1080/01621459.2012.688463.

Hahn, U., and Jensen, E.B.V. (2016). Hidden Second-order Stationary Spatial Point Processes. Scand. J. Stat. *43*, 455–475. .

Halatek, J., Brauns, F., and Frey, E. (2018). Self-organization principles of intracellular pattern formation. Philos. Trans. R. Soc. B Biol. Sci. *373*, 20170107. https://doi.org/10.1098/rstb.2017.0107.

Hammond, G.R.V., Dove, S.K., Nicol, A., Pinxteren, J.A., Zicha, D., and Schiavo, G. (2006). Elimination of plasma membrane phosphatidylinositol (4,5)-bisphosphate is required for exocytosis from mast cells. J. Cell Sci. *119*, 2084–2094. https://doi.org/10.1242/jcs.02912.

Hancock, E.J., Ang, J., Papachristodoulou, A., and Stan, G.-B. (2017). The Interplay between Feedback and Buffering in Cellular Homeostasis. Cell Syst. 5, 498-508.e23. https://doi.org/10.1016/j.cels.2017.09.013.

Hanson, P.I., and Cashikar, A. (2012). Multivesicular body morphogenesis. Annu. Rev. Cell Dev. Biol. *28*, 337–362. https://doi.org/10.1146/annurev-cellbio-092910-154152.

Hansson, K., Jafari-Mamaghani, M., and Krieger, P. (2013). RipleyGUI: software for analyzing spatial patterns in 3D cell distributions. Front. Neuroinformatics *7*, 5. https://doi.org/10.3389/fninf.2013.00005.

Harold, F.M. (2005). Molecules into cells: specifying spatial architecture. Microbiol. Mol. Biol. Rev. MMBR *69*, 544–564. https://doi.org/10.1128/MMBR.69.4.544-564.2005.

He, L., Wu, X.-S., Mohan, R., and Wu, L.-G. (2006). Two modes of fusion pore opening revealed by cell-attached recordings at a synapse. Nature *444*, 102–105. https://doi.org/10.1038/nature05250.

Heidelberger, R., Zhou, Z.-Y., and Matthews, G. (2002). Multiple components of membrane retrieval in synaptic terminals revealed by changes in hydrostatic pressure. J. Neurophysiol. *88*, 2509–2517. https://doi.org/10.1152/jn.00267.2002.

Helfrich, W. (1973). Elastic properties of lipid bilayers: theory and possible experiments. Z. Naturforschung Teil C Biochem. Biophys. Biol. Virol. *28*, 693–703. https://doi.org/10.1515/znc-1973-11-1209.

Hessvik, N.P., and Llorente, A. (2018). Current knowledge on exosome biogenesis and release. Cell. Mol. Life Sci. CMLS *75*, 193–208. https://doi.org/10.1007/s00018-017-2595-9.

Heuser, J.E., and Reese, T.S. (1973). Evidence for recycling of synaptic vesicle membrane during transmitter release at the frog neuromuscular junction. J. Cell Biol. *57*, 315–344. https://doi.org/10.1083/jcb.57.2.315.

Heybrock, S., Kanerva, K., Meng, Y., Ing, C., Liang, A., Xiong, Z.-J., Weng, X., Ah Kim, Y., Collins, R., Trimble, W., et al. (2019). Lysosomal integral membrane protein-2 (LIMP-2/SCARB2) is involved in lysosomal cholesterol export. Nat. Commun. *10*, 3521. https://doi.org/10.1038/s41467-019-11425-0.

Higuchi, Y., Ashwin, P., Roger, Y., and Steinberg, G. (2014). Early endosome motility spatially organizes polysome distribution. J. Cell Biol. *204*, 343–357. https://doi.org/10.1083/jcb.201307164.

Hill, A.V. (1910). The possible effects of the aggregation of the molecules of haemoglobin on its dissociation curves. J Physiol *40*, 4–7. .

Hiragi, S., Matsui, T., Sakamaki, Y., and Fukuda, M. (2021). TBC1D18, a novel Rab5-GAP, coordinates endosome maturation together with Mon1. 2021.11.11.468194. https://doi.org/10.1101/2021.11.11.468194.

Hirsch, J.G. (1959). Immunity to infectious diseases: review of some concepts of Metchnikoff. Bacteriol. Rev. *23*, 48–60. .

Hochmuth, R.M. (2000). Micropipette aspiration of living cells. J. Biomech. *33*, 15–22. https://doi.org/10.1016/s0021-9290(99)00175-x.

Höglinger, D., Burgoyne, T., Sanchez-Heras, E., Hartwig, P., Colaco, A., Newton, J., Futter, C.E., Spiegel, S., Platt, F.M., and Eden, E.R. (2019). NPC1 regulates ER contacts with endocytic organelles to mediate cholesterol egress. Nat. Commun. *10*, 4276. https://doi.org/10.1038/s41467-019-12152-2.

Hohmann, S. (2002). Osmotic Stress Signaling and Osmoadaptation in Yeasts. Microbiol. Mol. Biol. Rev. *66*, 300–372. https://doi.org/10.1128/MMBR.66.2.300-372.2002.

Holt, M., Varoqueaux, F., Wiederhold, K., Takamori, S., Urlaub, H., Fasshauer, D., and Jahn, R. (2006). Identification of SNAP-47, a novel Qbc-SNARE with ubiquitous expression. J. Biol. Chem. *281*, 17076–17083. https://doi.org/10.1074/jbc.M513838200.

Hong, W. (2005). SNAREs and traffic. Biochim. Biophys. Acta *1744*, 120–144. https://doi.org/10.1016/j.bbamcr.2005.03.014.

Honigmann, A., van den Bogaart, G., Iraheta, E., Risselada, H.J., Milovanovic, D., Mueller, V., Müllar, S., Diederichsen, U., Fasshauer, D., Grubmüller, H., et al. (2013). Phosphatidylinositol

4,5-bisphosphate clusters act as molecular beacons for vesicle recruitment. Nat. Struct. Mol. Biol. *20*, 679–686. https://doi.org/10.1038/nsmb.2570.

Hopkins, B., and Skellam, J.G. (1954). A New Method for determining the Type of Distribution of Plant Individuals. Ann. Bot. *18*, 213–227. https://doi.org/10.1093/oxfordjournals.aob.a083391.

Hoshino, D., Kirkbride, K.C., Costello, K., Clark, E.S., Sinha, S., Grega-Larson, N., Tyska, M.J., and Weaver, A.M. (2013). Exosome secretion is enhanced by invadopodia and drives invasive behavior. Cell Rep. *5*, 1159–1168. https://doi.org/10.1016/j.celrep.2013.10.050.

Houchmandzadeh, B., Dumonteil, E., Mazzolo, A., and Zoia, A. (2015). Neutron fluctuations: the importance of being delayed. Phys. Rev. E *92*, 052114. https://doi.org/10.1103/PhysRevE.92.052114.

Houk, A.R., Jilkine, A., Mejean, C.O., Boltyanskiy, R., Dufresne, E.R., Angenent, S.B., Altschuler, S.J., Wu, L.F., and Weiner, O.D. (2012). Membrane tension maintains cell polarity by confining signals to the leading edge during neutrophil migration. Cell *148*, 175–188. https://doi.org/10.1016/j.cell.2011.10.050.

Huotari, J., and Helenius, A. (2011). Endosome maturation. EMBO J. *30*, 3481–3500. https://doi.org/10.1038/emboj.2011.286.

Hutagalung, A.H., and Novick, P.J. (2011). Role of Rab GTPases in membrane traffic and cell physiology. Physiol. Rev. *91*, 119–149. https://doi.org/10.1152/physrev.00059.2009.

Huynh, K.K., Kay, J.G., Stow, J.L., and Grinstein, S. (2007). Fusion, Fission, and Secretion During Phagocytosis. Physiology *22*, 366–372. https://doi.org/10.1152/physiol.00028.2007.

Ichikawa, A. (1965). FINE STRUCTURAL CHANGES IN RESPONSE TO HORMONAL STIMULATION OF THE PERFUSED CANINE PANCREAS. J. Cell Biol. *24*, 369–385. https://doi.org/10.1083/jcb.24.3.369.

Ikarashi, R., Akechi, H., Kanda, Y., Ahmad, A., Takeuchi, K., Morioka, E., Sugiyama, T., Ebisawa, T., Ikeda, M., and Ikeda, M. (2017). Regulation of molecular clock oscillations and phagocytic activity via muscarinic Ca2+ signaling in human retinal pigment epithelial cells. Sci. Rep. *7*, 44175. https://doi.org/10.1038/srep44175.

Imachi, H., Nobu, M.K., Nakahara, N., Morono, Y., Ogawara, M., Takaki, Y., Takano, Y., Uematsu, K., Ikuta, T., Ito, M., et al. (2020). Isolation of an archaeon at the prokaryote–eukaryote interface. Nature *577*, 519–525. https://doi.org/10.1038/s41586-019-1916-6.

Ireton, K., Van Ngo, H., and Bhalla, M. (2018). Interaction of microbial pathogens with host exocytic pathways. Cell. Microbiol. *20*, e12861. https://doi.org/10.1111/cmi.12861.

Ishida, Y., Nayak, S., Mindell, J.A., and Grabe, M. (2013). A model of lysosomal pH regulation. J. Gen. Physiol. *141*, 705–720. https://doi.org/10.1085/jgp.201210930.

Israelachvili, J.N., Mitchell, D.J., and Ninham, B.W. (1976). Theory of self-assembly of hydrocarbon amphiphiles into micelles and bilayers. J. Chem. Soc. Faraday Trans. 2 Mol. Chem. Phys. *72*, 1525–1568. https://doi.org/10.1039/F29767201525.

Jacobo, A., and Hudspeth, A.J. (2014). Reaction–diffusion model of hair-bundle morphogenesis. Proc. Natl. Acad. Sci. *111*, 15444–15449. https://doi.org/10.1073/pnas.1417420111.

Jafari Mamaghani, M., Andersson, M., and Krieger, P. (2010). Spatial point pattern analysis of neurons using Ripley's K-function in 3D. Front. Neuroinformatics *4*. .

Jaiswal, J.K., Andrews, N.W., and Simon, S.M. (2002). Membrane proximal lysosomes are the major vesicles responsible for calcium-dependent exocytosis in nonsecretory cells. J. Cell Biol. *159*, 625–635. https://doi.org/10.1083/jcb.200208154.

Jamieson, J.D., and Palade, G.E. (1967). Intracellular transport of secretory proteins in the pancreatic exocrine cell. II. Transport to condensing vacuoles and zymogen granules. J. Cell Biol. *34*, 597–615. https://doi.org/10.1083/jcb.34.2.597.

Jamison, D.K., Driver, J.W., Rogers, A.R., Constantinou, P.E., and Diehl, M.R. (2010). Two Kinesins Transport Cargo Primarily via the Action of One Motor: Implications for Intracellular Transport. Biophys. J. *99*, 2967–2977. https://doi.org/10.1016/j.bpj.2010.08.025.

Jammalamadaka, A., Banerjee, S., Manjunath, B.S., and Kosik, K.S. (2013). Statistical analysis of dendritic spine distributions in rat hippocampal cultures. BMC Bioinformatics *14*, 287. https://doi.org/10.1186/1471-2105-14-287.

Jani, R.A., Mahanty, S., and Setty, S.R.G. (2016). SNAREs in the maturation and function of LROs. Bioarchitecture *6*, 1–11. https://doi.org/10.1080/19490992.2015.1131890.

Jiang, L., Phillips, T.E., Hamm, C.A., Drozdowicz, Y.M., Rea, P.A., Maeshima, M., Rogers, S.W., and Rogers, J.C. (2001). The protein storage vacuole: a unique compound organelle. J. Cell Biol. *155*, 991–1002. https://doi.org/10.1083/jcb.200107012.

Johannes, L., Pezeshkian, W., Ipsen, J.H., and Shillcock, J.C. (2018). Clustering on Membranes: Fluctuations and More. Trends Cell Biol. *28*, 405–415. https://doi.org/10.1016/j.tcb.2018.01.009.

Johnson, D.E., Ostrowski, P., Jaumouillé, V., and Grinstein, S. (2016). The position of lysosomes within the cell determines their luminal pH. J. Cell Biol. *212*, 677–692. https://doi.org/10.1083/jcb.201507112.

Jongsma, M.L.M., Berlin, I., Wijdeven, R.H.M., Janssen, L., Janssen, G.M.C., Garstka, M.A., Janssen, H., Mensink, M., van Veelen, P.A., Spaapen, R.M., et al. (2016). An ER-Associated Pathway Defines Endosomal Architecture for Controlled Cargo Transport. Cell *166*, 152–166. https://doi.org/10.1016/j.cell.2016.05.078.

Karsenti, E. (2008). Self-organization in cell biology: a brief history. Nat. Rev. Mol. Cell Biol. *9*, 255–262. https://doi.org/10.1038/nrm2357.

Kasai, H., Takahashi, N., and Tokumaru, H. (2012). Distinct initial SNARE configurations underlying the diversity of exocytosis. Physiol. Rev. *92*, 1915–1964. https://doi.org/10.1152/physrev.00007.2012.

Katz, L., and Brennwald, P. (2000). Testing the 3Q:1R "rule": mutational analysis of the ionic "zero" layer in the yeast exocytic SNARE complex reveals no requirement for arginine. Mol. Biol. Cell *11*, 3849–3858. https://doi.org/10.1091/mbc.11.11.3849.

Kaushik, S., and Cuervo, A.M. (2018). The coming of age of chaperone-mediated autophagy. Nat. Rev. Mol. Cell Biol. *19*, 365–381. https://doi.org/10.1038/s41580-018-0001-6.

Kedersha, N., Stoecklin, G., Ayodele, M., Yacono, P., Lykke-Andersen, J., Fritzler, M.J., Scheuner, D., Kaufman, R.J., Golan, D.E., and Anderson, P. (2005). Stress granules and processing bodies are dynamically linked sites of mRNP remodeling. J. Cell Biol. *169*, 871–884. https://doi.org/10.1083/jcb.200502088.

Keller, P., Toomre, D., Díaz, E., White, J., and Simons, K. (2001). Multicolour imaging of post-Golgi sorting and trafficking in live cells. Nat. Cell Biol. *3*, 140–149. https://doi.org/10.1038/35055042.

Kelly, F.P., and Ripley, B.D. (1976). A Note on Strauss's Model for Clustering. Biometrika *63*, 357–360. https://doi.org/10.2307/2335630.

Keren, K. (2011). Cell motility: the integrating role of the plasma membrane. Eur. Biophys. J. EBJ *40*, 1013–1027. https://doi.org/10.1007/s00249-011-0741-0.

Keren, K., Pincus, Z., Allen, G.M., Barnhart, E.L., Marriott, G., Mogilner, A., and Theriot, J.A. (2008). Mechanism of shape determination in motile cells. Nature *453*, 475–480. https://doi.org/10.1038/nature06952.

Keren-Kaplan, T., and Bonifacino, J.S. (2021). ARL8 Relieves SKIP Autoinhibition to Enable Coupling of Lysosomes to Kinesin-1. Curr. Biol. *31*, 540-554.e5. https://doi.org/10.1016/j.cub.2020.10.071.

Khan, S.A., and Tomatsu, S.C. (2020). Mucolipidoses Overview: Past, Present, and Future. Int. J. Mol. Sci. *21*, E6812. https://doi.org/10.3390/ijms21186812.

Khater, I.M., Nabi, I.R., and Hamarneh, G. (2020). A Review of Super-Resolution Single-Molecule Localization Microscopy Cluster Analysis and Quantification Methods. Patterns *1*, 100038. https://doi.org/10.1016/j.patter.2020.100038.

Kisiel, M., Majumdar, D., Campbell, S., and Stewart, B.A. (2011). Myosin VI contributes to synaptic transmission and development at the Drosophila neuromuscular junction. BMC Neurosci. *12*, 65. https://doi.org/10.1186/1471-2202-12-65.

Kisiel, M., McKenzie, K., and Stewart, B. (2014). Localization and Mobility of Synaptic Vesicles in Myosin VI Mutants of Drosophila. PLOS ONE *9*, e102988. https://doi.org/10.1371/journal.pone.0102988.

Kiskowski, M.A., Hancock, J.F., and Kenworthy, A.K. (2009). On the Use of Ripley's K-Function and Its Derivatives to Analyze Domain Size. Biophys. J. *97*, 1095–1103. https://doi.org/10.1016/j.bpj.2009.05.039.

Kittelberger, N., Breunig, M., Martin, R., Knölker, H.-J., and Miklavc, P. (2016). The role of myosin 1c and myosin 1b in surfactant exocytosis. J. Cell Sci. *129*, 1685–1696. https://doi.org/10.1242/jcs.181313.

Klein, D., Büssow, H., Fewou, S.N., and Gieselmann, V. (2005). Exocytosis of storage material in a lysosomal disorder. Biochem. Biophys. Res. Commun. *327*, 663–667. https://doi.org/10.1016/j.bbrc.2004.12.054.

Kliesch, T.-T., Dietz, J., Turco, L., Halder, P., Polo, E., Tarantola, M., Jahn, R., and Janshoff, A. (2017a). Membrane tension increases fusion efficiency of model membranes in the presence of SNAREs. Sci. Rep. *7*, 12070. https://doi.org/10.1038/s41598-017-12348-w.

Kliesch, T.-T., Dietz, J., Turco, L., Halder, P., Polo, E., Tarantola, M., Jahn, R., and Janshoff, A. (2017b). Membrane tension increases fusion efficiency of model membranes in the presence of SNAREs. Sci. Rep. *7*, 12070. https://doi.org/10.1038/s41598-017-12348-w.

Kloepper, T.H., Kienle, C.N., and Fasshauer, D. (2007). An Elaborate Classification of SNARE Proteins Sheds Light on the Conservation of the Eukaryotic Endomembrane System. Mol. Biol. Cell *18*, 3463–3471. https://doi.org/10.1091/mbc.E07-03-0193.

Kondo, S., and Asai, R. (1995). A reaction–diffusion wave on the skin of the marine angelfish Pomacanthus. Nature *376*, 765–768. https://doi.org/10.1038/376765a0.

Kondo, S., and Miura, T. (2010). Reaction-Diffusion Model as a Framework for Understanding Biological Pattern Formation. Science *329*, 1616–1620. https://doi.org/10.1126/science.1179047.

Koseoglu, S., Peters, C.G., Fitch-Tewfik, J.L., Aisiku, O., Danglot, L., Galli, T., and Flaumenhaft, R. (2015). VAMP-7 links granule exocytosis to actin reorganization during platelet activation. Blood *126*, 651–660. https://doi.org/10.1182/blood-2014-12-618744.

Kosmalska, A.J., Casares, L., Elosegui-Artola, A., Thottacherry, J.J., Moreno-Vicente, R., González-Tarragó, V., del Pozo, M.Á., Mayor, S., Arroyo, M., Navajas, D., et al. (2015). Physical principles of membrane remodelling during cell mechanoadaptation. Nat. Commun. *6*, 7292. https://doi.org/10.1038/ncomms8292.

Kowal, J., Tkach, M., and Théry, C. (2014). Biogenesis and secretion of exosomes. Curr. Opin. Cell Biol. *29*, 116–125. https://doi.org/10.1016/j.ceb.2014.05.004.

Kozlov, M.M., and Chernomordik, L.V. (2015). Membrane tension and membrane fusion. Curr. Opin. Struct. Biol. *33*, 61–67. https://doi.org/10.1016/j.sbi.2015.07.010.

Kvam, E., and Goldfarb, D.S. (2007). Nucleus-vacuole junctions and piecemeal microautophagy of the nucleus in S. cerevisiae. Autophagy *3*, 85–92. https://doi.org/10.4161/auto.3586.

Kwon, W., and Freeman, S.A. (2020). Phagocytosis by the Retinal Pigment Epithelium: Recognition, Resolution, Recycling. Front. Immunol. *11*. .

Lachuer, H., Mathur, P., Bleakley, K., and Schauer, K. (2020). Quantifying Spatiotemporal Parameters of Cellular Exocytosis in Micropatterned Cells. J. Vis. Exp. JoVE https://doi.org/10.3791/60801.

Lachuer, H., Le, L., Lévêque-Fort, S., Goud, B., and Schauer, K. (2022). Membrane tension spatially organizes lysosomal exocytosis. 2022.04.22.489160. https://doi.org/10.1101/2022.04.22.489160.

Lacombe, J., Karsenty, G., and Ferron, M. (2013). Regulation of lysosome biogenesis and functions in osteoclasts. Cell Cycle Georget. Tex *12*, 2744–2752. https://doi.org/10.4161/cc.25825.

Lagache, T., and Holcman, D. (2008). Quantifying intermittent transport in cell cytoplasm. Phys. Rev. E *77*, 030901. https://doi.org/10.1103/PhysRevE.77.030901.

Lagache, T., Dauty, E., and Holcman, D. (2009). Quantitative analysis of virus and plasmid trafficking in cells. Phys. Rev. E *79*, 011921. https://doi.org/10.1103/PhysRevE.79.011921.

Lagache, T., Lang, G., Sauvonnet, N., and Olivo-Marin, J.-C. (2013). Analysis of the Spatial Organization of Molecules with Robust Statistics. PLOS ONE *8*, e80914. https://doi.org/10.1371/journal.pone.0080914.

Lagache, T., Sauvonnet, N., Danglot, L., and Olivo-Marin, J.-C. (2015). Statistical analysis of molecule colocalization in bioimaging. Cytom. Part J. Int. Soc. Anal. Cytol. *87*, 568–579. https://doi.org/10.1002/cyto.a.22629.

Lang, T. (2007). SNARE proteins and "membrane rafts." J. Physiol. *585*, 693–698. https://doi.org/10.1113/jphysiol.2007.134346.

Lang, T., and Hochheimer, N. (2020). Tetraspanins. Curr. Biol. CB *30*, R204–R206. https://doi.org/10.1016/j.cub.2020.01.007.

Langemeyer, L., Fröhlich, F., and Ungermann, C. (2018). Rab GTPase Function in Endosome and Lysosome Biogenesis. Trends Cell Biol. *28*, 957–970. https://doi.org/10.1016/j.tcb.2018.06.007.

LaPlante, J.M., Sun, M., Falardeau, J., Dai, D., Brown, E.M., Slaugenhaupt, S.A., and Vassilev, P.M. (2006). Lysosomal exocytosis is impaired in mucolipidosis type IV. Mol. Genet. Metab. *89*, 339–348. https://doi.org/10.1016/j.ymgme.2006.05.016.

Lee, T.H., and Linstedt, A.D. (1999). Osmotically Induced Cell Volume Changes Alter Anterograde and Retrograde Transport, Golgi Structure, and COPI Dissociation. Mol. Biol. Cell *10*, 1445–1462. .

Lee, J.E., Cathey, P.I., Wu, H., Parker, R., and Voeltz, G.K. (2020). Endoplasmic reticulum contact sites regulate the dynamics of membraneless organelles. Science *367*, eaay7108. https://doi.org/10.1126/science.aay7108.

Li, F., Pincet, F., Perez, E., Eng, W.S., Melia, T.J., Rothman, J.E., and Tareste, D. (2007). Energetics and dynamics of SNAREpin folding across lipid bilayers. Nat. Struct. Mol. Biol. *14*, 890–896. https://doi.org/10.1038/nsmb1310.

Li, P., Bademosi, A.T., Luo, J., and Meunier, F.A. (2018a). Actin Remodeling in Regulated Exocytosis: Toward a Mesoscopic View. Trends Cell Biol. *28*, 685–697. https://doi.org/10.1016/j.tcb.2018.04.004.

Li, P., Gu, M., and Xu, H. (2019). Lysosomal Ion Channels as Decoders of Cellular Signals. Trends Biochem. Sci. *44*, 110–124. https://doi.org/10.1016/j.tibs.2018.10.006.

Li, W., Yu, X., Xie, F., Zhang, B., Shao, S., Geng, C., Aziz, A. ur R., Liao, X., and Liu, B. (2018b). A Membrane-Bound Biosensor Visualizes Shear Stress-Induced Inhomogeneous Alteration of Cell Membrane Tension. IScience *7*, 180–190. https://doi.org/10.1016/j.isci.2018.09.002.

Li, X., Rydzewski, N., Hider, A., Zhang, X., Yang, J., Wang, W., Gao, Q., Cheng, X., and Xu, H. (2016). A molecular mechanism to regulate lysosome motility for lysosome positioning and tubulation. Nat. Cell Biol. *18*, 404–417. https://doi.org/10.1038/ncb3324.

Liao, Y.-C., Fernandopulle, M.S., Wang, G., Choi, H., Hao, L., Drerup, C.M., Patel, R., Qamar, S., Nixon-Abell, J., Shen, Y., et al. (2019). RNA Granules Hitchhike on Lysosomes for Long-Distance Transport, Using Annexin A11 as a Molecular Tether. Cell *179*, 147-164.e20. https://doi.org/10.1016/j.cell.2019.08.050.

Lieber, A.D., Schweitzer, Y., Kozlov, M.M., and Keren, K. (2015). Front-to-Rear Membrane Tension Gradient in Rapidly Moving Cells. Biophys. J. *108*, 1599–1603. https://doi.org/10.1016/j.bpj.2015.02.007.

Lin, C., and Steinberg, G. (2017). Spatial organization of organelles in fungi: Insights from mathematical modelling. Fungal Genet. Biol. *103*, 55–59. https://doi.org/10.1016/j.fgb.2017.03.006.

Lin, C., Schuster, M., Guimaraes, S.C., Ashwin, P., Schrader, M., Metz, J., Hacker, C., Gurr, S.J., and Steinberg, G. (2016). Active diffusion and microtubule-based transport oppose myosin forces to position organelles in cells. Nat. Commun. *7*, 11814. https://doi.org/10.1038/ncomms11814.

Lin, S.X., Pfister, K.K., and Collins, C.A. (1996). Comparison of the intracellular distribution of cytoplasmic dynein and kinesin in cultured cells: motor protein location does not reliably predict function. Cell Motil. Cytoskeleton *34*, 299–312. https://doi.org/10.1002/(SICI)1097-0169(1996)34:4<299::AID-CM5>3.0.CO;2-3.

Linetti, A., Fratangeli, A., Taverna, E., Valnegri, P., Francolini, M., Cappello, V., Matteoli, M., Passafaro, M., and Rosa, P. (2010). Cholesterol reduction impairs exocytosis of synaptic vesicles. J. Cell Sci. *123*, 595–605. https://doi.org/10.1242/jcs.060681.

Lipowsky, R. (2014). Coupling of bending and stretching deformations in vesicle membranes. Adv. Colloid Interface Sci. *208*, 14–24. https://doi.org/10.1016/j.cis.2014.02.008.

Lipowsky, R. (2022). Remodeling of Membrane Shape and Topology by Curvature Elasticity and Membrane Tension. Adv. Biol. *6*, 2101020. https://doi.org/10.1002/adbi.202101020.

Liu, G.Y., and Sabatini, D.M. (2020). mTOR at the nexus of nutrition, growth, ageing and disease. Nat. Rev. Mol. Cell Biol. *21*, 183–203. https://doi.org/10.1038/s41580-019-0199-y.

López-García, P., and Moreira, D. (2020). The Syntrophy hypothesis for the origin of eukaryotes revisited. Nat. Microbiol. *5*, 655–667. https://doi.org/10.1038/s41564-020-0710-4.

Lou, X. (2018). Sensing Exocytosis and Triggering Endocytosis at Synapses: Synaptic Vesicle Exocytosis–Endocytosis Coupling. Front. Cell. Neurosci. *12*. .

Luo, G., Zhang, J., and Guo, W. (2014). The role of Sec3p in secretory vesicle targeting and exocyst complex assembly. Mol. Biol. Cell *25*, 3813–3822. https://doi.org/10.1091/mbc.E14-04-0907.

Machado, E., White-Gilbertson, S., van de Vlekkert, D., Janke, L., Moshiach, S., Campos, Y., Finkelstein, D., Gomero, E., Mosca, R., Qiu, X., et al. (2015). Regulated lysosomal exocytosis mediates cancer progression. Sci. Adv. *1*, e1500603. https://doi.org/10.1126/sciadv.1500603.

Machado, E.R., Annunziata, I., van de Vlekkert, D., Grosveld, G.C., and d'Azzo, A. (2021). Lysosomes and Cancer Progression: A Malignant Liaison. Front. Cell Dev. Biol. *9*, 642494. https://doi.org/10.3389/fcell.2021.642494.

Mackey, M.C., and Glass, L. (1977). Oscillation and Chaos in Physiological Control Systems. Science *197*, 287–289. https://doi.org/10.1126/science.267326.

Mahecic, D., Carlini, L., Kleele, T., Colom, A., Goujon, A., Matile, S., Roux, A., and Manley, S. (2021). Mitochondrial membrane tension governs fission. Cell Rep. *35*, 108947. https://doi.org/10.1016/j.celrep.2021.108947.

Maini, P.K., Woolley, T.E., Baker, R.E., Gaffney, E.A., and Lee, S.S. (2012). Turing's model for biological pattern formation and the robustness problem. Interface Focus *2*, 487–496. https://doi.org/10.1098/rsfs.2011.0113.

Malhotra, V., Orci, L., Glick, B.S., Block, M.R., and Rothman, J.E. (1988). Role of an N-ethylmaleimide-sensitive transport component in promoting fusion of transport vesicles with cisternae of the Golgi stack. Cell *54*, 221–227. https://doi.org/10.1016/0092-8674(88)90554-5.

Malikov, V., Cytrynbaum, E.N., Kashina, A., Mogilner, A., and Rodionov, V. (2005). Centering of a radial microtubule array by translocation along microtubules spontaneously nucleated in the cytoplasm. Nat. Cell Biol. *7*, 1213–1218. https://doi.org/10.1038/ncb1332.

Maly, I.V. (2002a). A Stochastic Model for Patterning of the Cytoplasm by the Saltatory Movement. J. Theor. Biol. *216*, 59–71. https://doi.org/10.1006/jtbi.2002.2531.

Maly, I.V. (2002b). Diffusion approximation of the stochastic process of microtubule assembly. Bull. Math. Biol. *64*, 213–238. https://doi.org/10.1006/bulm.2001.0265.

Manneville, J.-B., Casella, J.-F., Ambroggio, E., Gounon, P., Bertherat, J., Bassereau, P., Cartaud, J., Antonny, B., and Goud, B. (2008). COPI coat assembly occurs on liquid-disordered domains and the associated membrane deformations are limited by membrane tension. Proc. Natl. Acad. Sci. *105*, 16946–16951. https://doi.org/10.1073/pnas.0807102105.

Mao, F., Yang, Y., and Jiang, H. (2021). Endocytosis and exocytosis protect cells against severe membrane tension variations. Biophys. J. *120*, 5521–5529. https://doi.org/10.1016/j.bpj.2021.11.019.

Marcon, E., and Puech, F. (2009). Generalizing Ripley's K function to inhomogeneous populations.

de Marcos Lousa, C., and Denecke, J. (2016). Lysosomal and vacuolar sorting: not so different after all! Biochem. Soc. Trans. *44*, 891–897. https://doi.org/10.1042/BST20160050.

Martin, W.F., Tielens, A.G.M., Mentel, M., Garg, S.G., and Gould, S.B. (2017). The Physiology of Phagocytosis in the Context of Mitochondrial Origin. Microbiol. Mol. Biol. Rev. *81*. https://doi.org/10.1128/MMBR.00008-17.

Martinez-Arca, S., Alberts, P., Zahraoui, A., Louvard, D., and Galli, T. (2000). Role of tetanus neurotoxin insensitive vesicle-associated membrane protein (TI-VAMP) in vesicular transport mediating neurite outgrowth. J. Cell Biol. *149*, 889–900. https://doi.org/10.1083/jcb.149.4.889.

Marty, null (1999). Plant vacuoles. Plant Cell *11*, 587–600. https://doi.org/10.1105/tpc.11.4.587.

Maschi, D., Gramlich, M.W., and Klyachko, V.A. (2018). Myosin V functions as a vesicle tether at the plasma membrane to control neurotransmitter release in central synapses. ELife *7*, e39440. https://doi.org/10.7554/eLife.39440.

Mastrodonato, V., Morelli, E., and Vaccari, T. (2018). How to use a multipurpose SNARE: The emerging role of Snap29 in cellular health. Cell Stress *2*, 72–81. https://doi.org/10.15698/cst2018.04.130.

Matérn (1986). Spatial Variation.

Matheron, G. (1963). Principles of geostatistics. Econ. Geol. *58*, 1246–1266. https://doi.org/10.2113/gsecongeo.58.8.1246.

Mathur, P., Santos, C.D.B., Lachuer, H., Latgé, B., Radvanyi, F., Goud, B., and Schauer, K. (2022). Transcription Factor EB regulates phosphatidylinositol-3-phosphate levels on endomembranes and alters lysosome positioning in the bladder cancer model. 2020.07.10.196931. https://doi.org/10.1101/2020.07.10.196931.

Matthew, W.D., Tsavaler, L., and Reichardt, L.F. (1981). Identification of a synaptic vesicle-specific membrane protein with a wide distribution in neuronal and neurosecretory tissue. J. Cell Biol. *91*, 257–269. https://doi.org/10.1083/jcb.91.1.257.

Maurel, C., Boursiac, Y., Luu, D.-T., Santoni, V., Shahzad, Z., and Verdoucq, L. (2015). Aquaporins in Plants. Physiol. Rev. *95*, 1321–1358. https://doi.org/10.1152/physrev.00008.2015.

Mayorga, L.S., Verma, M., Hontecillas, R., Hoops, S., and Bassaganya-Riera, J. (2017). Agents and networks to model the dynamic interactions of intracellular transport. Cell. Logist. *7*, e1392401. https://doi.org/10.1080/21592799.2017.1392401.

Mayorga, L.S., Cebrian, I., Verma, M., Hoops, S., and Bassaganya-Riera, J. (2018). Reconstruction of endosomal organization and function by a combination of ODE and agent-based modeling strategies. Biol. Direct *13*, 25. https://doi.org/10.1186/s13062-018-0227-4.

McLaughlin, G.A., Langdon, E.M., Crutchley, J.M., Holt, L.J., Forest, M.G., Newby, J.M., and Gladfelter, A.S. (2020). Spatial heterogeneity of the cytosol revealed by machine learning-based 3D particle tracking. Mol. Biol. Cell *31*, 1498–1511. https://doi.org/10.1091/mbc.E20-03-0210.

McNeil, P.L. (2002). Repairing a torn cell surface: make way, lysosomes to the rescue. J. Cell Sci. *115*, 873–879. .

Medina, D.L., Fraldi, A., Bouche, V., Annunziata, F., Mansueto, G., Spampanato, C., Puri, C., Pignata, A., Martina, J.A., Sardiello, M., et al. (2011). Transcriptional activation of lysosomal exocytosis promotes cellular clearance. Dev. Cell *21*, 421–430. https://doi.org/10.1016/j.devcel.2011.07.016.

Medina, D.L., Di Paola, S., Peluso, I., Armani, A., De Stefani, D., Venditti, R., Montefusco, S., Scotto-Rosato, A., Prezioso, C., Forrester, A., et al. (2015). Lysosomal calcium signalling regulates autophagy through calcineurin and TFEB. Nat. Cell Biol. *17*, 288–299. https://doi.org/10.1038/ncb3114.

Melchionda, M., Pittman, J.K., Mayor, R., and Patel, S. (2016). Ca2+/H+ exchange by acidic organelles regulates cell migration in vivo. J. Cell Biol. *212*, 803–813. https://doi.org/10.1083/jcb.201510019.

Meng, Y., Heybrock, S., Neculai, D., and Saftig, P. (2020). Cholesterol Handling in Lysosomes and Beyond. Trends Cell Biol. *30*, 452–466. https://doi.org/10.1016/j.tcb.2020.02.007.

Mercier, V., Larios, J., Molinard, G., Goujon, A., Matile, S., Gruenberg, J., and Roux, A. (2020). Endosomal membrane tension regulates ESCRT-III-dependent intra-lumenal vesicle formation. Nat. Cell Biol. *22*, 947–959. https://doi.org/10.1038/s41556-020-0546-4.

Metchnikov, I. (1893). Lectures on the Comparative Pathology of Inflammation.

Meunier, F.A., and Gutiérrez, L.M. (2016). Captivating New Roles of F-Actin Cortex in Exocytosis and Bulk Endocytosis in Neurosecretory Cells. Trends Neurosci. *39*, 605–613. https://doi.org/10.1016/j.tins.2016.07.003.

Mijaljica, D., Prescott, M., and Devenish, R.J. (2011). Microautophagy in mammalian cells: revisiting a 40-year-old conundrum. Autophagy *7*, 673–682. https://doi.org/10.4161/auto.7.7.14733.

Miklavc, P., and Frick, M. (2020). Actin and Myosin in Non-Neuronal Exocytosis. Cells *9*, 1455. https://doi.org/10.3390/cells9061455.

Miklavc, P., Hecht, E., Hobi, N., Wittekindt, O.H., Dietl, P., Kranz, C., and Frick, M. (2012). Actin coating and compression of fused secretory vesicles are essential for surfactant secretion--a role for Rho, formins and myosin II. J. Cell Sci. *125*, 2765–2774. https://doi.org/10.1242/jcs.105262.

Milosevic, I., Sørensen, J.B., Lang, T., Krauss, M., Nagy, G., Haucke, V., Jahn, R., and Neher, E. (2005). Plasmalemmal phosphatidylinositol-4,5-bisphosphate level regulates the releasable vesicle pool size in chromaffin cells. J. Neurosci. Off. J. Soc. Neurosci. *25*, 2557–2565. https://doi.org/10.1523/JNEUROSCI.3761-04.2005.

Mindell, J.A. (2012). Lysosomal acidification mechanisms. Annu. Rev. Physiol. *74*, 69–86. https://doi.org/10.1146/annurev-physiol-012110-142317.

Misteli, T. (2001). The concept of self-organization in cellular architecture. J. Cell Biol. *155*, 181–186. https://doi.org/10.1083/jcb.200108110.

Monod, J. (1970). Le hasard et la nécessité: essai sur la philosophie naturelle de la biologie moderne (Éditions du Seuil).

Morales, J., Benavides-Piccione, R., Dar, M., Fernaud, I., Rodríguez, A., Anton-Sanchez, L., Bielza, C., Larrañaga, P., DeFelipe, J., and Yuste, R. (2014). Random Positions of Dendritic Spines in Human Cerebral Cortex. J. Neurosci. *34*, 10078–10084. https://doi.org/10.1523/JNEUROSCI.1085-14.2014.

Moran, P.A.P. (1950). Notes on Continuous Stochastic Phenomena. Biometrika *37*, 17–23. https://doi.org/10.2307/2332142.

Moreiras, H., Pereira, F.J.C., Neto, M.V., Bento-Lopes, L., Festas, T.C., Seabra, M.C., and Barral, D.C. (2020). The exocyst is required for melanin exocytosis from melanocytes and transfer to keratinocytes. Pigment Cell Melanoma Res. *33*, 366–371. https://doi.org/10.1111/pcmr.12840.

Morlot, S., Galli, V., Klein, M., Chiaruttini, N., Manzi, J., Humbert, F., Dinis, L., Lenz, M., Cappello, G., and Roux, A. (2012). Membrane Shape at the Edge of the Dynamin Helix Sets Location and Duration of the Fission Reaction. Cell *151*, 619–629. https://doi.org/10.1016/j.cell.2012.09.017.

Morris, C.E., and Homann, U. (2001). Cell Surface Area Regulation and Membrane Tension. J. Membr. Biol. *179*, 79–102. https://doi.org/10.1007/s002320010040.

Moya-Díaz, J., Bayonés, L., Montenegro, M., Cárdenas, A.M., Koch, H., Doi, A., and Marengo, F.D. (2020). Ca2+ -independent and voltage-dependent exocytosis in mouse chromaffin cells. Acta Physiol. Oxf. Engl. *228*, e13417. https://doi.org/10.1111/apha.13417.

Mullins, C. (2010). The Biogenesis of Cellular Organelles (Springer).

Murray, J.D. (1982). Parameter space for turing instability in reaction diffusion mechanisms: a comparison of models. J. Theor. Biol. *98*, 143–163. https://doi.org/10.1016/0022-5193(82)90063-7.

Murrell-Lagnado, R.D., and Frick, M. (2019). P2X4 and lysosome fusion. Curr. Opin. Pharmacol. *47*, 126–132. https://doi.org/10.1016/j.coph.2019.03.002.

Nambiar, R., McConnell, R.E., and Tyska, M.J. (2009). Control of cell membrane tension by myosin-I. Proc. Natl. Acad. Sci. U. S. A. *106*, 11972–11977. https://doi.org/10.1073/pnas.0901641106.

Nassoy, P., and Lamaze, C. (2012). Stressing caveolae new role in cell mechanics. Trends Cell Biol. *22*, 381–389. https://doi.org/10.1016/j.tcb.2012.04.007.

Ñeco, P., Fernández-Peruchena, C., Navas, S., Gutiérrez, L.M., de Toledo, G.Á., and Alés, E. (2008). Myosin II Contributes to Fusion Pore Expansion during Exocytosis*. J. Biol. Chem. *283*, 10949–10957. https://doi.org/10.1074/jbc.M709058200.

Nédélec, F., Surrey, T., and Maggs, A.C. (2001). Dynamic concentration of motors in microtubule arrays. Phys. Rev. Lett. *86*, 3192–3195. https://doi.org/10.1103/PhysRevLett.86.3192.

Needham, D., and Hochmuth, R.M. (1992). A sensitive measure of surface stress in the resting neutrophil. Biophys. J. *61*, 1664–1670. https://doi.org/10.1016/S0006-3495(92)81970-7.

Neefjes, J., Jongsma, M.M.L., and Berlin, I. (2017). Stop or Go? Endosome Positioning in the Establishment of Compartment Architecture, Dynamics, and Function. Trends Cell Biol. *27*, 580–594. https://doi.org/10.1016/j.tcb.2017.03.002.

Neiss, W.F. (1984). A coat of glycoconjugates on the inner surface of the lysosomal membrane in the rat kidney. Histochemistry *80*, 603–608. .

Neiss, W.F. (1986). Ultracytochemistry of intracellular membrane glycoconjugates. Adv. Anat. Embryol. Cell Biol. *99*, 1–92. https://doi.org/10.1007/978-3-642-71347-7.

Neveu, E., Khalifeh, D., Salamin, N., and Fasshauer, D. (2020). Prototypic SNARE Proteins Are Encoded in the Genomes of Heimdallarchaeota, Potentially Bridging the Gap between the Prokaryotes and Eukaryotes. Curr. Biol. CB *30*, 2468-2480.e5. https://doi.org/10.1016/j.cub.2020.04.060.

Neyman, J., and Scott, E.L. (1958). Statistical Approach to Problems of Cosmology. J. R. Stat. Soc. Ser. B Methodol. *20*, 1–43. .

Nguyen, X.X., and Zessin, H. (1977). Integral and differential characterizations of the Gibbs process. Adv. Appl. Probab. *9*, 446–447. https://doi.org/10.2307/1426106.

Nichol, J.A., and Hutter, O.F. (1996). Tensile strength and dilatational elasticity of giant sarcolemmal vesicles shed from rabbit muscle. J. Physiol. *493 (Pt 1)*, 187–198. https://doi.org/10.1113/jphysiol.1996.sp021374.

Nicovich, P.R., Owen, D.M., and Gaus, K. (2017). Turning single-molecule localization microscopy into a quantitative bioanalytical tool. Nat. Protoc. *12*, 453–460. https://doi.org/10.1038/nprot.2016.166.

Nightingale, T.D., Pattni, K., Hume, A.N., Seabra, M.C., and Cutler, D.F. (2009). Rab27a and MyRIP regulate the amount and multimeric state of VWF released from endothelial cells. Blood *113*, 5010–5018. https://doi.org/10.1182/blood-2008-09-181206.

Nightingale, T.D., White, I.J., Doyle, E.L., Turmaine, M., Harrison-Lavoie, K.J., Webb, K.F., Cramer, L.P., and Cutler, D.F. (2011). Actomyosin II contractility expels von Willebrand factor from Weibel–Palade bodies during exocytosis. J. Cell Biol. *194*, 613–629. https://doi.org/10.1083/jcb.201011119.

Nishimura, Y., Itoh, K., Yoshioka, K., Tokuda, K., and Himeno, M. (2003). Overexpression of ROCK in human breast cancer cells: evidence that ROCK activity mediates intracellular

membrane traffic of lysosomes. Pathol. Oncol. Res. POR *9*, 83–95. https://doi.org/PAOR.2003.9.2.0083.

Novick, P., and Schekman, R. (1979). Secretion and cell-surface growth are blocked in a temperature-sensitive mutant of Saccharomyces cerevisiae. Proc. Natl. Acad. Sci. U. S. A. *76*, 1858–1862. .

Novick, P., Field, C., and Schekman, R. (1980). Identification of 23 complementation groups required for post-translational events in the yeast secretory pathway. Cell *21*, 205–215. https://doi.org/10.1016/0092-8674(80)90128-2.

Novick, P., Ferro, S., and Schekman, R. (1981). Order of events in the yeast secretory pathway. Cell *25*, 461–469. https://doi.org/10.1016/0092-8674(81)90064-7.

Novikoff, A.B., Beaufay, H., and De Duve, C. (1956). Electron microscopy of lysosomerich fractions from rat liver. J. Biophys. Biochem. Cytol. *2*, 179–184. .

Obino, D., Diaz, J., Sáez, J.J., Ibañez-Vega, J., Sáez, P.J., Alamo, M., Lankar, D., and Yuseff, M.-I. (2017). Vamp-7-dependent secretion at the immune synapse regulates antigen extraction and presentation in B-lymphocytes. Mol. Biol. Cell *28*, 890–897. https://doi.org/10.1091/mbc.E16-10-0722.

Ohya, T., Miaczynska, M., Coskun, Ü., Lommer, B., Runge, A., Drechsel, D., Kalaidzidis, Y., and Zerial, M. (2009). Reconstitution of Rab- and SNARE-dependent membrane fusion by synthetic endosomes. Nature *459*, 1091–1097. https://doi.org/10.1038/nature08107.

Olivares, M.J., González-Jamett, A.M., Guerra, M.J., Baez-Matus, X., Haro-Acuña, V., Martínez-Quiles, N., and Cárdenas, A.M. (2014). Src Kinases Regulate De Novo Actin Polymerization during Exocytosis in Neuroendocrine Chromaffin Cells. PLOS ONE *9*, e99001. https://doi.org/10.1371/journal.pone.0099001.

Olsen, L.F., and Degn, H. (1977). Chaos in an enzyme reaction. Nature *267*, 177–178. https://doi.org/10.1038/267177a0.

Olsen, L.F., and Degn, H. (1985). Chaos in biological systems. Q. Rev. Biophys. *18*, 165–225. https://doi.org/10.1017/S0033583500005175.

Osaki, M., and Okada, F. (2019). Exosomes and Their Role in Cancer Progression. Yonago Acta Med. *62*, 182–190. https://doi.org/10.33160/yam.2019.06.002.

Ostrowski, M., Carmo, N.B., Krumeich, S., Fanget, I., Raposo, G., Savina, A., Moita, C.F., Schauer, K., Hume, A.N., Freitas, R.P., et al. (2010). Rab27a and Rab27b control different steps of the exosome secretion pathway. Nat. Cell Biol. *12*, 19–30; sup pp 1-13. https://doi.org/10.1038/ncb2000.

Pacheco, C.D., and Lieberman, A.P. (2008). The pathogenesis of Niemann-Pick type C disease: a role for autophagy? Expert Rev. Mol. Med. *10*, e26. https://doi.org/10.1017/S146239940800080X.

Pageon, S.V., Cordoba, S.-P., Owen, D.M., Rothery, S.M., Oszmiana, A., and Davis, D.M. (2013). Superresolution microscopy reveals nanometer-scale reorganization of inhibitory natural killer cell receptors upon activation of NKG2D. Sci. Signal. *6*, ra62. https://doi.org/10.1126/scisignal.2003947.

Palade, G. (1975). Intracellular aspects of the process of protein synthesis. Science *189*, 347–358. https://doi.org/10.1126/science.1096303.

Pang, Z.P., and Südhof, T.C. (2010). Cell Biology of Ca2+-Triggered Exocytosis. Curr. Opin. Cell Biol. *22*, 496–505. https://doi.org/10.1016/j.ceb.2010.05.001.

Pangarkar, C., Dinh, A.T., and Mitragotri, S. (2005). Dynamics and spatial organization of endosomes in mammalian cells. Phys. Rev. Lett. *95*, 158101. https://doi.org/10.1103/PhysRevLett.95.158101.

Pangarkar, C., Dinh, A.-T., and Mitragotri, S. (2012). Endocytic pathway rapidly delivers internalized molecules to lysosomes: an analysis of vesicle trafficking, clustering and mass transfer. J. Control. Release Off. J. Control. Release Soc. *162*, 76–83. https://doi.org/10.1016/j.jconrel.2012.05.022.

Papadopulos, A., Tomatis, V.M., Kasula, R., and Meunier, F.A. (2013). The cortical acto-Myosin network: from diffusion barrier to functional gateway in the transport of neurosecretory vesicles to the plasma membrane. Front. Endocrinol. *4*, 153. https://doi.org/10.3389/fendo.2013.00153.

Papangelou, F. (1974). The conditional intensity of general point processes and an application to line processes. Z. Für Wahrscheinlichkeitstheorie Verwandte Geb. *28*, 207–226. https://doi.org/10.1007/BF00533242.

Park, Y., and Ryu, J.-K. (2018). Models of synaptotagmin-1 to trigger Ca2+-dependent vesicle fusion. FEBS Lett. *592*, 3480–3492. https://doi.org/10.1002/1873-3468.13193.

Parpaite, T., and Coste, B. (2017). Piezo channels. Curr. Biol. CB *27*, R250–R252. https://doi.org/10.1016/j.cub.2017.01.048.

Parton, R.G., and Hancock, J.F. (2004). Lipid rafts and plasma membrane microorganization: insights from Ras. Trends Cell Biol. *14*, 141–147. https://doi.org/10.1016/j.tcb.2004.02.001.

Pécot, T., Zengzhen, L., Boulanger, J., Salamero, J., and Kervrann, C. (2018). A quantitative approach for analyzing the spatio-temporal distribution of 3D intracellular events in fluorescence microscopy. ELife *7*, e32311. https://doi.org/10.7554/eLife.32311.

Pelham, H.R. (1996). The dynamic organisation of the secretory pathway. Cell Struct. Funct. *21*, 413–419. https://doi.org/10.1247/csf.21.413.

Perin, M.S., Fried, V.A., Mignery, G.A., Jahn, R., and Südhof, T.C. (1990). Phospholipid binding by a synaptic vesicle protein homologous to the regulatory region of protein kinase C. Nature *345*, 260–263. https://doi.org/10.1038/345260a0.

Peters, P.J., Borst, J., Oorschot, V., Fukuda, M., Krähenbühl, O., Tschopp, J., Slot, J.W., and Geuze, H.J. (1991). Cytotoxic T lymphocyte granules are secretory lysosomes, containing both perforin and granzymes. J. Exp. Med. *173*, 1099–1109. https://doi.org/10.1084/jem.173.5.1099.

Pezzarossa, A., Zosel, F., and Schmidt, T. (2015). Visualization of HRas Domains in the Plasma Membrane of Fibroblasts. Biophys. J. *108*, 1870–1877. https://doi.org/10.1016/j.bpj.2015.03.006.

Pfeffer, S.R. (2019). NPC intracellular cholesterol transporter 1 (NPC1)-mediated cholesterol export from lysosomes. J. Biol. Chem. *294*, 1706–1709. https://doi.org/10.1074/jbc.TM118.004165.

Phillips, R., Kondev, J., Theriot, J., and Garcia, H. (2012). Physical Biology of the Cell (Boca Raton London New York: Garland Science).

Piazzolla, F., Mercier, V., Assies, L., Sakai, N., Roux, A., and Matile, S. (2021). Fluorescent Membrane Tension Probes for Early Endosomes. Angew. Chem. Int. Ed Engl. *60*, 12258–12263. https://doi.org/10.1002/anie.202016105.

Pinot, M., Vanni, S., Pagnotta, S., Lacas-Gervais, S., Payet, L.-A., Ferreira, T., Gautier, R., Goud, B., Antonny, B., and Barelli, H. (2014). Polyunsaturated phospholipids facilitate membrane deformation and fission by endocytic proteins. Science *345*, 693–697. https://doi.org/10.1126/science.1255288.

Platt, F.M., d'Azzo, A., Davidson, B.L., Neufeld, E.F., and Tifft, C.J. (2018). Lysosomal storage diseases. Nat. Rev. Dis. Primer *4*, 27. https://doi.org/10.1038/s41572-018-0025-4.

Pols, M.S., and Klumperman, J. (2009). Trafficking and function of the tetraspanin CD63. Exp. Cell Res. *315*, 1584–1592. https://doi.org/10.1016/j.yexcr.2008.09.020.

Pontes, B., Monzo, P., and Gauthier, N.C. (2017a). Membrane tension: A challenging but universal physical parameter in cell biology. Semin. Cell Dev. Biol. *71*, 30–41. https://doi.org/10.1016/j.semcdb.2017.08.030.

Pontes, B., Monzo, P., Gole, L., Le Roux, A.-L., Kosmalska, A.J., Tam, Z.Y., Luo, W., Kan, S., Viasnoff, V., Roca-Cusachs, P., et al. (2017b). Membrane tension controls adhesion positioning at the leading edge of cells. J. Cell Biol. *216*, 2959–2977. https://doi.org/10.1083/jcb.201611117.

Prior, I.A., Muncke, C., Parton, R.G., and Hancock, J.F. (2003). Direct visualization of Ras proteins in spatially distinct cell surface microdomains. J. Cell Biol. *160*, 165–170. https://doi.org/10.1083/jcb.200209091.

Proux-Gillardeaux, V., Raposo, G., Irinopoulou, T., and Galli, T. (2007). Expression of the Longin domain of TI-VAMP impairs lysosomal secretion and epithelial cell migration. Biol. Cell *99*, 261–271. https://doi.org/10.1042/BC20060097.

Pryor, P.R., Mullock, B.M., Bright, N.A., Lindsay, M.R., Gray, S.R., Richardson, S.C.W., Stewart, A., James, D.E., Piper, R.C., and Luzio, J.P. (2004). Combinatorial SNARE complexes with VAMP7 or VAMP8 define different late endocytic fusion events. EMBO Rep. *5*, 590–595. https://doi.org/10.1038/sj.embor.7400150.

Pu, J., Guardia, C.M., Keren-Kaplan, T., and Bonifacino, J.S. (2016). Mechanisms and functions of lysosome positioning. J. Cell Sci. *129*, 4329–4339. https://doi.org/10.1242/jcs.196287.

Pyrcz, M., and Deutsch, C. (2003). The whole story on the hole effect. Geostat. Assoc. Australas. Newsl. *18*. .

Rabanal-Ruiz, Y., Byron, A., Wirth, A., Madsen, R., Sedlackova, L., Hewitt, G., Nelson, G., Stingele, J., Wills, J.C., Zhang, T., et al. (2021). mTORC1 activity is supported by spatial association with focal adhesions. J. Cell Biol. *220*, e202004010. https://doi.org/10.1083/jcb.202004010.

Raiborg, C., Wenzel, E.M., Pedersen, N.M., Olsvik, H., Schink, K.O., Schultz, S.W., Vietri, M., Nisi, V., Bucci, C., Brech, A., et al. (2015). Repeated ER-endosome contacts promote endosome translocation and neurite outgrowth. Nature *520*, 234–238. https://doi.org/10.1038/nature14359.

Raucher, D., and Sheetz, M.P. (1999a). Characteristics of a membrane reservoir buffering membrane tension. Biophys. J. *77*, 1992–2002. .

Raucher, D., and Sheetz, M.P. (1999b). Membrane Expansion Increases Endocytosis Rate during Mitosis. J. Cell Biol. *144*, 497–506. https://doi.org/10.1083/jcb.144.3.497.

Rebsamen, M., Pochini, L., Stasyk, T., de Araújo, M.E.G., Galluccio, M., Kandasamy, R.K., Snijder, B., Fauster, A., Rudashevskaya, E.L., Bruckner, M., et al. (2015). SLC38A9 is a component of the lysosomal amino acid sensing machinery that controls mTORC1. Nature *519*, 477–481. https://doi.org/10.1038/nature14107.

Reed, M.C., and Blum, J.J. (1986). Theoretical analysis of radioactivity profiles during fast axonal transport: effects of deposition and turnover. Cell Motil. Cytoskeleton *6*, 620–627. https://doi.org/10.1002/cm.970060610.

Ren, Q., Barber, H.K., Crawford, G.L., Karim, Z.A., Zhao, C., Choi, W., Wang, C.-C., Hong, W., and Whiteheart, S.W. (2007). Endobrevin/VAMP-8 Is the Primary v-SNARE for the Platelet Release Reaction. Mol. Biol. Cell *18*, 24–33. https://doi.org/10.1091/mbc.E06-09-0785.

Rickman, C., Medine, C.N., Dun, A.R., Moulton, D.J., Mandula, O., Halemani, N.D., Rizzoli, S.O., Chamberlain, L.H., and Duncan, R.R. (2010). t-SNARE protein conformations patterned by the lipid microenvironment. J. Biol. Chem. *285*, 13535–13541. https://doi.org/10.1074/jbc.M109.091058.

Riggi, M., Niewola-Staszkowska, K., Chiaruttini, N., Colom, A., Kusmider, B., Mercier, V., Soleimanpour, S., Stahl, M., Matile, S., Roux, A., et al. (2018). Decrease in plasma membrane tension triggers PtdIns(4,5)P2 phase separation to inactivate TORC2. Nat. Cell Biol. *20*, 1043–1051. https://doi.org/10.1038/s41556-018-0150-z.

Riggi, M., Bourgoint, C., Macchione, M., Matile, S., Loewith, R., and Roux, A. (2019). TORC2 controls endocytosis through plasma membrane tension. J. Cell Biol. *218*, 2265–2276. https://doi.org/10.1083/jcb.201901096.

Riggi, M., Kusmider, B., and Loewith, R. (2020). The flipside of the TOR coin – TORC2 and plasma membrane homeostasis at a glance. J. Cell Sci. *133*, jcs242040. https://doi.org/10.1242/jcs.242040.

Ringuette Goulet, C., Bernard, G., Tremblay, S., Chabaud, S., Bolduc, S., and Pouliot, F. (2018). Exosomes Induce Fibroblast Differentiation into Cancer-Associated Fibroblasts through TGFβ Signaling. Mol. Cancer Res. MCR *16*, 1196–1204. https://doi.org/10.1158/1541-7786.MCR-17-0784.

Rink, J., Ghigo, E., Kalaidzidis, Y., and Zerial, M. (2005). Rab conversion as a mechanism of progression from early to late endosomes. Cell *122*, 735–749. https://doi.org/10.1016/j.cell.2005.06.043.

Ripley, B.D. (1976). The Second-Order Analysis of Stationary Point Processes. J. Appl. Probab. *13*, 255–266. https://doi.org/10.2307/3212829.

Ripley, B.D. (1977). Modelling Spatial Patterns. J. R. Stat. Soc. Ser. B Methodol. *39*, 172–212. .

Rituper, B., Flašker, A., Guček, A., Chowdhury, H.H., and Zorec, R. (2012). Cholesterol and regulated exocytosis: A requirement for unitary exocytotic events. Cell Calcium *52*, 250–258. https://doi.org/10.1016/j.ceca.2012.05.009.

Rituper, B., Guček, A., Lisjak, M., Gorska, U., Šakanović, A., Bobnar, S.T., Lasič, E., Božić, M., Abbineni, P.S., Jorgačevski, J., et al. (2020). Redistribution of cholesterol from vesicle to plasmalemma controls fusion pore geometry. 2020.04.06.027169. https://doi.org/10.1101/2020.04.06.027169.

Rivera-Molina, F., and Toomre, D. (2013). Live-cell imaging of exocyst links its spatiotemporal dynamics to various stages of vesicle fusion. J. Cell Biol. *201*, 673–680. https://doi.org/10.1083/jcb.201212103.

Rizo, J., and Südhof, T.C. (2002). Snares and munc18 in synaptic vesicle fusion. Nat. Rev. Neurosci. *3*, 641–653. https://doi.org/10.1038/nrn898.

Rocha, N., Kuijl, C., van der Kant, R., Janssen, L., Houben, D., Janssen, H., Zwart, W., and Neefjes, J. (2009). Cholesterol sensor ORP1L contacts the ER protein VAP to control Rab7–RILP–p150 ^{Glued} and late endosome positioning. J. Cell Biol. *185*, 1209–1225. https://doi.org/10.1083/jcb.200811005.

Roffay, C., Molinard, G., Kim, K., Urbanska, M., Andrade, V., Barbarasa, V., Nowak, P., Mercier, V., García-Calvo, J., Matile, S., et al. (2021). Passive coupling of membrane tension and cell volume during active response of cells to osmosis. Proc. Natl. Acad. Sci. *118*. https://doi.org/10.1073/pnas.2103228118.

Rojo Pulido, I., Nightingale, T.D., Darchen, F., Seabra, M.C., Cutler, D.F., and Gerke, V. (2011). Myosin Va acts in concert with Rab27a and MyRIP to regulate acute von-Willebrand factor release from endothelial cells. Traffic Cph. Den. *12*, 1371–1382. https://doi.org/10.1111/j.1600-0854.2011.01248.x.

Rouiller, C., and Bernhard, W. (1956). “MICROBODIES” AND THE PROBLEM OF MITOCHONDRIAL REGENERATION IN LIVER CELLS. J. Biophys. Biochem. Cytol. *2*, 355–360.
.

Ruan, Y., Yin, P., Li, F., Li, D., Lin, Q., and Li, K. (2019). The Accuracy of Determining Cluster Size by Analyzing Ripley’s K Function in Single Molecule Localization Microscopy. Appl. Sci. *9*, 3271. https://doi.org/10.3390/app9163271.

Rubinow, S.I., and Blum, J.J. (1980). A theoretical approach to the analysis of axonal transport. Biophys. J. *30*, 137–147. https://doi.org/10.1016/S0006-3495(80)85082-X.

Rudnik, S., and Damme, M. (2021). The lysosomal membrane-export of metabolites and beyond. FEBS J. *288*, 4168–4182. https://doi.org/10.1111/febs.15602.

Sabatini, D.D., and Adesnik, M. (2013). Christian de Duve: Explorer of the cell who discovered new organelles by using a centrifuge. Proc. Natl. Acad. Sci. U. S. A. *110*, 13234–13235. https://doi.org/10.1073/pnas.1312084110.

Sáez, J.J., Diaz, J., Ibañez, J., Bozo, J.P., Cabrera Reyes, F., Alamo, M., Gobert, F.-X., Obino, D., Bono, M.R., Lennon-Duménil, A.-M., et al. (2019). The exocyst controls lysosome secretion and antigen extraction at the immune synapse of B cells. J. Cell Biol. *218*, 2247–2264. https://doi.org/10.1083/jcb.201811131.

Saftig, P., and Klumperman, J. (2009). Lysosome biogenesis and lysosomal membrane proteins: trafficking meets function. Nat. Rev. Mol. Cell Biol. *10*, 623–635. https://doi.org/10.1038/nrm2745.

Saha, S., Nagy, T.L., and Weiner, O.D. (2018). Joining forces: crosstalk between biochemical signalling and physical forces orchestrates cellular polarity and dynamics. Philos. Trans. R. Soc. B Biol. Sci. *373*, 20170145. https://doi.org/10.1098/rstb.2017.0145.

Saleem, M., Morlot, S., Hohendahl, A., Manzi, J., Lenz, M., and Roux, A. (2015). A balance between membrane elasticity and polymerization energy sets the shape of spherical clathrin coats. Nat. Commun. *6*, 6249. https://doi.org/10.1038/ncomms7249.

Samacoits, A., Chouaib, R., Safieddine, A., Traboulsi, A.-M., Ouyang, W., Zimmer, C., Peter, M., Bertrand, E., Walter, T., and Mueller, F. (2018). A computational framework to study sub-cellular RNA localization. Nat. Commun. *9*, 4584. https://doi.org/10.1038/s41467-018-06868-w.

Samie, M.A., and Xu, H. (2014). Lysosomal exocytosis and lipid storage disorders. J. Lipid Res. *55*, 995–1009. https://doi.org/10.1194/jlr.R046896.

Schauer, K., Duong, T., Bleakley, K., Bardin, S., Bornens, M., and Goud, B. (2010a). Probabilistic density maps to study global endomembrane organization. Nat. Methods *7*, 560–566. https://doi.org/10.1038/nmeth.1462.

Schauer, K., Duong, T., Bleakley, K., Bardin, S., Bornens, M., and Goud, B. (2010b). Probabilistic density maps to study global endomembrane organization. Nat. Methods *7*, 560–566. https://doi.org/10.1038/nmeth.1462.

Schauer, K., Grossier, J.-P., Duong, T., Chapuis, V., Degot, S., Lescure, A., Del Nery, E., and Goud, B. (2014). A Novel Organelle Map Framework for High-Content Cell Morphology Analysis in High Throughput. SLAS Discov. *19*, 317–324. https://doi.org/10.1177/1087057113497399.

Schekman, R., and Novick, P. (2004). 23 genes, 23 years later. Cell *116*, S13-15, 1 p following S19. https://doi.org/10.1016/s0092-8674(03)00972-3.

Schiavo, G.G., Benfenati, F., Poulain, B., Rossetto, O., de Laureto, P.P., DasGupta, B.R., and Montecucco, C. (1992). Tetanus and botulinum-B neurotoxins block neurotransmitter release by proteolytic cleavage of synaptobrevin. Nature *359*, 832–835. https://doi.org/10.1038/359832a0.

Schiefermeier, N., Scheffler, J.M., de Araujo, M.E.G., Stasyk, T., Yordanov, T., Ebner, H.L., Offterdinger, M., Munck, S., Hess, M.W., Wickström, S.A., et al. (2014). The late endosomal p14-MP1 (LAMTOR2/3) complex regulates focal adhesion dynamics during cell migration. J. Cell Biol. *205*, 525–540. https://doi.org/10.1083/jcb.201310043.

Schmoranzer, J., Goulian, M., Axelrod, D., and Simon, S.M. (2000). Imaging Constitutive Exocytosis with Total Internal Reflection Fluorescence Microscopy. J. Cell Biol. *149*, 23–32. .

Schröder, B.A., Wrocklage, C., Hasilik, A., and Saftig, P. (2010). The proteome of lysosomes. Proteomics *10*, 4053–4076. https://doi.org/10.1002/pmic.201000196.

Schwanhäusser, B., Busse, D., Li, N., Dittmar, G., Schuchhardt, J., Wolf, J., Chen, W., and Selbach, M. (2011). Global quantification of mammalian gene expression control. Nature *473*, 337–342. https://doi.org/10.1038/nature10098.

Schweitzer, Y., Lieber, A.D., Keren, K., and Kozlov, M.M. (2014). Theoretical Analysis of Membrane Tension in Moving Cells. Biophys. J. *106*, 84–92. https://doi.org/10.1016/j.bpj.2013.11.009.

Scotto Rosato, A., Montefusco, S., Soldati, C., Di Paola, S., Capuozzo, A., Monfregola, J., Polishchuk, E., Amabile, A., Grimm, C., Lombardo, A., et al. (2019). TRPML1 links lysosomal calcium to autophagosome biogenesis through the activation of the CaMKKβ/VPS34 pathway. Nat. Commun. *10*, 5630. https://doi.org/10.1038/s41467-019-13572-w.

Sebastian, R., Diaz, M.-E., Ayala, G., Letinic, K., Moncho-Bogani, J., and Toomre, D. (2006). Spatio-temporal analysis of constitutive exocytosis in epithelial cells. IEEE/ACM Trans. Comput. Biol. Bioinform. *3*, 17–32. https://doi.org/10.1109/TCBB.2006.11.

Segura, J., Gil, A., and Soria, B. (2000). Modeling study of exocytosis in neuroendocrine cells: influence of the geometrical parameters. Biophys. J. *79*, 1771–1786. .

Seilacher, A. (1970). Arbeitskonzept Zur Konstruktions-Morphologie. Lethaia *3*, 393–396. https://doi.org/10.1111/j.1502-3931.1970.tb00830.x.

Sekimura, T., Venkataraman, C., and Madzvamuse, A. (2015). A Model for Selection of Eyespots on Butterfly Wings. PLOS ONE *10*, e0141434. https://doi.org/10.1371/journal.pone.0141434.

Sel'kov, E.E. (1968). Self-Oscillations in Glycolysis 1. A Simple Kinetic Model. Eur. J. Biochem. *4*, 79–86. https://doi.org/10.1111/j.1432-1033.1968.tb00175.x.

Sens, P., and Plastino, J. (2015). Membrane tension and cytoskeleton organization in cell motility. J. Phys. Condens. Matter Inst. Phys. J. *27*, 273103. https://doi.org/10.1088/0953-8984/27/27/273103.

Settembre, C., and Medina, D.L. (2015). Chapter 3 - TFEB and the CLEAR network. In Methods in Cell Biology, F. Platt, and N. Platt, eds. (Academic Press), pp. 45–62.

Shang, S., Zhu, F., Liu, B., Chai, Z., Wu, Q., Hu, M., Wang, Y., Huang, R., Zhang, X., Wu, X., et al. (2016). Intracellular TRPA1 mediates Ca2+ release from lysosomes in dorsal root ganglion neurons. J. Cell Biol. *215*, 369–381. https://doi.org/10.1083/jcb.201603081.

Shen, D., Wang, X., Li, X., Zhang, X., Yao, Z., Dibble, S., Dong, X., Yu, T., Lieberman, A.P., Showalter, H.D., et al. (2012). Lipid storage disorders block lysosomal trafficking by inhibiting a TRP channel and lysosomal calcium release. Nat. Commun. *3*, 731. https://doi.org/10.1038/ncomms1735.

Shen, Y.-T., Gu, Y., Su, W.-F., Zhong, J.-F., Jin, Z.-H., Gu, X.-S., and Chen, G. (2016). Rab27b is Involved in Lysosomal Exocytosis and Proteolipid Protein Trafficking in Oligodendrocytes. Neurosci. Bull. *32*, 331–340. https://doi.org/10.1007/s12264-016-0045-6.

Shi, Z., Graber, Z.T., Baumgart, T., Stone, H.A., and Cohen, A.E. (2018). Cell Membranes Resist Flow. Cell *175*, 1769-1779.e13. https://doi.org/10.1016/j.cell.2018.09.054.

Shillcock, J.C., and Lipowsky, R. (2005). Tension-induced fusion of bilayer membranes and vesicles. Nat. Mater. *4*, 225–228. https://doi.org/10.1038/nmat1333.

Shin, H.R., and Zoncu, R. (2020). The Lysosome at the Intersection of Cellular Growth and Destruction. Dev. Cell *54*, 226–238. https://doi.org/10.1016/j.devcel.2020.06.010.

Shin, W., Ge, L., Arpino, G., Villarreal, S.A., Hamid, E., Liu, H., Zhao, W.-D., Wen, P.J., Chiang, H.-C., and Wu, L.-G. (2018). Visualization of Membrane Pore in Live Cells Reveals a Dynamic-Pore Theory Governing Fusion and Endocytosis. Cell *173*, 934-945.e12. https://doi.org/10.1016/j.cell.2018.02.062.

Shitara, A., and Weigert, R. (2015). Imaging Membrane Remodeling During Regulated Exocytosis in Live Mice. Exp. Cell Res. *337*, 219–225. https://doi.org/10.1016/j.yexcr.2015.06.018.

Shuai, J., and Parker, I. (2005). Optical single-channel recording by imaging Ca2+ flux through individual ion channels: theoretical considerations and limits to resolution. Cell Calcium *37*, 283–299. https://doi.org/10.1016/j.ceca.2004.10.008.

Sinha, B., Köster, D., Ruez, R., Gonnord, P., Bastiani, M., Abankwa, D., Stan, R.V., Butler-Browne, G., Vedie, B., Johannes, L., et al. (2011). Cells Respond to Mechanical Stress by Rapid Disassembly of Caveolae. Cell *144*, 402–413. https://doi.org/10.1016/j.cell.2010.12.031.

Sitarska, E., and Diz-Muñoz, A. (2020). Pay attention to membrane tension: Mechanobiology of the cell surface. Curr. Opin. Cell Biol. *66*, 11–18. https://doi.org/10.1016/j.ceb.2020.04.001.

Slepchenko, B.M., Schaff, J.C., Carson, J.H., and Loew, L.M. (2002). Computational cell biology: spatiotemporal simulation of cellular events. Annu. Rev. Biophys. Biomol. Struct. *31*, 423–441. https://doi.org/10.1146/annurev.biophys.31.101101.140930.

Slepchenko, B.M., Semenova, I., Zaliapin, I., and Rodionov, V. (2007). Switching of membrane organelles between cytoskeletal transport systems is determined by regulation of the microtubule-based transport. J. Cell Biol. *179*, 635–641. https://doi.org/10.1083/jcb.200705146.

Smith, D.A., and Simmons, R.M. (2001). Models of motor-assisted transport of intracellular particles. Biophys. J. *80*, 45–68. .

Smith, D.E., Clémençon, B., and Hediger, M.A. (2013). Proton-coupled oligopeptide transporter family SLC15: physiological, pharmacological and pathological implications. Mol. Aspects Med. *34*, 323–336. https://doi.org/10.1016/j.mam.2012.11.003.

Sokac, A.M., and Bement, W.M. (2006). Kiss-and-Coat and Compartment Mixing: Coupling Exocytosis to Signal Generation and Local Actin Assembly. Mol. Biol. Cell *17*, 1495–1502. https://doi.org/10.1091/mbc.e05-10-0908.

Soleimanpour, S., Colom, A., Derivery, E., Gonzalez-Gaitan, M., Roux, A., Sakai, N., and Matile, S. (2016). Headgroup engineering in mechanosensitive membrane probes. Chem. Commun. *52*, 14450–14453. https://doi.org/10.1039/C6CC08771J.

Söllner, T., Whiteheart, S.W., Brunner, M., Erdjument-Bromage, H., Geromanos, S., Tempst, P., and Rothman, J.E. (1993). SNAP receptors implicated in vesicle targeting and fusion. Nature *362*, 318–324. https://doi.org/10.1038/362318a0.

Soni, L.E., Warren, C.M., Bucci, C., Orten, D.J., and Hasson, T. (2005). The unconventional myosin-VIIa associates with lysosomes. Cell Motil. Cytoskeleton *62*, 13–26. https://doi.org/10.1002/cm.20080.

Sotelo, J.R., and Porter, K.R. (1959). An electron microscope study of the rat ovum. J. Biophys. Biochem. Cytol. *5*, 327–342. https://doi.org/10.1083/jcb.5.2.327.

Spitz, C., Schlosser, C., Guschtschin-Schmidt, N., Stelzer, W., Menig, S., Götz, A., Haug-Kröper, M., Scharnagl, C., Langosch, D., Muhle-Goll, C., et al. (2020). Non-canonical Shedding of TNFα by SPPL2a Is Determined by the Conformational Flexibility of Its Transmembrane Helix. IScience *23*, 101775. https://doi.org/10.1016/j.isci.2020.101775.

Steffen A, Le Dez G, Poincloux R, Recchi C, Nassoy P, Rottner K, Galli T, and Chavrier P (2008). MT1-MMP-dependent invasion is regulated by TI-VAMP/VAMP7. Curr. Biol.

Stehbens, S.J., Paszek, M., Pemble, H., Ettinger, A., Gierke, S., and Wittmann, T. (2014). CLASPs link focal-adhesion-associated microtubule capture to localized exocytosis and adhesion site turnover. Nat. Cell Biol. *16*, 561–573. https://doi.org/10.1038/ncb2975.

Stenmark, H. (2009). Rab GTPases as coordinators of vesicle traffic. Nat. Rev. Mol. Cell Biol. *10*, 513–525. https://doi.org/10.1038/nrm2728.

Stephens, D.C., Osunsanmi, N., Sochacki, K.A., Powell, T.W., Taraska, J.W., and Harris, D.A. (2019). Spatiotemporal organization and protein dynamics involved in regulated exocytosis of MMP-9 in breast cancer cells. J. Gen. Physiol. *151*, 1386–1403. https://doi.org/10.1085/jgp.201812299.

Storrie, B., and Desjardins, M. (1996). The biogenesis of lysosomes: is it a kiss and run, continuous fusion and fission process? BioEssays News Rev. Mol. Cell. Dev. Biol. *18*, 895–903. https://doi.org/10.1002/bies.950181108.

Straková, K., López-Andarias, J., Jiménez-Rojo, N., Chambers, J.E., Marciniak, S.J., Riezman, H., Sakai, N., and Matile, S. (2020). HaloFlippers: A General Tool for the Fluorescence Imaging of Precisely Localized Membrane Tension Changes in Living Cells. ACS Cent. Sci. *6*, 1376–1385. https://doi.org/10.1021/acscentsci.0c00666.

Stratton, B.S., Warner, J.M., Wu, Z., Nikolaus, J., Wei, G., Wagnon, E., Baddeley, D., Karatekin, E., and O'Shaughnessy, B. (2016). Cholesterol Increases the Openness of SNARE-Mediated Flickering Fusion Pores. Biophys. J. *110*, 1538–1550. https://doi.org/10.1016/j.bpj.2016.02.019.

Strauss, D.J. (1975). A model for clustering. Biometrika *62*, 467–475. https://doi.org/10.1093/biomet/62.2.467.

Strauss, W. (1954). Isolation and biochemical properties of droplets from the cells of rat kidney. Jouurnal Biol. Chem.

Stroupe, C., Hickey, C.M., Mima, J., Burfeind, A.S., and Wickner, W. (2009). Minimal membrane docking requirements revealed by reconstitution of Rab GTPase-dependent membrane fusion from purified components. Proc. Natl. Acad. Sci. *106*, 17626–17633. https://doi.org/10.1073/pnas.0903801106.

Südhof, T.C. (2012). The Presynaptic Active Zone. Neuron *75*, 11–25. https://doi.org/10.1016/j.neuron.2012.06.012.

Südhof, T.C., and Rothman, J.E. (2009). Membrane Fusion: Grappling with SNARE and SM Proteins. Science *323*, 474–477. https://doi.org/10.1126/science.1161748.

Südhof, T.C., Baumert, M., Perin, M.S., and Jahn, R. (1989). A synaptic vesicle membrane protein is conserved from mammals to Drosophila. Neuron *2*, 1475–1481. https://doi.org/10.1016/0896-6273(89)90193-1.

Sun, W., Tian, B.-X., Wang, S.-H., Liu, P.-J., and Wang, Y.-C. (2020). The function of SEC22B and its role in human diseases. Cytoskeleton *77*, 303–312. https://doi.org/10.1002/cm.21628.

Sung, B.H., Zhu, X., Kaverina, I., and Weaver, A.M. (2011). Cortactin Controls Cell Motility and Lamellipodial Dynamics by Regulating ECM Secretion. Curr. Biol. *21*, 1460–1469. https://doi.org/10.1016/j.cub.2011.06.065.

Sutton, R.B., Fasshauer, D., Jahn, R., and Brunger, A.T. (1998). Crystal structure of a SNARE complex involved in synaptic exocytosis at 2.4 A resolution. Nature *395*, 347–353. https://doi.org/10.1038/26412.

Syeda, R., Qiu, Z., Dubin, A.E., Murthy, S.E., Florendo, M.N., Mason, D.E., Mathur, J., Cahalan, S.M., Peters, E.C., Montal, M., et al. (2016). LRRC8 Proteins Form Volume-Regulated Anion Channels that Sense Ionic Strength. Cell *164*, 499–511. https://doi.org/10.1016/j.cell.2015.12.031.

Tam, C., Idone, V., Devlin, C., Fernandes, M.C., Flannery, A., He, X., Schuchman, E., Tabas, I., and Andrews, N.W. (2010). Exocytosis of acid sphingomyelinase by wounded cells promotes endocytosis and plasma membrane repair. J. Cell Biol. *189*, 1027–1038. https://doi.org/10.1083/jcb.201003053.

Tan, R., Foster, P.J., Needleman, D.J., and McKenney, R.J. (2018). Cooperative Accumulation of Dynein-Dynactin at Microtubule Minus-Ends Drives Microtubule Network Reorganization. Dev. Cell *44*, 233-247.e4. https://doi.org/10.1016/j.devcel.2017.12.023.

Tancini, B., Buratta, S., Delo, F., Sagini, K., Chiaradia, E., Pellegrino, R.M., Emiliani, C., and Urbanelli, L. (2020). Lysosomal Exocytosis: The Extracellular Role of an Intracellular Organelle. Membranes *10*, E406. https://doi.org/10.3390/membranes10120406.

Tarafder, A.K., Bolasco, G., Correia, M.S., Pereira, F.J.C., Iannone, L., Hume, A.N., Kirkpatrick, N., Picardo, M., Torrisi, M.R., Rodrigues, I.P., et al. (2014). Rab11b mediates melanin transfer between donor melanocytes and acceptor keratinocytes via coupled exo/endocytosis. J. Invest. Dermatol. *134*, 1056–1066. https://doi.org/10.1038/jid.2013.432.

Tarnita, C.E. (2018). Ecology: Termite Patterning at Multiple Scales. Curr. Biol. *28*, R1394–R1396. https://doi.org/10.1016/j.cub.2018.10.058.

Tekirdag, K., and Cuervo, A.M. (2018). Chaperone-mediated autophagy and endosomal microautophagy: Joint by a chaperone. J. Biol. Chem. *293*, 5414–5424. https://doi.org/10.1074/jbc.R117.818237.

Teng, J., Loukin, S., Anishkin, A., and Kung, C. (2015). The Force-From-Lipid (FFL) principle of mechanosensitivity, at large and in elements. Pflugers Arch. *467*, 27–37. https://doi.org/10.1007/s00424-014-1530-2.

Théry, M., Racine, V., Piel, M., Pépin, A., Dimitrov, A., Chen, Y., Sibarita, J.-B., and Bornens, M. (2006a). Anisotropy of cell adhesive microenvironment governs cell internal organization and orientation of polarity. Proc. Natl. Acad. Sci. *103*, 19771–19776. https://doi.org/10.1073/pnas.0609267103.

Théry, M., Pépin, A., Dressaire, E., Chen, Y., and Bornens, M. (2006b). Cell distribution of stress fibres in response to the geometry of the adhesive environment. Cell Motil. *63*, 341–355. https://doi.org/10.1002/cm.20126.

Thomas, M. (1949). A Generalization of Poisson's Binomial Limit For use in Ecology. Biometrika *36*, 18–25. https://doi.org/10.2307/2332526.

Thottacherry, J.J., Kosmalska, A.J., Kumar, A., Vishen, A.S., Elosegui-Artola, A., Pradhan, S., Sharma, S., Singh, P.P., Guadamillas, M.C., Chaudhary, N., et al. (2018). Mechanochemical feedback control of dynamin independent endocytosis modulates membrane tension in adherent cells. Nat. Commun. *9*, 4217. https://doi.org/10.1038/s41467-018-06738-5.

Tomatis, V.M., Papadopulos, A., Malintan, N.T., Martin, S., Wallis, T., Gormal, R.S., Kendrick-Jones, J., Buss, F., and Meunier, F.A. (2013). Myosin VI small insert isoform maintains exocytosis by tethering secretory granules to the cortical actin. J. Cell Biol. *200*, 301–320. https://doi.org/10.1083/jcb.201204092.

Torisawa, T., Ichikawa, M., Furuta, A., Saito, K., Oiwa, K., Kojima, H., Toyoshima, Y.Y., and Furuta, K. (2014). Autoinhibition and cooperative activation mechanisms of cytoplasmic dynein. Nat. Cell Biol. *16*, 1118–1124. https://doi.org/10.1038/ncb3048.

Tran, D.T., and Ten Hagen, K.G. (2017). Real-time insights into regulated exocytosis. J. Cell Sci. *130*, 1355–1363. https://doi.org/10.1242/jcs.193425.

Tran, D.T., Masedunskas, A., Weigert, R., and Ten Hagen, K.G. (2015). Arp2/3-mediated F-actin formation controls regulated exocytosis in vivo. Nat. Commun. *6*, 10098. https://doi.org/10.1038/ncomms10098.

Trapani, J.A. (2012). Granzymes, cytotoxic granules and cell death: the early work of Dr. Jurg Tschopp. Cell Death Differ. *19*, 21–27. https://doi.org/10.1038/cdd.2011.156.

Trimble, W.S., Cowan, D.M., and Scheller, R.H. (1988). VAMP-1: a synaptic vesicle-associated integral membrane protein. Proc. Natl. Acad. Sci. *85*, 4538–4542. https://doi.org/10.1073/pnas.85.12.4538.

Turing, A.M. (1952). The chemical basis of morphogenesis. Philos. Trans. R. Soc. Lond. B. Biol. Sci. *237*, 37–72. https://doi.org/10.1098/rstb.1952.0012.

Umbrecht-Jenck, E., Demais, V., Calco, V., Bailly, Y., Bader, M.-F., and Chasserot-Golaz, S. (2010). S100A10-mediated translocation of annexin-A2 to SNARE proteins in adrenergic chromaffin cells undergoing exocytosis. Traffic Cph. Den. *11*, 958–971. https://doi.org/10.1111/j.1600-0854.2010.01065.x.

Urbina, F.L., and Gupton, S.L. (2020). SNARE-Mediated Exocytosis in Neuronal Development. Front. Mol. Neurosci. *13*, 133. https://doi.org/10.3389/fnmol.2020.00133.

Urbina, F.L., Gomez, S.M., and Gupton, S.L. (2018). Spatiotemporal organization of exocytosis emerges during neuronal shape change. J. Cell Biol. *217*, 1113–1128. https://doi.org/10.1083/jcb.201709064.

Urbina, F.L., Menon, S., Goldfarb, D., Edwards, R., Ben Major, M., Brennwald, P., and Gupton, S.L. (2021). TRIM67 regulates exocytic mode and neuronal morphogenesis via SNAP47. Cell Rep. *34*, 108743. https://doi.org/10.1016/j.celrep.2021.108743.

Vaes, G. (1968). ON THE MECHANISMS OF BONE RESORPTION : The Action of Parathyroid Hormone on the Excretion and Synthesis of Lysosomal Enzymes and on the Extracellular Release of Acid by Bone Cells. J. Cell Biol. *39*, 676–697. https://doi.org/10.1083/jcb.39.3.676.

Vagne, Q., Vrel, J.-P., and Sens, P. (2020). A minimal self-organisation model of the Golgi apparatus. ELife *9*, e47318. https://doi.org/10.7554/eLife.47318.

Vaidžiulytė, K., Coppey, M., and Schauer, K. (2019). Intracellular organization in cell polarity - placing organelles into the polarity loop. J. Cell Sci. *132*, jcs230995. https://doi.org/10.1242/jcs.230995.

Valm, A.M., Cohen, S., Legant, W.R., Melunis, J., Hershberg, U., Wait, E., Cohen, A.R., Davidson, M.W., Betzig, E., and Lippincott-Schwartz, J. (2017). Applying systems-level spectral imaging and analysis to reveal the organelle interactome. Nature *546*, 162–167. https://doi.org/10.1038/nature22369.

Vasilyeva, L.N., and Stephenson, S.L. (2013). An Essentialistic View of the Species Problem (IntechOpen).

Venkova, L., Vishen, A.S., Lembo, S., Srivastava, N., Duchamp, B., Ruppel, A., Williart, A., Vassilopoulos, S., Deslys, A., Garcia Arcos, J.M., et al. (2022). A mechano-osmotic feedback couples cell volume to the rate of cell deformation. ELife *11*, e72381. https://doi.org/10.7554/eLife.72381.

Verderio, C., Cagnoli, C., Bergami, M., Francolini, M., Schenk, U., Colombo, A., Riganti, L., Frassoni, C., Zuccaro, E., Danglot, L., et al. (2012). TI-VAMP/VAMP7 is the SNARE of secretory lysosomes contributing to ATP secretion from astrocytes. Biol. Cell *104*, 213–228. https://doi.org/10.1111/boc.201100070.

Verweij, F.J., Bebelman, M.P., Jimenez, C.R., Garcia-Vallejo, J.J., Janssen, H., Neefjes, J., Knol, J.C., de Goeij-de Haas, R., Piersma, S.R., Baglio, S.R., et al. (2018). Quantifying exosome secretion from single cells reveals a modulatory role for GPCR signaling. J. Cell Biol. *217*, 1129–1142. https://doi.org/10.1083/jcb.201703206.

Vestre, K., Persiconi, I., Borg Distefano, M., Mensali, N., Guadagno, N.A., Bretou, M., Wälchli, S., Arnold-Schrauf, C., Bakke, O., Dalod, M., et al. (2021). Rab7b regulates dendritic cell migration by linking lysosomes to the actomyosin cytoskeleton. J. Cell Sci. *134*, jcs259221. https://doi.org/10.1242/jcs.259221.

Villanueva, J., Viniegra, S., Gimenez-Molina, Y., García-Martinez, V., Expósito-Romero, G., del Mar Frances, M., García-Sancho, J., and Gutiérrez, L.M. (2014). The position of mitochondria and ER in relation to that of the secretory sites in chromaffin cells. J. Cell Sci. *127*, 5105–5114. https://doi.org/10.1242/jcs.160242.

Vogel, K., and Roche, P.A. (1999). SNAP-23 and SNAP-25 are palmitoylated in vivo. Biochem. Biophys. Res. Commun. *258*, 407–410. https://doi.org/10.1006/bbrc.1999.0652.

Vogel, G.F., Klee, K.M.C., Janecke, A.R., Müller, T., Hess, M.W., and Huber, L.A. (2015). Cargo-selective apical exocytosis in epithelial cells is conducted by Myo5B, Slp4a, Vamp7, and Syntaxin 3. J. Cell Biol. *211*, 587–604. https://doi.org/10.1083/jcb.201506112.

Vonaesch, P., Cardini, S., Sellin, M.E., Goud, B., Hardt, W.-D., and Schauer, K. (2013). Quantitative insights into actin rearrangements and bacterial target site selection from Salmonella Typhimurium infection of micropatterned cells. Cell. Microbiol. *15*, 1851–1865. https://doi.org/10.1111/cmi.12154.

Waddington, C.H. (1968). Towards a theoretical biology. Nature *218*, 525–527. https://doi.org/10.1038/218525a0.

Wade, N., Bryant, N.J., Connolly, L.M., Simpson, R.J., Luzio, J.P., Piper, R.C., and James, D.E. (2001). Syntaxin 7 Complexes with Mouse Vps10p Tail Interactor 1b, Syntaxin 6, Vesicle-associated Membrane Protein (VAMP)8, and VAMP7 in B16 Melanoma Cells*. J. Biol. Chem. *276*, 19820–19827. https://doi.org/10.1074/jbc.M010838200.

Walton, Z.E., Patel, C.H., Brooks, R.C., Yu, Y., Ibrahim-Hashim, A., Riddle, M., Porcu, A., Jiang, T., Ecker, B.L., Tameire, F., et al. (2018). Acid Suspends the Circadian Clock in Hypoxia through Inhibition of mTOR. Cell *174*, 72-87.e32. https://doi.org/10.1016/j.cell.2018.05.009.

Wang, G., and Galli, T. (2018). Reciprocal link between cell biomechanics and exocytosis. Traffic *19*, 741–749. https://doi.org/10.1111/tra.12584.

Wang, F., Gómez-Sintes, R., and Boya, P. (2018a). Lysosomal membrane permeabilization and cell death. Traffic Cph. Den. *19*, 918–931. https://doi.org/10.1111/tra.12613.

Wang, G., Nola, S., Bovio, S., Bun, P., Coppey-Moisan, M., Lafont, F., and Galli, T. (2018b). Biomechanical Control of Lysosomal Secretion Via the VAMP7 Hub: A Tug-of-War between VARP and LRRK1. IScience *4*, 127–143. https://doi.org/10.1016/j.isci.2018.05.016.

Wang, S., Tsun, Z.-Y., Wolfson, R.L., Shen, K., Wyant, G.A., Plovanich, M.E., Yuan, E.D., Jones, T.D., Chantranupong, L., Comb, W., et al. (2015). Metabolism. Lysosomal amino acid transporter SLC38A9 signals arginine sufficiency to mTORC1. Science *347*, 188–194. https://doi.org/10.1126/science.1257132.

Wang, S., Li, Y., Gong, J., Ye, S., Yang, X., Zhang, R., and Ma, C. (2019). Munc18 and Munc13 serve as a functional template to orchestrate neuronal SNARE complex assembly. Nat. Commun. *10*, 69. https://doi.org/10.1038/s41467-018-08028-6.

Wang, W., Zhang, X., Gao, Q., and Xu, H. (2014). TRPML1: an ion channel in the lysosome. Handb. Exp. Pharmacol. *222*, 631–645. https://doi.org/10.1007/978-3-642-54215-2_24.

Wang, W., Zhang, X., Gao, Q., Lawas, M., Yu, L., Cheng, X., Gu, M., Sahoo, N., Li, X., Li, P., et al. (2017). A voltage-dependent K+ channel in the lysosome is required for refilling lysosomal Ca2+ stores. J. Cell Biol. *216*, 1715–1730. https://doi.org/10.1083/jcb.201612123.

Wang, Y., Foo, L.Y., Guo, K., Gan, B.Q., Zeng, Q., Hong, W., and Tang, B.L. (2006). Syntaxin 9 is enriched in skin hair follicle epithelium and interacts with the epidermal growth factor receptor. Traffic Cph. Den. *7*, 216–226. https://doi.org/10.1111/j.1600-0854.2005.00378.x.

Ward, D.M., Pevsner, J., Scullion, M.A., Vaughn, M., and Kaplan, J. (2000). Syntaxin 7 and VAMP-7 are soluble N-ethylmaleimide-sensitive factor attachment protein receptors required for late endosome-lysosome and homotypic lysosome fusion in alveolar macrophages. Mol. Biol. Cell *11*, 2327–2333. https://doi.org/10.1091/mbc.11.7.2327.

Warner, J.D., Peters, C.G., Saunders, R., Won, J.H., Betzenhauser, M.J., Gunning, W.T., Yule, D.I., and Giovannucci, D.R. (2008). Visualizing form and function in organotypic slices of the

adult mouse parotid gland. Am. J. Physiol. Gastrointest. Liver Physiol. *295*, G629-640. https://doi.org/10.1152/ajpgi.90217.2008.

Wedlich-Söldner, R., and Betz, T. (2018). Self-organization: the fundament of cell biology. Philos. Trans. R. Soc. B Biol. Sci. *373*, 20170103. https://doi.org/10.1098/rstb.2017.0103.

Weidman, P.J., Melançon, P., Block, M.R., and Rothman, J.E. (1989). Binding of an N-ethylmaleimide-sensitive fusion protein to Golgi membranes requires both a soluble protein(s) and an integral membrane receptor. J. Cell Biol. *108*, 1589–1596. https://doi.org/10.1083/jcb.108.5.1589.

Weimbs, T., Low, S.H., Chapin, S.J., Mostov, K.E., Bucher, P., and Hofmann, K. (1997). A conserved domain is present in different families of vesicular fusion proteins: a new superfamily. Proc. Natl. Acad. Sci. U. S. A. *94*, 3046–3051. https://doi.org/10.1073/pnas.94.7.3046.

Wen, P.J., Grenklo, S., Arpino, G., Tan, X., Liao, H.-S., Heureaux, J., Peng, S.-Y., Chiang, H.-C., Hamid, E., Zhao, W.-D., et al. (2016). Actin dynamics provides membrane tension to merge fusing vesicles into the plasma membrane. Nat. Commun. *7*, 12604. https://doi.org/10.1038/ncomms12604.

Wijdeven, R.H., Janssen, H., Nahidiazar, L., Janssen, L., Jalink, K., Berlin, I., and Neefjes, J. (2016). Cholesterol and ORP1L-mediated ER contact sites control autophagosome transport and fusion with the endocytic pathway. Nat. Commun. *7*, 11808. https://doi.org/10.1038/ncomms11808.

Willett, R., Martina, J.A., Zewe, J.P., Wills, R., Hammond, G.R.V., and Puertollano, R. (2017). TFEB regulates lysosomal positioning by modulating TMEM55B expression and JIP4 recruitment to lysosomes. Nat. Commun. *8*, 1580. https://doi.org/10.1038/s41467-017-01871-z.

Williams, K.C., McNeilly, R.E., and Coppolino, M.G. (2014). SNAP23, Syntaxin4, and vesicle-associated membrane protein 7 (VAMP7) mediate trafficking of membrane type 1-matrix metalloproteinase (MT1-MMP) during invadopodium formation and tumor cell invasion. Mol. Biol. Cell *25*, 2061–2070. https://doi.org/10.1091/mbc.E13-10-0582.

Willy, N.M., Ferguson, J.P., Huber, S.D., Heidotting, S.P., Aygün, E., Wurm, S.A., Johnston-Halperin, E., Poirier, M.G., and Kural, C. (2017). Membrane mechanics govern spatiotemporal heterogeneity of endocytic clathrin coat dynamics. Mol. Biol. Cell *28*, 3480–3488. https://doi.org/10.1091/mbc.E17-05-0282.

Wilson, D.W., Wilcox, C.A., Flynn, G.C., Chen, E., Kuang, W.-J., Henzel, W.J., Block, M.R., Ullrich, A., and Rothman, J.E. (1989). A fusion protein required for vesicle-mediated transport in both mammalian cells and yeast. Nature *339*, 355–359. https://doi.org/10.1038/339355a0.

Winsor, E.J., and Welch, J.P. (1978). Genetic and demographic aspects of Nova Scotia Niemann-Pick disease (type D). Am. J. Hum. Genet. *30*, 530–538. .

Wollman, R., and Meyer, T. (2012). Coordinated oscillations in cortical actin and Ca2+ correlate with cycles of vesicle secretion. Nat. Cell Biol. *14*, 1261–1269. https://doi.org/10.1038/ncb2614.

Wu, B., and Guo, W. (2015). The Exocyst at a Glance. J. Cell Sci. *128*, 2957–2964. https://doi.org/10.1242/jcs.156398.

Wu, J., Lewis, A., and Grandl, J. (2017a). Touch, Tension, and Transduction – the Function and Regulation of Piezo Ion Channels. Trends Biochem. Sci. *42*, 57–71. https://doi.org/10.1016/j.tibs.2016.09.004.

Wu, X.-S., Elias, S., Liu, H., Heureaux, J., Wen, P.J., Liu, A.P., Kozlov, M.M., and Wu, L.-G. (2017b). Membrane Tension Inhibits Rapid and Slow Endocytosis in Secretory Cells. Biophys. J. *113*, 2406–2414. https://doi.org/10.1016/j.bpj.2017.09.035.

Wu, X.-S., Elias, S., Liu, H., Heureaux, J., Wen, P.J., Liu, A.P., Kozlov, M.M., and Wu, L.-G. (2017c). Membrane Tension Inhibits Rapid and Slow Endocytosis in Secretory Cells. Biophys. J. *113*, 2406–2414. https://doi.org/10.1016/j.bpj.2017.09.035.

Xiang, L., Chen, K., Yan, R., Li, W., and Xu, K. (2020). Single-molecule displacement mapping unveils nanoscale heterogeneities in intracellular diffusivity. Nat. Methods *17*, 524–530. https://doi.org/10.1038/s41592-020-0793-0.

Xu, H., and Ren, D. (2015). Lysosomal physiology. Annu. Rev. Physiol. *77*, 57–80. https://doi.org/10.1146/annurev-physiol-021014-071649.

Xu, J., Toops, K.A., Diaz, F., Carvajal-Gonzalez, J.M., Gravotta, D., Mazzoni, F., Schreiner, R., Rodriguez-Boulan, E., and Lakkaraju, A. (2012). Mechanism of polarized lysosome exocytosis in epithelial cells. J. Cell Sci. *125*, 5937–5943. https://doi.org/10.1242/jcs.109421.

Xu, Y., Toomre, D.K., Bogan, J.S., and Hao, M. (2017). Excess cholesterol inhibits glucose-stimulated fusion pore dynamics in insulin exocytosis. J. Cell. Mol. Med. *21*, 2950–2962. https://doi.org/10.1111/jcmm.13207.

Yadav, A., Gao, Y.Z., Rodriguez, A., Dickstein, D.L., Wearne, S.L., Luebke, J.I., Hof, P.R., and Weaver, C.M. (2012). Morphologic Evidence for Spatially Clustered Spines in Apical Dendrites of Monkey Neocortical Pyramidal Cells. J. Comp. Neurol. *520*, 2888–2902. https://doi.org/10.1002/cne.23070.

Yamagishi, T., Sahni, S., Sharp, D.M., Arvind, A., Jansson, P.J., and Richardson, D.R. (2013). P-glycoprotein mediates drug resistance via a novel mechanism involving lysosomal sequestration. J. Biol. Chem. *288*, 31761–31771. https://doi.org/10.1074/jbc.M113.514091.

Yang, C., and Wang, X. (2021). Lysosome biogenesis: Regulation and functions. J. Cell Biol. *220*, e202102001. https://doi.org/10.1083/jcb.202102001.

Yang, Z., and Klionsky, D.J. (2010). Eaten alive: a history of macroautophagy. Nat. Cell Biol. *12*, 814–822. https://doi.org/10.1038/ncb0910-814.

Yang, Y., Zhai, X., and El Hiani, Y. (2020). TRPML1—Emerging Roles in Cancer. Cells *9*, 2682. https://doi.org/10.3390/cells9122682.

Young, M., Lewis, A.H., and Grandl, J. (2022). Physics of mechanotransduction by Piezo ion channels. J. Gen. Physiol. *154*, e202113044. https://doi.org/10.1085/jgp.202113044.

Yu, I.-M., and Hughson, F.M. (2010). Tethering factors as organizers of intracellular vesicular traffic. Annu. Rev. Cell Dev. Biol. *26*, 137–156. https://doi.org/10.1146/annurev.cellbio.042308.113327.

Yuan, T., Lu, J., Zhang, J., Zhang, Y., and Chen, L. (2015). Spatiotemporal detection and analysis of exocytosis reveal fusion "hotspots" organized by the cytoskeleton in endocrine cells. Biophys. J. *108*, 251–260. https://doi.org/10.1016/j.bpj.2014.11.3462.

Yunta, M.L., Lagache, T., Santi-Rocca, J., Bastin, P., and Olivo-Marin, J.-C. (2014). A statistical analysis of spatial clustering along cell filaments using Ripley's K function. In 2014 IEEE 11th International Symposium on Biomedical Imaging (ISBI), pp. 541–544.

Zhang, C., and Zhou, Z. (2002). Ca2+-independent but voltage-dependent secretion in mammalian dorsal root ganglion neurons. Nat. Neurosci. *5*, 425–430. https://doi.org/10.1038/nn845.

Zhang, L., Del Castillo, A.R., and Trifaró, J.-M. (1995). Histamine-Evoked Chromaffin Cell Scinderin Redistribution, F-Actin Disassembly, and Secretion: In the Absence of Cortical F-Actin Disassembly, an Increase in Intracellular Ca2+ Fails to Trigger Exocytosis. J. Neurochem. *65*, 1297–1308. https://doi.org/10.1046/j.1471-4159.1995.65031297.x.

Zhang, L., Sheng, R., and Qin, Z. (2009). The lysosome and neurodegenerative diseases. Acta Biochim. Biophys. Sin. *41*, 437–445. https://doi.org/10.1093/abbs/gmp031.

Zhang, Y., Jiang, X., Deng, Q., Gao, Z., Tang, X., Fu, R., Hu, J., Li, Y., Li, L., and Gao, N. (2019). Downregulation of MYO1C mediated by cepharanthine inhibits autophagosome-lysosome fusion through blockade of the F-actin network. J. Exp. Clin. Cancer Res. *38*, 457. https://doi.org/10.1186/s13046-019-1449-8.

Zhao, H., Ito, Y., Chappel, J., Andrews, N.W., Teitelbaum, S.L., and Ross, F.P. (2008). Synaptotagmin VII Regulates Bone Remodeling by Modulating Osteoclast and Osteoblast Secretion. Dev. Cell *14*, 914–925. https://doi.org/10.1016/j.devcel.2008.03.022.

Zheng, H., Fan, J., Xiong, W., Zhang, C., Wang, X.-B., Liu, T., Liu, H.-J., Sun, L., Wang, Y.-S., Zheng, L.-H., et al. (2009). Action Potential Modulates Ca2+-Dependent and Ca2+-Independent Secretion in a Sensory Neuron. Biophys. J. *96*, 2449–2456. https://doi.org/10.1016/j.bpj.2008.11.037.

Zhu, H., Li, Q., Liao, T., Yin, X., Chen, Q., Wang, Z., Dai, M., Yi, L., Ge, S., Miao, C., et al. (2021). Metabolomic profiling of single enlarged lysosomes. Nat. Methods *18*, 788–798. https://doi.org/10.1038/s41592-021-01182-8.

Zwiewka, M., Nodzyński, T., Robert, S., Vanneste, S., and Friml, J. (2015). Osmotic Stress Modulates the Balance between Exocytosis and Clathrin-Mediated Endocytosis in Arabidopsis thaliana. Mol. Plant *8*, 1175–1187. https://doi.org/10.1016/j.molp.2015.03.007.

(1834). Rapport sur la marche et les effets du choléra-morbus dans Paris et les communes rurales du département de la Seine : année 1832 ([Reprod.]) / par la Commission nommée, avec l'approbation de M. le ministre du Commerce et des travaux publics, par MM. les préfets de la Seine et de police.

(1996). Oscillatory enzymes: simple periodic behaviour in an allosteric model for glycolytic oscillations. In Biochemical Oscillations and Cellular Rhythms: The Molecular Bases of Periodic and Chaotic Behaviour, A. Goldbeter, ed. (Cambridge: Cambridge University Press), pp. 31–88.

I sincelerely aknwlodge the editors who accepted to gave me the licence to freely reproduced figures from papers and books in this thesis manuscript. Especially, figures 15, 17 and 35 are From MOLECULAR BIOLOGY OF THE CELL, SIXTH EDITION by Bruce Alberts, et al. Copyright © 2015 by Bruce Alberts, Alexander Johnson, Julian Lewis, David Morgan, Martin Raff, Keith Roberts, and Peter Walter. Used by permission of W.W. Norton & Company, Inc. In addition to this permission, each figure is cited accordingly.

RÉSUMÉ

Le vivant est caractérisé par son organisation, présente à plusieurs échelles et sous différentes formes. Durant ma thèse, j'ai travaillé sur l'organisation spatiale des sites d'exocytose lysosomale. Alors qu'il est admis que les sites d'exocytose des vésicules Golgienne ne sont pas aléatoirement distribués, mais agrégés, il n'y a pas de donnée quantitative sur l'exocytose lysosomale. J'ai exploré cette question grâce à de l'imagerie en direct de la v-SNARE lysosomale VAMP7 marquée par la pHluorine par microscopie à fluorescence en réflexion totale. L'imagerie en direct permet l'obtention de cartes d'exocytose, interprétées comme des motifs de points analysés avec les outils des statistiques spatiales. Un grand jeu de données contenant environ 180 cellules et 30 000 événements d'exocytose révèle sans ambigüité que l'exocytose lysosomale est agrégée dans le modèle des cellules épithéliales de rétine RPE1. Les événements d'exocytose apparaissent partiellement aux adhésions focales, et leur agrégation est réduite après une inhibition des adhésions focales. En plus du rôle des adhésions focales, la littérature indique que la tension de membrane régule également l'exocytose. Des perturbations de la tension de membrane par des chocs hypo-osmotiques ou un traitement au méthyl-β-cyclodextrine augmentent l'agrégation. Pour explorer le lien entre adhésions focales et tension de membranes, les cellules ont été cultivées sur des micropatrons adhésifs en forme d'anneau et la sonde méchanosensible de microscopie par temps de vie de fluorescence Flipper-TR a été utilisée. De façon inattendue, ce protocole a révélé que les cellules ensemencées sur ces micropatrons présentent un gradient radial de tension de membrane. En modifiant le diamètre des micropatrons, nous avons également montré que ce gradient ainsi que l'agrégation de l'exocytose pouvaient être contrôlés. Ces données indiquent que l'agrégation spatiale de l'exocytose lysosomale repose sur l'organisation de la tension de membrane contrôlée par l'organisation spatiale des adhésions focales.

MOTS CLÉS

Exocytose – Lysosome – Adhésion focale – VAMP7 – Tension de membrane – Fonction K de Ripley – statistiques spatiales – FLIM – TIRFM – Flipper-TR – Micropatron

ABSTRACT

Life is characterized by its organization, present at many scales and under different forms. In this thesis, I worked on the spatial organization of lysosomal exocytosis sites. While it is consensual that Golgi-derived vesicles exocytosis sites are not randomly distributed but clustered, quantitative data was lacking for lysosomal exocytosis. I explored this question thanks to live imaging of the pHluorin tagged lysosomal v-SNARE VAMP7 by total internal reflection fluorescence microscopy. Live-imaging allows the obtention of exocytosis maps, interpreted as a pattern of points analyzed with tools from spatial statistics. A large dataset of about 180 cells and 30 000 exocytosis events reveals without ambiguity that lysosomal exocytosis is clustered in the RPE1 retinal epithelial cell model. Exocytosis events partially appear at focal adhesions and their clustering is reduced upon removal of focal adhesions. In addition to focal adhesions, literature indicates that membrane tension also regulates exocytosis. Changes in membrane tension following a hypo-osmotic shock or treatment with methyl-β-cyclodextrin was found to increase clustering. To investigate the link between focal adhesions and membrane tension, cells were cultured on adhesive ring-shaped micropatterns and the mechanosensitive fluorescence-lifetime imaging microscopy probe Flipper-TR has been used. Unexpectedly, this protocol revealed that cells seeded on these micropatterns display a radial gradient of membrane tension. By changing the diameter of micropatterned substrates, we further showed that this gradient as well as the extent of exocytosis clustering can be controlled. Together, our data indicate that the spatial clustering of lysosomal exocytosis relies on membrane tension patterning controlled by the spatial organization of focal adhesions.

KEYWORDS

Exocytosis – Lysosome – Focal adhesion – VAMP7 – Membrane tension – Ripley's K function – Spatial statistics – FLIM – TIRFM – Flipper-TR – Micropattern